

THE UNIVERSITY OF HULL

---

Radio-echo Sounding of Pine Island  
Glacier, West Antarctica: Understanding  
the Past from Observations, Analysis and  
Modelling of Internal Layering

---

being a Thesis submitted for the Degree of  
Doctor of Philosophy  
in the University of Hull

by

*Nanna Bjørnholt Karlsson*

(bach.scient., cand.scient., University of Copenhagen)

November, 2010



# Abstract

Pine Island Glacier is one of the fastest and most dynamic glaciers in West Antarctica. The stability of the glacier may thus have profound impact on the overall stability of the West Antarctic Ice Sheet and its contribution to global sea-level rise. This thesis addresses questions concerning the past dynamics of the glacier using observations of the internal layers in the ice imaged by radio-echo sounding.

Results from an extensive internal layer classification showed that no major spatial changes have taken place in the glacier although the analyses did identify signs indicating a past change of flow pattern in several localised areas in the northern part of the catchment basin. Results also indicated that different parts of Pine Island Glacier are likely to respond in different ways to external forcing. The analyses of the radar data were facilitated by the development of new methods for layer classification and tracing.

The second part of this thesis focussed on modelling the internal layers using two- and three-dimensional numerical ice flow models. Comparisons between the observed layers and results from the three-dimensional model indicated that a likely change in accumulation rate and pattern had taken place during the past 7 kyr - 17.5 kyr. The model also indicated a time scale for the changes in flow pattern of approximately 6 - 10 kyr. Results from the two-dimensional model further highlighted areas likely to have undergone changes in past ice flow pattern.

The results from this study can feed into current efforts to understand the past dynamics of WAIS in order to establish its response to future climate change.



# Acknowledgements

This thesis could not have been completed without the support and encouragement from my supervisor David M. Rippin. Throughout my project he has provided invaluable guidance into the wondrous world of radioglaciology, given me direction through the labyrinth that is a Ph.D. project, patiently walked me up the mountain of scientific writing and dragged me out of the holes I at times have dug myself into.

I am also very grateful for the supervision of Robert G. Bingham, whose expertise I have greatly benefited from and who with great insight has corrected many mistakes along the way. While he has been a supervisor from a distance (even from Antarctica) during most of my Ph.D. he has always responded with enthusiasm and knowledge to matters big and small.

I am lucky to have had supervisors who, no matter how busy, always have found the time to provide feedback and comments, and who always have expressed great interest in my work. For this I cannot thank you enough. It has been a pleasure working with you both.

My thanks go also to Richard C. A. Hindmarsh for letting me use his ice flow model and for always finding the time in his busy schedule to answer my questions. Thanks also to Julian B. T. Scott for providing me with the flowline program. I would also like to acknowledge Carlos Martin for numerous theoretical conversations about numerical modelling and for patiently giving advice on the same topic. Also thanks to David G. Vaughan for hosting me at the British Antarctic Survey's IceSheets group during the last part of my Ph.D., and to Thomas Coulthard and Graham Ferrier.

I greatly appreciate the comments and corrections from Rosie Williams, who listened to my grumblings and who liked my equations. Comments from fellow-student Michael Prior-Jones were also much appreciated.

Finally, a thanks to my parents and my sister for being there through the ups

and downs of this Ph.D. journey, and to Dave who caught all the little mistakes, fed me pizza, saw me through it and whose support and company have kept me sane.

I gratefully acknowledge the financial support of the Ph.D. studentship program at The University of Hull and Department of Geography, University of Hull. I also wish to acknowledge the support from the Research Support Fund at Department of Geography and the Grad School's Conference Presentation Fund at University of Hull, as well as the Anglo-Danish Society, the International Glaciological Society and the British Antarctic Survey. Additional monies from Dr. J. W. Holt, (NASA grant NAG5-12693), The Institute for Geophysics, University of Texas at Austin, The Antarctic Science Bursary, The Geological Remote Sensing Group and the Dudley Stamp Memorial Fund of The Royal Geographical Society with IBG enabled me to extend my Ph.D. work to the Martian ice caps. Although results from that work does not feature directly in this thesis it provided many additional insights that benefited the work presented here.

# Contents

|   |            |
|---|------------|
| <b>List of Figures</b>  | <b>xv</b>  |
| <b>List of Tables</b>   | <b>xxi</b> |
| <b>1 Introduction</b>   | <b>1</b>   |
| 1.1 The West Antarctic Ice Sheet . . . . .                    | 2          |
| 1.1.1 Reconstructing the History of the WAIS . . . . .        | 3          |
| 1.1.1.1 Data Sources . . . . .                                | 4          |
| 1.1.1.2 WAIS in the Pleistocene and Pliocene . . . . .        | 6          |
| 1.1.1.3 WAIS during the Holocene . . . . .                    | 8          |
| 1.2 Radio Echo Sounding in Glaciology . . . . .               | 12         |
| 1.3 Aims of the Thesis . . . . .                              | 15         |
| 1.4 Thesis Organisation . . . . .                             | 17         |
| <b>2 Background to Radioglaciology and Ice Flow Modelling</b> | <b>19</b>  |
| 2.1 Introduction to Radioglaciology . . . . .                 | 19         |
| 2.1.1 Electrical Properties of Ice . . . . .                  | 21         |
| 2.2 Internal Reflections in Ice . . . . .                     | 23         |
| 2.2.1 Origins of Internal Layers . . . . .                    | 23         |
| 2.2.1.1 Changes in Permittivity . . . . .                     | 24         |
| 2.2.1.2 Changes in Conductivity . . . . .                     | 26         |
| 2.2.1.3 Echo-Free Zone . . . . .                              | 27         |
| 2.2.2 RES Data Processing . . . . .                           | 27         |
| 2.2.2.1 Signal Attenuation . . . . .                          | 28         |
| 2.2.2.2 Data Processing . . . . .                             | 30         |
| 2.2.3 Internal Ice-Sheet Structure . . . . .                  | 32         |
| 2.2.4 Past Accumulation Rates . . . . .                       | 33         |
| 2.2.5 Basal Melting . . . . .                                 | 35         |
| 2.2.6 Internal Layering and Ice Flow Dynamics . . . . .       | 36         |
| 2.2.7 Summary . . . . .                                       | 38         |

|          |  |           |
|----------|--|-----------|
| 2.3      | Other RES Measurements . . . . .                     | 38        |
| 2.3.1    | Ice Thickness Measurements . . . . .                 | 39        |
| 2.3.2    | Basal Conditions . . . . .                           | 40        |
| 2.3.3    | Subglacial Lakes . . . . .                           | 41        |
| 2.4      | Modelling Internal Layers in Glaciers . . . . .      | 43        |
| 2.4.1    | Introduction to Ice Flow Modelling . . . . .         | 43        |
| 2.4.2    | Age Distribution in Flowing Ice . . . . .            | 44        |
| 2.4.3    | Deformation of Ice Crystals . . . . .                | 45        |
| 2.4.4    | Continuum Mechanics of Ice . . . . .                 | 46        |
| 2.4.4.1  | The Stress Tensor . . . . .                          | 47        |
| 2.4.4.2  | Strain Rates . . . . .                               | 49        |
| 2.4.5    | The Shallow Ice Flow Approximation . . . . .         | 49        |
| 2.4.5.1  | Flow along a Flowline . . . . .                      | 51        |
| 2.4.5.2  | The Dansgaard-Johnsen Model . . . . .                | 53        |
| 2.5      | Chapter Summary . . . . .                            | 54        |
| <b>3</b> | <b>Pine Island Glacier</b>                           | <b>57</b> |
| 3.1      | The Significance of Pine Island Glacier . . . . .    | 58        |
| 3.2      | Flow Configuration and Topography . . . . .          | 61        |
| 3.3      | Observations of Rapid Change . . . . .               | 64        |
| 3.3.1    | Ice Velocities and Acceleration . . . . .            | 64        |
| 3.3.2    | Ice Surface Elevation Change . . . . .               | 66        |
| 3.3.3    | Grounding Line Retreat . . . . .                     | 68        |
| 3.4      | Potential Forcing Mechanisms . . . . .               | 69        |
| 3.5      | Summary . . . . .                                    | 70        |
| <b>4</b> | <b>Methodology</b>                                   | <b>73</b> |
| 4.1      | Datasets from Pine Island Glacier . . . . .          | 73        |
| 4.1.1    | Radio-Echo Sounding of Pine Island Glacier . . . . . | 74        |
| 4.1.2    | InSAR Observations of Pine Island Glacier . . . . .  | 76        |
| 4.1.3    | Map Projections . . . . .                            | 77        |
| 4.2      | Radar Data Analysis . . . . .                        | 77        |
| 4.2.1    | Qualitative Classification . . . . .                 | 77        |
| 4.2.2    | Quantitative Classification . . . . .                | 80        |
| 4.2.2.1  | Observations on Radar Data . . . . .                 | 81        |
| 4.2.2.2  | Quantitative Methods . . . . .                       | 82        |
| 4.2.2.3  | Test of Different Methods . . . . .                  | 87        |
| 4.2.3    | Further Data Analysis Methods . . . . .              | 91        |
| 4.2.3.1  | Layer Tracing . . . . .                              | 92        |

|          |  |            |
|----------|--|------------|
| 4.2.3.2  | Exploring Surface Roughness . . . . .                                | 94         |
| 4.2.4    | Summary . . . . .  | 95         |
| 4.3      | Ice Flow Models . . . . .  | 97         |
| 4.3.1    | Three-Dimensional Model . . . . .                                    | 97         |
| 4.3.1.1  | EISMINT Topography . . . . .   | 99         |
| 4.3.1.2  | Fitting Layers to Model . . . . .                                    | 101        |
| 4.3.2    | Two-Dimensional Model . . . . .                                      | 101        |
| 4.3.2.1  | Model set-up . . . . .   | 101        |
| 4.3.2.2  | Finite Differences Method . . . . .                                  | 102        |
| 4.3.2.3  | Layer Fitting . . . . .  | 107        |
| 4.3.2.4  | Test of Model Results . . . . .                                      | 107        |
| 4.3.2.5  | Summary . . . . .  | 109        |
| 4.3.3    | Summary . . . . .  | 109        |
| <b>5</b> | <b>Radar Data Analyses</b>   | <b>111</b> |
| 5.1      | Qualitative Classification of Layers . . . . .                       | 111        |
| 5.1.1    | Results . . . . .  | 111        |
| 5.1.1.1  | General Layer Classification . . . . .                               | 112        |
| 5.1.1.2  | Subglacial Lakes . . . . .   | 114        |
| 5.1.1.3  | Buckled and Missing Layering . . . . .                               | 115        |
| 5.1.1.4  | Whirlwind-like Features . . . . .                                    | 117        |
| 5.1.2    | Interpretation of Qualitative Layer Classification Results . . . . . | 120        |
| 5.1.2.1  | Buckled Layering . . . . .   | 123        |
| 5.1.2.2  | Whirlwinds . . . . .   | 123        |
| 5.1.2.3  | Subglacial Water . . . . .   | 124        |
| 5.1.3    | Summary . . . . .  | 124        |
| 5.2      | Quantitative Classification . . . . .                                | 126        |
| 5.2.1    | Results . . . . .  | 126        |
| 5.2.1.1  | A Detailed Study of Flightline 14 . . . . .                          | 126        |
| 5.2.1.2  | Flightlines 10 - 14 . . . . .  | 131        |
| 5.2.1.3  | Comparison with Qualitative Method . . . . .                         | 133        |
| 5.2.1.4  | Other Flightlines . . . . .  | 133        |
| 5.2.2    | Summary . . . . .  | 133        |
| 5.3      | Layer Tracing . . . . .  | 136        |
| 5.3.1    | Layer Statistics . . . . .   | 136        |
| 5.3.2    | Retrieving Information from a Layer Package . . . . .                | 137        |
| 5.3.3    | Summary . . . . .  | 138        |
| 5.4      | Stresses and Internal Layering in PIG . . . . .                      | 141        |

|          |   |            |
|----------|---|------------|
| 5.4.1    | Driving Stress and Deformation . . . . .                              | 141        |
| 5.4.1.1  | Results . . . . .   | 141        |
| 5.4.1.2  | Interpretation . . . . .  | 142        |
| 5.4.2    | Internal Layering and Basal Shear Stress . . . . .                    | 143        |
| 5.4.2.1  | Results . . . . .   | 144        |
| 5.4.2.2  | Interpretation . . . . .  | 145        |
| 5.5      | Surface Roughness . . . . .   | 146        |
| 5.5.1    | Results . . . . .   | 146        |
| 5.5.2    | Comparison with Basal Roughness and Shear Stress . . . . .            | 147        |
| 5.5.3    | Interpretation . . . . .  | 148        |
| 5.6      | Discussion . . . . .  | 151        |
| 5.7      | Conclusion . . . . .  | 155        |
| <b>6</b> | <b>Investigating Internal Layering with a Three-Dimensional Model</b> | <b>157</b> |
| 6.1      | Modelling Approach . . . . .  | 157        |
| 6.1.1    | Layer Fitting . . . . .   | 158        |
| 6.1.1.1  | General Layer Fitting . . . . .                                       | 159        |
| 6.1.1.2  | Tephra Layer . . . . .  | 159        |
| 6.1.1.3  | Layer Package . . . . .   | 159        |
| 6.1.2    | Parameter Choices . . . . .   | 160        |
| 6.1.2.1  | Surface and Bed Topography . . . . .                                  | 160        |
| 6.1.2.2  | Control Scenario . . . . .  | 161        |
| 6.1.2.3  | Accumulation Pattern . . . . .  | 161        |
| 6.1.2.4  | Basal melting . . . . .   | 164        |
| 6.1.2.5  | Flow Mode . . . . .   | 166        |
| 6.1.2.6  | Vertical and Horizontal Resolution . . . . .                          | 166        |
| 6.1.2.7  | Estimating Optimum Parameters . . . . .                               | 167        |
| 6.1.3    | Calculating the Surface Velocity . . . . .                            | 167        |
| 6.1.4    | Quantifying the Fit . . . . .   | 168        |
| 6.2      | Individual Layer Fitting . . . . .                                    | 170        |
| 6.2.1    | Effects of Varying Parameters . . . . .                               | 170        |
| 6.2.1.1  | Accumulation Pattern . . . . .  | 172        |
| 6.2.1.2  | Basal melting . . . . .   | 172        |
| 6.2.1.3  | Vertical and Horizontal Resolution . . . . .                          | 173        |
| 6.2.1.4  | Flow Mode . . . . .   | 174        |
| 6.2.1.5  | Additional Considerations . . . . .                                   | 176        |
| 6.2.2    | Interpretation . . . . .  | 177        |
| 6.3      | Tephra Layer . . . . .  | 181        |

|          |   |            |
|----------|---|------------|
| 6.3.1    | Effects of Varying Parameters . . . . .                               | 181        |
| 6.3.1.1  | Accumulation Pattern . . . . .  | 181        |
| 6.3.1.2  | Basal Melting . . . . .   | 182        |
| 6.3.1.3  | Horizontal and Vertical Resolution . . . . .                          | 183        |
| 6.3.1.4  | Flow Mode . . . . .   | 183        |
| 6.3.2    | Estimating Optimum Parameters . . . . .                               | 184        |
| 6.3.3    | Interpretation . . . . .  | 185        |
| 6.4      | Layer Package . . . . .   | 187        |
| 6.4.1    | Effects of Varying Parameters . . . . .                               | 190        |
| 6.4.1.1  | Accumulation Pattern . . . . .  | 190        |
| 6.4.1.2  | Basal Melting . . . . .   | 191        |
| 6.4.1.3  | Flow Mode . . . . .   | 194        |
| 6.4.1.4  | Horizontal and Vertical Resolution . . . . .                          | 196        |
| 6.4.2    | Estimating Optimum Parameters . . . . .                               | 196        |
| 6.4.2.1  | Localised Melting or Accumulation . . . . .                           | 197        |
| 6.4.2.2  | Internal Deformation and Increased Vertical Res-<br>olution . . . . . | 197        |
| 6.4.2.3  | Summary of Parameter Estimation . . . . .                             | 200        |
| 6.4.3    | Interpretation . . . . .  | 200        |
| 6.5      | Estimating Age and Accumulation Values . . . . .                      | 202        |
| 6.5.1    | Methods . . . . .   | 203        |
| 6.5.2    | Results . . . . .   | 205        |
| 6.5.3    | Interpretation . . . . .  | 205        |
| 6.6      | Discussion . . . . .  | 208        |
| 6.7      | Conclusion . . . . .  | 211        |
| <b>7</b> | <b>Two-Dimensional Flow Model</b>                                     | <b>213</b> |
| 7.1      | Modelling Approach . . . . .  | 213        |
| 7.1.1    | Model Parameters . . . . .  | 214        |
| 7.1.1.1  | Surface and Bed Topography Input . . . . .                            | 214        |
| 7.1.1.2  | Surface Velocity . . . . .  | 215        |
| 7.1.1.3  | Boundary Condition . . . . .  | 215        |
| 7.2      | Results . . . . .   | 216        |
| 7.2.1    | Test of Two-Dimensional Model . . . . .                               | 216        |
| 7.2.2    | Comparison with Radar Data . . . . .                                  | 216        |
| 7.2.3    | Layer Fitting . . . . .   | 219        |
| 7.3      | Interpretation . . . . .  | 223        |
| 7.4      | Discussion . . . . .  | 225        |

---

|          |   |            |
|----------|---|------------|
| 7.5      | Conclusion . . . . .  | 225        |
| <b>8</b> | <b>Discussion and Conclusion</b>                            | <b>227</b> |
| 8.1      | Summary and Discussion . . . . .                            | 228        |
| 8.1.1    | Classification of Internal Layering . . . . .               | 228        |
| 8.1.2    | Flow Patterns from Other Properties . . . . .               | 229        |
| 8.1.3    | Comparison between Modelled and Observed Layering . . . . . | 230        |
| 8.1.4    | Paleo-flow conditions of PIG . . . . .                      | 231        |
| 8.2      | Impacts of the Research . . . . .                           | 232        |
| 8.3      | Conclusion . . . . .  | 233        |
| 8.4      | Future Work . . . . .                                       | 234        |
|          | <b>References</b>   | <b>237</b> |
| <b>A</b> | <b>Construction of a Two-Dimensional Ice Flow Model</b>     | <b>261</b> |

# Glossary

## Abbreviations and Acronyms

**AUV** Autonomous Underwater Vehicle

**BAS** British Antarctic Survey

**BASISM** British Antarctic Survey Ice Sheet Model (see Section 4.3.1)

**EAIS** East Antarctic Ice Sheet

**ERS-1/2** European Remote Sensing satellite 1 or 2

**FD** Finite Difference

**FFT** Fast Fourier Transform

**HF/VHF** High Frequency/Very High Frequency

**InSAR** Interferometric Synthetic Aperture Radar

**ITASE** International Trans-Antarctic Scientific Expedition

**LIMA** Landsat Image Mosaic Of Antarctica

**MOA** MODIS Mosaic of Antarctica

**MODIS** Moderate-resolution Imaging Spectroradiometer

**PASIN** Polarimetric Airborne Survey INstrument (see Section 4.1.1)

**PIG** Pine Island Glacier

**RES** Radio-Echo Sounding

**SIA** Shallow Ice-Flow Approximation

**SPRI-NSF-TUD** Scott Polar Research Institute, National Science Foundation  
and Technical University of Denmark

**US-ITASE** US portion of the International Trans-Antarctic Scientific Expedition

**UTIG** University of Texas Institute for Geophysics

**WAIS** West Antarctic Ice Sheet

## List of Symbols

| Symbol                 | Parameter   | Unit                            |
|------------------------|---|---------------------------------|
| $\mathbf{r} = r(x, y)$ | $(x, y)$ -coordinate vector   | m                               |
| $z$                    | Vertical coordinate   | m                               |
| $\zeta$                | Normalised $z$ -coordinate  | -                               |
| $t$                    | Time  | s or yr                         |
| $\Delta_{xy}$          | Horizontal resolution   | m                               |
| $\Delta_{\zeta}$       | Vertical normalised resolution  | -                               |
| $\nabla$               | Gradient $\left(\frac{\partial}{\partial x}, \frac{\partial}{\partial y}, \frac{\partial}{\partial z}\right)$ | -                               |
| $\nabla_H$             | Horizontal gradient $\left(\frac{\partial}{\partial x}, \frac{\partial}{\partial y}\right)$                   | -                               |
| $H$                    | Ice thickness   | m                               |
| $L$                    | Length of ice cap   | m                               |
| $s$                    | Surface elevation   | m                               |
| $\alpha$               | Surface slope   | -                               |
| $b$                    | Bed elevation   | m                               |
| $a$                    | Accumulation  | $\text{m yr}^{-1}$              |
| $m$                    | Basal melt rate   | $\text{m yr}^{-1}$              |
| $\rho$                 | Density   | $\text{kg m}^{-3}$              |
| $\theta$               | Temperature   | K                               |
| $k_i$                  | Thermal conductivity  | $\text{W K}^{-1} \text{m}^{-1}$ |
| $c_p$                  | Heat capacity   | $\text{J g}^{-1} \text{K}^{-1}$ |
| $\epsilon$             | Relative permittivity   | -                               |
| $\sigma$               | Electrical conductivity   | $\text{S m}^{-1}$               |
| $X$                    | Age   | yr                              |
| $f$                    | Frequency   | Hz                              |
| $\omega$               | Angular frequency   | Hz                              |
| $v_{ice}$              | Speed of radar waves in ice   | $\text{m s}^{-1}$               |
| $c$                    | Speed of radar waves in free space  | $\text{m s}^{-1}$               |
| $R$                    | Power reflection coefficient  | -                               |
| $P$                    | Power of radar signal   | W                               |

|   |                              |                                   |
|---|------------------------------|-----------------------------------|
| $\mathbf{v} = (u, v, w)$                    | Velocity field               | $\text{m yr}^{-1}$                |
| $\mathbf{u}(\mathbf{r}, \zeta, \mathbf{t})$ | Horizontal ice flow velocity | $\text{m yr}^{-1}$                |
| $\mathbf{w}(\mathbf{r}, \zeta, \mathbf{t})$ | Vertical ice flow velocity   | $\text{m yr}^{-1}$                |
| $\bar{u}$                                   | Average horizontal velocity  | $\text{m yr}^{-1}$                |
| $u_s$                                       | Horizontal surface velocity  | $\text{m yr}^{-1}$                |
| $F_B$                                       | Basal sliding ratio          | -                                 |
| $v$   | Velocity shape function      | -                                 |
| $Q$   | Mass flux                    | $\text{m}^2 \text{yr}^{-1}$       |
| $q$   | Partial (mass) flux          | $\text{m}^2 \text{yr}^{-1}$       |
| $\bar{\sigma}$                              | Stress tensor                | Pa                                |
| $\sigma_i$                                  | Normal stress                | Pa                                |
| $\tau_{ij}$                                 | Shear stress                 | Pa                                |
| $\tau_d$                                    | Driving stress               | Pa                                |
| $\dot{\epsilon}$                            | Strain rate                  | $\text{yr}^{-1}$                  |
| $A$   | Ice flow law parameter       | $\text{s}^{-1} (\text{kPa})^{-3}$ |
| $n$   | Flow law exponent            | -                                 |
| $g$   | Gravitational constant       | $\text{m s}^{-2}$                 |
| $\Phi$                                      | Frictional heat              | J                                 |
| $h$   | Kink height                  | m                                 |
| $B$   | Viscosity parameter          | $\text{Pa yr}^{1/3}$              |
| $\psi$                                      | Quantitative layer value     | -                                 |

# List of Figures

|      |   |    |
|------|---|----|
| 1.1  | Overview map of Antarctica . . . . .  | 2  |
| 1.2  | Velocity map of Antarctic glaciers . . . . .                                | 4  |
| 1.3  | The Vostok ice core records . . . . .                                       | 5  |
| 1.4  | Extent of the WAIS during three stages . . . . .                            | 7  |
| 1.5  | Antarctica at the LGM . . . . .   | 8  |
| 1.6  | Glacial landforms in Pine Island Bay . . . . .                              | 10 |
| 1.7  | Ionogram . . . . .  | 13 |
| 2.1  | Example of radargram . . . . .  | 20 |
| 2.2  | Ice crystal structure . . . . .   | 21 |
| 2.3  | Density and permittivity . . . . .  | 26 |
| 2.4  | Example of SPRI data . . . . .  | 31 |
| 2.5  | Example of near surface layers . . . . .                                    | 34 |
| 2.6  | Example of three different kinds of layering . . . . .                      | 37 |
| 2.7  | Subglacial lakes . . . . .  | 41 |
| 2.8  | Overview of ice sheet processes . . . . .                                   | 44 |
| 2.9  | Strain and strain rate relation . . . . .                                   | 46 |
| 2.10 | Stress and strain . . . . .   | 48 |
| 2.11 | Force balance on a slab of ice . . . . .                                    | 50 |
| 2.12 | Mass conservation in a column of ice . . . . .                              | 52 |
| 3.1  | Surface elevation of Antarctica . . . . .                                   | 59 |
| 3.2  | Surface elevation change over West Antarctica . . . . .                     | 60 |
| 3.3  | MOA surface imagery and surface elevation contours of PIG . . . . .         | 62 |
| 3.4  | Surface velocities of PIG . . . . .   | 63 |
| 3.5  | Bed elevation of PIG . . . . .  | 64 |
| 3.6  | Surface velocities of PIG in 1974, 1987, 1992, 1996 and 2001-2005 . . . . . | 65 |
| 3.7  | Ice discharge from PIG in 1974, 1996, 2000, 2006 and 2007 . . . . .         | 66 |
| 3.8  | Surface elevation change of PIG in 1995 and 2006 . . . . .                  | 68 |
| 4.1  | Photograph of the Twinotter aircraft . . . . .                              | 74 |

|      |   |     |
|------|---|-----|
| 4.2  | Map of PASIN data coverage . . . . .  | 75  |
| 4.3  | Example of chirped and pulsed data . . . . .  | 76  |
| 4.4  | Example of three different kinds of internal layering . . . . .   | 79  |
| 4.5  | Examples of whirlwinds-like features . . . . .  | 80  |
| 4.6  | Example of internal layers from flightline 12 . . . . .   | 82  |
| 4.7  | Example of two wiggle plots from flightline 12 . . . . .  | 83  |
| 4.8  | Radargram and wiggle plot from trace 34000, flightline 12 . . . . .   | 86  |
| 4.9  | Radargram and wiggle plot from trace 41000, flightline 12 . . . . .   | 86  |
| 4.10 | Flightline 12 masked for lacunarity analysis . . . . .  | 88  |
| 4.11 | (a) Radargram from flightline 12, (b) Correlation coefficient and<br>(c) Area under curve . . . . .                               | 89  |
| 4.12 | (a) Radargram from flightline 12, (b) $\psi$ -values and (c) the results<br>of the lacunarity analysis . . . . .                  | 90  |
| 4.13 | (a) Radargram from “Duckfoot” C and (b) $\psi$ -values . . . . .  | 92  |
| 4.14 | Example of layer tracing . . . . .  | 93  |
| 4.15 | Example of surface undulations . . . . .  | 94  |
| 4.16 | (a) Example of surface undulations (b) detrended surface topogra-<br>phy and (c) natural logarithm of surface roughness . . . . . | 96  |
| 4.17 | Examples of (a) surface and bed elevation (b) changed to nor-<br>malised elevation . . . . .                                      | 98  |
| 4.18 | (a) Surface and bed topography used in the EISMINT test and (b)<br>context map for Figures 4.19a and 4.19b . . . . .              | 100 |
| 4.19 | Cross section through (a) the centre of the ice-sheet and (b) diag-<br>onally . . . . .   | 100 |
| 4.20 | Illustration of the finite differences method . . . . .   | 103 |
| 4.21 | Isochrones in a 2D velocity field with increased basal melting . . . . .  | 108 |
| 4.22 | Isochrones in a 2D velocity field with a bumpy bedrock . . . . .  | 110 |
| 5.1  | Classification of internal layering in flightlines 10-14 . . . . .  | 112 |
| 5.2  | Classification of internal layering in flightlines 10 - 14 with bed<br>topography . . . . .                                       | 114 |
| 5.3  | Classification of internal layering in all flightlines . . . . .  | 115 |
| 5.4  | Classification of internal layering in all flightlines for entire PIG<br>catchment . . . . .                                      | 116 |
| 5.5  | Map of subglacial lakes . . . . .   | 117 |
| 5.6  | Map of buckled layering in flightlines 10 - 14 . . . . .  | 118 |
| 5.7  | Map of whirlwind features in flightlines 10 - 14 . . . . .  | 119 |
| 5.8  | Map of whirlwind features in all flightlines . . . . .  | 121 |
| 5.9  | $\psi$ -values for all of flightline 14 . . . . .   | 127 |

|      |   |     |
|------|---|-----|
| 5.10 | $\psi$ -values for flightline 14, box 1 . . . . .   | 128 |
| 5.11 | $\psi$ -values for flightline 14, box 2 . . . . .   | 129 |
| 5.12 | $\psi$ -values for flightline 14, box 3 . . . . .   | 130 |
| 5.13 | $\psi$ -values for flightline 14, box 4 . . . . .   | 131 |
| 5.14 | $\psi$ -values for flightlines 10-14 smoothed over (a) 100 and (b) 1000<br>traces . . . . .   | 132 |
| 5.15 | Example of changes in acquisition height from flightline 06 . . . . .   | 134 |
| 5.16 | Average layer (a) length and (b) normalised elevation . . . . .   | 136 |
| 5.17 | Example of the layer package and map of its location . . . . .  | 139 |
| 5.18 | Gridded elevation map of Layer 1 . . . . .  | 140 |
| 5.19 | Gridded elevation map of Layer 2 . . . . .  | 140 |
| 5.20 | (a) Deformational velocity and (b) observed surface velocity . . . . .  | 142 |
| 5.21 | Deformational velocity and subglacial topography . . . . .  | 143 |
| 5.22 | (a) Basal shear stress and (b) internal layering . . . . .  | 144 |
| 5.23 | (a) Basal shear stress and (b) classification of the internal layering . . . . .  | 145 |
| 5.24 | Surface roughness . . . . .   | 146 |
| 5.25 | Surface roughness - Tributaries 5 and 7 . . . . .   | 147 |
| 5.26 | Basal roughness . . . . .   | 148 |
| 5.27 | (a) Surface roughness and (b) basal shear stress . . . . .  | 150 |
| 5.28 | Balance velocities . . . . .  | 152 |
| 6.1  | Map of all layers traced . . . . .  | 158 |
| 6.2  | Surface topography map in 1 km and 2 km resolution . . . . .  | 160 |
| 6.3  | Modern accumulation as (a) original data points and (b) gridded<br>map . . . . .  | 163 |
| 6.4  | Accumulation decreasing with surface elevation . . . . .  | 164 |
| 6.5  | Areas of increased melting . . . . .  | 166 |
| 6.6  | (a) Balance velocities and (b) InSAR velocities . . . . .   | 167 |
| 6.7  | Example of observed and modelled layer . . . . .  | 168 |
| 6.8  | Difference between modelled and observed layers for the control case . . . . .  | 171 |
| 6.9  | Difference between modelled layers for two different accumulation<br>patterns . . . . .   | 172 |
| 6.10 | Difference between modelled layers for different basal melt rates . . . . .   | 173 |
| 6.11 | Radargram with control and basal melt scenario . . . . .  | 174 |
| 6.12 | Difference between model results for 31 vertical points and 11 ver-<br>tical points and between observed and modelled layers for lower<br>horizontal resolution . . . . . | 175 |
| 6.13 | Difference between modelled layers for different flow modes . . . . .   | 176 |
| 6.14 | Median layer misfit with depth for two accumulation scenarios . . . . .   | 177 |

|      |  |     |
|------|--|-----|
| 6.15 | Median layer misfit with depth for two basal melt scenarios . . . .  | 178 |
| 6.16 | Median layer misfit as a function of layer length . . . . .  | 179 |
| 6.17 | Difference between observed and modelled layers for the control case for the tephra layer . . . . .              | 182 |
| 6.18 | Difference between observed and modelled layers for the linear accumulation case for the tephra layer . . . . .  | 183 |
| 6.19 | Difference between plug flow and internal deformation for the tephra layer . . . . .                             | 184 |
| 6.20 | Difference between observed and modelled layers for localised basal melting accumulation . . . . .               | 185 |
| 6.21 | 3D view of intersection of two flightlines . . . . .   | 187 |
| 6.22 | Difference between observed and modelled layers for Layer 1 and 2, control case . . . . .                        | 189 |
| 6.23 | Radargram with internal layering from the control scenario . . . .   | 190 |
| 6.24 | Difference between observed and modelled layers for modern accumulation for Layer 1 and 2 . . . . .              | 191 |
| 6.25 | Radargram with internal layering from the modern accumulation scenario . . . . .                                 | 192 |
| 6.26 | Difference between observed and modelled layers for linear accumulation variation for Layer 1 and 2 . . . . .    | 193 |
| 6.27 | Difference between observed and modelled layers for non-uniform basal melting for Layer 1 and 2 . . . . .        | 195 |
| 6.28 | Difference between observed and modelled layers for the scenario with Layer 2 for internal deformation . . . . . | 196 |
| 6.29 | Difference between observed and modelled layers for non-uniform basal melting for Layer 1 and 2 . . . . .        | 198 |
| 6.30 | Example of US-ITASE radar data . . . . .   | 202 |
| 6.31 | Depth of Layer 2 and the 17.5kyr horizon . . . . .   | 203 |
| 6.32 | Age of buckled layering . . . . .  | 207 |
| 6.33 | Distance between Layer 1 and Layer 2 . . . . .   | 209 |
| 7.1  | Flowlines and flightlines for two-dimensional model . . . . .  | 214 |
| 7.2  | Results from 2D model along flowline 3 . . . . .   | 217 |
| 7.3  | (a) Radar data from flightline 11 and (b) modelled layers in flightline 11 in contours . . . . .                 | 218 |
| 7.4  | (a) Radar data from flightline 14 and (b) modelled layers in flightline 14 in contours . . . . .                 | 220 |
| 7.5  | (a) Radar data from flightline 24 and (b) modelled layers in flightline 24 in contours . . . . .                 | 221 |

|     |   |     |
|-----|---|-----|
| 7.6 | Layer fitting with 2D and 3D model . . . . .                      | 222 |
| 7.7 | Horizontal velocities from 2D and 3D model along flowline 2 . . . | 224 |



# List of Tables

|     |   |     |
|-----|---|-----|
| 2.1 | Electrical properties of materials typically sounded by RES (from Plewes and Hubbard, 2001). . . . .                              | 25  |
| 3.1 | Change in volume in 1995 and 2006 of the trunk of Pine Island Glacier and the trunk and tributaries (from Wingham et al. (2009)). | 61  |
| 4.1 | Test parameters for the runs described in Section 4.3.2.4. . . . .  | 109 |
| 5.1 | Statistics for Layer 1 and 2 in a layer package. . . . .  | 138 |
| 6.1 | Model scenarios . . . . .   | 162 |
| 6.2 | Results from individual layer fitting . . . . .   | 170 |
| 6.3 | Results for fitting of the tephra layer. . . . .  | 181 |
| 6.4 | Results for different scenarios for fitting the layer package. . . . .  | 188 |
| 6.5 | Median values of the misfit for different combined scenarios. . . . .   | 199 |
| 6.6 | Depths of Layer 2 and the 17.5 kyr horizon . . . . .  | 204 |
| 6.7 | Estimated ages of Layer 1 and 2 . . . . .   | 205 |
| 7.1 | Results from 2D layer fitting . . . . .   | 222 |



# Chapter 1

## Introduction

The Antarctic continent has for centuries been the object of exploration and investigation. Interest in this remote region has increased in recent years as the debate on climate change, and especially the future of the polar regions, is becoming ever more widespread - and more politically heated.

This thesis addresses the question of past stability and flow dynamics of Pine Island Glacier (PIG), a particularly dynamic sector of the West Antarctic Ice Sheet (WAIS) (see map in Figure 1.1). The future of the WAIS is of crucial importance because it is potentially unstable and a total collapse of the ice sheet could raise global sea levels by up to 3.3 m (Bamber et al., 2009b). This potential instability of the WAIS was demonstrated over 30 years ago by Mercer (1978) and an increasing amount of observational evidence (e.g. Shepherd and Wingham, 2007; Rignot et al., 2008; Pritchard et al., 2009) has confirmed that some parts of the ice sheet are highly dynamic. Changes in the flow of individual glaciers, such as PIG, are thought to have a significant impact on the dynamics of the system, thus the stability of the ice sheet might be controlled by a handful of small, rapidly changing areas (Rignot et al., 2008). Of these areas PIG is one of the most rapidly changing and has therefore become the object of recent glaciological research (e.g. Vaughan et al., 2006; Rignot, 2008; Scott et al., 2009). This thesis contributes to the ongoing investigations of PIG with a focus on the analysis, interpretation and numerical modelling of internal layers in the ice imaged by radio-echo sounding (RES).

In this chapter the Antarctic Ice Sheets are introduced with an emphasis on the West Antarctic Ice Sheet (Section 1.1) followed by a brief summary of the history of radio-echo sounding in glaciology (Section 1.2). The aims and objectives of the thesis are presented in Section 1.3 and the organisation of the thesis in Section 1.4.

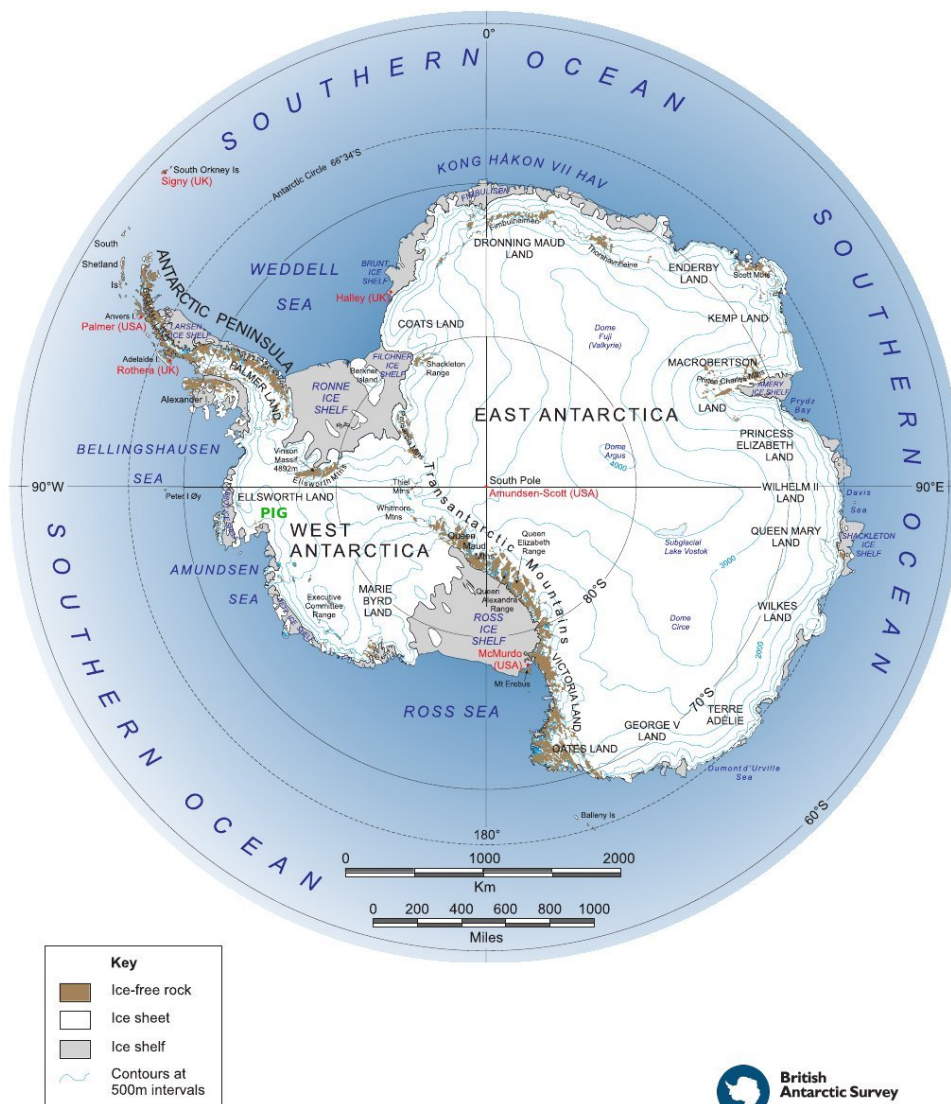


Figure 1.1: Overview map of Antarctica (image credit: British Antarctic Survey). The location of Pine Island Glacier (PIG) has been added in green.

## 1.1 The West Antarctic Ice Sheet

The Fourth Assessment report of the Intergovernmental Panel on Climate Change (IPCC Solomon et al., 2007) emphasised a consistent picture of decline in the Earth's ice masses, and highlighted an urgent need to extend the monitoring and measurement of their changes. Overall it is clear that fluctuations in the balance of the Earth's ice covered regions will have significant effects on sea-level, radiation balance and ocean circulation (Wingham et al., 2006), this especially applies to Antarctica that holds most of the Earth's ice. Thus one of the great challenges in glaciology today is to determine the cause of the changes observed recently in Antarctica and ultimately arrive at a conclusion as to what is causing

the change - anthropogenic activity or natural variability (Payne et al., 2006). A better understanding of past conditions of the Antarctic Ice Sheets and an improved ability to model Antarctic ice will greatly contribute to meeting that challenge.

The Antarctic Ice Sheets are characterised by slow moving ice in the interior converging to fast flowing ice streams and eventually floating ice shelves (Figure 1.2). The Antarctic Ice Sheets are divided into two parts; the East Antarctic Ice Sheet (EAIS) and the West Antarctic Ice Sheet (WAIS). The EAIS contains over three-quarters of the combined Antarctic ice mass with most of the ice grounded above sea-level on a contiguous landmass (Lythe et al., 2001). This configuration means that the EAIS is considered to be relatively stable (Lythe et al., 2001).

The WAIS has a large proportion of its ice grounded below sea-level (Lythe et al., 2001) and is therefore thought to be inherently unstable and potentially a rapid and large contributor to global sea-level rise (e.g. Mercer, 1978; Hughes, 1982; Bamber et al., 2009b). Mercer (1978) was the first to predict the potential instability of the WAIS, using theoretical principles, thus creating a paradigm for Antarctic researchers and greatly influencing the direction of subsequent research (Vaughan, 2008). However, significant changes in the WAIS were not directly observed until satellite observations became available in the 1990s, showing, for example, changes in the Amundsen Sea area. This led to a revived interest in Mercer's concerns in the early 2000s (Vaughan, 2008). Today, a primary imperative is to establish to what extent Mercer's hypothesis is true and hence predict the response of the WAIS to climate change (Vaughan, 2008). It is thus important not only to further our understanding of the past of the WAIS but also to continue to monitor its present dynamics and flow regime.

### 1.1.1 Reconstructing the History of the WAIS

It has been known for several decades that the orbital parameters of the Earth exercise a fundamental control on the timing of ice ages (Hays et al., 1976). However, the impact of the fluctuations on the Antarctic ice sheets continues to be an object of debate (e.g. MacAyeal, 1992; Naish et al., 2009) in particular in regards to the potential instability of the WAIS (Vaughan, 2008). Although the extent and precise timing of recorded WAIS collapses are still uncertain there is general agreement that at least one full or partial collapse has occurred in the mid- to late Pleistocene (Scherer et al., 1998; Pollard and DeConto, 2009) and that the WAIS was at a maximum extent during the Last Glacial Maximum (LGM, 12 - 20 kyr ago) (e.g. Bindshadler, 1998; Anderson et al., 2002).

In the following sections the current understanding of the past history of the

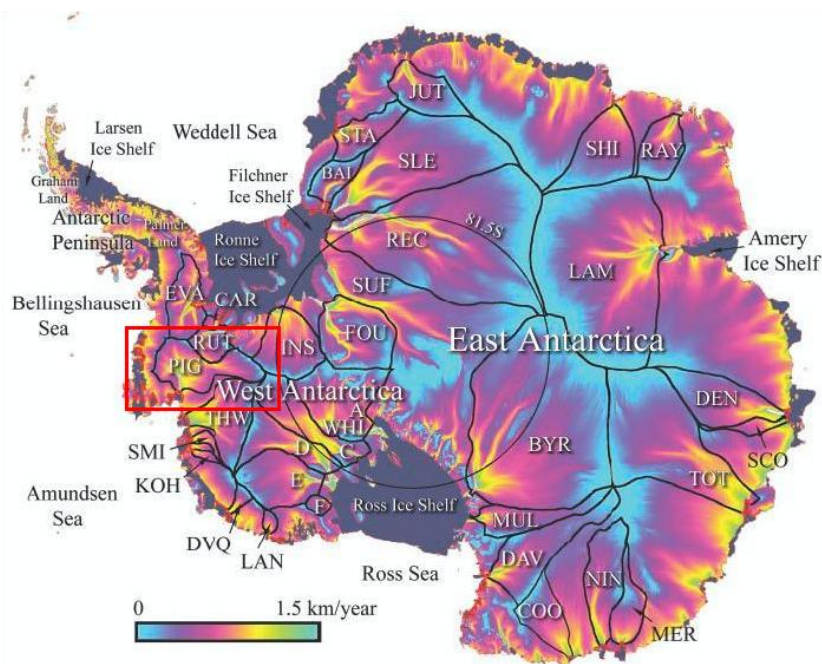


Figure 1.2: *Velocity map of Antarctic glaciers (Rignot and Thomas, 2002, Figure 2). Note the very slow moving ice in the interior of the East Antarctic Ice Sheet. The location of PIG is marked with a red box.*

WAIS will be presented. The primary focus will be the Quaternary period that started approximately 2.6 Myr ago but the Pliocene epoch (approximately 2.6 - 5.3 Myr ago) will also be briefly discussed. The Quaternary period consists of two epochs: the Pleistocene that spans the period 11.7 kyr - 2.6 Myr ago and the Holocene that began approximately 11.7 kyr ago. The Holocene is an interglacial period and characterised by a relatively stable, warm climate. The previous interglacial period - the Eemian - took place approximately 131 - 114 kyr ago. The interglacial periods are relatively short compared to the glacials that not only are colder but also have a less stable climate with abrupt climate changes (referred to as Dansgaard-Oeschger cycles) (e.g. Petit et al., 1999; Johnsen et al., 2001). Figure 1.3 shows the relationship between solar insolation (curve (e)) and temperature (curve (b)) for the last 420 kyr based on data from the Vostok ice core (see also below). The Holocene is located to the far left exhibiting high, stable temperatures.

#### 1.1.1.1 Data Sources

The past extent of the WAIS is often deduced from sediment samples or cores retrieved either in the sea off the shore of the WAIS (e.g. Hillenbrand et al., 2002) or under ice streams (e.g. Scherer et al., 1998). The sediments are then analysed for a number of parameters that indicate the conditions under which they were

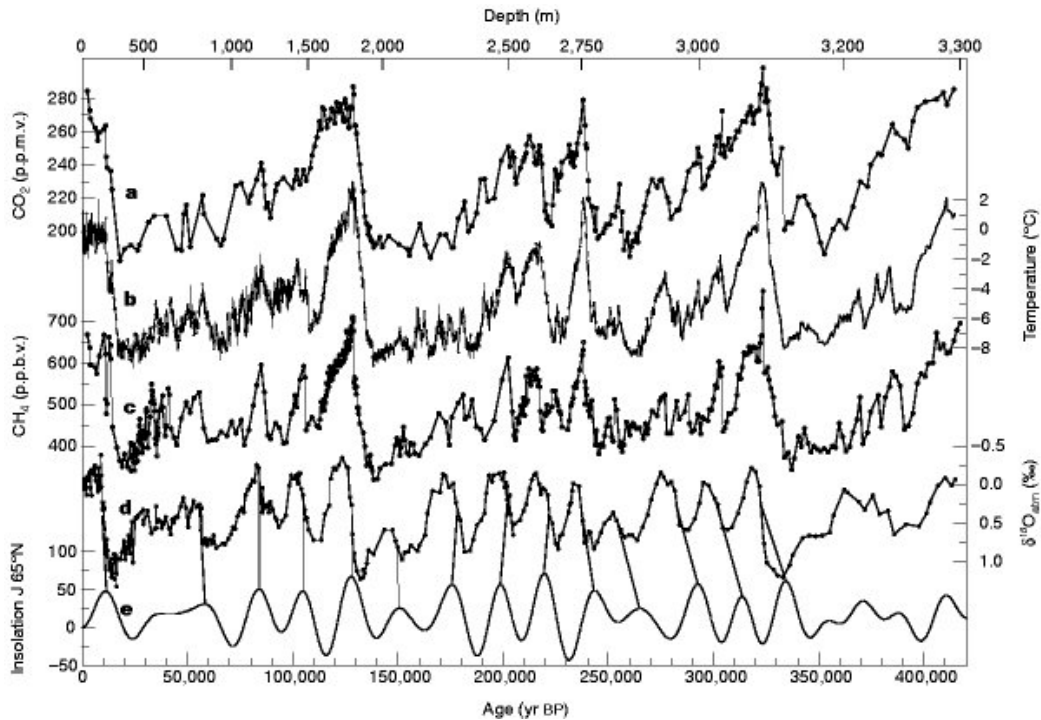


Figure 1.3: Figure 3 from Petit et al. (1999) showing Vostok ice core depth (top axis) and time series (bottom axis) with (a)  $\text{CO}_2$ , (b) isotopic temperature of the atmosphere, (c)  $\text{CH}_4$ , (d) atmospheric  $\delta^{18}\text{O}$ , and (e) mid-June insolation at  $65^\circ\text{N}$  (in  $\text{W m}^{-2}$ ), see Petit et al. (1999) for details.

deposited. Other data sources include dating of exposed glacial landforms (e.g. Ackert et al., 1999; Stone et al., 2003), swath bathymetry for highly detailed mapping of the sea floor (e.g. Ó Cofaigh et al., 2005; Graham et al., 2009), and seismic data that can help characterise the sediments (e.g. Dowdeswell et al., 2007).

The underlying thought of the sea sediment cores is that any fluctuations in the volume of the WAIS will be reflected in the rate and type of sediments deposited on the sea bed, and in the traces of biological activity in the sediments. For example, increased iceberg discharge from the Ross and Amundsen Seas as predicted by MacAyeal (1992) will lead to higher rates of depositions of ice-rafted debris off the continental shelf. This has been extensively observed in the North Atlantic where deposition is thought to have been caused by the advances and retreats of the Laurentide Ice Sheet (e.g. Hemming, 2004). Furthermore, a collapse of the WAIS would lead to different source regions of the icebergs which would be reflected in different concentrations of sediments, for example, varying amounts of volcanic detritus (Hillenbrand et al., 2009).

The use of samples retrieved from under ice streams is exemplified by the study by Scherer et al. (1998). The authors used samples from Whillans Ice

Stream (formerly Ice Stream B) to measure the content of diatoms and  $^{10}\text{Be}$  (beryllium-10). Both parameters are coupled to the occurrence of open marine waters, with significantly lower quantities of diatoms and  $^{10}\text{Be}$  occurring in ice-covered areas.

Isotopes such as  $^{10}\text{Be}$  can also be used to date the exposure age of rocks on glacial landforms, where the ages then indicate a timeline for glacial retreat (e.g. Stone et al., 2003). In these cases the exposure ages often increase with altitude thus providing a tool for mapping the thinning of ice with time (Sugden et al., 2006). Other isotopes used for estimating the exposure age of rocks include aluminium-26, helium-3 and chlorine-36 (e.g. Ackert et al., 1999; Sugden et al., 2006).

While sediment cores and samples provide point measurements of past conditions, swath bathymetry and seismic data can be used to image the bed rock of past ice streams and search for evidence of palaeo-ice sheet retreat. Thus the datasets improve the understanding of basal controls on ice streams in general, but they also provide a snapshot image of deformation of the bed under palaeo ice streams (e.g. Ó Cofaigh et al., 2005; Graham et al., 2009).

Finally, indirect evidence of the extent of WAIS can be obtained from ice core records. Ice cores provide information on past atmospheric conditions, temperatures (from isotopes) and changes in elevation (e.g. Petit et al., 1999; Masson et al., 2000; Johnsen et al., 2001; Vinther et al., 2009), which can be compared to geological evidence. The link between solar insolation and climatic variability is often quite clear from these records as can be seen in Figure 1.3.

#### 1.1.1.2 WAIS in the Pleistocene and Pliocene

It has been established from numerous geological records such as sea sediment cores that the Earth's climate system was dominated by a 40 kyr cyclicity during the Pliocene and early-Pleistocene periods (Naish et al., 2009). For example, a sea sediment core from the Ross Sea show evidence of numerous oscillations of ice-sheet extent (McKay et al., 2009). Thus during the Pliocene and early Pleistocene frequent retreats and collapses of the WAIS are thought to have occurred in response to the 40 kyr cycle with one major retreat predicted at Marine Isotope Stage (MIS) 31 (approximately 1.07 Myr ago) (Pollard and DeConto, 2009).

Sediments from the Pleistocene further indicate that the WAIS has collapsed at least once during the past 800 kyr. For example, the occurrence of  $^{10}\text{Be}$  in samples recovered from the base of the Whillans Ice Stream indicate that an open marine environment existed in the Ross Sea Embayment in the late Pleistocene (Scherer et al., 1998). The authors interpret this to mean a complete collapse of

the ice sheet has occurred and suggest that the most likely period for this collapse is MIS 11 (400 kyr ago). However, Hillenbrand et al. (2002) have argued that the findings do not necessarily imply a full collapse of the WAIS, since sediment cores retrieved from the Amundsen Sea do not support a complete disintegration of the WAIS. Other sediment cores from the Amundsen Sea Embayment and the Weddell Sea further indicate that the environmental conditions on the West Antarctic continental margin were relatively warm during the time interval spanning MIS 15 - MIS 13 (621 - 478 kyr ago), thus questioning the potential timing of a partial collapse (Hillenbrand et al., 2009). The findings suggest that if the WAIS volume was reduced it is more likely to have occurred in that time period which may have coincided with a considerable drawdown of the Greenland Ice Sheet (Hillenbrand et al., 2009).

Modelling work has aimed at explaining the cyclic advances and retreats of the WAIS and results indicate that the WAIS was particularly sensitive to changes in solar insolation during the Pleistocene with increased surface ablation possibly acting as a controlling factor (Pollard and DeConto, 2009). The results also showed that retreats may occur rapidly within a few thousands years (Pollard and DeConto, 2009). Figure 1.4 shows predicted configurations of the WAIS from Pollard and DeConto (2009) during different climatic periods. Although the WAIS retreats happened in response to a cyclic external forcing the timing of the retreats have been found to be sporadic and even chaotic in behaviour (MacAyeal, 1992). This is thought to be due to the great response time of the ice sheets causing a time lag and to the interaction between ice and bed rock, since basal conditions greatly influence the flow of an ice sheet (MacAyeal, 1992). While some of the retreat can be explained by increased solar insolation the sensitivity of the ice sheet to basal melting at its terminus caused by warm ocean water should also be considered (Pollard and DeConto, 2009).

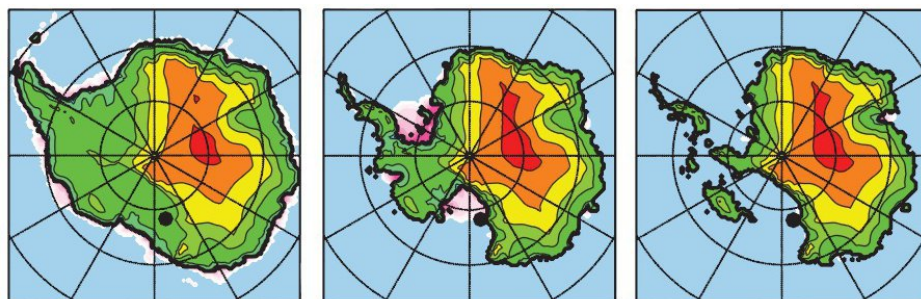


Figure 1.4: *Extent of the WAIS during three stages: full glacial (left), modern interglacial (middle), and extreme interglacial (right) (Pollard and DeConto, 2009, Figure 1 (modified)). The colours show ice sheet elevation (green to red colours) and sea-ice extent (white to magenta colours).*

### 1.1.1.3 WAIS during the Holocene

There is general agreement that the extent of the WAIS was at a maximum during the Last Glacial Maximum (see Figure 1.5). It is likely that the configuration of the WAIS during this period has changed and there is evidence of rapid retreat occurring (Anderson et al., 2002). The overall retreat of the WAIS initiated between 12 kyr and 15 kyr ago and continued into the Holocene (e.g. Anderson et al., 2002) and ice cores record a widespread warming of Antarctica in this period (Masson et al., 2000).

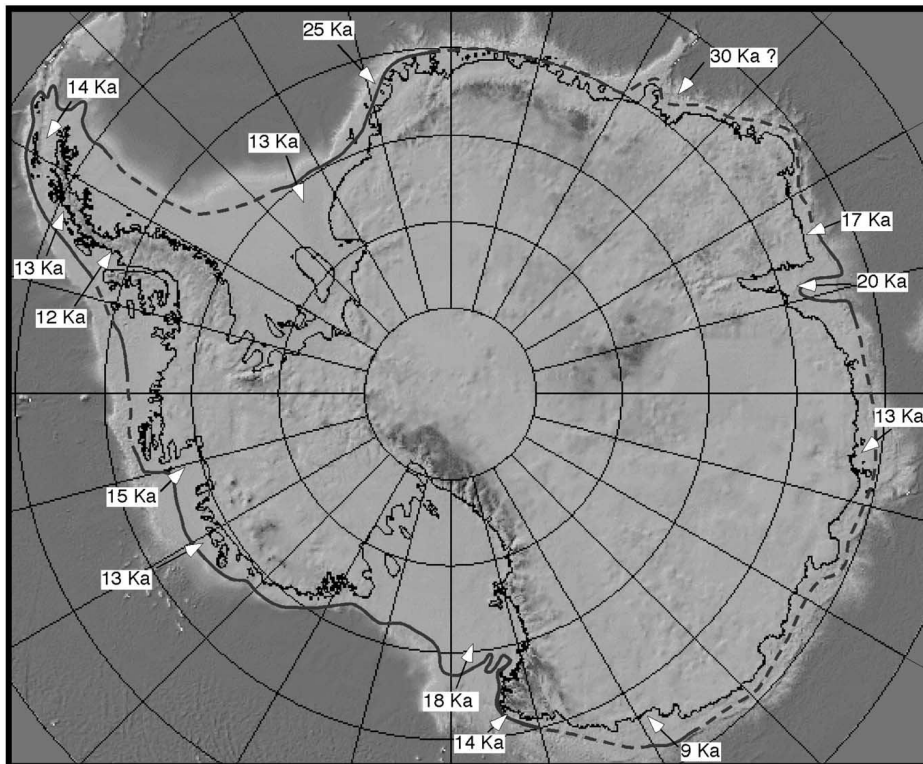


Figure 1.5: *The extent of the Antarctic Ice Sheets during the LGM. Black lines outline the modern ice sheet, thick grey line shows the maximum extent and dark grey shades indicate the continental shelf. The oldest radio-carbon dates from glacial-marine deposits are also shown (Anderson et al., 2002, Figure 13).*

Several studies have confirmed this scenario. For example, a study by Conway et al. (1999) made use of carbon-dated organic material, geological landforms and radio-echo sounding data to reconstruct the past extent of the WAIS in the Ross Sea Embayment. They concluded that the grounding line of the WAIS was at its maximum extent at the beginning of the Holocene where grounded ice filled the Ross Sea Embayment entirely. This finding has been confirmed by sea sediment cores showing extensive glaciation in the late Pleistocene (McKay et al., 2009). The retreat of the grounding line took place over several thousands of years with most of the recession happening during the middle to late Holocene. In

conjunction with this ice core records indicate a warm period in the Ross Sea sector 6 - 8 kyr ago (Masson et al., 2000). Conway et al. (1999) suggest that, although the timing of the retreat of the grounding line is consistent with rising sea levels, the continued retreat during the Holocene happened in the absence of external forcing, and the retreat observed today might therefore also continue without any external forcing. This has been confirmed by multiple observational evidence showing that changes are still ongoing inspite of no external forcings (e.g. Bindshadler and Vornberger, 1998). Conway et al. (1999) also suggest that the retreat took form as a simple “swinging gate” (with the hinging point just north of Roosevelt Island), however, studies of geomorphic signatures on the shelf indicate a more complex retreat pattern with the ice streams of the Ross Shelf behaving independently of each other (Anderson et al., 2002).

Irrespective of the individual dynamics in different parts of the WAIS the picture of retreat since the Holocene is consistent. For example, exposure ages of rocks in Marie Byrd land show thinning and retreat of the ice for the past approximately 10 kyr (Sugden et al., 2006). The glaciers of Marie Byrd Land drains into the Amundsen Sea and large glacial troughs have been observed on the continental shelf, indicating that ice sheets have indeed extended much further out than present day (Anderson et al., 2002).

For the Amundsen Sea Embayment the glacial history is not well constrained (Graham et al., 2009) and the exact position of the grounding line during the LGM is still uncertain (Anderson et al., 2002). Evidence suggests that ice in Pine Island Bay has extended at least to the middle of the continental shelf (e.g. Lowe and Anderson, 2002) and probably all the way to the shelf edge (e.g. Evans et al., 2006; Graham et al., 2010). Several extensive studies (Lowe and Anderson, 2002; Evans et al., 2006; Graham et al., 2009, 2010) have used bathymetry and seismics to map the sea floor identifying widespread glacial lineations, drumlins and meltwater channels (see Figure 1.6). They found indications of the presence of a large palaeo ice stream flowing over a soft, easily deformable bed (Evans et al., 2006; Graham et al., 2010). Studies by Anderson et al. (2002) and Lowe and Anderson (2002) have suggested that a rapid retreat of the ice occurred at the beginning of the Holocene with a pause in retreat marked by a grounding-zone wedge (Figure 1.6) on the middle shelf of Pine Island Bay. When the retreat resumed it may have proceeded rapidly to its present day position (Lowe and Anderson, 2002). This two-phase retreat was in part dictated by the subglacial geology and the presence of substantial amounts of subglacial meltwater that may have been sufficient to cause ungrounding of the ice (Lowe and Anderson, 2003). The rapidity of the second retreat can be explained by a deepening inner

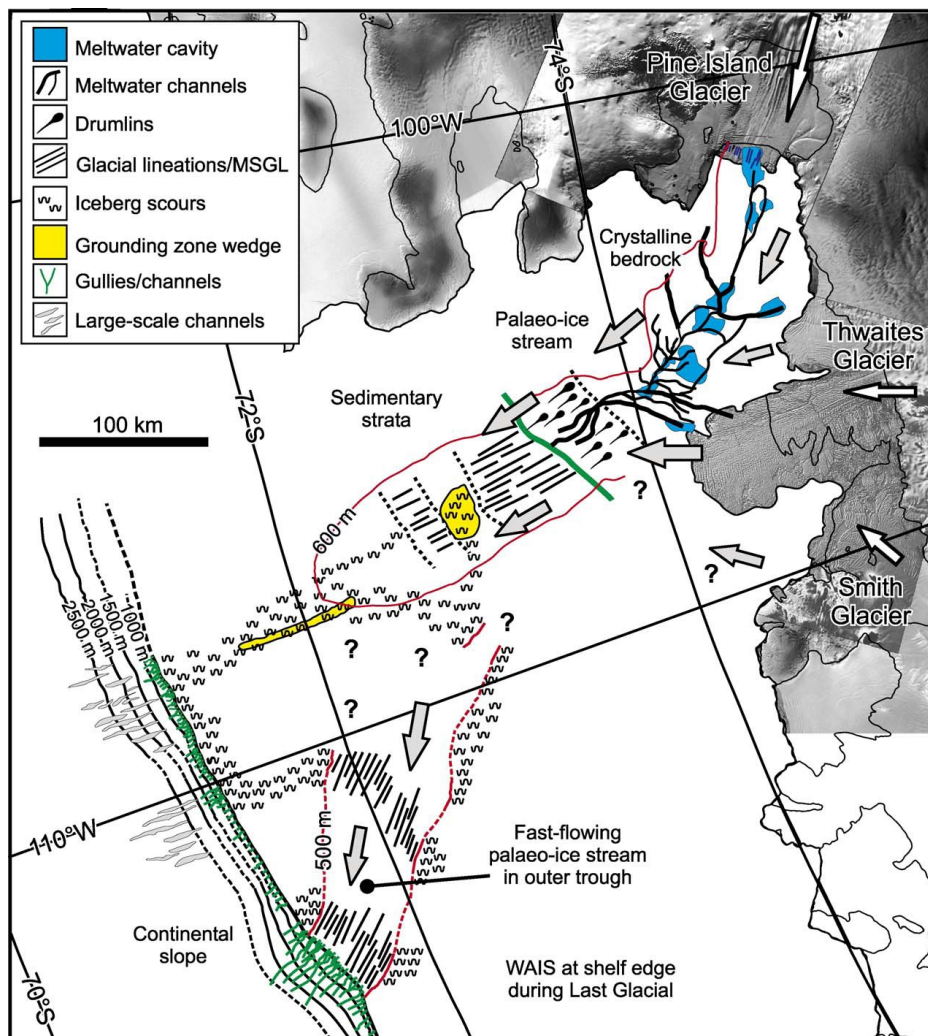


Figure 1.6: *Glacial landforms in Pine Island Bay (Evans et al., 2006, Figure 8) based on studies by Anderson et al. (2002) and Evans et al. (2006).*

shelf and a weak grounding on the sea floor such that a small change in sea-level would be sufficient to cause a degrounding of the ice (Lowe and Anderson, 2002). The authors estimate the time scale for this retreat to be between 2 kyr to 4 kyr, indicating that a large amount of ice was lost in a short timespan (Lowe and Anderson, 2002). A later study by Graham et al. (2010) found that the grounding-zone wedge identified by Anderson et al. (2002) was a “complex of back stepping wedges”. However, the data overall supported the interpretation by Lowe and Anderson (2003) and pointed to the sloping bed in Pine Island Bay as instrumental in the retreat of the glacier (Graham et al., 2010) in agreement with other studies of ice shelf dynamics (e.g. Vaughan and Arthern, 2007).

Models that capture the dynamic behaviour of the WAIS since the LGM indicate that the retreat of the grounding lines is triggered by a rise in sea-levels but with a time-lag between the onset of a climate warming and ice retreat

(Huybrechts, 2002). The models also indicate that although the environmental forcings stabilise the retreats continue for another six thousand years and a new equilibrium will not be reached for another thousand years (Huybrechts, 2002). Earlier studies have estimated that it will be another 4 - 7 kyr before this process of retreat is complete (Bindshadler, 1998; Conway et al., 1999), however, Huybrechts (2002) argue that the isostatic adjustment of, for example, the Ross Sea Embayment will mean that the retreat will be reversed sooner. Finally, Huybrechts (2002) has shown that most of the volume changes of the Antarctic Ice Sheets since the LGM have taken place in the WAIS and on the Antarctic Peninsula. This highlights the importance of improving the understanding of WAIS dynamics. Although models provide important insights into possible evolution scenarios of the WAIS they still face at least two major challenges; capturing the interaction between ice and basal sediments (e.g. MacAyeal, 1992), which has proven to be of great significance, and the influence of the ocean water on ice shelves and upstream dynamics (Pollard and DeConto, 2009).

In summary, evidence from sea sediment cores, samples from beneath ice streams, dating of glacial landforms, swath bathymetry and seismic data agree that the volume of the WAIS has fluctuated substantially during the Quaternary period. The precise timing of the events and the possibility of a complete collapse is, however, still uncertain. It is clear that since the LGM the WAIS has retreated from a position with grounding lines at or close to the continental shelf to its present extent. This retreat seems likely to continue even without significant external forcing indicating that the WAIS is not yet in a stable, steady state. In the Amundsen Sea and Pine Island Bay the last retreat happened within 2 - 4 kyr releasing a substantial amount of water.

The sections above have demonstrated the dynamic nature of the WAIS. The last two decades of satellite observations have further accentuated this and the observations show that mass loss from the WAIS has been especially focussed along the Amundsen and Bellingshausen coastlines (Rignot et al., 2008). In light of recent observations the question emerges if the observed rapid changes are a product of an adjustment process that has been ongoing since the end of the LGM, or if the changes are a response to climate warming in the last century. Especially the glaciers draining into the Amundsen Sea, including PIG, have been the object of great interest in recent years after observations revealed significant changes in surface elevation and velocities (e.g. Rignot, 1998; Shepherd et al., 2001, 2002; Rignot, 2002; Joughin et al., 2003; Rignot, 2008; Scott et al., 2009; Wingham et al., 2009). Furthermore, ice streams such as PIG may very well have

response times that are as short as a decade when it was previously thought that processes that influenced ice streams worked on thousands to tens of thousands of years (Payne et al., 2006). PIG thus exemplifies many of the concerns over the future stability of the WAIS and an improved understanding of PIG will contribute towards a wider understanding of the past and present dynamics of the WAIS.

## 1.2 Radio Echo Sounding in Glaciology

The majority of our knowledge of the subglacial topography of the Antarctic ice sheets and the geometry of the Antarctic ice shelves stems from radio-echo sounding (RES) surveys of the ice, most notably the surveys undertaken from 1967-1979 by a consortium of British and American (and later Danish) scientists. The successful application of RES on ice-sheets is based on the fact that ice is largely transparent to radar waves in high frequency (HF) and very high frequency (VHF) bands (approx. 3 - 300 MHz).

The discovery of the transparency of ice to RES waves was accidental in more than one sense of the word (Turchetti et al., 2008). Although the effect was first suggested as early as the 1930s it was forgotten again until the 1950s. The renewed interest in the effect was partly spurred by several incidents of aircraft crashes, where American aircrafts travelling across the Antarctic reported gross errors in the radar altimeter readings (e.g. Behrendt, 2005). The errors occurred because the radar waves would penetrate the ice and the pilots thus mistake the bedrock under the ice for the ice surface in that way misjudging the distance to the ground (Turchetti et al., 2008). The electromagnetic properties of ice thus became an object of investigation for the US military with the conclusion that relying on radar altimeters could be “fatally dangerous” over ice (Waite and Schmidt, 1962).

Almost simultaneously with the events described above, studies in Antarctica of ionospheric echoes showed unexplained gaps in the data (Figure 1.7). Investigations of the gaps revealed that they occurred because the radar signal scattered by the ionosphere would penetrate the ice, get reflected by the bedrock and then interfere with the original signal (e.g. Evans, 1961). This is an example of how what is considered noise by one researcher is another researcher’s data (Turchetti et al., 2008).

The investigations of RES as a tool for measuring ice properties and the later deployment of an Antarctic airborne field program was furthered by important political events (Dean et al., 2008; Turchetti et al., 2008). In 1957-58 the world

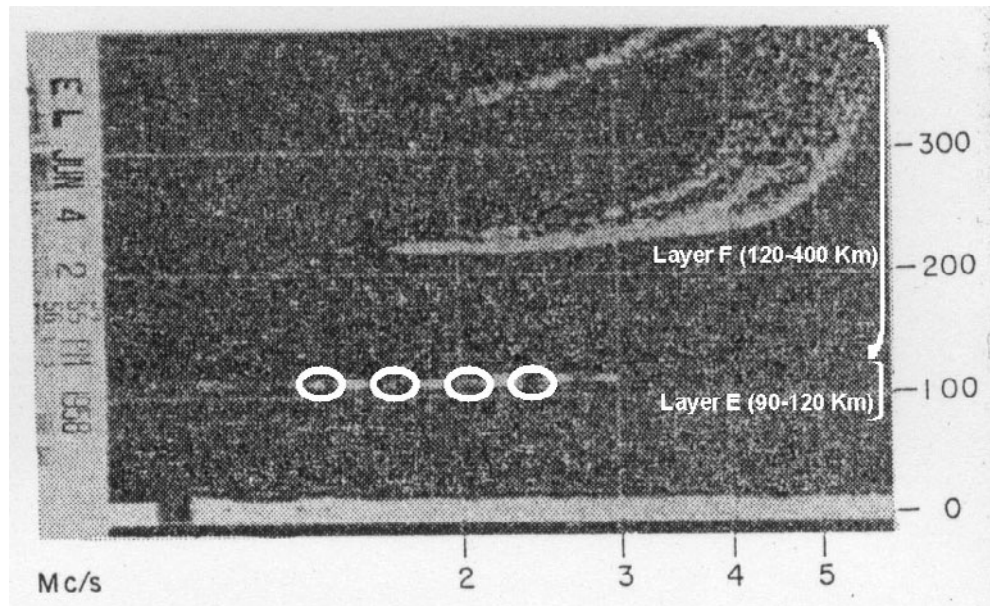


Figure 1.7: *Ionogram from Ellsworth (Evans, 1961, Figure 2) with the data gaps marked with white circles by Turchetti et al. (2008).*

celebrated the International Geophysical Year (IGY) with a wide range of scientific activities and it was seen as an example of how science could overcome political differences between nations (Naylor et al., 2008). It was proposed that during the IGY all nations should have free and full access to the entire continent. For the American government this was seen as an opportunity to acquire valuable information about other nations' Antarctic territories while at the same time forcing the USSR to make their research public (Naylor et al., 2008). In this way the IGY became a precursor for the Antarctic Treaty that was signed in 1959. In the treaty the Antarctic continent achieved a unique status as a non-military zone where the signing members agreed to explore Antarctica only for peaceful purposes. The treaty also stipulated that no new territorial claims could be made while at the same time all existing claims were suspended (a copy of the original 1959 Antarctic Treaty can be found on the homepage of the Secretariat of the Antarctic Treaty [http://www.ats.aq/e/ats\\_treaty.htm](http://www.ats.aq/e/ats_treaty.htm)). Thus everyone was to have free access to any area. This paved the way for international collaborations between polar scientists.

After successful tests of radio-echo sounders in Greenland in 1963 (e.g. Evans, 1963) and Canada (1966) the US National Science Foundation (NSF) decided to fund an “airborne laboratory” for Antarctic research to carry among other things RES equipment for mapping the subglacial topography. It was well known that researchers from the Soviet Union were conducting ground-based RES measurements of Antarctica and the motivation for developing an airborne data collection

method was partly based on a wish to beat the Russians to it (Turchetti et al., 2008). Indeed, for the US government scientific collaborations and data exchange were considered a useful way of promoting American interests (Naylor et al., 2008) although it was often brought forward as an example of “disinterested” American science (Dean et al., 2008). This “airborne laboratory” was carried out in a collaboration between the NSF and the Scott Polar Research Institute (SPRI) in Cambridge, UK, which to the Americans also added a certain propaganda value to the project by demonstrating the international efforts that were being undertaken (Turchetti et al., 2008). A record of the early years of the RES surveys can be found in, for example, Evans and Robin (1966) and Evans (1967).

The end result was that an Antarctic field program using airborne RES was deployed in the years 1967-1979. Initially the radar was built by SPRI, but from 1974-75 the Technical University of Denmark took over the radar design (Turchetti et al., 2008). Thus the surveys are often today referred to as the “SPRI-NSF-TUD” surveys. During these years several new developments in RES techniques impacted the surveys, in particular two developments were instrumental to their success. The first was the development of a recording device for the RES equipment where the data were recorded on film continuously instead of using an oscilloscope. This means that to this date the data are still available and can be used for scientific investigations (Turchetti et al., 2008). The second was the development of a new navigational system that significantly reduced errors in navigation. This was not only important when planning the acquisition lines but also for later interpretation of the data, since error margins on the navigational data were reduced from approximately 30 km to errors in the order of 5 km or less (Drewry, 1975).

The compiled results of the surveys can be found in Drewry (1983), although substantial amounts of material were also published elsewhere (e.g. Robin et al., 1969) and new methods later added additional value to the datasets (cf. Siegert, 1999). At the end of the SPRI-NSF-TUD surveys the collected datasets comprised over 70,000 ice-thickness values and still provide the base for our current understanding of the Antarctic Ice Sheet (Drewry, 1983).

In the following years the RES surveys got more specialised and the frequency of the radar was optimised for different environments, for example, low-frequency radars were developed for sounding temperate glaciers (Gogineni et al., 1998). The first ice sounding measurements only detected the power or amplitude of the returned signal. With the introduction of coherent radar systems that record both amplitude and phase of the signal it became easier to quantify the reflection

and scattering of the signal and thereby characterise the englacial environment (Peters et al., 2005). Finally, the use of GPS meant that the accuracy in the location of the RES surveys was greatly improved and the uncertainty in position is now usually 10 m or less (Gogineni et al., 1998).

The majority of the surveys in recent years have aimed at mapping bed topography and ice thickness, or at specific goals such as locating optimum drill sites or investigating the internal layering in high resolution (Bingham and Siegert, 2007b). Currently several major airborne survey are being undertaken in Antarctica. For example, as part of the International Polar Year the AGAP project has explored the subglacial Gamburtsev mountains in East Antarctica with participation from the US, the UK, Australia and several other nations creating three-dimensional maps of the bed topography. Another large airborne survey is the ICE Bridge project led by NASA (National Aeronautics and Space Administration), with the mission to bridge the gap between the end of the satellite mission ICESat-I and the launch of its successor ICESat-II. Finally the ICECAP project, primarily involving scientists from University of Texas and University of Edinburgh, is conducting airborne surveys out of the Australian base Casey Station.

As described above the most common use of RES is mapping the bed topography of a glacier to obtain the volume of ice (e.g. Drewry, 1983). A further use of RES is the imaging of internal layers within the ice, whose geometry contains information on past accumulation rates, basal conditions and internal ice flow mechanisms (e.g. Conway et al., 2002; Rippin et al., 2003b; Siegert and Payne, 2004). The internal layers also serve as valuable input in numerical models in order to assimilate the past behaviour of a glacier (Leysinger Vieli et al. (2007); Hindmarsh et al. (2009), a full introduction to RES and its use in modelling is given in Chapter 2). This thesis focusses on the use of internal layers to interpret past flow and their assimilation into ice-sheet models. The dataset that forms the base of this Ph.D. project is from a survey conducted by the British Antarctic Survey and the University of Texas in 2004/2005 covering the catchments Thwaites, Smith and Pine Island (see Holt et al., 2006; Vaughan et al., 2006).

### 1.3 Aims of the Thesis

The overall aim of this Ph.D.-project is to investigate the dynamics of Pine Island Glacier based on observations of past flow dynamics from radio-echo sounding. In a broader context the project addresses the stability of the WAIS and our

understanding of the ice sheet. Until recently the glaciology of Pine Island Glacier, along with the other catchment basins that drain into the Amundsen sea, was not very well understood as the area is remote and therefore seldom visited (Vaughan et al., 2001). Recent surveys conducted over PIG have sounded the subglacial topography in more detail (Vaughan et al., 2006) and identified an area of past volcanic activity (Corr and Vaughan, 2008). However, the extensive internal layering that was imaged during the survey has so far been left unused.

In view of the importance of PIG for the dynamics of the entire West Antarctic Ice Sheet in combination with the vast amount of information that the internal layers contain, it is imperative that this source of new information concerning PIG is explored fully. With the use of the newly acquired radio-echo sounding data and numerical ice flow modelling, this Ph.D. project aims to answer the questions:

1. What are the characteristics of the past flow pattern of PIG?
2. What are the significant differences between the inferred past flow pattern and that observed today?
3. What are the implications for the future stability of PIG?
4. What other parameters, such as accumulation patterns and rates, may have experienced significant changes?

To achieve these aims an extensive analysis of the radio-echo sounding dataset is carried out aiming to

- (i) classify and interpret the internal layering
- (ii) construct an objective classification system for internal layering
- (iii) explore other properties of the radar dataset that can yield information on current or past flow patterns
- (iv) compare observed internal layering to modelled layering from numerical ice flow models
- (v) retrieve information on parameters influencing the ice flow such as accumulation, basal melting and ice deformation using observations and numerical ice flow models

Together these will lead to an improved understanding of the dynamics of PIG.

## 1.4 Thesis Organisation

The research carried out in order to meet the aims listed above is described in the following chapters. The first part of Chapter 2 provides a background to radioglaciology and remote sensing of internal layers. It also includes a description of other applications of RES in glaciology. The second part of Chapter 2 contains an introduction to numerical modelling of ice flow. Chapter 3 introduces the study area of this thesis; Pine Island Glacier, and provides an overview of the current knowledge of PIG and observations of recent change. The methodology behind this thesis is explained in Chapter 4, including the methods behind the radar data analysis, the set-up of the three-dimensional ice flow model BASISM and the construction of a two-dimensional ice flow model. Thus the first three chapters provide useful background knowledge for discussion of the results in the chapters to follow.

In Chapter 5 the results from the radar data analyses are presented and discussed in view of our current knowledge of the flow pattern of PIG. Chapter 6 contains the results from an extensive three-dimensional modelling study of the observed internal layering and in Chapter 7 the layering is investigated in more detail with a simpler, high-resolution two-dimensional model.

Finally, Chapter 8 concludes this thesis and summarises the main findings, the implications of the results and suggestions for future work.



## Chapter 2

# Background to Radioglaciology and Ice Flow Modelling

This chapter gives an introduction to radioglaciology. Section 2.1 describes the background to radio-echo sounding in glaciology and the electrical properties of ice. Section 2.2 gives a detailed description of internal reflections in ice, the cause of the reflections and how information on internal ice sheet structure, past accumulation rates, basal melt and ice flow dynamics can be retrieved from the reflections. Section 2.3 describes other applications of radars in glaciology such as ice thickness measurements and characterisation of basal conditions of glaciers. The focus is mainly on the application of radioglaciology in the Antarctic.

The second part of the chapter contains an introduction to ice flow modelling (Section 2.4) focussing on the modelling of internal layers in flowing ice. The terminology of ice flow models will be introduced along with different common approaches to modelling the flow of ice.

### 2.1 Introduction to Radioglaciology

Radio-echo sounding (RES), also known as ice-penetrating radar, in glaciology is based on the transmission of electromagnetic waves through ice. It takes advantage of the fact that cold ice to a great extent is transparent to electromagnetic waves in the high frequency (HF) and very high frequency (VHF) bands (i.e. 3-300 MHz) (e.g. Evans, 1961; Drewry et al., 1982). RES equipment typically comprises of a transmitter that emits electromagnetic waves and a nearby receiver that detects. The basic function of RES equipment is to collect the two-way travel time of the radar signal, i.e. the time it takes for the signal to travel from the transmitter to a reflecting surface and back to the receiver. The transmitter and receiver will most often be moving continuously either on the surface of the

ice or on an aircraft above the surface. From the time delay in the return signal, the ice thickness and depths of internally reflecting layers can be inferred, while changes in the phase and amplitude of the signal can give information on, for example, bed roughness (Bogorodsky et al., 1985).

RES is usually conducted in two ways; airborne or ground based. Both approaches have their advantages and disadvantages. While ground based surveying captures a lot of detail and often will have a very clear signal from the bed, it is a time-consuming task. A ground based survey is unlikely to be able to cover large areas of an ice sheet and will often have to be conducted focussing specifically on one study area. Airborne surveys on the other hand are substantially more expensive but can cover large areas of ground relatively fast (Bingham and Siegert, 2007b). They can also be conducted simultaneously with gravimetric and aeromagnetic measurements and thus contribute to a more complete picture of a region (e.g. Vaughan et al., 2006; Jordan et al., 2009). Much of our current knowledge of the Antarctic subglacial topography stems from airborne surveys (e.g. Drewry, 1983).

Radar data can be presented in a number of different ways depending on the kind of information that one wishes to retrieve from them (e.g. Plewes and Hubbard, 2001). Figure 2.1 shows an example of data plotted in (a) A-scope format and (b) Z-scope format, sometimes referred to as wiggle plot and radargram respectively. The A-scope shows a single radar trace while the Z-scope illustrates the intensity of the returned radar signals for a whole array of radar traces. The image shows how the ice surface, internal layering and bedrock clearly are visible in the data as bright reflecting lines against a darker background in Z-scope format. The interpretation of these features relies on knowledge of how the radar waves travel through the ice and depends on the electrical properties of ice.

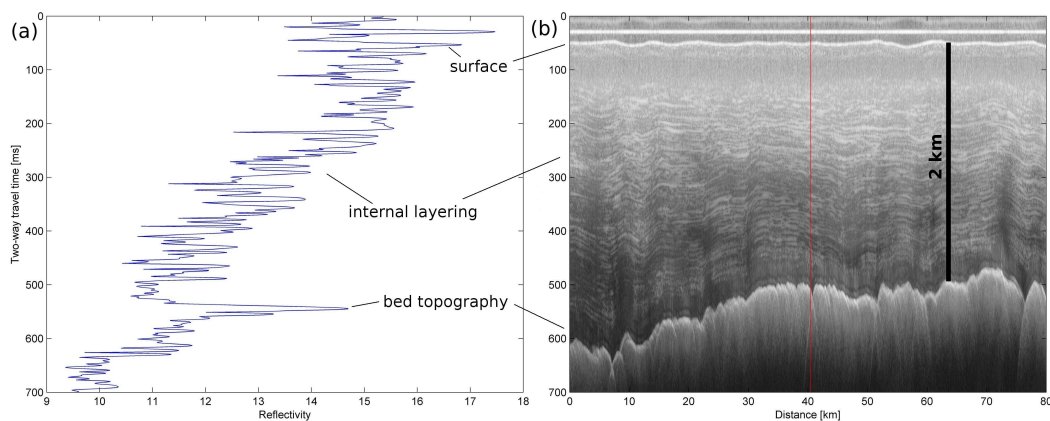


Figure 2.1: Example of radar data from the PASIN radar plotted in (a) A-scope and (b) Z-scope format. The ice surface, internal layering and bedrock are clearly visible. The red line in (b) shows the location of (a).

### 2.1.1 Electrical Properties of Ice

The electrical properties of ice are linked to the structure of the  $\text{H}_2\text{O}$  molecule that is composed of an oxygen atom and two hydrogen atoms. The oxygen atom has eight electrons, four of which are bound in two inner stable orbits close to the nucleus. The remaining four electrons orbit the nucleus and the orbits form the corners of a tetrahedron. In the  $\text{H}_2\text{O}$  molecule two of the four outer electrons from the oxygen atom will each share their orbits with an electron from a hydrogen atom, leaving the two remaining electrons to form an excess negative charge in two corners of the tetrahedron, while the two hydrogen nuclei form a positive charge in the other two corners of the tetrahedron. Each negative corner will attract a positive corner of a neighbouring  $\text{H}_2\text{O}$  molecule forming a “hydrogen bond”. When  $\text{H}_2\text{O}$  crystallises into ice the molecules form hexagonal rings in layers (Bogorodsky et al., 1985). Figure 2.2 shows the positions of the oxygen atoms in an ice crystal. Each hexagonal ring is in two planes and each layer is a mirror image of the layer above and below it. The plane of a layer of hexagonal rings is called a basal plane while the direction at right angles to the basal plane is called the c-axis (Paterson, 2002; Bogorodsky et al., 1985).

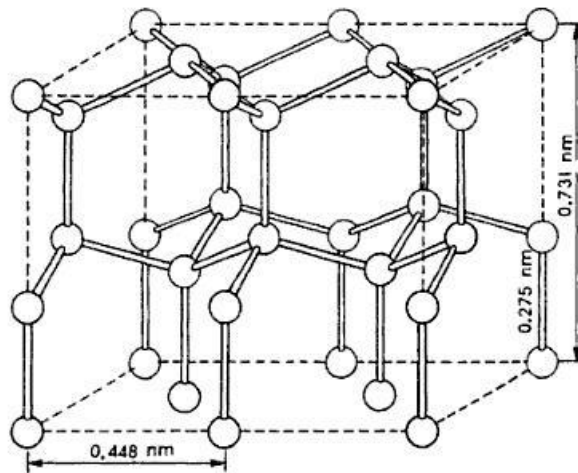


Figure 2.2: A diagram of the positions of the oxygen atoms in an ice crystal structure. The distance between two oxygen atoms in neighbouring basal planes is approximately 0.275 nm. Dimensions correspond to ice at a temperature of 77K (from Bogorodsky et al. (1985), Fig. 13).

Defects in the basic crystalline structure - such as protons jumping from one atom to another or the excitation of an oxygen atom leading to an ionised state - influence the electrical properties of ice. Some of the defects are temperature-dependent as higher temperatures will increase the energy of the proton towards to the activation energy required to make a jump (Bogorodsky et al., 1985).

In radar applications the electrical properties of ice are usually characterised in terms of permittivity and conductivity. Permittivity can be thought of as a medium's ability to store an electrical charge. When a time-varying electric field  $E$  is applied to ice, the electrical displacement  $D$  caused by the field is given as  $D = \epsilon E$ , where  $\epsilon$  is the permittivity of the ice.  $\epsilon$  is often described relative to the permittivity of free space and named the relative permittivity or the dielectric constant (Bogorodsky et al., 1985). In the HF/VHF bands the permittivity reaches a plateau and therefore for all practical purposes, including in this thesis, it can be considered as constant and thus independent of the electrical field (Miners, 1998; Dowdeswell and Evans, 2004).

The electrical conductivity describes how well a material conducts an electrical current. The conduction of electricity in ice depends heavily on the ionisation of the molecules and therefore the conductivity will depend exponentially on the temperature of the ice (Bogorodsky et al., 1985). The conductivity also reaches a plateau in the HF/VHF bands and is therefore often regarded as frequency-independent in radioglaciology (Miners, 1998; Dowdeswell and Evans, 2004). The introduction of impurities in the ice significantly changes the activation energy for ionisation of the molecules thus ice with high impurity content will have a different conductivity (Bogorodsky et al., 1985).

Critical to the use of RES in glaciology is the fact that radar waves reflect off any surfaces that represent a change in conductivity, permittivity or a combination of both. As is shown in Figure 2.1 the largest changes in dielectric properties (e.g. the ability to conduct or store electric energy) when sounding glacial ice occur between air and the ice surface, the ice and the bedrock and in internal layers within the glacier, thus causing a large reflection of the radar waves. Other features such as subglacial lakes and crevasses can also be identified in RES data (Bogorodsky et al., 1985). While the basic products derived from RES are ice thickness and bed topography the main aim of this thesis is the internal layering. Section 2.2 describes internal reflections in more detail while Section 2.3 introduces other information that can be retrieved from RES surveys, such as ice thickness and basal condition.

## 2.2 Internal Reflections in Ice

The presence of internal reflections in glacial ice was first reported by Bailey et al. (1964). In glaciological literature the reflections are some times referred to as internal reflection horizons or radio-echo layering but in this thesis the terms “internal layering” and “internal layers” will be used.

Some of the earliest published data on internal layers in Antarctica originates from the SPRI-NSF-TUD surveys conducted by the Scott Polar Research Institute, University of Cambridge, the Technical University of Denmark and the US National Science Foundation (hereafter referred to as the SPRI surveys, see also Chapter 1). The layers were observed to extend over tens or sometimes hundreds of kilometres and to be relatively smooth (Drewry, 1983). An example of the data returned from the SPRI surveys clearly showing internal layering can be seen in Figure 2.4. Although the data from the SPRI surveys have been widely used to reconstruct the ice volume of the Antarctic Ice Sheets, the internal layering in the West Antarctic Ice Sheet was initially only subject to a general classification based on the continuity of the layers as described in Drewry (1983) and Siegert et al. (2005b). This classification scheme will be discussed in more detail in Section 2.2.6.

Internal layering has been the object of considerable interest in glaciological studies. Early studies pointed towards internal layers being isochrones i.e. layers of the same age (Robin et al., 1969; Millar, 1981). This implies that the layer stratigraphy preserves important information concerning accumulation, basal conditions (specifically melting) and ice flow dynamics (e.g. Bingham and Siegert, 2007b). In spite of the critical value of such parameters for ice-sheet modelling the vast majority of RES studies have concentrated on the basal reflector, often for the purpose of mapping subglacial topography; and relatively few studies have utilised the vast database of internal layers that have been imaged over Antarctica.

The next sections will discuss in more detail the origin of internal layers and typical data processing steps used to highlight them in RES data (Section 2.2.1) and applications of the layers in glaciological contexts (Sections 2.2.3, 2.2.4, 2.2.5 and 2.2.6).

### 2.2.1 Origins of Internal Layers

When a radar wave encounters a change in dielectric properties, i.e. an internal layer, part of the signal is reflected back to the receiver. This can be seen in the radargram as a line of increased reflection (e.g. Figure 2.1). Unlike the

reflections caused by the ice surface and bed topography, reflections produced by internal layering does not necessarily mean that the layers consist of two different materials. Instead the layers represent a change in dielectric properties caused by variations in permittivity, conductivity or a combination of both. The processes causing these changes can be density differences, variations in acidity or changes in ice crystal orientation (e.g. Harrison, 1973; Paren and Robin, 1975).

The strength of the returned signal energy is called the reflectivity, and can be described quantitatively by the power reflection coefficient  $R$ . The power reflection coefficient due to permittivity  $R_p$  and conductivity  $R_c$  follow two different equations (Fujita et al., 1999):

$$R_p \propto \Delta\epsilon^2 \quad (2.1)$$

$$R_c \propto \left(\frac{\Delta\sigma}{f}\right)^2 \quad (2.2)$$

Where  $\epsilon$  is the permittivity,  $\sigma$  is the conductivity and  $f$  is the frequency of the radar signal. Note that while  $R_c$  is (inversely) proportional to the frequency of the radar,  $R_p$  is frequency-independent. This fact was used in a study by Fujita et al. (1999) to distinguish between layers caused by different kinds of change in dielectric properties in a survey along an 1150 km transect in East Antarctica. The RES equipment used in the study operated at two different frequencies: 60 MHz and 179 MHz. Thus while  $R_p$  should remain the same for both wavelengths a change in  $R_c$  should be expected. The results from the study led to a characterisation of the englacial environment based on the primary cause of the internal layers.

### 2.2.1.1 Changes in Permittivity

For pure ice a typical value of the permittivity is  $\epsilon = 3 - 4$  (see Table 2.1). However, this value depends on a number of factors. It is well known that a change in density will affect the permittivity of the ice and several equations have been suggested to describe the relation between density  $\rho$  and permittivity  $\epsilon$  such as (Miners et al., 2002)

$$\epsilon = (1 + 0.51 * 10^{-3} \rho)^3 \quad (2.3)$$

Density variations in glacial ice occur in the upper part of a glacier when snow accumulates on the surface and subsequently gets buried by snowfall. This densification process leads to a solidification of snow into firn and ultimately into ice. Internal layering occurring in the upper part of a glacier is therefore

| Material    | Permittivity $\epsilon$ | Conductivity $\sigma$ [mS m <sup>-1</sup> ] |
|-------------|-------------------------|---|
| Ice         | 3 - 4                   | 0.01  |
| Fresh water | 80                      | 0.5   |
| Salt water  | 80                      | 3000  |
| Air         | 1                       | 0   |

Table 2.1: Electrical properties of materials typically sounded by RES (from Plewes and Hubbard, 2001).

usually attributed to the variations in density (Robin et al., 1969). Empirically the depth-density relation can be described as an exponential function (Paterson, 2002)

$$\rho(z) = \rho_i - (\rho_i - \rho_s)e^{-Cz} \quad (2.4)$$

Where  $\rho(z)$  is the density at depth  $z$ ,  $\rho_i$  is the density of ice,  $\rho_s$  is the density of snow at the surface and  $C$  is a constant that depends on the location. Figure 2.3 shows plots based on Equations (2.3) and (2.4) with the parameters  $\rho_i = 918 \text{ g cm}^{-3}$ ,  $\rho_s = 0.4 \text{ g cm}^{-3}$ ,  $C=0.005$ . Note how the permittivity increases exponentially with depth down as the density increases. In areas with surface melt the variation in density can be even larger as the surface snow might melt, permeate down in the ice and then refreeze. The reflections caused by density variations usually do not obscure other echoes from further down in the ice or attenuate the signal significantly (Fujita et al., 1999). Fujita et al. (1999) found that at their study site the layers in the upper 700 - 900 m of the ice sheet were without exception dominated by changes in density, and although other effects were probably present as well they were obscured by the strong density signal.

Measurements have shown that the permittivity can also be affected by the orientation of the c-axis of the ice to the incident radar waves. Harrison (1973) first suggested ice crystal orientation as a cause of internal layering when internal layers were observed at depths where no density variations were thought to occur. It was later established that when ice is subjected to high shear stress the ice crystals can become highly ordered with the vertical c-axis, i.e. anisotropic, while ice not subjected to high stress may retain a random crystal orientation, i.e. isotropic (e.g. Paterson, 2002). This may also affect the flow of the ice (see also Section 2.4.4). A region with ice crystals whose c-axes are aligned will have a different permittivity than a region with highly disordered crystal alignment and a sharp boundary between two such regions will produce a strong echo return (Dowdeswell and Evans, 2004). This effect is mainly observed in deep ice where the stresses are high or where the configuration of the flow regime introduces additional stresses (e.g. Fujita et al., 1999; King, 2009). Fujita et al. (1999) found

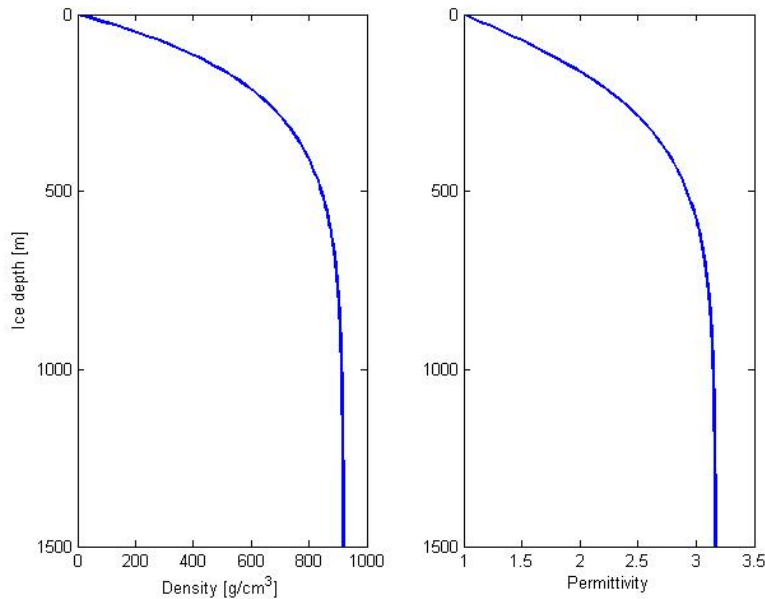


Figure 2.3: *Variation in density and permittivity from Equations (2.3) and (2.4). As density increases with depth so does the permittivity.*

that the difference between zones dominated by changes in ice crystal orientation and zones with variations in acidity depended on whether or not the total strain was large enough to cause contrasts in crystal-orientation fabric.

### 2.2.1.2 Changes in Conductivity

Changes in conductivity of glacial ice are often related to snowfall events with high impurity content that causes a reduction in the activation energy required to trigger ionised states (Bogorodsky et al., 1985). For example, while the conductivity of ice and distilled water is of the order of  $10^{-2} \text{ mS m}^{-1}$  the conductivity of salt water is  $3000 \text{ mS m}^{-1}$  (see Table 2.1). Thus if a layer (or several layers) have a higher impurity content than their neighbouring layers this leads to a change in received signal power (Paren and Robin, 1975). For example, acid layers from volcanic activity have been observed to correlate with brightly reflecting horizons in RES data from the area around the core retrieved by the Greenland Ice Core Project (Hempel et al., 2000) and in the area around Byrd ice core station, West Antarctica (Jacobel and Welch, 2005).

It has been established that internal layers occur because of changes in permittivity, conductivity or both; previous work has suggested that in practice these variations are brought about by changes in (i) density, (ii) acidity and (iii) crystal fabric orientations (e.g. Fujita et al., 1999). Reflections caused by changes in

acidity have greatly aided in the dating of internal layers. For example, a strongly reflecting layer observed in the US-ITASE traverse of West Antarctica could be linked to an acidity anomaly in the Byrd ice core (Jacobel and Welch, 2005) (see also Section 6.5). The impact of ice crystal orientation on radar waves can be utilised to characterise the ice fabric and identify areas of anisotropic ice (Matsuoka et al., 2003) or areas of increased strain due to ice flow dynamics (King, 2009).

### 2.2.1.3 Echo-Free Zone

Curiously, in the lower several hundred metres of the ice above the bed there is often an echo-free zone (EFZ) that cannot be explained by signal attenuation but only by a change in power reflection coefficient (Fujita et al., 1999). It is generally attributed to folding and mixing of the layers above, thus obliterating the isochrones, and the boundary between areas with layers and EFZ is often sharp (e.g. Robin and Millar, 1982; Fujita et al., 1999).

This section has established that internal layers result from changes in the physical properties of ice, such as changes in density, acidity content and/or crystal fabric which affect permittivity and/or conductivity. It is important now to consider in more detail how such changes are represented in RES systems, and to consider how the RES system can be set up to image internal layers.

## 2.2.2 RES Data Processing

In order to interpret the internal layers correctly it is important to have knowledge of the radar system, in particular the propagation of the radar waves through the ice and the properties that may affect this propagation. The main processes that affect the returned signal are scattering, geometrical spreading and dielectric absorption often referred to collectively as signal attenuation.

The depth of any given reflector  $d$  is inferred from the time difference between the echo returned from the surface of the ice and the echo returned from the reflector  $\Delta t$

$$d = \Delta t / 2 * v_{ice} \quad (2.5)$$

Where  $v_{ice}$  is the velocity of radar waves in ice. In other words, knowledge of the velocity of the radar waves is essential in order to convert the two-way travel time to the depth of a given reflector, for example, an internal layer. The velocity of

radar waves in ice  $v_{ice}$  is often given by (e.g. Plewes and Hubbard, 2001)

$$v_{ice} = \frac{c}{((\epsilon/2)((1 + P^2) + 1))^{1/2}} \quad (2.6)$$

where  $c$  is the speed of the radar wave in free space (i.e. the speed of light). In this context  $P$  can be considered as a “loss factor” that depends on permittivity, conductivity and  $\omega$ :  $P = \sigma\omega\epsilon$ , where  $\omega$  is the angular frequency,  $2\pi f$ , with  $f$  as the frequency (Plewes and Hubbard, 2001). In other words, the propagation of radar signals in ice depends mainly on the permittivity  $\epsilon$ , the conductivity  $\sigma$  and the frequency  $f$  of the radar waves (Plewes and Hubbard, 2001). Often a value for  $v_{ice}$  of  $1.67 * 10^8 \text{ m s}^{-1}$  is used which is based on measurements at a frequency of 35 MHz and a temperature of  $-20^\circ\text{C}$  (Robin, 1975). However, this value varies not only with radio frequency but also with temperature and water content of the ice (e.g. Navarro et al., 2009).

### 2.2.2.1 Signal Attenuation

As the waves propagate through the ice a loss of signal strength occurs. This loss is referred to as signal attenuation. The signal attenuation is caused by multiple effects such as scattering, dielectric absorption and geometrical spreading, which will be described in the sections below. The attenuation coefficient, that describes the overall loss of radar wave energy per unit distance travelled from the source in  $\text{dB m}^{-1}$ , can be written as (Plewes and Hubbard, 2001)

$$\alpha = \omega \left( \frac{\epsilon}{2} \left\{ \left( \frac{1 + \sigma^2}{\omega^2 \epsilon^2} \right)^{1/2} - 1 \right\} \right)^{1/2} \quad (2.7)$$

Where  $\omega$  is the angular frequency and  $\sigma$  the conductivity. The attenuation coefficient is a theoretical number that describes the loss of signal to be expected if the radar system is operating perfectly, i.e. the signal loss that is solely due to external factors.

## Scattering

The term scattering covers the loss of signal by processes such as reflection, refraction and diffraction. Reflection means that the radar waves are reflected by a surface. In an idealised case the ratio of the power of the signal that is transmitted  $P_t$  through the material to the power of the reflected signal  $P_r$  will depend on the properties of the two materials as well as other parameters such as the area of the receiving antenna  $A_r$ , the transmitting antenna gain  $G_t$  and the length of

the travel path  $z$ , as follows (e.g. Bogorodsky et al., 1985)

$$\frac{P_r}{P_t} = \frac{G_t A_r q R}{16\pi z^2 L} \quad (2.8)$$

The term  $q$  is the refraction coefficient described below,  $L$  is the dielectric loss.  $L = \exp(4\alpha d)$  in the two way path  $d$  and  $R$  describes the refraction index of the two media (Bogorodsky et al., 1985).

Refraction is the change in direction of a wave when it passes from one medium to another with different transmission properties. Refraction can occur in ice where the ice is inhomogeneous but has also been observed in firn or snow layers on top of ice (Plewes and Hubbard, 2001). For an antenna carried at a height above the surface the effect of the refraction is to increase the power density returned to the receiver by a factor (e.g. Dowdeswell and Evans, 2004)

$$q = \left( \frac{h + d}{h + (d/n')} \right) \quad (2.9)$$

Where  $n'$  is the refracting medium index. Although the increase in return signal power is advantageous (especially when the height of the antenna above the surface  $h$  is much smaller than the depth of the refracting medium  $d$ ), the refraction rarely contributes to losses with more than a few dB in the radar configurations used in radioglaciology (Bogorodsky et al., 1985; Dowdeswell and Evans, 2004).

Diffraction is the apparent bending of the electromagnetic waves around an object often of the same size as the wavelength of the wave. When encountering rough surfaces the backscattered signal will have an increase in power due to the diffraction (Plewes and Hubbard, 2001). This is rarely the case for internal layering, unless the layer is due to material that includes impurities on a metre-scale.

### Geometrical Spreading

Geometrical spreading is the loss of signal power due to the geometry of the radar signal. This is a well-known problem in radar technology (e.g. Bogorodsky et al., 1985). As the radar signal is transmitted as a cone shape the energy will spread out geometrically with distance from the transmitter at a rate of  $1/r^2$  where  $r$  is the distance from the source (Bogorodsky et al., 1985). Thus even if no other signal attenuation occurs (e.g. the wave travels through vacuum) the signal strength will still decrease with distance from the source. This is one of the reasons why deep internal layers will almost always have a weaker reflection than layers close to the surface.

## Dielectric Absorption

Dielectric absorption is caused by two processes: relaxation, which is the loss of energy due to oscillations of the water molecules, and conduction, which is energy loss due to small shifts in electron positions relative to the water nuclei (Plewes and Hubbard, 2001). This process is heavily influenced by the impurity content of the ice due to the resulting change in conductivity which is why pure water ice has a much lower signal attenuation due to dielectric absorption than ice that contains for example sea salt (Bogorodsky et al., 1985; Corr et al., 1993).

The combined effect of signal attenuation is to reduce the strength of the returned signal with increased ice thickness. As the radar wave travels down through the ice the signal strength decreases due to the geometrical spreading, scattering and/or dielectric absorption. This means that deep internal layers are much harder to identify than shallow layers. Since the signal attenuation is positively related to the frequency, lower frequencies will generally have less signal attenuation. However, lower frequencies also have lower resolution, i.e. less ability to differentiate between two reflectors next to each other (in space or time) (Bogorodsky et al., 1985; Plewes and Hubbard, 2001). For the purpose of retrieving information on the internal layering in ice a trade-off must necessarily be made between high resolution of the upper layers, with the risk of losing the signal from the lower layers, or lower frequencies that can penetrate of the entire ice thickness but with a resolution that might not be able to resolve all internal layers. All of these effects are relevant to the PASIN data that form the basis of this thesis (Section 4.1.1). With a frequency of 150 MHz the radar easily resolves numerous internal layers, however, the deep layers appear generally less clear than the shallow layers due to the signal attenuation.

### 2.2.2.2 Data Processing

In order to bring out the deeper layers in the ice and generally to make the internal layers stand out several data processing steps can be applied. Often the background noise will be removed from the radar data, a process that is usually built in automatically in radar processing software. Then some form of correction for the signal attenuation with depth will be applied in order to bring out the deep internal layers. This can be done by, for example, normalising the deeper layers using an exponential function (Fahnestock et al., 2001b).

In order to retrieve information from the internal layers it is often necessary to trace them. This can be a tedious and time-consuming process and very few

automated processes have been evolved that can do this without human interaction (e.g. Fahnestock et al., 2001b; Sime et al., 2010, in press). For example, the SPRI datasets covering West Antarctica have been traced manually to retrieve information on past accumulation rates (Leysinger Vieli et al., 2004) and to classify them according to their continuity (Siegert et al., 2005b). Naturally this approach introduces human errors in tracing the correct layer and in assessing continuity. In areas where the data (or layers) are not as good short gaps between the layering may occur and it is often necessary to estimate where the layer continues by matching the internal layering on each side of the gap, increasing the likelihood of the operator/tracer making a mistake in judging the layer stratigraphy (Siegert et al., 2005b). An example from the SPRI dataset of typical internal layering can be seen in Figure 2.4.

Fahnestock et al. (2001b) developed a method for semi-automatically tracing internal layers. When a layer is identified by the user/operator the routine centres a window around the point and searches for similar pattern using cross-correlation. This is repeated until the spatial coherence decreases. This method decreases the subjectivity in layer tracing and the need for extensive human interaction. Part of the reason for the success of this method lies in the type of dataset. The dataset was acquired at a frequency of 150 MHz but with a much denser sampling rate than the SPRI data. Secondly, since the survey was conducted along the ice divide the ice had experienced very little flow and most of the layering was therefore clearly visible with hardly any disruptions. Compared to this dataset the PASIN data from PIG contains substantially more disrupted internal layering, partly due to the fast flow of the ice and partly due to the steep bed relief. This contributes significantly to the difficulty of constructing automatic layer tracing.

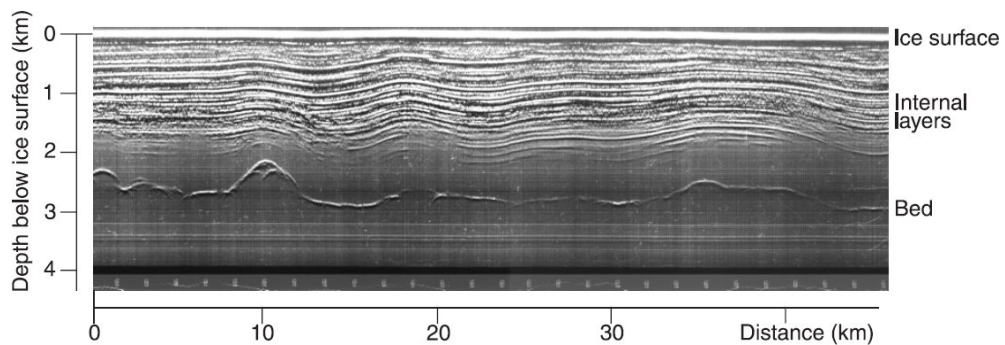


Figure 2.4: *Example of internal layering clearly visible in a radargram from the SPRI dataset (Siegert et al., 2005b, Figure 2a)*

To summarise, internal layers in ice-sheets and glaciers are isochrones that

hold valuable information on the past of a glacier. The internal layers can be imaged by different radio-echo sounding techniques. However, the return signal of the radar waves is affected by several processes that attenuate the signal as the radar waves propagate down in the ice. The signal attenuation depends on the frequency of the radar waves, the dielectric properties of the ice and increases with depth of the ice. Knowledge of these properties means that the signal attenuation to some extent can be corrected for, however, the nature of this correction varies between different studies. When the corrections have been applied an impressive amount of information can be retrieved from the layers, which will be discussed in more detail in the sections below.

### 2.2.3 Internal Ice-Sheet Structure

In areas where survey lines are closely spaced RES data can be used to build a three-dimensional image of the internal layering and thus provide information on the internal ice-sheet structure. This is usually only possible if there is one or more very distinctive layers that can be identified in different lines. One example is a study by Hodgkins et al. (2000) who traced three internal layers in the area around Dome C, East Antarctica, in order to construct a three-dimensional map of the internal structure of the region. Another example is the identification of a highly reflective layer north of the main trunk of PIG enabling a correlation of the layer stratigraphy between flightlines and thus the construction of a three-dimensional elevation map of the internal layer (Corr and Vaughan, 2008).

If a RES survey intersects an ice core site the internal layering can often be correlated with the ice core thus providing knowledge of the age-depth relation and even in some cases an age for the internal layers observed in the radar data (e.g. Siegert et al., 1998). Efforts have even been made to approach the age problem from a different angle and model the radar signal based on knowledge of the ice properties from an ice core allowing for better determination of radar wave propagation velocities (Eisen et al., 2004, 2006).

The SPRI dataset has been used to extend internal layers observed over Lake Vostok, where an ice core has been drilled and dated, to a new ice core site at Dome C (Siegert et al., 1998). This was possible because the dataset in the area had fairly dense coverage thus enabling construction of three-dimensional maps of the internal layers (Hodgkins et al., 2000). The maps also helped highlight differences in the ice deformation history of the area. These studies exemplify how different datasets from one region can be utilised to provide an in-depth image of the past of an area (Siegert et al., 2005b).

Of particular interest to this thesis is the ground-based surveys that took

place over a four year period with starting point at Byrd Station and with one of the traverses crossing the PIG basin. In the surveys a remarkably bright layer was identified and was found to correspond to a layer of increased acidity in the Byrd ice core. The layer could therefore be dated to an age of around 17.5 kyr based on the age-depth relation from the ice core (Jacobel and Welch, 2005). The significance of the findings for this thesis will be discussed in Section 6.5, but in essence it provides an age-depth relationship for a small area of the PIG basin.

### 2.2.4 Past Accumulation Rates

Accumulation rates over the Antarctic can be estimated on a regional scale from atmospheric modelling combined with satellite measurements (Rignot et al., 2008) or by interpolating satellite data using field measurements (Arthern et al., 2006). However, the resolution is not good enough to capture local variations in accumulation and direct field measurements of accumulation rates in Antarctica are naturally sparse compared to the size of the continent (e.g. Magand et al., 2007). By using internal layers to infer accumulation rates the resolution obtained will not only be on a local scale but also provide a temporal dimension since the stratigraphy of the layers will reflect the accumulation history since their deposition (e.g. MacGregor et al., 2009).

Internal layers in the near-surface can be used to identify recent local accumulation variations. For example, Vaughan et al. (1999) found that internal layers in Fletcher Promontory, Antarctica, that displayed stratigraphy unrelated to the bed topography, could be linked to localised accumulation variations. Figure 2.5 shows an example of data from that study where the internal layers dip down due to a local accumulation maximum. The dip is caused by the fact that the addition of extra snow increases the vertical velocity of the ice flow.

The past accumulation rate over an area can be reconstructed from deeper internal layering since the depth of an internal layer depends primarily on the surface mass balance and the ice flow. This is particularly applicable in areas where the ice flow is slow and thus fairly easy to model. Essentially this approach assumes that once the deformation of the layers due to ice flow has been taken into account, the depth of the internal layer will reflect the accumulation rate since its deposition (e.g. Siegert et al., 2003a; Leysinger Vieli et al., 2004). For example, internal layers have been traced along the ice divide of the Greenland Ice Sheet, where the layers are dominated by vertical thinning. Thus the deformation of the layers can be modelled with a simple Dansgaard-Johnson ice flow model, that describes the vertical variation of the velocity in an ice column and is especially suited for areas of slow flow (Dansgaard and Johnsen, 1969). Fahnestock et al.

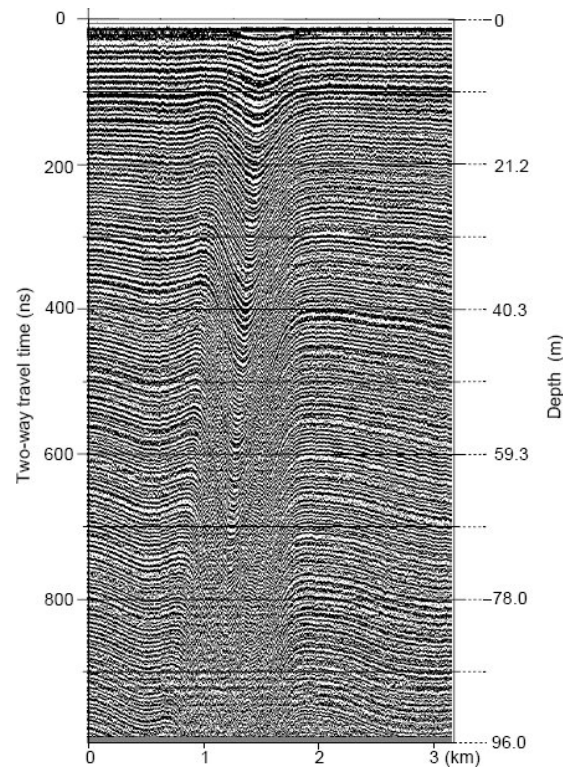


Figure 2.5: *Example of undulating near surface layers caused by local variations in accumulation from Fletcher Promotory, West Antarctica (Vaughan et al., 1999, Figure 2c).*

(2001b) used this model to account for the influence of ice flow on the layer stratigraphy and from that information reconstructed the past accumulation rate. Since several ice cores have been drilled along the ice divide (e.g. North Greenland Ice Core Project members, 2004) the age-depth relation was fairly well known and helped constrain the age of the internal layers enabling an age estimate for the accumulation rate extending several thousand years back in time (Fahnestock et al., 2001b).

This approach is applicable to a wide range of areas using different modelling techniques depending on the region and the complexity required to account for the ice flow. A study by Siegert and Payne (2004) reconstructed accumulation rates in the area around the Byrd ice core in West Antarctica using internal layering and a one dimensional vertical ice compression model. As the age-depth relation was known from the ice core the variations in accumulation could be reconstructed temporally as well as spatially going back tens of thousands years. The results from the study showed a spatial variation in the accumulation pattern and that accumulation rates had fluctuated in the past 16 kyr ago. In this area a fold in the internal layering further indicate that a change in flow direction have taken place within the past 1.5 kyr (Siegert et al., 2004b).

Sometimes the dynamics of the ice flow in an area require more complex models to be applied. For example, the area in the foreground of the Transantarctic Mountains has ice flowing over a large subglacial hill. To account for the influence of this bed topography on internal layers Siegert et al. (2003a) used a two dimensional ice flow model to model the internal layers by matching the model outputs with the observations through adjustment of the accumulation rate. Another example of using more a complex model is a study from the Lake Vostok area by MacGregor et al. (2009) where both a local layer approximation and a formal inverse method was used to retrieve the past accumulation pattern. This study particularly highlighted the differences between the two methods when it comes to the interpretation of the deeper internal layers that may have a more complicated flow history (MacGregor et al., 2009).

### 2.2.5 Basal Melting

The effect from basal melting on internal layering is to drag the layers downwards as the basal melting increases the vertical velocity at the base of the ice. Thus the vertical velocity and vertical thinning of internal layers in areas with increased basal melting will be higher than in areas of low basal melting. It is often easy to identify areas of increased basal melting in RES data when other factors that may influence the layers can be ruled out.

If the ice flow and accumulation rate is known, the rate of basal melting can often be inferred from the stratigraphy of the internal layers. For example, a study by Fahnestock et al. (2001a) included basal melting in a simple ice flow model and, based on the fit between the model and the observed layers, was able to retrieve basal melt rates under central Greenland. In Antarctica increased basal melting can at times give rise to the formation of subglacial lakes under the ice (e.g. Siegert et al., 1996; Siegert, 2005)). Naturally, the study of basal melting in these areas is tied into the characterisation of these lakes. The detection of subglacial lakes is described in more detail in Section 2.3.3.

The rate of basal melting becomes particularly important in relation to the search for new ice core drilling sites. The International Partnerships in Ice Core Sciences (IPICS, a planning group of ice core scientists, engineers, and drillers from 18 nations) have identified the need to drill an ice core that contains ice older than 1.5 million years (IPICS white paper, Wolff et al., 2006). In this case it is essential to chose a drill site with the minimum amount of basal melting, since basal melting will have removed the oldest ice and significantly lowered the age of the ice at the bed. An example of this is the NorthGRIP ice core from Greenland where ice from the Eemian interglacial period 130-115 kyr ago was found much

closer to the bedrock than expected due to increased basal melt rates (North Greenland Ice Core Project members, 2004). A study of RES data from the area revealed large spatial variation in the basal melt rates under the northern part of the Greenland ice sheet. Buchardt and Dahl-Jensen (2007) calculated the basal melting in the area by optimising the fit of the internal layers to a Dansgaard-Johnsen model using inverse methods and estimated accumulation rates from shallow ice core studies and the NorthGRIP ice core.

### 2.2.6 Internal Layering and Ice Flow Dynamics

The initial classification by Drewry (1983) of the layering in the SPRI dataset forms the basis for categorisation of internal layering in RES data. Later studies (e.g. Siegert et al., 2003b; Rippin et al., 2003b, 2006) have continued to use the classification scheme that distinguishes between three types of layers:

1. Well-preserved continuous layers, where the amplitudes of the undulations of the layers do not exceed those of the bed topography. Figure 2.6a are examples of this kind of layering.
2. Buckled, disrupted or discontinuous layering, and layering with amplitudes greater than those of the bed topography. Figure 2.6b is an example of this kind of layering.
3. Absent layers. The absence of layers can either be an artefact caused by signal loss in the radar instrument or an actual physical feature of the glacier. Figure 2.6c is an example of this kind of layering.

In Figure 2.6 note how the continuous layers follow the bed topography with decreasing amplitudes moving from the lower to the upper layers, while discontinuous layers only occur in broken layer packages.

The classification of layers is often very subjective and can be prone to errors especially since no automated classification method has been widely agreed on. Furthermore, the distinction between buckled layers and continuous layers is not always straightforward. Robin and Millar (1982) developed a criterion for continuous layers specifying that the wavelength of the undulations of the layers must be smaller than that of the bed topography. Based on this criterion Siegert et al. (2003b) in a study of Kamb Ice Stream (formerly Ice Stream C) classified layers as buckled if the amplitude of the wavelength is greater than that of the bed. To aid distinguishing between continuous and buckled layers the study also made use of Fast Fourier transformations in order to compare the variations in amplitude between bed topography and layers. This is one of the few examples

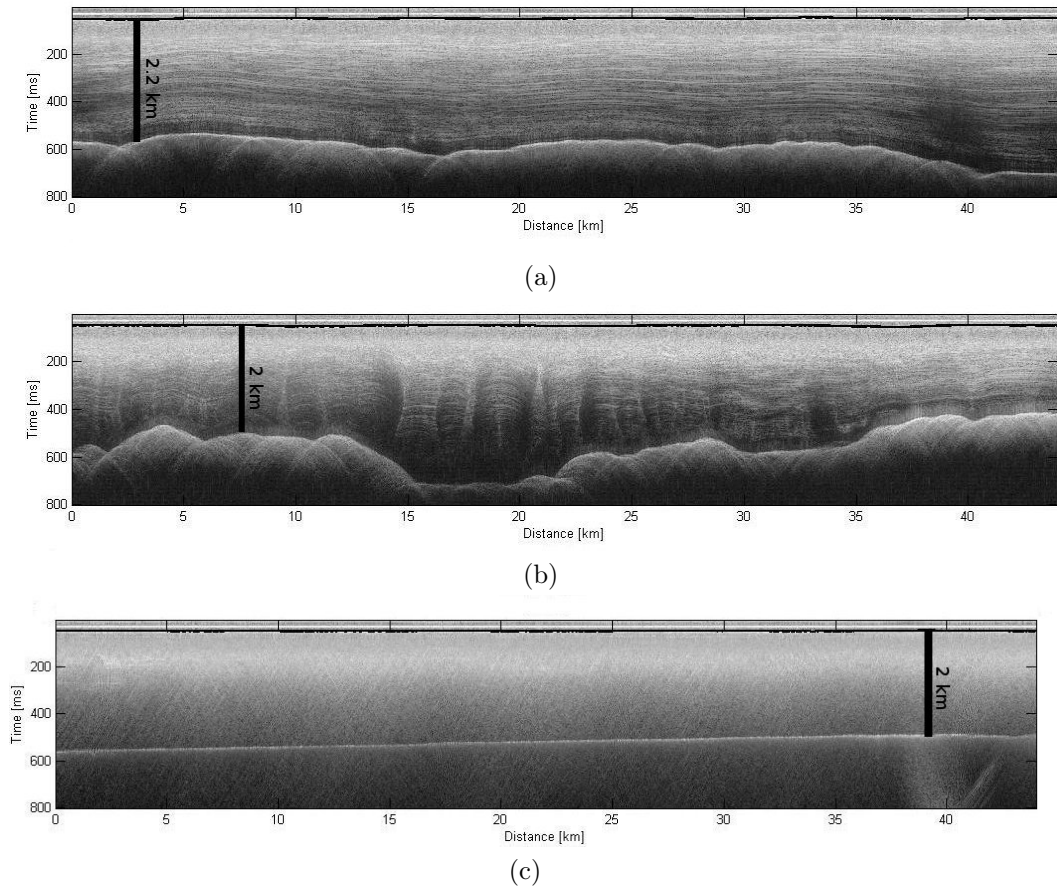


Figure 2.6: *Example of the three different kinds of internal layering showing (a) continuous, (b) discontinuous and (c) missing layering. All three radargrams are from the PASIN dataset over PIG from the neck between the northern and southern basin, across Tributary 3 and in the main trunk respectively.*

where a more quantitative approach has been taken to classifying internal layers. In most other studies (e.g. Rippin et al., 2003b, 2006; Catania et al., 2005) the classification has been done qualitatively.

The link between ice flow dynamics and the internal layering is of great importance. In areas where the ice is slow-moving the layers are generally continuous and easy to trace often over hundreds of km (e.g. Robin and Millar, 1982; Siegert et al., 2003b). When the ice speeds up into ice streams the layering gets deformed and their stratigraphy no longer resemble the bed topography but rather is thought to be a product of the ice flow dynamics (Jacobel et al., 1993). Furthermore, transition zones between continuous and discontinuous layers often correspond to a change in ice flow velocity (Bell et al., 1998; Rippin et al., 2003b). Absence of internal layers often occurs in areas of extremely fast flow, suggesting that the deformation of the ice in these areas is so great that the internal layers are obliterated (Siegert et al., 2003b; Rippin et al., 2006). In Coats Land, East Antarctica, RES sounding has revealed areas with significant disruption of layers

in spite of a flat bed topography. This was interpreted as an indication of a relic fast flow area that is no longer active (Rippin et al., 2006). Other areas where internal layering reveal changes in ice dynamics include the WAIS divide where an anomalous fold in the layering is thought to have been caused by a change in flow direction (Siegert et al., 2004b) and similar features in the Kamb Ice Stream (Ng and Conway, 2004).

Since the internal layering essentially preserves a record of past influences from ice flow dynamics numerous studies have attempted to extract information on the past of the Antarctic Ice Sheets based on their stratigraphy. Examples of such studies include the use of the SPRI datasets over East and West Antarctica to identify relict ice streams (e.g. Rippin et al., 2003b; Siegert et al., 2003b) and studies of the ice streams draining into the Ross Ice Shelf (e.g. Jacobel et al., 2000; Siegert et al., 2003b; Catania et al., 2005) in an attempt to reconstruct the past of the region. Other examples include a study of Byrd Glacier where two regions were identified with distinctly different internal layering that could have significance for historical and modern ice flow dynamics (Welch et al., 2009).

### 2.2.7 Summary

Internal layers in glaciers are caused by changes in dielectric properties due to variations in density, acidity content or crystal orientation. The detection of the layers depends on the radar system and several effects can contribute to radar signal attenuation leading to a decrease in signal strength with depth. The interpretation of the internal layering in glaciers can be used to extract information on ice flow dynamics, basal conditions and internal ice-sheet structure. In spite of the wide usage of the internal layers there exists very little general agreement on how to best process the radar data, how to trace the internal layers and the best way to quantify the continuity of the layers.

## 2.3 Other RES Measurements

Internal layering is by no means the only information that RES surveys of glaciers yield. Although the focus of this thesis is the internal layering other processes are also of importance and a brief introduction to the main pieces of information that RES can return is given below.

### 2.3.1 Ice Thickness Measurements

The initial motivation for undertaking RES surveys of Antarctica was to obtain measurements of ice thickness and bed topography. Internal layering was merely a byproduct. With the arrival of satellite radar (e.g. Shepherd et al., 2001; Wingham et al., 2009) and laser altimeters (e.g. Zwally et al., 2002; Pritchard et al., 2009) the surface elevation is now measured mostly from satellite (e.g. Bamber and Gomez-Dans, 2005), but RES is still the primary tool for retrieving ice thickness (Dowdeswell and Evans, 2004).

Ice thickness  $h$  is inferred from the time difference  $\Delta t$  between the echo returned from the surface of the ice and the echo returned from the bedrock/ice interface (Equation 2.5) (e.g. Bogorodsky et al., 1985). This is the most common use of RES in glaciology. The most well-known example of ice thickness measurements is the SPRI dataset that comprises over 70 000 ice-thickness values and provides the base for our current understanding of the Antarctic Ice Sheet. For example, the data returned from the surveys revealed that the Antarctic Ice Sheet was on average 2.5 km thick and had a maximum depth of 4.7 km (Drewry et al., 1982).

Equally important to ice thickness data is information on the bed topography that can be inferred from the ice thickness if the surface elevation is known. Many ice streams are controlled by their bed topography and knowledge of the bed is therefore instrumental in understanding the flow dynamics of a glacier. Examples of Antarctic glaciers controlled by basal topography include the Bailey/Slessor region (Rippin et al., 2003a), the ice streams on the Siple Coast (Joughin et al., 2002), several of the Filchner-Ronne ice streams (Joughin et al., 2006) and Pine Island Glacier (Vaughan et al., 2006). Finally, in order to successfully model ice flow it is crucial to have knowledge of the bed topography and ice thickness both on larger and smaller scales (e.g. Huybrechts et al., 2004; Hindmarsh et al., 2009).

Following the SPRI surveys a number of airborne surveys of Antarctica have mainly focussed on more detailed mapping of the bedrock at specific sites of interest. In connection with the European Project for Ice Coring (EPICA) the area around Dome C in East Antarctica was densely surveyed with RES to locate the ideal drill site (Tabacco et al., 1998; Rémy and Tabacco, 2000; Forieri et al., 2004). Surveys of WAIS include measurements of the subglacial topography of the Siple Coast (e.g. Retzlaff et al., 1993), the drainage basins of the glaciers flowing into the Amundsen Sea (Vaughan et al., 2006; Holt et al., 2006) and the Rutford Ice Stream (e.g. Vaughan et al., 2008; King, 2009).

In 2001 a database of the bed topography and ice thickness of the Antarctic ice sheet was compiled from the data collected over the past 50 years. The new

“BEDMAP” database gave an unprecedented view of the subglacial topography of the entire continent with a resolution of 5 km<sup>2</sup> (Lythe et al., 2001). Recent years have seen a combined effort to further improve the knowledge of the surface and subglacial topography (e.g. Bamber et al., 2009a; Le Brocq et al., 2010) working towards a release of an updated version of BEDMAP.

### 2.3.2 Basal Conditions

The bed reflection coefficient carries information on the bed properties including the nature of the subglacial geology, the roughness of the bed, the possible presence of water and whether or not the bed is frozen or at the pressure melting point (e.g. Jankowski and Drewry, 1981; Catania et al., 2003; Bingham and Siegert, 2007a).

The smoothness of the bed has a large impact on the dynamics of a glacier. A smoother and/or softer bed is often associated with fast ice flow since it offers less resistance to the ice movement, though the effect acts both ways as fast ice flow might smooth the bed by erosion (Siegert et al., 2004a; Bingham and Siegert, 2007b). Often the bed roughness is retrieved from RES data by analysing the wavelength of the variations of the bed topography using Fast Fourier Transformation (Taylor et al., 2004). One example of this is a study of the Institute and Möller ice streams, where the bed was found to be rougher in slow-flowing regions and smoother in fast-flowing regions (Bingham and Siegert, 2007a). Another study used RES data to study basal roughness in central East Antarctica and extract information on past ice flow dynamics (Siegert et al., 2005c).

Studies have shown that the onset of ice streams is often closely linked to the presence of a wet base (e.g. Bentley et al., 1998; Fahnestock et al., 2001a; Catania et al., 2003). The presence of water at the base of an ice sheet - either in the form of liquid water or as easily deformable water saturated sediments - causes a decrease in the basal stress and allows for more rapid ice flow (Bell, 2008). Since the strength of the basal reflector solely depends on the dielectric contrast between the ice and the bed rock, the basal reflectivity can be used to infer the presence of water or water saturated sediments. As a general rule, areas of low basal reflectivity will often correspond to a frozen bed while regions with high reflectivity indicates a wet base (Catania et al., 2003). A recent study of Kamb Ice Stream in West Antarctica measured the bed reflectivity in a ground-based survey and found that high reflectivity corresponded to high surface velocities as measured from InSAR and low reflectivity spots had the lowest surface velocity (Jacobel et al., 2009). Furthermore, the high reflectivity values were similar to those found at a borehole site with wet basal conditions (Jacobel et al., 2009). However, the

relation between basal reflectivity and surface velocity is not straightforward as a study of the Siple Dome found that a soft, water-saturated bed alone does not necessarily enable fast ice flow (Gades et al., 2000).

The geology of the bed can often be characterised from variations in the subglacial roughness combined with measurements of gravity and magnetics (Dowdeswell and Evans, 2004; Bingham and Siegert, 2007b). Several subglacial basins and geological divides in Antarctica have been identified using these methods (e.g. Jankowski and Drewry, 1981). Modern day surveys often collect gravity and magnetic measurements while simultaneously acquiring RES data enabling a direct comparison between the data types. These surveys have particularly highlighted the correlation between subglacial geology and ice streams (e.g. Bell et al., 1998) and the presence of active volcanism in West Antarctica (Blankenship et al., 1993).

### 2.3.3 Subglacial Lakes

Although the surface temperature of the Antarctic Ice Sheets is usually well below freezing, the ice works as an insulating layer thus causing an increase in temperature downwards in the ice due to the geothermal heat. Figure 2.7a shows how the temperature can rise above the pressure melting point and lakes can form under the ice. This typically requires ice thickness in excess of 3 km, but lakes can also form in areas where internal ice deformation and sliding in addition to the geothermal heat flux produce enough energy to cause melting (Siegert, 2005).

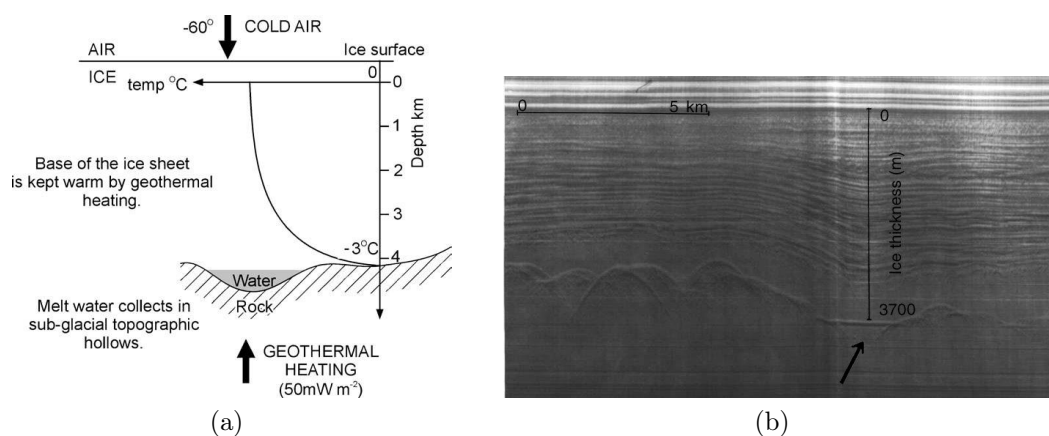


Figure 2.7: (a) Diagram showing how water can occur in subglacial environments due to geothermal heat (Siegert, 2005, Figure 1). (b) Example of a subglacial lake on RES data (Siegert et al., 1996, Figure 2).

Since the dielectric properties of liquid water is substantially different to those of ice (cf. Table 2.1), the presence of subglacial lakes can often be identified on

radargrams. In RES data the lakes exhibit several distinctive characteristics: stronger reflection at the ice-sheet base than the nearby subglacial bedrock and much smoother, virtually horizontal surfaces (Siegert et al., 1996) as shown in Figure 2.7b. Due to the frequency of most RES surveys it is rarely possible to infer the depth of a subglacial lake based on RES data alone since the thickness of water the radar wave is able to penetrate will often be less than the thickness of the layer of water (Dowdeswell and Evans, 2004).

The subglacial lakes in Antarctica were first observed during the SPRI surveys. In the late 1990s the list of identified subglacial lakes based on this database included over 77 lakes occupying approx. 10% of the ice-sheet base (Siegert et al., 1996). An updated list of Antarctic subglacial lakes included 145 locations with lake-type reflections estimated to contain a volume of 4,000-12,000 km<sup>3</sup> (Siegert et al., 2005a). The majority of the Antarctic subglacial lakes are located in the interior of the ice sheet and have a depth of 50-250 m (Dowdeswell and Siegert, 1999). The largest known subglacial lake is Lake Vostok that holds approximately 5000 km<sup>3</sup> of water (Siegert, 2005). In recent years satellite measurements of elevation change have been used to identify more subglacial lakes and their drainage pattern (e.g. Fricker et al., 2007; Smith et al., 2009). The subglacial lakes are also interesting due to the fact that they are likely to have been isolated since their formation estimated to be 10<sup>5</sup> - 10<sup>6</sup> years ago and thus contain unknown forms of bacterial life (e.g. Abyzov et al., 2001; Castello and Rogers, 2005).

## 2.4 Modelling Internal Layers in Glaciers

Internal layers contain a vast amount of information of the past about glaciers including information on accumulation pattern, basal conditions and flow dynamics (e.g. Leysinger Vieli et al., 2004; Buchardt and Dahl-Jensen, 2007; Rippin et al., 2003b). Some of that information can be retrieved by looking at the stratigraphy of the layers, their depth and reflectivity. In order to optimise the information that can be extracted from internal layers in ice sheets, ice flow models are commonly employed. The use of flow models enables the influence of ice flow on layering to be determined quantitatively and hence, for example, accumulation patterns can be explored more fully (e.g. Fahnestock et al., 2001b; Siegert and Payne, 2004). In this section the key concepts of ice flow modelling will be introduced providing an overview of the basic principles, focussing on how internal layers in an ice sheet can be modelled. More comprehensive introductions to the subject can be found in, for example, Hutter (1983); van der Veen (1999) and Paterson (2002).

### 2.4.1 Introduction to Ice Flow Modelling

Ice flow modelling represents an attempt to investigate the dynamics of glacial ice both on a regional scale and global scale (e.g. Oerlemans et al., 1998). Ice flow models also play an important part in investigating the past and projecting the future of ice sheets and glaciers and constructing age-depth relationships of ice cores (e.g. Dansgaard and Johnsen, 1969; Parrenin et al., 2004). In recent years efforts have also been made to couple ice-sheet models with global circulation models to simulate forcing from the climate and the feedback from the ice (e.g. Huybrechts et al., 2004). Furthermore, observations of the polar regions are leading to increasing concerns over the impact of the Antarctic and Greenland ice-sheets on global sea-level rise (e.g. Shepherd and Wingham, 2007; Vaughan, 2008). During the past few decades there has therefore especially been an interest in developing models to predict the mass balance of ice sheets (e.g. Arthern and Hindmarsh, 2003) in a bid to quantify their contribution to present sea-level rise and to understand their impact on the climate system. The overarching goal of ice sheet modelling is to be able to define the present state of glacial ice, however, in order to do so the model would have to include a large number of (non-linear) processes that each are important on different temporal and spatial scales (e.g. Hindmarsh et al., 2009). Figure 2.8 shows some of the parameters that influence an ice-sheet. The processes include, for example, basal conditions influenced by geothermal heat flux and subglacial topography, and grounding line

motion controlled by sea-level and ocean temperatures. Finally, the internal ice dynamics themselves and their response to external forcing are far from simple and often approximations are necessary. Most ice flow models therefore focus on describing some of the controlling mechanisms rather than the entire system.

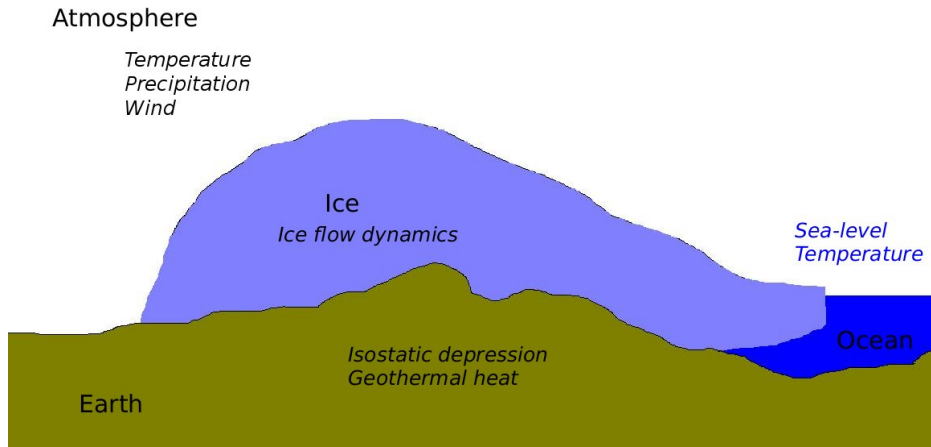


Figure 2.8: An overview of some of the processes that influence ice sheets (adapted from Rutt (2009)).

### 2.4.2 Age Distribution in Flowing Ice

Models that aim to calculate the age of internal layers often aim to connect the geometry of the layers with the flow field of the glacier. This relationship was first studied by Weertman (1976) in a study of the impact on internal layers of a transition from ice flow sliding over the bed to ice flow with no sliding (i.e. deforming ice). Weertman (1976) concluded that as ice moves through a sliding-no sliding transition zone the upper part of the ice sheet is stretched and the lower part is compressed. Parrenin and Hindmarsh (2007) explored this further in an analytical study of the behaviour of isochrones for sliding and no-sliding conditions and at ice divides, demonstrating that internal layers sink towards the bed when the ice flow changes from no-sliding to sliding.

One approach to the problem of calculating the shape of internal layers is to consider the age of the internal layers in ice as an advection or transport equation and solve it accordingly. Following Hindmarsh (1999, 2001); Hindmarsh et al. (2009) and Leysinger Vieli et al. (2007) age is denoted  $X$  and the mapped ageing equation is

$$\frac{\partial X}{\partial t} + \mathbf{v} \cdot \nabla \mathbf{X} = \delta \quad (2.10)$$

where  $\mathbf{v}$  is the velocity field and  $\delta$  assumes the values of 1 for an ageing equation or 0 for a tracer equation respectively. This thesis concerns itself only with the

age equation e.g.  $\delta = 1$ . The physical interpretation of this is that within the model the age of a particle increases one time step as it moves down in the ice. This equation is deceptively simple but in reality quite complicated to solve. It presents a well-known problem in glaciology as the need for a stable, smooth solution must be traded-off against a good representation of the real physical system (cf. Greve et al., 2002; Hindmarsh et al., 2009). The solution of the equation in two and three dimensions will be discussed in more detail in Section 4.3.1 and Section 4.3.2.

Using the age equation to calculate the age of the layers often entails an assumption of steady state as well as knowledge of surface and bed topography and mass balance of the glacier. The calculation of the velocity field is based on knowledge of the mechanical (and thermomechanical) properties of ice which will be discussed below.

### 2.4.3 Deformation of Ice Crystals

The structure of ice-crystals has already been described in Section 2.1.1 as well as its implications for the electrical properties of ice. Following Paterson (2002) this section explains how the ice-crystal structure affects the deformation of ice. In order to clarify the concepts of stress a brief introduction to the nomenclature of continuum mechanics is given here: stress is defined as the force acting on a body per area. The stress working perpendicular to an area is called the normal stress, while the stresses working in the same plane are called shear stresses. The strain describes the change in length (normal strain) and/or shape (shear strain) of a material compared to its original shape (assuming that the deformation is small). Usually it is the strain rate rather than the strain that is considered, where the strain rate is defined as the change of the strain in time and has dimensions  $\text{time}^{-1}$ .

Deformation of a single ice crystal when a constant stress is applied will normally take place by gliding along the basal planes of the crystal. One can visualise this as “a pack of cards where the pack can easily deform by the cards gliding over each other” (Paterson, 2002). Although crystals can deform along other axes as well the stress needed to produce deformation is 100 times larger than that for basal gliding (Paterson, 2002).

Polycrystalline ice deforms more slowly than a single ice crystal since the randomly aligned crystals will not be at an orientation favourable for basal gliding. If a volume of randomly oriented ice crystals is subjected to a constant stress the initial response of the ice is an elastic deformation (elastic deformation is an immediate change in shape of a material when a stress is applied, when the stress

is removed the material will return to its original shape thus elastic deformation can be considered as reversible), followed by three periods of creep (primary, secondary and tertiary creep) illustrated in Figure 2.9. After the elastic deformation the strain rate decreases (primary creep) until it reaches a minimum value due to the resistance between crystals of different orientation (secondary creep rate). Then the strain rate increases again when the crystals reform in an orientation more favourable for gliding in the direction of the stress (tertiary creep) (Barnes et al., 1971; Paterson, 1977, 2002). As the tertiary creep rate becomes steady the crystals reach an equilibrium size, that is independent of the initial size and depends primarily on the stress, where higher stress lead to smaller crystals (Paterson, 2002). The minimum value state of the secondary creep is often interpreted as a steady state although it technically is not. Even so, in the secondary creep rate state and for the range of stresses that are important in normal glacier flow (50 - 200 kPa) the relation between the strain rates and the stresses has been described by empirical fits and this relation is often referred to as Glen's Law, which forms the basis of most ice flow models (Glen, 1955; Paterson, 2002).

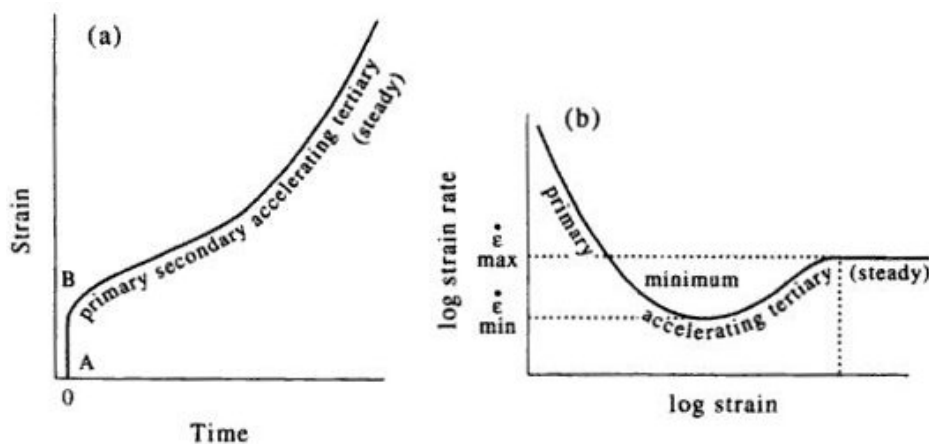


Figure 2.9: *The variation of strain with time (a) and the relation between strain rate and strain (b) from (Paterson, 2002, Chapter 5, Fig. 5.2)*

#### 2.4.4 Continuum Mechanics of Ice

Glacial ice is a polycrystalline material, in which crystals are assumed to form with a random (isotropic) orientation. While recent work has shown that some glacial ice contains aligned crystals inherited from past flow and impacting on further deformation (Gillet-Chaulet et al., 2005; Greve et al., 2009; Martín et al., 2009), anisotropy has yet to be represented effectively in most ice flow models and is beyond the scope of the work presented in this thesis. Instead, almost all ice

flow models make the important assumption that the ice being modelled is an isotropic medium, enabling it to be treated as a viscous fluid.

The assumption that ice can be treated as a viscous fluid means that the movement of the ice can be computed using the laws of continuum mechanics. They describe the conservation of mass, momentum, angular momentum and energy. Comprehensive reviews of the continuum mechanics of ice can be found in, for example, Hutter (1983); van der Veen (1999) and Paterson (2002). The following overview builds on these sources as well as Pattyn (2003).

The conservation of mass is generally written as the gradient of the velocity field assuming that ice is incompressible:  $\nabla \cdot \mathbf{v} = 0$ , where  $\mathbf{v}(x, y, z) = (u, v, w)$  is the velocity field. The equation for conservation of mass can therefore be written as:

$$\frac{\partial u}{\partial x} + \frac{\partial v}{\partial y} + \frac{\partial w}{\partial z} = 0 \quad (2.11)$$

In glaciological literature Equation 2.11 is commonly termed the continuity equation. The second governing equation is the conservation of momentum:

$$\rho \frac{d\mathbf{v}}{dt} = \nabla \cdot \sigma + \rho \mathbf{g} \quad (2.12)$$

where  $\rho$  is the density of ice,  $\mathbf{g}$  is the gravitational acceleration and  $\sigma$  represents the stress tensor (see below). The acceleration term  $d\mathbf{v}/dt$  is generally negligible for ice flow, and the equation can therefore be simplified to

$$\nabla \cdot \sigma = -\rho \mathbf{g} \quad (2.13)$$

Finally the third equation of state for ice flow is the heat conduction equation:

$$\rho \frac{d(c_p \theta)}{dt} = \nabla \cdot (k_i \nabla \theta) + \Phi \quad (2.14)$$

where  $c_p$  is the heat capacity of ice,  $\theta$  is the ice temperature,  $k_i$  is the thermal conductivity (note that the thermal conductivity is not the same parameter as the electrical conductivity) and  $\Phi$  is the heating generated due to friction when the ice deforms. The three equations above are collectively termed field equations (e.g. Pattyn (2003)) and together they describe the mechanical and thermomechanical properties of ice.

#### 2.4.4.1 The Stress Tensor

Stress is defined as the force acting on a material divided by the surface area. Considering a cube of ice, the forces per area acting on the ice from different

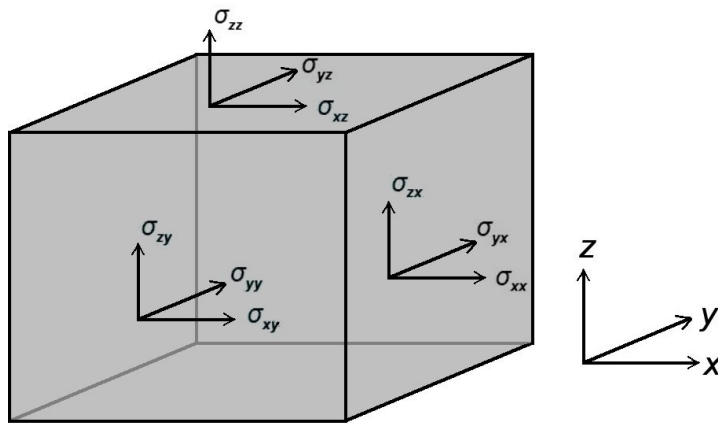


Figure 2.10: Normal and shear stresses on a cube of ice (adapted from Paterson (2002) and Rutt (2009)).

directions can be specified completely by nine components of a stress tensor, that describes the response of internal forces within a body as a reaction to an external force. Figure 2.10 shows the direction of the stresses on an ice cube. The stress tensor includes three normal stresses and six shear stresses where the normal stresses act perpendicular to the ice surface while the shear stresses act parallel to it. The stress tensor is defined as:

$$\bar{\sigma} = \begin{pmatrix} \sigma_{xx} & \sigma_{xy} & \sigma_{xz} \\ \sigma_{yx} & \sigma_{yy} & \sigma_{yz} \\ \sigma_{zx} & \sigma_{zy} & \sigma_{zz} \end{pmatrix} = \begin{pmatrix} \sigma_x & \tau_{xy} & \tau_{xz} \\ \tau_{yx} & \sigma_y & \tau_{yz} \\ \tau_{zx} & \tau_{zy} & \sigma_z \end{pmatrix} \quad (2.15)$$

where  $\sigma_i$  is the normal stress and  $\tau_{ij}$  is the shear stress. The components of the stress tensor are not all independent. In fact it turns out that  $\tau_{ij} = \tau_{ji}$ . From the stress tensor the full form of Equation 2.13 is then:

$$\frac{\partial \sigma_{xx}}{\partial x} + \frac{\partial \sigma_{xy}}{\partial y} + \frac{\partial \sigma_{xz}}{\partial z} = 0 \quad (2.16a)$$

$$\frac{\partial \sigma_{yx}}{\partial x} + \frac{\partial \sigma_{yy}}{\partial y} + \frac{\partial \sigma_{yz}}{\partial z} = 0 \quad (2.16b)$$

$$\frac{\partial \sigma_{zx}}{\partial x} + \frac{\partial \sigma_{zy}}{\partial y} + \frac{\partial \sigma_{zz}}{\partial z} = \rho g \quad (2.16c)$$

where Equations 2.16a and 2.16b represent the horizontal components of Equation 2.13 and Equation 2.16c the vertical component. Models that include every component of the stress tensor are often referred as full Stokes models.

### 2.4.4.2 Strain Rates

Instead of considering the strain of ice it is more practical to consider the strain rate, the change in strain over time. The strain rate is also a tensor and is defined as the derivatives of the velocity field:

$$\begin{pmatrix} \dot{\epsilon}_x & \dot{\epsilon}_{xy} & \dot{\epsilon}_{xz} \\ \dot{\epsilon}_{yx} & \dot{\epsilon}_y & \dot{\epsilon}_{yz} \\ \dot{\epsilon}_{zx} & \dot{\epsilon}_{zy} & \dot{\epsilon}_z \end{pmatrix} = \begin{pmatrix} \frac{\partial u}{\partial x} & \frac{1}{2}\left(\frac{\partial u}{\partial y} + \frac{\partial v}{\partial x}\right) & \frac{1}{2}\left(\frac{\partial u}{\partial z} + \frac{\partial w}{\partial x}\right) \\ \frac{1}{2}\left(\frac{\partial v}{\partial x} + \frac{\partial u}{\partial y}\right) & \frac{\partial v}{\partial y} & \frac{1}{2}\left(\frac{\partial v}{\partial z} + \frac{\partial w}{\partial y}\right) \\ \frac{1}{2}\left(\frac{\partial w}{\partial x} + \frac{\partial u}{\partial z}\right) & \frac{1}{2}\left(\frac{\partial w}{\partial z} + \frac{\partial v}{\partial y}\right) & \frac{\partial w}{\partial z} \end{pmatrix} \quad (2.17)$$

Note that the dot over the  $\epsilon$  follows Newton's notation for a time derivative, e.g.  $\dot{\epsilon} = \frac{\partial \epsilon}{\partial t}$ . The relation between the shear stresses and shear strain rate  $\dot{\epsilon}$  is called Glen's Law in glaciology and is given as (Glen, 1955)

$$\dot{\epsilon}_{xz} = A\tau_{xz}^n \quad (2.18)$$

Where  $A$  is the so-called ice flow law parameter. This relation is well known in other material sciences in a more generalised form (e.g. Hutter, 1983; Paterson, 2002) and its application to glaciological problems was originally discussed in several early studies by for example Nye (1952, 1959). The value of  $n$  in Glen's Law describes the flow type, where  $n = 1$  implies a simple viscous flow (e.g. the strain rate changes linearly with the stress). Measurements in laboratory and in the field suggest values for  $n$  between 1 and 4 depending on temperature and stresses in the ice. Usually in glaciology  $n$  is set equal to 3 which assumes that flow takes place due to dislocation creep (secondary creep) (Paterson, 2002). In Equation 2.18  $A$  depends exponentially on the temperature of the ice, but also on the water content, the hydrostatic pressure and crystal size and orientation. Measurements of  $A$  have returned values ranging from  $10^{-15}$  to  $10^{-18}\text{s}^{-1}\text{kPa}^{-3}$  for temperatures between 0 and  $-50^\circ\text{C}$  (Paterson, 2002).

Using Glen's Law the velocity gradients can be related to the momentum conservation equation (Equation 2.13). The full solution of these equations is extremely complicated and the sections below will describe different common approximations and simplifications that often are made in glaciological flow models.

### 2.4.5 The Shallow Ice Flow Approximation

The full range of flow models spans from simple isothermal, one-dimensional models to three-dimensional models that include the temperature of the ice and solve for all stresses.

This section focuses on the shallow ice flow approximation, which is thoroughly

discussed in Hutter (1983). Many ice sheet models are based on this approximation since it is valid for most glacial settings. However, at the ice divide and near the terminus of a glacier the shallow ice flow approximation is not valid because it is based on the assumption that the ice thickness  $H$  is considerably smaller than the ice length  $L$ :  $H \ll L$ . Flow will then primarily be controlled by internal deformation caused by gravity. This leads to the assumption that the vertical component of the force balance (Equation 2.16c) is dominated by the normal stress and that the horizontal shear gradients are unimportant for the horizontal components (Equations 2.16a and 2.16b). Figure 2.11 shows the complete forces acting on a slab of ice (a) and the forces that are included in the shallow ice flow approximation (b). In this way Equation 2.13 is reduced to

$$\begin{aligned}\frac{\partial \sigma_x}{\partial x} + \frac{\partial \tau_{xz}}{\partial z} &= 0 \\ \frac{\partial \sigma_y}{\partial y} + \frac{\partial \tau_{yz}}{\partial z} &= 0 \\ \frac{\partial \sigma_z}{\partial z} &= -\rho g\end{aligned}\tag{2.19}$$

simplifying it significantly. Full three-dimensional models that rely on the shallow ice flow approximation include models by Huybrechts (1990) and Greve (1997). Part of the reason why the shallow ice flow approximation is widely applied, in spite of its limitations, is the complexity of the full stress equations coupled with the difficulty in achieving a steady solution and the computational costs involved in running it (Pattyn, 2003). One example of a full Stokes (or higher-order) model is work by Pattyn (2003). For a discussion and comparison of the shallow ice flow approximation and the full Stokes solution see Hindmarsh (2004).

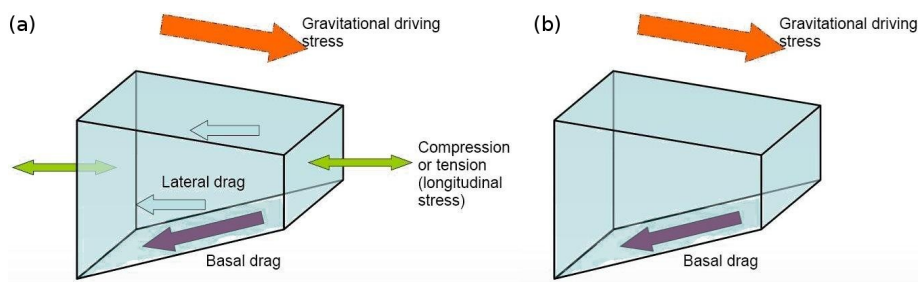


Figure 2.11: Force balance from Rutt (2009) showing (a) all the forces and (b) the forces included in the shallow ice approximation.

In this thesis the model that is primarily used to calculate the age of the internal layering is based on the age equation (Equation 2.10) and the shallow ice flow approximation. When solving the age equation the shallow ice flow approximation is used to calculate the velocity field from Glen's flow law and

Equation 2.19.

In the sections that follow two simple examples of applications of the shallow ice flow approximation are discussed. They are both common approaches to solving a recurring problem in glaciology; that of limited computational power.

#### 2.4.5.1 Flow along a Flowline

One way of simplifying Equation 2.13 is to consider flow in only two dimensions. This implies that the model is following the flow of ice along a flow line i.e. the movement of ice is restricted to the  $(x, z)$ -plane. Flow line models are easier to construct than three-dimensional models, much simpler and thus requires substantially less computational power. However, by disregarding the  $y$ -direction any influences from lateral drag (i.e. any drag from the sides) and from longitudinal stresses (e.g. stretching or compression) are discarded. The flowline approach is often useful for glaciers that have a simple geometry and to test the different parameters that influence the ice flow, for example, basal sliding or calving at the front (e.g. Vieli et al., 2000; Nick et al., 2009). Work on flow line geometries includes a model in Microsoft Excel by Pattyn (2006) available as an open source program.

As an example, an overview of the governing equations for a shallow ice flow approximation flow line model is given below. It is assumed that the mass balance and surface and bed topography are known. The first step is then to calculate the horizontal velocity of the ice. From Equation 2.17 and following Paterson (2002) the shear strain is equal to

$$\dot{\epsilon}_{xz} = \frac{1}{2} \left( \frac{\partial u}{\partial z} + \frac{\partial w}{\partial x} \right) \quad (2.20)$$

Using Glen's Law (Equation 2.18) and assuming that the change in vertical velocity with  $x$  is negligible the horizontal velocity is

$$\frac{1}{2} \frac{\partial u}{\partial z} = A \tau_{xz}^n \quad (2.21)$$

Assuming that  $\tau_{xz}$  is the only stress component gives

$$\tau_{xz} = \rho g (H - z) \sin \alpha \quad (2.22)$$

where  $\alpha$  is the surface slope  $= \frac{\partial s}{\partial x}$ . This assumption corresponds to assuming that the shear stress in the ice is caused by deformation as a response to gravity alone. At the base of the ice it is also termed  $\tau_b$ ; the basal or driving stress. By

integrating Equation 2.21 twice the mean horizontal velocity is found to be:

$$\bar{u} = \frac{2A(\rho g)^n}{n+2} \left( \frac{\partial s}{\partial x} \right)^n H^{n+1} \quad (2.23)$$

In ice flow models the key interest is to retrieve information on the response of the system to some input of mass. Most often the parameter of interest will be the change in ice thickness. Defining  $Q = \bar{u}H$  as the mass flux, the change in ice elevation must be the mass input  $m$ , i.e. the accumulation and ablation, minus the change in mass flux across the length of the glacier (illustrated in Figure 2.12):

$$\frac{\partial s}{\partial t} = m - \frac{\partial(\bar{u}H)}{\partial x} \quad (2.24)$$

where  $m$  is the mass balance. Since the mean horizontal velocity is already known from Equation 2.23 the change in ice surface over time can now be calculated using Equation 2.24. The numerical solution of Equation 2.24 can be done using standard numerical approximations to differential equations, such as finite differences or finite elements methods. This will be addressed in more detail in Section 4.3.

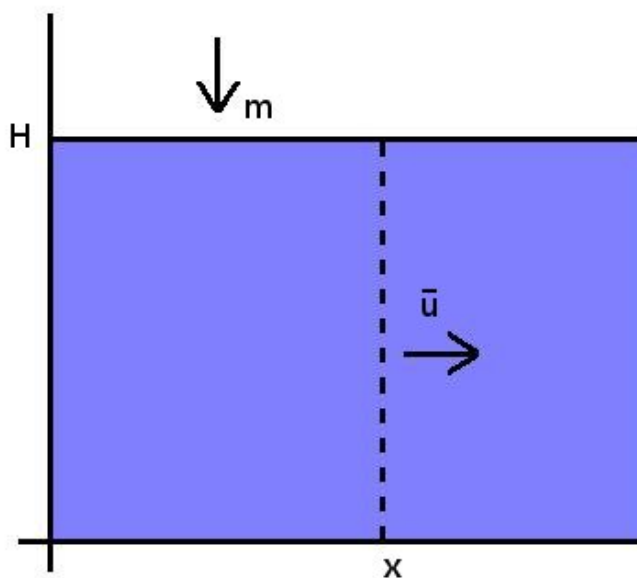


Figure 2.12: Volume conservation in a column of ice. Input  $m$  along the length  $x$  will equal the output over the entire ice thickness  $H$  if there is no change in the surface elevation.  $\bar{u}$  denotes average horizontal velocity (e.g. the ice is flowing to the right).

### 2.4.5.2 The Dansgaard-Johnsen Model

One of the most well-known models for modelling the age of internal layers was developed by Dansgaard and Johnsen (1969) for flow near an ice-divide. This model assumes that the horizontal velocity is equal to the surface velocity in the upper part of the ice until a prescribed depth  $h$  where the velocity decreases linearly.

$$u(x, z) = \begin{cases} u_s(x) & z \in [h, H] \\ u_s(x) \left( F_B + (1 - F_B) \frac{z}{h} \right) & z \in [0, h[ \end{cases} \quad (2.25)$$

where  $h$  is the so-called kink height,  $u_s$  is the surface velocity and  $F_B$  is the fraction of sliding over the bed. The vertical velocity can then be found using Equation 2.11 and based on the velocity field the paths of the individual particles can be calculated. The accuracy of the Dansgaard-Johnsen model depends on determining the correct value of  $h$ , which essentially represents the elevation where  $u$  decreases with depth, and will depend on a number of parameters such as bed topography and temperature of the ice. Even so, if  $h$  is chosen correctly the model achieves a good approximation of the horizontal velocity (Philberth and Federer, 1971). One of the strengths of the model is its simplicity. This makes it possible to use as input in inverse models to retrieve information on, for example, basal melting (Bucharth and Dahl-Jensen, 2007), since inverse models require multiple runs which can be done with reasonably small computational requirements with the shallow ice flow approximation. The simplicity of the model is also one of its weaknesses since it was developed for the slow flowing areas near an ice-divide and therefore unlikely to be applicable in areas of faster flow. Examples of successful applications of the Dansgaard-Johnsen model includes the calculation of past accumulation rates in West Antarctica and Greenland by Siegert and Payne (2004) and Fahnestock et al. (2001b).

## 2.5 Chapter Summary

Radio-echo sounding relies on the fact that ice is transparent to electromagnetic waves in the HF and VHF bands and it has been used extensively since RES surveys of Antarctica started in the 1960s. Due to different dielectric properties the surface, internal layers and bedrock can usually be readily identified. Error sources in the return signal such as geometrical spreading and signal attenuation can often be calculated based on knowledge of the radar system and the physical properties of the ice.

In glaciology RES is an extremely important tool for retrieving information on ice thickness, subglacial topography and basal conditions of glaciers and ice sheets. Of particular importance in relation to this thesis is the internal layering in glaciers. The internal layers are caused either by density variations in the upper few hundred metres, changes in ice crystal orientation or variations in impurity content. The stratigraphy of the internal layers is the product of the combined influence from mass balance, ice flow and basal melting. They therefore hold information on the past of the glaciers such as temporal and spatial variations in accumulation rates and changes in ice flow. The continuity of the layers often correlate with ice flow velocity. These pieces of information can be used to infer information about the past flow regime of a glacier and comparisons between observations of internal layers and output from flow models further provide insights into the dynamics of a glacier.

In order to retrieve information from internal layering in ice it is often useful to estimate the influence of ice flow on the layer stratigraphy by using ice flow models to describe the flow. All ice flow models rely on some form for representation of the internal stresses in ice. The complexity of this representation decides the accuracy of the model. Simpler models that do not include all stresses are common and often present a computationally less expensive alternative. These models usually include different components of the stress tensor depending on which part of the ice sheet system they are aiming to describe and can be quite accurate for the specific problem. The shallow ice flow approximation is the most common and is based on the assumption that the thickness of the ice typically will be substantially smaller than the length.

The age of internal layers can be regarded as a transport/advection equation, that is a well-known, but not necessarily straight-forward, differential equation. Based on the transport/advection equation and the shallow ice flow approximation the age of the internal layers can be found as described in Leysinger Vieli et al. (2007); Hindmarsh et al. (2009) and in Section 4.3.1 below. Another sim-

pler method for calculating the age-depth relationship for internal layers is the Dansgaard-Johnsen model, which is mainly valid in areas near ice-divides.

Ice flow models are a powerful tool for obtaining additional information from internal layering that cannot be gathered from considering the stratigraphy and layer appearance alone. However, it is important to keep the limitations of the models in mind, especially what problem they are built to solve and how well they can be expected to assimilate reality given these limitations.

### **Radioglaciology and ice flow modelling in bullet points:**

- Radio-echo sounding of ice reveals surfaces that mark a change in dielectric properties
- Internal layers represent a change in permittivity and/or conductivity of the ice
- A change in permittivity and/or conductivity can be caused by variations in density, acidity or crystal orientation
- Internal layers are isochrones and their stratigraphy is the result of mass balance, ice flow and basal melting
- The layers can be used to reconstruct past accumulation rates and identify areas of increased basal melt
- The continuity of the layers often correlate with ice flow velocity
- Other uses of RES data include measurements of ice thickness and basal conditions
- The aim of ice flow models is to assimilate the deformation of ice typically in response to gravity
- Ice flow models rely on a representation of the internal stresses in ice
- The most common approximation of the stresses is the shallow ice flow approximation
- The age of internal layers in an ice sheet can be solved as a transport/advection equation



# Chapter 3

## Pine Island Glacier

The study area of this thesis is the Pine Island Glacier catchment basin. This chapter aims to explain why the stability of the Pine Island Glacier is important for the entire WAIS (Section 3.1). Then follows a description of the flow configuration and topography of PIG (Section 3.2), and an introduction to the current observations of change (Section 3.3). Finally, potential forcing mechanisms behind the observed changes are discussed in Section 3.4.

### Notes on field site nomenclature

In traditional glaciological literature (e.g. Sugden and John, 1976) the term *glacier* refers to a mass of ice moving continuously from higher to lower ground, its flow typically constrained by topography. An *ice stream* is an area of fast moving ice bounded by slower-moving ice, distinguished from a glacier in terms of its generally larger size and not obviously (i.e. on the basis of surface observations) being directed by topography. Over 90% of the Antarctic Ice Sheet is drained by ice streams, where flow speeds exceed  $100 \text{ m yr}^{-1}$ , that drain relatively stable and inactive source regions, with flow speeds less than  $5 \text{ m yr}^{-1}$ . The flow often takes place via a complex system of tributaries, which represent a transitional flow regime with velocities between  $5 \text{ m yr}^{-1}$  and  $100 \text{ m yr}^{-1}$  (e.g. Joughin et al., 1999; Bingham et al., 2007). All Antarctic ice streams ultimately flow into the sea and start to float; the point where floating initiates is termed the *grounding line*, and the location of the grounding line greatly influences ice-stream stability (Paterson, 2002).

Pine Island Glacier refers to the  $175,000 \text{ km}^2$  ice-drainage catchment; although containing the word “glacier” in its title, it is not in fact a glacier in the terms defined above but a *catchment* drained by an ice stream fed by several tributaries (Vaughan et al., 2001). Henceforth this thesis will use Pine Island Glacier (or PIG) to refer to the drainage catchment.

### 3.1 The Significance of Pine Island Glacier

PIG is one of the largest catchment basins in WAIS (Figure 3.1). It is part of a system of ice streams that transports ice from the WAIS into the Amundsen Sea. The remoteness of this Amundsen Sea Sector of WAIS (red box in Figure 3.1) meant that until recently only a limited number of observations from the area were available. However, since the early 1990s an increasing amount of data from satellite observations have allowed for the first meaningful assessment of change across this region, including estimates of changes in elevation, surface velocity and mass balance (e.g. Stenoién and Bentley, 2000; Shepherd et al., 2002; Rignot, 2008; Wingham et al., 2009; Pritchard et al., 2009). During the last ten years the satellite records have been supplemented by several surveys carried out by aircraft (Thomas et al., 2004a; Holt et al., 2006; Vaughan et al., 2006) and on the ground (Scott et al., 2009).

The Amundsen Sea Sector is thought to be particularly vulnerable to instability or rapid retreat. This is a consequence of the marine ice sheet instability hypothesis wherein removal of a downstream ice shelf can result in the rapid and irreversible inland migration towards the interior (Weertman, 1974; Mercer, 1978; Thomas, 1979; Bamber et al., 2009b). PIG, its neighbour Thwaites Glacier, and other catchments draining into the Amundsen Sea such as Smith and Kohler Glaciers (Figure 3.2) have no significant ice shelves. Recent surveys (as described in Section 4.1) also confirm that PIG is largely grounded below sea level and has a reverse-sloping bed (Vaughan et al., 2006). Thirty years ago, recognising its potential vulnerability, Hughes (1982) dubbed the Amundsen Sea Sector “the weak underbelly” of the WAIS, but at that time observational evidence for retreat was lacking. Over the past twenty years, however, satellite observations over the Amundsen Sea Sector have reinstated concerns about the region’s vulnerability (Vaughan, 2008), showing that PIG and neighbouring catchments are undergoing significant changes (Rignot, 1998; Shepherd et al., 2002; Rignot et al., 2008; Pritchard et al., 2009). For example, measurements from the European Remote Sensing satellites (ERS-1 and ERS-2) showed that the Amundsen Sea sector lost over  $150 \text{ km}^3$  of ice during 1991-2001, corresponding to a total of 0.43 mm of eustatic sea level rise (Shepherd et al., 2002). In late 2002 the area was surveyed from an aircraft by the Chilean Centro de Estudios Científicos (CECS) and the American National Aeronautics and Space Administration (NASA) and results from the survey showed that the entire catchment region of the Amundsen Sea glaciers is out of balance by 60% which is sufficient to raise sea-levels by  $0.24 \text{ mm yr}^{-1}$  (Thomas et al., 2004a). However, the contribution from PIG itself

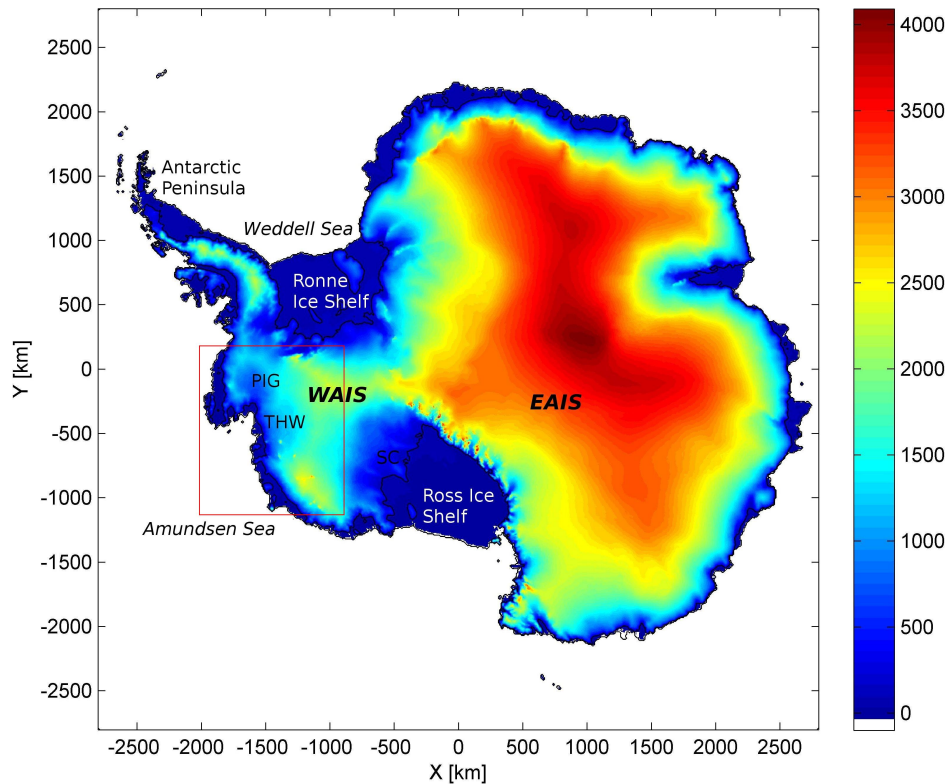


Figure 3.1: *Surface elevation of Antarctica (Bamber and Gomez-Dans, 2005) in metres. The black lines outline the coast and the 120 m surface elevation that roughly corresponds to the outline of several ice shelves. WAIS: West Antarctic Ice Sheet, EAIS: East Antarctic Ice Sheet, PIG: Pine Island Glacier, THW: Thwaites Glacier, SC: Siple Coast. The red box outlines the Amundsen Sea Sector.*

has been estimated to be at most 2.7 cm per century (Joughin et al., 2010). Another study used observations of surface lowering based on data from 1995-2005 (shown in Figure 3.2) combined with atmospheric modelling and concluded that the mass loss of the glaciers draining into the Amundsen Sea had increased from  $41 \pm 27 \text{ Gt yr}^{-1}$  in 1996 to  $64 \pm 27 \text{ Gt yr}^{-1}$  in 2000 and to  $90 \pm 27 \text{ Gt yr}^{-1}$  in 2006 (Rignot et al., 2008).

Of the glaciers draining into the Amundsen Sea PIG is the most dynamic; it has the highest balance flux of all West Antarctic glaciers and one of the highest in the entire Antarctic Ice Sheet (Vaughan et al., 2001). Furthermore, during the last 35 yr PIG has experienced at least two episodes of acceleration separated by a period of steady flow from 1987-1994 (Joughin et al., 2003). The velocity at the grounding line was observed to be as high as  $3.75 \pm 0.1 \text{ km yr}^{-1}$  in 2006 (Rignot, 2008). Part of the explanation for the high velocity of PIG can be found in the high precipitation rates compared to the rest of the Antarctic continent leading to a significant mass transport of ice from the interior of the WAIS (Vaughan et al., 2001). Only the Antarctic Peninsula experiences higher precipitation rates

(Arthern et al., 2006).

Apart from changes in velocity satellite observations also show a retreat of the grounding line and a decrease in ice thickness at the grounding line. In 1992-1996 the thinning at the grounding line was of the order of  $3.5 \pm 0.9$  m ice yr<sup>-1</sup> (Rignot, 1998) with increasing rates ever since (e.g Thomas et al., 2004b; Wingham et al., 2009). Figure 3.2 shows that a substantial part of PIG and Thwaites glacier display widespread surface lowering. Based on these observations Wingham et al. (2009) estimated the average rate of volume loss to have increased from  $2.6 \pm 0.3$  km<sup>3</sup> yr<sup>-1</sup> in 1995 to  $10.1 \pm 0.3$  km<sup>3</sup> yr<sup>-1</sup> in 2006 (see Table 3.1).

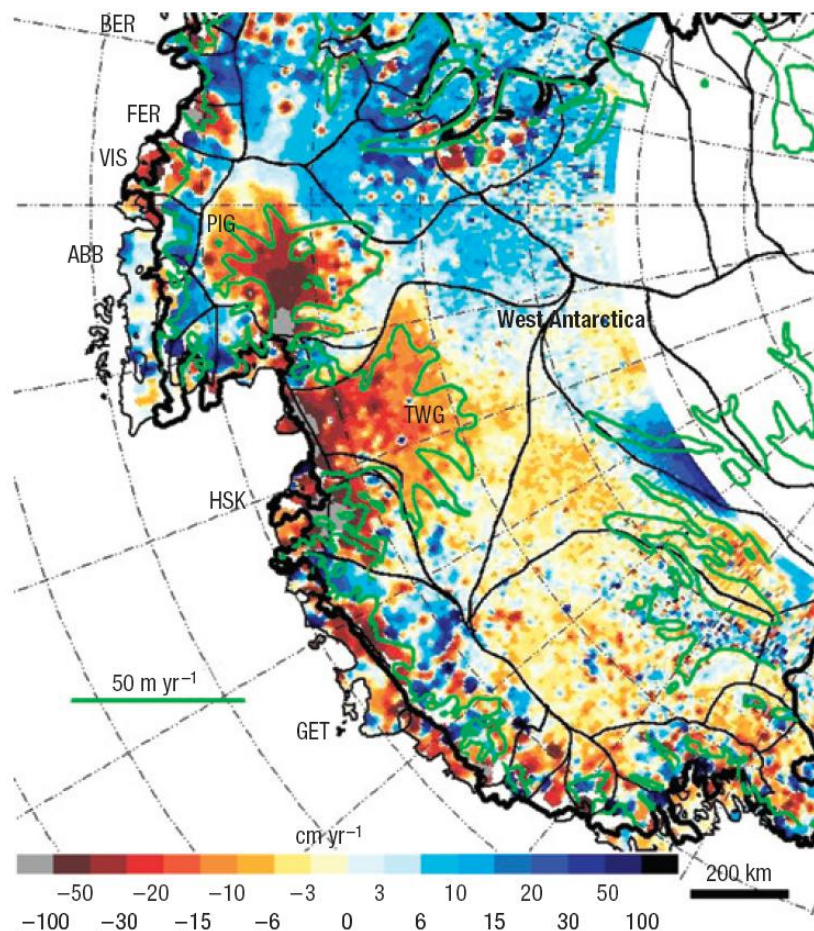


Figure 3.2: *Surface elevation change over West Antarctica derived from ERS-2 and Envisat data 1995-2005. Pine Island Glacier (noted PIG in figure) clearly shows extreme rates of thinning at the grounding line and substantial surface lowering (from Rignot et al., 2008, Figure 2).*

The first GPS measurements of PIG were made between 2006 and 2008 and were also part of the first major, ground-based study of PIG (Scott et al., 2009). The GPS measurements agree with other studies that PIG is not in a steady state and not showing any signs of approaching one, but rather is moving further out of balance (Scott et al., 2009).

| Area   | Volume rate in 1995                           | Volume rate in 2006                            |
|--|---|--|
| Trunk (5400 km <sup>2</sup> )                  | -2.60 ± 0.32 km <sup>3</sup> yr <sup>-1</sup> | -10.09 ± 0.32 km <sup>3</sup> yr <sup>-1</sup> |
| Trunk and tributaries (12800 km <sup>2</sup> ) | -5.10 ± 0.51 km <sup>3</sup> yr <sup>-1</sup> | -23.02 ± 0.51 km <sup>3</sup> yr <sup>-1</sup> |

Table 3.1: Change in volume in 1995 and 2006 of the trunk of Pine Island Glacier and the trunk and tributaries (from Wingham et al. (2009)).

In summary the changes in flux and ice thickness are well-documented but it is unknown whether they are caused by deglaciation as a response to climate change or simply natural variations in ice volume (Vaughan et al., 2006). Since a collapse of PIG would have great implications for the stability of the entire WAIS and potentially global significance in terms of sea-level rise it is urgent to understand the present state and predict the future dynamics of PIG (e.g Hughes, 1982; Corr et al., 2001; Vaughan et al., 2006). In the sections below the current knowledge of the PIG catchment is presented and the flow configuration, bed topography and the changing dynamics of the system are discussed in light of the available observations.

## 3.2 Flow Configuration and Topography

PIG consists of a floating part and two basins; a slow moving southern basin and a faster moving northern basin that are connected via a narrow “neck” less than 100 km across (Vaughan et al., 2001). Figure 3.3 shows the outline of the catchment basin with 50 m surface elevation contours. The fact that the basin encompasses a large range of flow velocities implies that the flow of the catchment consists of a range of different flow mechanics; slow-moving ice that could be cold-based, faster moving tributaries, and finally a fast flowing part that will be referred to as the main trunk (often defined as the area outlined by the 200 m yr<sup>-1</sup> velocity contour (e.g. Shepherd et al., 2002)), that flows into the sea (Vaughan et al., 2001). The different flow velocities also indicate different basal properties and modelling studies suggest that bed properties vary between weakly deforming till and a stronger bed that can support higher driving stresses (Joughin et al., 2009). It can be seen clearly in Figure 3.3 that the elevation decreases from the southern basin to the northern. The figure also shows how the main trunk is flanked by steep surface slopes to the north, east and south and flows westwards onto a floating part.

The floating part of PIG has significant impact on the flow further upstream (e.g Thomas et al., 2004b) and although studies have argued that it does not constitute a significant ice shelf, Vaughan et al. (2001) note that considering the

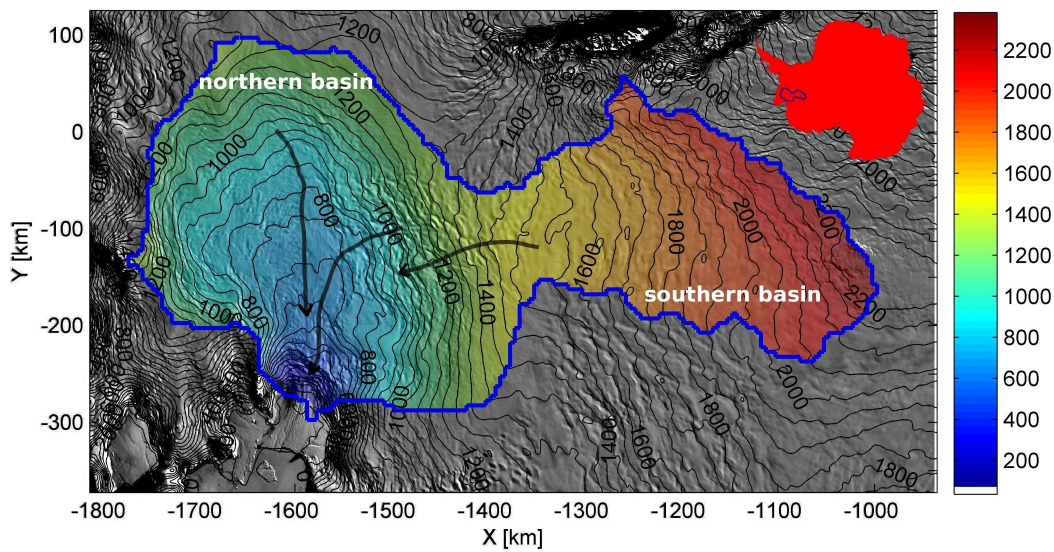


Figure 3.3: *MODIS Mosaic of Antarctica (MOA) imagery (Haran et al., 2006) with surface elevation in colour and contours as black lines (Vaughan et al., 2006) and the PIG catchment basin outlined with a solid blue line. The general direction of flow is indicated with three grey arrows.*

definition of an ice shelf as a “floating ice sheet of considerable thickness attached to a coast” it can be regarded as an ice shelf. Above the grounding line an “ice plain” has been identified constituting a lightly grounded area that could become afloat with increasing grounding line retreat (Corr et al., 2001; Payne et al., 2004).

Compared with many Antarctic ice streams, satellite observations have shown that PIG has a complex flow configuration. The main trunk that drains the northern basin into Pine Island Bay is fed by a set of tributaries that can easily be distinguished in surface velocity data (Figure 3.4). The tributary layout highlights the fact that PIG is a complex system of flow and accumulation. The first two-dimensional image of the tributary system and the velocity of PIG was constructed by Stenoien and Bentley (2000) using data from ERS-1 and ERS-2 covering the years 1992-1996. The study identified several tributaries that were found to flow into the low-slope main trunk, and whose onset could not be determined from the available data. The study also suggested a scheme for numbering the tributaries that will be followed in this thesis (see Figure 3.4).

The location of the tributaries and the main trunk are thought to be controlled by the bed topography (Vaughan et al., 2006). The first map of PIG subglacial topography was constructed by Jankowski and Drewry (1981) from airborne radar data. Later a new bedmap was calculated by Vaughan et al. (2001) and incorporated into the Antarctic-wide BEDMAP (Lythe et al., 2001). In 2004/2005 an extensive airborne survey was undertaken across PIG substantially improving knowledge of its subglacial topography (Vaughan et al., 2006, and see Section

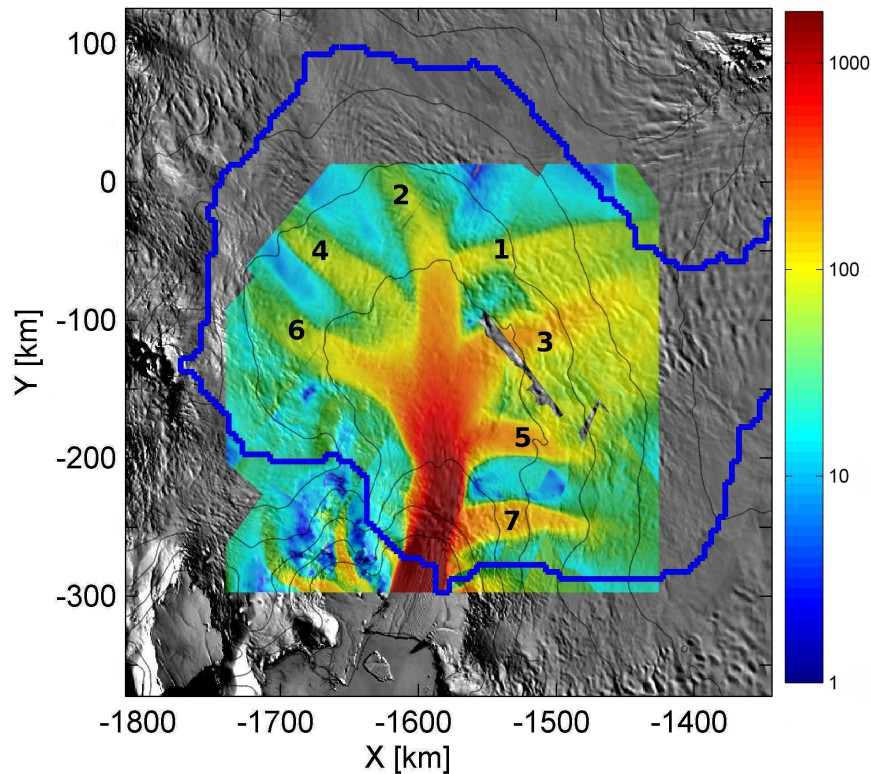


Figure 3.4: *Surface velocities in  $\text{myr}^{-1}$  measured from satellite interferometry (Rignot, 2006) overlain on MOA imagery (Haran et al., 2006). The blue line outlines the northern part of the PIG catchment and the thin black lines are the 200 m surface elevation contours. The numbers refer to the tributaries following the scheme by Stenoien and Bentley (2000).*

4.1.1). The results from this survey, shown in Figure 3.5, represent the most up-to-date knowledge of PIG subglacial topography. Ground radar surveying undertaken across PIG's northern basin in 2007/2008 did not show any substantial difference (R. Bingham, pers. communication, 2010). When combined with surface velocity measurements (red lines in Figure 3.5) the map highlights how most of the fast flow in PIG corresponds with deep confined subglacial troughs indicating that the flow pattern is strongly controlled by the bed topography (Vaughan et al., 2006).

A very significant feature of the PIG subglacial topography is the fact that the subglacial bed deepens inland of the grounding line, a configuration that may affect the stability of the catchment basin (Vaughan et al., 2006). Early studies argued that this configuration, in combination with a lack of a significant ice shelf, is unstable and will lead to increased glacier discharge (e.g. Weertman, 1974), but later studies (e.g. van der Veen, 2001) claimed that such force perturbations in a glacier would be balanced by increased advection of ice from the interior over quite short distances. However, models by Payne et al. (2004) and Thomas et al.

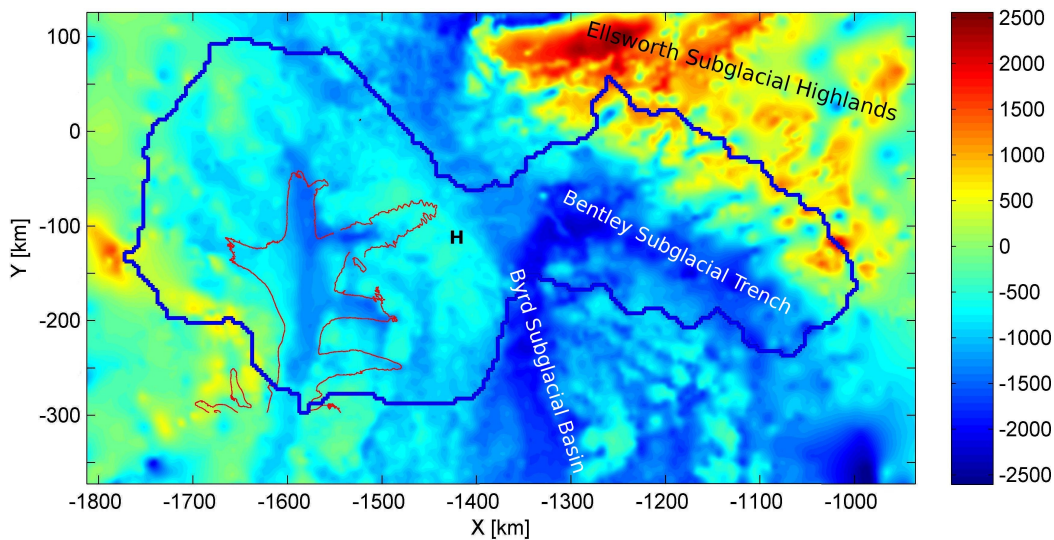


Figure 3.5: *Bed elevation in metres from (Vaughan et al., 2006) in colours. The solid red lines outline the  $100 \text{ m yr}^{-1}$  surface velocity contour and the solid blue line marks the PIG catchment basin. The bed high between the northern and southern basins is marked with an “H”. The high elevation area in the upper right corner above the southern basin is the Ellsworth Subglacial Highlands.*

(2004b) argue that changes in the floating portion of PIG and/or its ice plain might be transmitted rapidly upstream on decadal time-scales and that this effect can account for the observed changes in velocity. This has been further supported by work by Joughin et al. (2010). Because the northern and the southern parts of the drainage basin are separated by a bed high (marked *H* in Figure 3.5), a collapse of the grounding line will most likely mainly affect the northern part and not proceed into the deeper parts of the West Antarctic Ice Sheet (Vaughan et al., 2006).

### 3.3 Observations of Rapid Change

#### 3.3.1 Ice Velocities and Acceleration

The velocity map of PIG shown in Figure 3.4 was acquired by Interferometric Synthetic Aperture Radar (InSAR) and a brief introduction to the technique will be given in Section 4.1.2. This section will focus on what the surface velocity measurements imply for the state of PIG.

Results derived by Stenoien and Bentley (2000) using data from ERS-1 and ERS-2 from 1992-1996 showed that most of the tributaries had a gradual increase in velocity downstream with no sudden onset of acceleration. A later study by Rignot et al. (2002) using data from 1996-2000 showed that parts of PIG

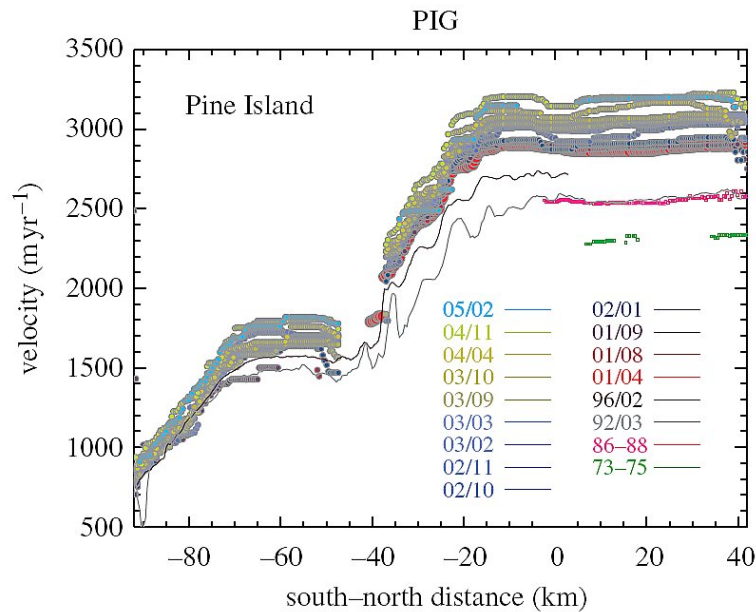


Figure 3.6: *Surface velocities of PIG from 1974, 1987, 1992, 1996 (ERS-1/2) and 2001-2005 (Radarsat-1) versus distance along the centre of the main trunk. The 0 km mark indicates the position of the grounding line in 1996 (Rignot, 2006, Figure 5).*

were experiencing increased velocities relative to 1992-1996 and that these parts coincided with the areas that were already fast-flowing. The velocity was found to be largest at the grounding line but the area of acceleration extended over 100 km upstream with decreasing rates inland. Data from April 2001 compared to January-February 2003 data showed an increase in velocity in the main trunk by  $3.5 \pm 0.5\%$  (Thomas et al., 2004a). A plot of measured surface velocities from ERS-1/2 and Radarsat-1 can be seen in Figure 3.6 showing a general increase in surface velocities during the measurement period. New ground-based GPS measurements acquired between 2006 and 2008 show that the velocity increases further inland than has been possible to demonstrate with InSAR data to date (Scott et al., 2009). Using velocity estimates from 1996 from InSAR and GPS measurements from 2007/2008, Scott et al. (2009) found an annual increase in velocity of between 2% and 3% with decreasing values upstream. This agrees with the most recent measurements from satellites that indicate a  $\sim 4\%$  speedup from 2009 to 2010 (Joughin et al., 2010)

Still more significant than the velocity increases in themselves is the fact that the ice in the main trunk of PIG and progressively inland across its northern basin has been accelerating since the 1990s (e.g. Rignot, 2006). Measurements of acceleration at the grounding line show that in 1974-1987 the acceleration was  $0.8\% \text{ yr}^{-1}$  which increased to  $2.4\% \text{ yr}^{-1}$  in 1996-2000 (Rignot et al., 2002;

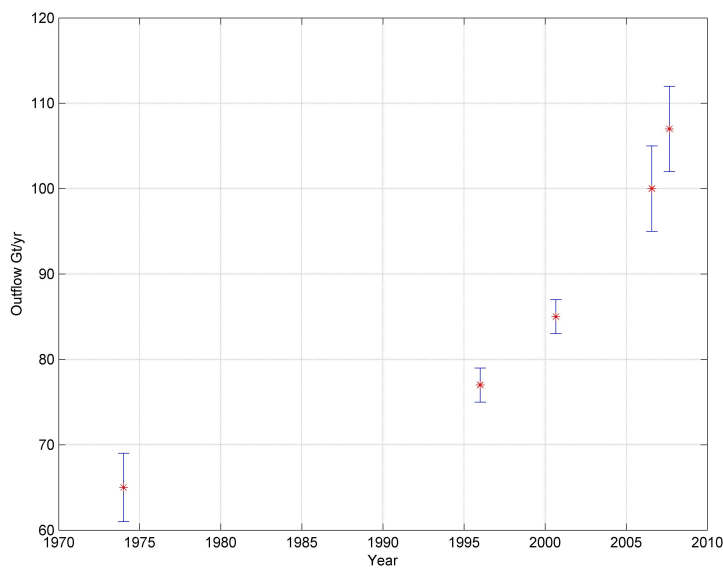


Figure 3.7: Ice discharge from PIG in 1974, 1996 (January), 2000 (October), 2006 (August) and 2007 (October) based on combining surface velocity measurements with ice thickness data from 2002 (for comparison the estimated mass influx is  $61 \pm 9 \text{ Gt yr}^{-1}$ ) (data from Rignot, 2008, Table 1).

Rignot, 2006). During 16 months from 2006 the velocity increased another 8%, which confirms an escalation in acceleration making the total increase in speed 42% since 1996 and 73% since 1974 (Rignot, 2008). These numbers imply that the catchment was nearly in balance when measurements began in the 1970s (based on an estimate of mass influx of  $61 \pm 9 \text{ Gt yr}^{-1}$ ) but is now increasingly becoming more and more out of balance (Rignot, 2008). Figure 3.7 shows the corresponding increase in ice discharge for the years 1974, 1996 (January), 2000 (October), 2006 (August) and 2007 (October) based on a combination of surface velocity measurements and ice thickness data from 2002 (Rignot, 2008).

GPS measurements found the annual increase in velocity to be significantly higher in 2007 over the entire length of PIG than what had been estimated for the previous 12-year period; with an increase up to 6.4% at a distance of 55 km from the grounding line (Scott et al., 2009). This increase in acceleration may indicate that the perturbation originally causing the acceleration is progressing rapidly upstream (Scott et al., 2009).

### 3.3.2 Ice Surface Elevation Change

When discussing potential mass loss from the PIG catchment it is important to distinguish between observations that directly imply thinning and observations of surface lowering. The former relies on sufficient knowledge of the processes causing the observed lowering of the surface to rule out all other causes than

a thinning of the ice. This is the case close to the grounding line where the ice is starting to exhibit floating behaviour and any surface lowering must be counterbalanced by melting at the base (e.g. Fricker and Padman, 2006). In contrast a lowering of the ice surface on grounded ice may be due to thinning but can also be caused by other processes such as subglacial erosion of sediments and snowfall variation. At present the subglacial erosion rates of PIG are unknown but recent measurements suggests that substantial erosion of subglacial sediments is taking place in the main trunk of PIG (A. M. Smith, pers. communication, 2010). Interpreting surface lowering in areas with grounded ice as thinning must therefore be done with caution and estimates of ice mass loss based on these observations provide an upper boundary for the amount of ice lost to the sea.

Substantial changes in the surface elevation of PIG were first reported by Rignot (1998) and Shepherd et al. (2001) from ERS data. Between 1992 and 1999 the surface in the interior of the catchment lowered at a rate of  $\sim 0.1 \text{ m yr}^{-1}$ , while the surface lowering near the grounding line was  $1.6 \pm 0.2 \text{ m yr}^{-1}$  and could be observed as far as 150 km upstream (Shepherd et al., 2001). The rate of surface lowering was not observed to be changing and it was only affecting the main trunk of PIG and not the tributaries (Shepherd et al., 2001). While the surface elevation change of the interior was within the expected variability of snowfall, the change in the main trunk was far greater than expected from changes in snowfall and Shepherd et al. (2001) concluded that it must be linked to ice flow dynamics. Based on these data Shepherd et al. (2001) estimated that the ice plain of PIG could be afloat within 600 yr. A later study extended the dataset to include data from 2001 and confirmed that the elevation change was largely confined to the trunk of PIG (Shepherd et al., 2002). In the period 2002-2003 and 2004 the surface of PIG further lowered with an average rate of  $1.2 \text{ m yr}^{-1}$  reaching as far as 100-300 km inland (Thomas et al., 2004a). On the ice plain the surface elevation was observed to have decreased by 20-30 m in 2002 since a 1998 survey over the same area (Thomas et al., 2004a).

Recent studies have shown that the pattern of elevation change has accelerated and spread inland (see Figure 3.8) and is no longer limited to the central trunk of PIG (Wingham et al., 2009). This is in agreement with ground-based measurements that showed a decrease in surface elevation over 150 km from the grounding line although the largest changes were observed closest to the grounding line (Scott et al., 2009). If the observed surface lowering is caused by thinning of the ice, predictions of the impact on sea-level rise from PIG must now include the potential mass loss from its drainage basin (Wingham et al., 2009). The data showed no evidence of PIG approaching a steady state condition as would be

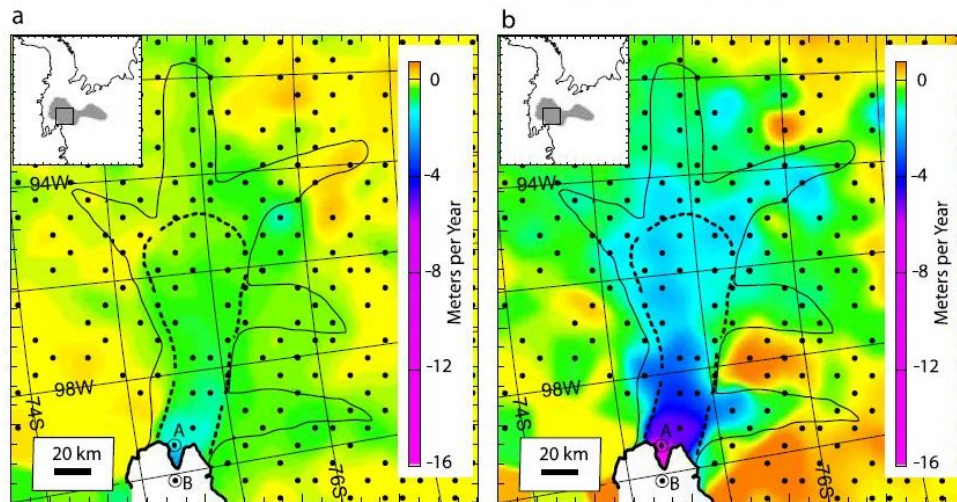


Figure 3.8: Surface elevation change interpreted as thinning in (a) 1995 and (b) 2006. The black dots show the location of the time-series, the boundary of the main trunk (dashed black line) and tributaries (thin black line) and the 1996 grounding line (thick black line) are also shown (from Wingham et al., 2009, Figure 2).

expected if it merely was responding to an episode of accelerated flow (Wingham et al., 2009).

### 3.3.3 Grounding Line Retreat

The location of the grounding line greatly influences the stability of a glacier (Paterson, 2002) and studies have argued that the acceleration of PIG is controlled by its floating portion and the position of the grounding line in the ice plain (Corr et al., 2001). Indeed, Shepherd et al. (2004) proposed that the observed pattern of surface elevation change and acceleration of PIG can be explained by thinning at and retreat of the grounding line, a contention supported by recent GPS observations (Scott et al., 2009). Thomas et al. (2004b) found that an ungrounding of approximately 10% of the ice plain could explain the velocity increase between 1996 - 2000. They further concluded that thinning of the main trunk can cause progressive ungrounding of the ice plain leading to an acceleration and thinning, which in turn will enhance a grounding line retreat.

Accurate measurements of the position of the grounding line, the velocity at the grounding line and its retreat are therefore of great importance. One of the first studies of the PIG grounding line is based on a survey conducted in 1981. In this study Crabtree and Doake (1982) used RES data and LandsAT imagery to calculate the position of the grounding line. In a later study Rignot (1998) used InSAR to show that the grounding line was about 30 km downstream of the

position found by Crabtree and Doake (1982). This study also contained some of the first reliable data for the grounding line retreat of PIG. Here it was reported that between 1992 and 1996 the grounding line retreated  $1.2 \pm 0.3 \text{ km yr}^{-1}$ , which was interpreted to indicate a thinning of  $3.5 \pm 0.9 \text{ m yr}^{-1}$  (Rignot, 1998). The rapid retreat of the grounding line was later confirmed by, for example, Rignot et al. (2002). Based on data acquired between 1991-2001 Shepherd et al. (2002) measured the maximum rate of retreat of the grounding line as  $0.8 \text{ km yr}^{-1}$ , which was thought to be slightly underestimated as the measurement was at a distance of 13 km from the actual grounding line (Shepherd et al., 2002). Lately Rignot (2008) found indications that the grounding line had retreated a total of  $15 \pm 6 \text{ km}$  between January 1996 and December 2007 and also found signs of a transition to flotation of the ice plain. If that is the case this could result in a shift of the grounding line over the part of the glacier bed that is horizontal and below sea-level, according to the marine ice-sheet instability hypothesis (see Section 3.1), and potentially lead to a doubling of the glacier speed (Thomas et al., 2004b; Rignot, 2008). However, studies by Joughin et al. (2010) found evidence for a slowing in grounding line retreat since 2009 indicating that the position of the grounding line is stabilising although thinning of PIG is likely to continue.

### 3.4 Potential Forcing Mechanisms

The increase in thinning at the grounding line, the observations of surface lowering, and the fact that the lowering is spreading from the grounding line to the main trunk and tributaries, coupled with the increase in acceleration, point to a forcing downstream of the main trunk. This is supported by studies showing that relatively small changes in basal stress and/or grounding line position can reproduce the observed pattern of acceleration and surface elevation change to a large extent (e.g. Schmelz et al., 2002; Payne et al., 2004).

Several studies have put forth that the floating part of PIG is exerting a buttressing effect, and the decrease in the floating part causes the acceleration to increase (Rignot, 2008) thus pointing to an effect coupled to ocean circulation (Rignot et al., 2002). This hypothesis is partly based on data from an oceanographic survey conducted in 1994 that revealed that PIG had an unusually high basal melt rate compared to what had been measured at other Antarctic glaciers (Jacobs et al., 1996). The increased basal melting is thought to be caused by influx of Circumpolar Deep Water penetrating beyond the continental shelf to the base of the floating part of PIG (Jenkins et al., 1997). Based on data from this survey Jenkins et al. (1997) estimated the basal melt rate to be  $12 \pm 3 \text{ m yr}^{-1}$  from

an assumption of steady state. Later measurements from satellite showed that this rate was likely to be even higher with an average of  $24 \pm 4 \text{ m yr}^{-1}$  (Rignot, 1998). In later studies the ice thinning, flow acceleration, grounding line retreat and ice-plain un-grounding have all been attributed to enhanced basal melting of the floating ice by a warmer ocean (e.g. Shepherd et al., 2004; Rignot et al., 2004). This is further supported by the fact that the speed up of PIG coincides with an increase in the temperature of the water in the Amundsen Sea (Rignot, 2008) and that similar changes have been observed in the neighbouring Thwaites and Smith glaciers (Shepherd et al., 2002).

Even so, new data from an autonomous underwater vehicle (AUV) that was deployed under the floating part of PIG indicate that other processes could be influencing the retreat and thinning of the floating ice (Jenkins et al., 2010). The AUV returned high resolution images of the sea floor revealing the existence of a ridge between the ice front and grounding line. Jenkins et al. (2010) interpreted this as a previous point of ice grounding and suggested that the ungrounding from the highest point of the ridge coincided with the rapid acceleration observed in the 1970s. After this event the rate of retreat might only have been influenced modestly by oceanic variability. Jenkins et al. (2010) further conclude that retreat of the grounding line is likely to continue inland until the next rise in subglacial bed topography i.e. 200 km from the current grounding line. Although the further retreat of the grounding line might not have been triggered by increased seawater temperatures, the warm water flowing into the cavity between the ridge and grounded ice is causing ice thinning through a positive feedback mechanism where the thinner ice allows more ocean heat into the inner cavity (Jenkins et al., 2010).

All recent studies thus agree that there is no sign that the forcing mechanisms are likely to cease or that the system is reaching mass balance. Finally, Rignot (2008) concludes that if this forcing continues it is likely to fuel the retreat and acceleration of ice even deeper in the WAIS.

### 3.5 Summary

There is no doubt that the PIG catchment basin is a system undergoing rapid change. Due to the fact that the PIG bed topography deepens inland and the lack of a significant ice shelf the system may be potentially unstable and changes in PIG's floating portion and/or ice plain might be transmitted rapidly upstream on decadal time-scales (Payne et al., 2004; Thomas et al., 2004b). Between 1996 and 2007 PIG is estimated to have lost  $30 \text{ Gt yr}^{-1}$  of mass (Rignot et al., 2008) and

the acceleration of PIG has increased in speed to 42% since 1996 and 73% since 1974 (Rignot, 2008). GPS measurements found the annual increase in velocity to be significantly higher in 2007 over the entire length of PIG than what had been estimated for the previous 12-year period indicating that the perturbation originally causing the acceleration is progressing rapidly upstream (Scott et al., 2009). This is confirmed by the fact that the pattern of surface lowering of PIG has accelerated and is no longer limited to the main trunk (Wingham et al., 2009). If this acceleration continues the main trunk of PIG will be floating within a time scale of 100 years (Wingham et al., 2009).

Lately Rignot (2008) found indications that the grounding line had retreated a total of  $15 \pm 6$  km between January 1996 and December 2007 and also found signs of a transition to flotation of the ice plain. If that is the case this will have major impacts on the evolution of PIG as the grounding line will reach the part of the glacier bed that is well below sea level thus potentially leading to a doubling of the glacier speed (Thomas et al., 2004b; Rignot, 2008).

The forcing mechanism behind the changes in PIG is not well understood but is most likely acting downstream of the glacier. Since the speed up of PIG has been found to coincide with an increase in the temperature of the water in the Amundsen Sea (Rignot, 2008) several studies have suggested that the changes are caused by long-term warming of the southern oceans or a variability of the ocean circulation on a decadal scale (e.g. Shepherd et al., 2004; Wingham et al., 2009). However, the observation of a ridge in the sea floor between the ice front and the grounding line, that could be a previous point of grounding, raises new questions as to the cause of the grounding line retreat (Jenkins et al., 2010). Regardless of the nature of the forcing mechanism there is general agreement that there is no sign that the forcing mechanisms are likely to cease or that the system is reaching a steady state.

Looking back at what is known of the history of the glaciers draining into the Amundsen Sea several points of similarity arise (cf. Chapter 1). The retreat of the ice in Pine Island Bay from its maximum extent to its present condition seems to have occurred in two stages with a pause that formed a grounding-zone wedge (Anderson et al., 2002). It is thought that the presence of substantial amounts of subglacial meltwater could have caused ungrounding of the ice (Lowe and Anderson, 2003) and the rapidity of the second retreat can be explained by a deepening inner shelf and a weak grounding on the sea floor such that a small change in sea-level would be sufficient to cause a degrounding of the ice (Lowe and Anderson, 2002). Is it then possible that the current observations are signs of a third retreat after an ungrounding from the ridge identified by Jenkins et al.

(2010)? This implies that the changes in PIG are part of an ongoing adjustment of the drainage basin since the LGM although the speed with which the changes are happening could be furthered by changes in the climate system.

Considering the significance of PIG for the overall stability of WAIS and potential future sea-level rise it is imperative to increase our understanding of the dynamics of the glacier and not only to gather as much information as possible about PIG but also make best use of the data available from this remote region. Due to limited knowledge of the bed topography it was not until very recently that significant attempts at modelling the catchment basin were made. Except for one study of a single highly-reflecting layer (Corr and Vaughan, 2008) to date no one has made use of the extensive internal layering that were imaged by in an airborne survey conducted by the British Antarctic Survey and University of Texas in 2004/2005 (see Section 4.1.1).

This thesis aims to employ ice flow models to simulate the glacier dynamics using the newest bed topography data and available radar data from the 2004/2005 field season. Coupling the vast amounts of information that the internal layers contain on the past of PIG with an ice flow model of the glacier will lead to an increased understanding of the processes that have influenced PIG in the past and present. In the following chapter the dataset from PIG will be introduced along with the methods behind the radar data analysis and the ice flow modelling.

# Chapter 4

## Methodology

This chapter contains three distinct sections. The first section (Section 4.1) introduces the key datasets on PIG used in this thesis, derived predominantly from airborne radar (the “PASIN” system) and Interferometric Synthetic Aperture Radar (InSAR, a satellite-based system). The second section (Section 4.2) introduces the different methods used to analyse the dataset, including layer classification schemes. The section also outlines the methods constructed for layer tracing and the surface roughness studies. Finally the third section (Section 4.3) gives a more detailed background of the ice flow models used in this thesis and the construction of the two-dimensional model.

### 4.1 Datasets from Pine Island Glacier

To date knowledge of the PIG catchment basin mainly stems from satellite observations that have provided evidence of acceleration, surface lowering and retreat of the grounding line (as discussed in Chapter 3). It has been suggested that the current behaviour of PIG may represent the onset of an instability that may trigger irreversible ice loss from the catchment. However, to project future change across PIG realistically, it is important to understand how PIG has behaved in the past, whether changes similar to those being witnessed today have occurred in the past, and if so whether evidence of these past changes has been preserved in the ice. Answering this question would greatly improve our understanding of current observations.

The dataset that underpins this thesis is an RES dataset over PIG acquired by the British Antarctic Survey (BAS) and University of Texas in 2004/2005. The RES data contain not only measurements of current surface and bed topography, but also numerous internal layering that are a product of past conditions and therefore provide a means towards answering the question. The dataset and

the instrumentation are described in more detail below together with another important source of information: satellite observations of the surface velocity.

### 4.1.1 Radio-Echo Sounding of Pine Island Glacier

In the austral summer 2004/2005 a consortium of the British Antarctic Survey (BAS) and Institute for Geophysics, University of Texas (UTIG) conducted an airborne survey of the glaciers draining into the Amundsen Sea performing radio-echo sounding (RES), gravimetry and magnetics measurements (see map of Antarctica in Chapter 1). The focus of this thesis is on the survey across PIG (Vaughan et al., 2006); a description of the part of the survey that covered the Thwaites, Smith and Kohler basins, including aircraft and instrumentation details, can be found in Holt et al. (2006).

The BAS-UTIG data comprise  $\sim 35,000$  km of airborne RES data collected by the ice-sounding radar system PASIN (Polarimetric Airborne Survey INSTRument) mounted on an aircraft also equipped with dual-frequency carrier-wave GPS for navigation, a radar altimeter, wing-tip magnetometers and a gravity meter (a photograph of the Twin Otter aircraft is shown in Figure 4.1). During data acquisition the position of the aircraft was known with an accuracy better than  $\pm 1$  m.



Figure 4.1: *Photograph by D. G. Vaughan of the BAS-UTIG field camp and BAS's Twin Otter aircraft mounted with RES, gravimetry, GPS and magnetics equipment during the 2004/2005 field season.*

Of significance for the data analyses undertaken in this thesis, data were collected in two modes. The majority of the flights were carried out for the acquisition of gravity measurements with a constant elevation and therefore with lower radar layer quality data (yellow lines in Figure 4.2). However, five flights over the main trunk of PIG were carried out with a constant terrain clearance of 150 m above the ice surface (red lines in Figure 4.2) (Vaughan et al., 2006).

The PASIN instrument collected data with a transmit power of 4 kW around a central frequency of 150 MHz. The system was configured such that a  $0.1 \mu\text{s}$  pulse optimised for imaging near-surface layering was interleaved with a  $4 \mu\text{s}$ , 10 MHz chirp (e.g. frequency sweep from 145 - 155 MHz) optimised for detecting the basal

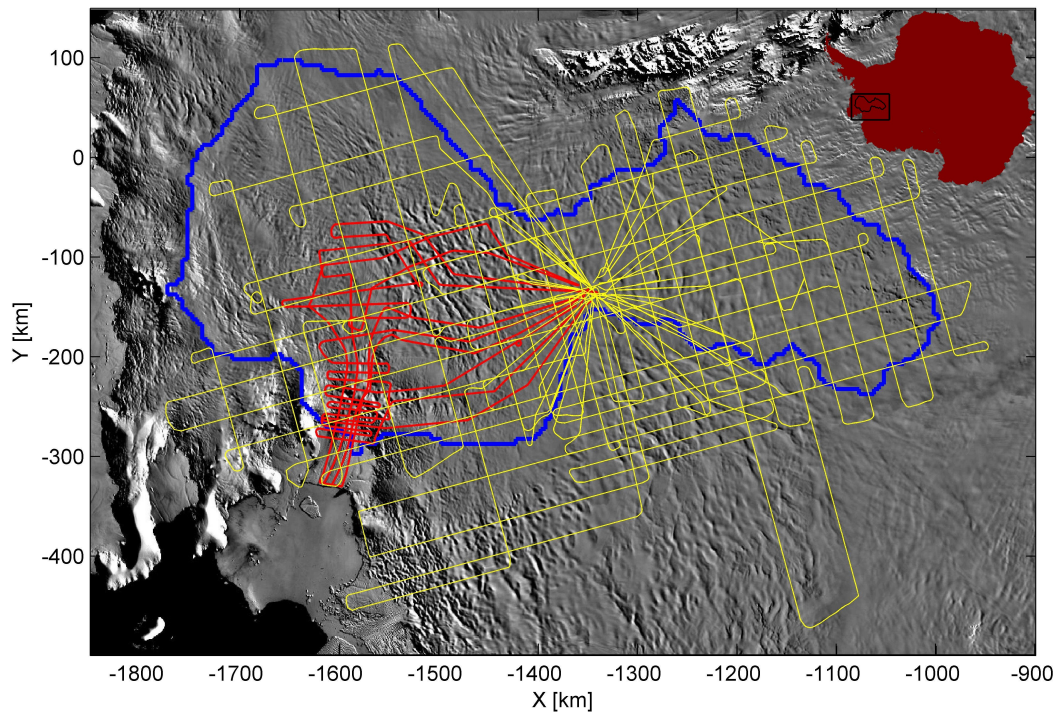


Figure 4.2: *Map of the RES data coverage (Vaughan et al., 2006) overlain on MOA imagery (Haran et al., 2006). The blue line outlines the PIG basin, yellow lines show flightlines acquired with constant elevation for gravity data and the red lines show the lines acquired with constant terrain clearance.*

reflector in ice up to 4.2 km thick (see Corr et al. (2007), for further details of PASIN). While the principal aim of the RES survey was to image the bed and map subglacial topography across PIG (see Figure 3.5) (Vaughan et al., 2006), the “chirp” data also imaged numerous deep internal layers which form the focus of this work. An example of the difference between the chirped and the pulsed data can be seen in Figure 4.3. Although both data types show internal layering, the layering through the full ice column is much clearer in the chirped data as is the bed (Figure 4.3a) and it is this dataset that therefore forms the basis of the data analysis. Further examples of chirped data showing internal layering can be seen in Figure 2.6 in Chapter 2.

The internal layers were analysed from the radar data processed as follows: the baseband radar data were sampled at 22 MHz and coherent integration of 25 consecutive radar records was performed in hardware on board the aircraft, providing an average spatial sampling interval of 0.2 m. Post processing of the data commenced with chirp compression (with a Blackman window which is a moving filter) followed by incoherent stacking of 10 consecutive traces. Finally, the data were decimated to provide a complete record for every 20 m of along-track movement, and converted to SEG-Y format (standard format developed by the Society of Exploration Geophysicists). The surface and bed elevation were

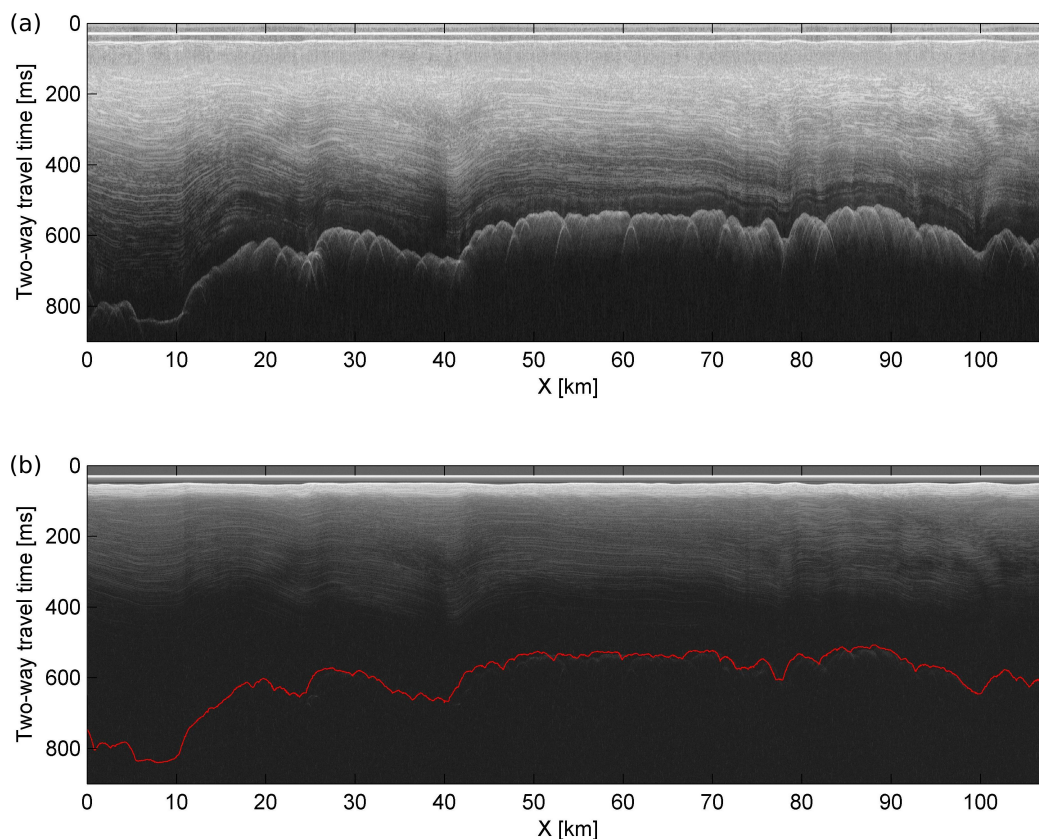


Figure 4.3: *Example of (a) chirped and (b) pulsed data from flightline 10. The red line in (b) follows the bed topography.*

picked using the software package ProMax (H. J. F. Corr, pers. communication, 2009).

#### 4.1.2 InSAR Observations of Pine Island Glacier

The surface velocity measurements used in this work were acquired by Interferometric Synthetic Aperture Radar (InSAR) and are from studies by Rignot et al. (2002) and Rignot (2006) using ERS-1/2 data from 1996 (the surface velocity data are shown in Figure 3.4). This method relies on several satellite images being acquired within a short time span (a few days). Essentially the satellite data are used to construct a digital elevation model (DEM), then the topographic signal is removed from the satellite images. The remaining information contains signals that are due to the motion of the ice between each acquired image. Thus the resolution will depend on the wavelength of the radar and changes can be detected on a centimetre to millimetre scale leading to the construction of interferograms that show the ice displacement. One of the first examples of the use of InSAR for ice flow measurements is a study over the Rutford Ice Stream by Goldstein et al. (1993). For more details on the use of InSAR see, for example,

Stenoien and Bentley (2000) and Rignot (2006) and references therein.

Due to the way that InSAR data are constructed the data basically give a “snap-shot” image of the surface velocity that may or may not reflect short-term effects (A. Shepherd, pers. communication, 2010). However, new ground-based GPS measurements from 2006-08 (Scott et al., 2009) do not show significant short-time variations and although the older satellite data show lower velocities, they most likely reflect a long-term pattern.

### 4.1.3 Map Projections

All data in this thesis have been converted to a polar stereographic projection using the WGS-84 ellipsoid with  $71^{\circ}\text{S}$  as standard parallel following the guidelines for Antarctic mapping endorsed by the Scientific Committee on Antarctic Research. Most of the data were already in this projection but some of the data had to be converted from longitudinal and latitudinal coordinates. See, for example, Snyder (1987) for more information on map projections and conversion between different coordinate systems.

## 4.2 Radar Data Analysis

This section describes the methods behind the radar data analysis, including qualitative (Section 4.2.1) and quantitative classifications (Section 4.2.2) of internal layering. Section 4.2.3 describes the layer tracing routine that was constructed partly to aid the classification and a quantification method for measuring the surface roughness of a glacier.

### 4.2.1 Qualitative Classification

The correlation between internal layering and ice flow was introduced in Section 2.2.6. Here the methods used in this thesis are discussed in more detail. Firstly, the layers are divided into three categories, that are based on the initial classification by Drewry (1983) of the layering in the SPRI dataset. Later studies (e.g. Siegert et al., 2003b; Rippin et al., 2003b, 2006; Bingham et al., 2007) have continued to use the same classification scheme and divide layers into three groups or types:

1. Well-preserved continuous layers, where the amplitudes of the undulations of the layers do not exceed those of the bed topography.

2. Buckled, disrupted or discontinuous layering, possibly with amplitudes greater than those of the bed topography.
3. Absent layers. The absence of layers can either be an artefact caused by signal loss in the radar instrument or an actual physical feature of the glacier.

Examples of the three types of layering are shown in Figure 4.4. It is important to keep in mind that this kind of classification of layers can be very subjective and prone to errors especially since no automated classification method has been widely agreed on.

The PIG data are in SEG Y format. Internal layers were analysed from the SEG Y profiles loaded first into the software package ReflexW. The classification was carried out in two steps. Following the criteria listed above the unprocessed data were classified as exhibiting (i) continuous layering if the layers were visible, had a smaller amplitude than the bed topography and could be traced for over several hundred traces, (ii) discontinuous layering if layering was visible, but did not meet the criteria for a continuous area, or (iii) missing layering if no layers were visible. The data were then processed in ReflexW by removing the background noise and adjusting for the energy decay of the radar signal by a “dewow” function with moving a window of 10 ms. A second classification was then performed and compared to the results from the first classification. Both classifications had to agree for an area to be determined to contain, for example, discontinuous layering.

It is worth noting that this classification scheme means that the discontinuous layer type will encompass a large range of internal layering that could have been caused by a multitude of different processes. Thus the term discontinuous will be applied to layers that can only be traced over short distances, and a subset of the discontinuous layering will be termed buckled in order to describe layers that are not necessarily traceable over short distances but nevertheless do not conform to the bed topography.

Another subset of the discontinuous layering is the parts that contain structures that can most easily be described as whirlwind-like (Figure 4.5). They are vertical features that penetrate almost the entire depth of the ice and disrupt the internal layers. Some of the whirlwinds contain visible layers while others do not and the spacing between the vertical features varies quite substantially in different areas. An example of the different kinds of whirlwinds can be seen in Figure 4.5 where the images show, from left to right: whirlwinds without layers (dark blue frame), whirlwinds with layers (cyan frame) and whirlwinds with

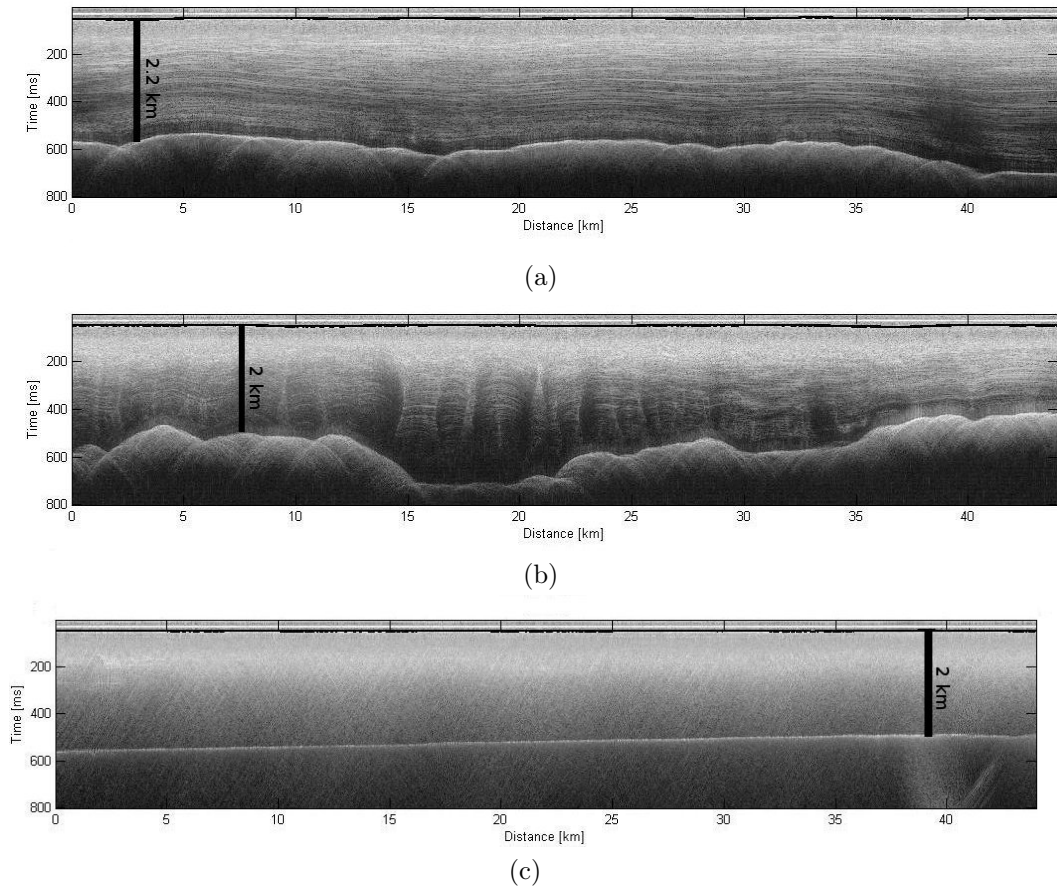


Figure 4.4: *Example of the three different kinds of internal layering (a) continuous, (b) discontinuous and (c) missing layering. All three radargrams are from the PASIN dataset over PIG from the neck between the northern and southern basin, across Tributary 3 and in the main trunk respectively.*

layers and widely spaced vertical structures (magenta frame). The criteria for a widely spaced whirlwind was that the distance between each vertical structure over 100 traces (or approximately 3 km).

The classification was carried out using the chirped radar data. Comparison between the chirped and the pulsed data revealed visible layers in the upper part of the ice where no layers had been identified in the chirped data. This introduced a subcategory, splitting the missing layer type into two groups: no layers identified in either chirped or pulsed data and no layers identified in the chirped data, but some layering present in the pulsed data. The significance of this discovery will be discussed in Chapter 5. This is a good example of why the classification of the layers into only three distinct groups can be problematic.

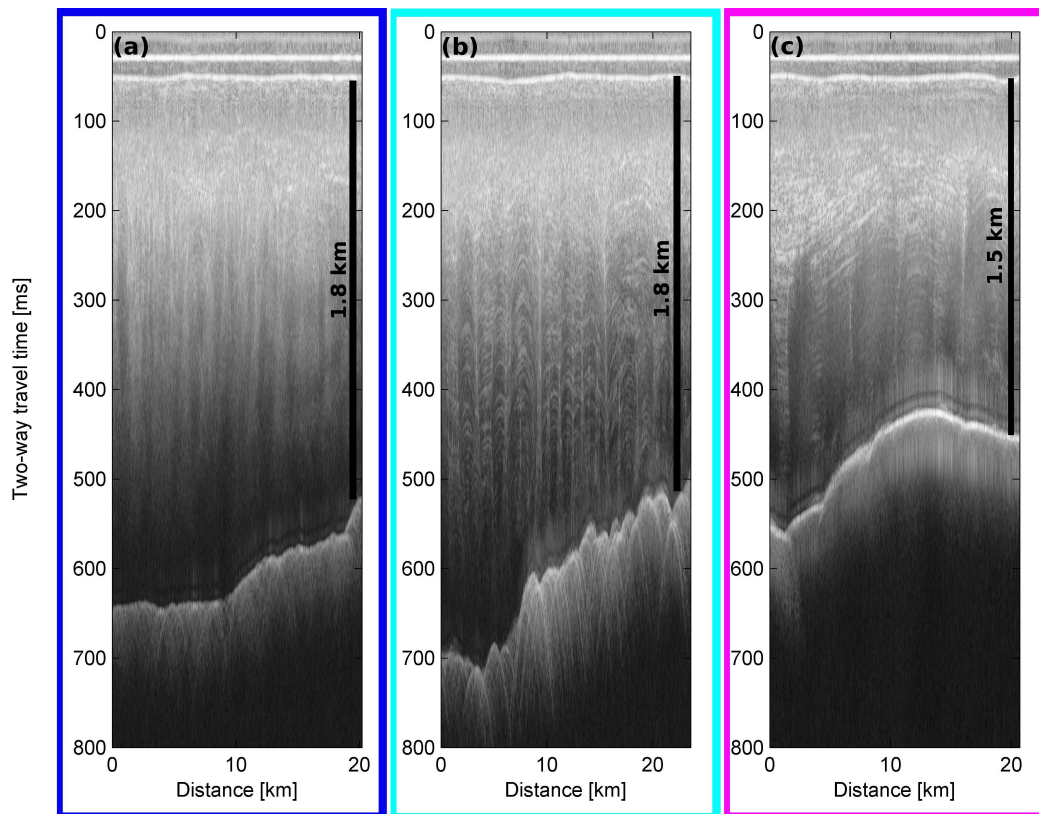


Figure 4.5: *Example of whirlwind-like features observed in the radar data from left to right: (a) whirlwinds without layers (dark blue frame), (b) whirlwinds with layers (cyan frame) and (c) whirlwinds with layers and widely spaced vertical structures (magenta frame).*

#### 4.2.2 Quantitative Classification

While the qualitative approach to classifying layers has proven demonstrably useful in previous studies (e.g. Rippin et al., 2003b; Bingham et al., 2007) it is also highly time-consuming, subjective and, as has been highlighted, prone to different interpretations. Consequently, it would therefore be advantageous to construct a quantitative approach that is more objective as well as less time consuming. The principal goal of a quantitative method should be to assign values along flightlines that reflect the continuity of the layers at each location. Furthermore the method should ideally meet as many as possible of the following criteria:

- applicable to datasets other than the Pine Island Glacier data
- independent of flight height during data acquisition
- independent of ice thickness
- intuitively understandable

- low computational time
- require no (or very few) prior data processing steps

Meeting the above criteria proved challenging for several reasons. Firstly, the individual wiggle plots in areas of continuous or discontinuous layers are in fact quite similar. It is the overall pattern of several wiggle plots that manifests itself in different layer types in the qualitative classification scheme. Secondly, for the human eye it is easy to connect dots and lines in images, indeed, we do this all the time in everyday life. For a computer, however, this process needs to be prescribed formally in a programme which is far from trivial.

This section introduces some general observations of the nature of individual wiggle plots versus layer type and different approaches that have been followed in this thesis to link the two properties. The method that proved to work the best is named the absolute derivative method, however, for completeness other methods will be discussed as well.

#### 4.2.2.1 Observations on Radar Data

RES data consist of individual data shots or traces. In each trace the radar wave has been reflected by the surface of the glacier, the internal layers within the glacier and the bedrock beneath the glacier. As described in Chapter 2, the returned reflectivity can be shown as wiggle plots for each trace (A-scope) or as images (Z-scope) comprising several traces. An example of a Z-scope plot is shown in Figure 4.6. The two red lines corresponds to the wiggle plots that can be seen in Figures 4.7a (discontinuous) and Figure 4.7b (continuous). The general decrease in reflectivity with depth is due to the signal attenuation causing a loss of signal in the deeper part of the ice (see also Section 2.2.2). When tracing internal layers it is an advantage to remove background noise and compensate for the energy decay (for example, by using build-in functions in radar data software) to bring out the deeper layers. However, keeping the criteria listed above in mind, it is preferable not to include either process as the quantitative method should rely on as few prior processing steps as possible, this is partly in order to reduce the time needed to perform a quantitative classification and but mainly to avoid that the success of the quantitative method depends on how the data are processed.

Avoiding data processing means that other steps must be taken in order to minimise noise in the signal. Since the main focus in this thesis is on the deep internal layers this was addressed to some extent by considering only the middle of the wiggle plot and discarding the top fifth and the bottom fifth in all the methods presented below. By discarding the upper part of the plots signals from

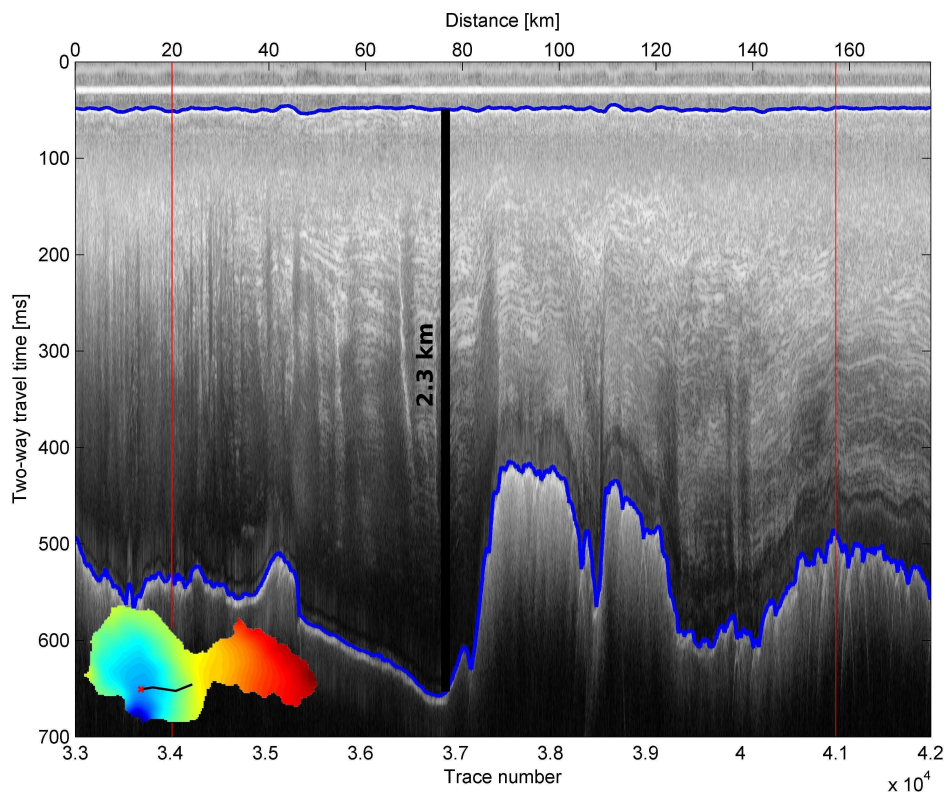


Figure 4.6: *Example of internal layering in flightline 12. The left part of the image shows missing and discontinuous layering. To the right the layers become increasingly more well-defined and continuous. The blue lines follow the surface and bed topography. The red star on the context image corresponds to the far left of the radargram. The two red lines mark the positions of the wiggle plots in Figure 4.7.*

the density differences in the uppermost layers of the ice are avoided. Surveys (e.g. Fujita et al., 1999) have concluded that the lowest part of an ice sheet is often free from internal layers and this part of the data has also been discarded to avoid additional noise.

#### 4.2.2.2 Quantitative Methods

##### Method I: Correlation coefficient

Considering the definition of continuous internal layering, one would expect that adjacent wiggle plots from continuous areas are more similar to each other than wiggle plots from discontinuous areas. Comparing the two individual wiggle plots in Figure 4.7 the difference between the plots is not obvious at a first glance. A more formalised way of comparing the similarity between datasets is to use the correlation coefficient, which is a common statistical tool derived from the mean  $E$  and variance  $\sigma$  of a dataset (see for example Kreyszig, 1999). The mean of a

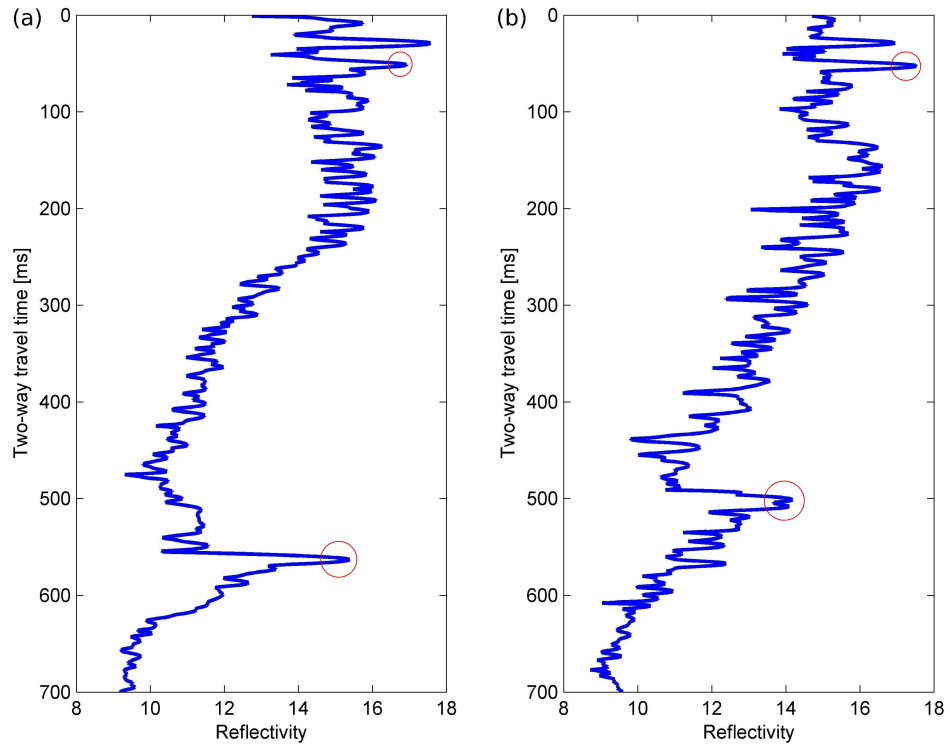


Figure 4.7: Example of two wiggle plots from flightline 12 corresponding to the two red lines in Figure 4.6, at traces (a) 34000 and (b) 41000. The surface and bed reflections are marked with red circles.

data sample is defined as:

$$E(X) = \frac{1}{n} \sum_{j=1}^n X_j \quad (4.1)$$

where  $n$  is the number of samples. If the mean of a sample  $X$  is named  $\mu_X$  the variance  $\sigma_X$  of the sample can be written as:

$$\sigma_X^2 = \frac{1}{n} \sum_{j=1}^n (X_j - \mu_X)^2 \quad (4.2)$$

The variance describes the variability of a data sample. From the variance the correlation coefficient  $\rho$  is defined as:

$$\rho = \frac{\sigma_{XY}}{\sigma_X \sigma_Y} \quad (4.3)$$

where  $\sigma_{XY}$  is the covariance of  $X$  and  $Y$  (and  $Y$  is another sample set) defined as

$$\sigma_{XY} = \frac{1}{n} \sum_{j=1}^n (X_j - \mu_X)(Y_j - \mu_Y) \quad (4.4)$$

and  $\sigma_X$  and  $\sigma_Y$  are the variances of  $X$  and  $Y$ . The correlation coefficient  $\rho$  is a measure of how close two measurements are to a linear relation and is by definition  $-1 \leq \rho \leq 1$ . If the value of  $\rho$  is close to  $\pm 1$  then the two measurements have a positive/negative linear relationship while values close to or equal to 0 implies that there is no linear relationship. Thus calculating the correlation coefficient between a wiggle plot and its neighbour should return a measure that reveals the degree of similarity between them.

## Method II: Absolute Derivative Method

Closer examination of the data revealed that one of the main differences between continuous and discontinuous areas is that discontinuous areas often constitute regions where small “patches” with visible internal layers are interspersed with patches with no visible layering. This means that for an area of discontinuity the average number of internal layers along track is lower than for a continuous area. Obviously this is only applicable to areas that are discontinuous because of these blank patches i.e. the internal layers are present only over very short distances. Furthermore, the internal layers represent points of high reflectivity surrounded by lower reflectivity and the patterns of high-low reflectivity variations occur repeatedly from radar trace to radar trace. Wiggle plots from areas containing numerous internal layers thus fluctuate from extreme values to extreme values (high reflection / low reflection). Wiggle plots from areas with no layers still vary but to a smaller extent and the variation is more likely caused by, for example, single scattering objects in the glacier or signal noise. Thus a wiggle plot from an area with layers should display, if not a larger range of reflection coefficient values, then more rapid oscillations between these values than a wiggle plot from an area with no layers.

The absolute derivative method is based on the oscillations of each individual wiggle plot (e.g. Figures 4.8 and 4.9). The method is constructed such that it returns a value for each wiggle plot that depends on how many and how large the oscillations of the wiggle plots are. The oscillations are highlighted by considering the gradient of each wiggle plot. Since only the size of the oscillation is of interest and not its sign, the method uses the absolute value of the derivative (Figures 4.8d and 4.9d). In order to retrieve a single value for each wiggle plot the mean of the absolute value of the derivative is considered, hereafter named  $\psi$ . Having obtained a  $\psi$ -value for each individual wiggle plot the average number of internal layers in an area is quantified by averaging the  $\psi$ -values over 100 traces and 1000 traces. The method proposed here is essentially a way of counting the average number of layers and since discontinuous areas often exhibit regions where small

patches with visible internal are interspersed with patches with no visible layering, discontinuous areas will have on average a lower  $\psi$ -value than continuous areas.

### Method IIb: Area under Curve

The method presented above relies on quantifying the internal layers and then linking areas with few internal layers to discontinuity. This naturally gives rise to the question if there is another and perhaps better way of counting the internal layers. One approach might be to rely on the area under the wiggle plots instead of their derivative, since the area under the curve also will reflect the number of oscillations in the wiggle plot. The problem with integrating the “raw” wiggle plot is that the lower part of the wiggle plots generally displays smaller reflection values than the upper part and this area will therefore contribute very little to the final value. This problem is addressed to some extent by using the natural logarithm on the data to bring out the deeper layers. The value for the area under the curve is calculated using the built in Matlab function *trapz* that calculates numerical integrals using unit spacing and trapezoidal approximations.

### Method III: Lacunarity Analysis

Lacunarity analysis is a method for describing spatial variability in datasets and is coupled to the variance and mean of the data. It is often applied in ecology when describing distributions of plant species. The following is based on Plotnick et al. (1996), see this study and references therein for a more thorough introduction to lacunarity analysis.

In lacunarity analysis the fraction of sites occupied is compared against other statistical values. Defining  $M$  as the number of samples and  $S$  as the number of occupied sites, a box of length  $r$  is now placed at the origin of the dataset and the number of occupied sites (named box mass  $s$ ) within the box is determined. The box is then moved one space and the box mass is again calculated. By repeating this process over the entire dataset a frequency distribution  $n(s, r)$  is obtained, and by dividing  $n$  with the total number of boxes  $N$  the probability distribution  $Q(s, r)$  is obtained. The probability function describes how likely a box of size  $r^2$  is to contain  $s$  number of occupied sites. The length of the box  $r$  is often varied in order to capture the spatial scales on which the data are clustered. The first and second moment of the probability distribution is determined from

$$Z_1 = \sum sQ(s, r) \quad (4.5)$$

$$Z_2 = \sum s^2Q(s, r) \quad (4.6)$$

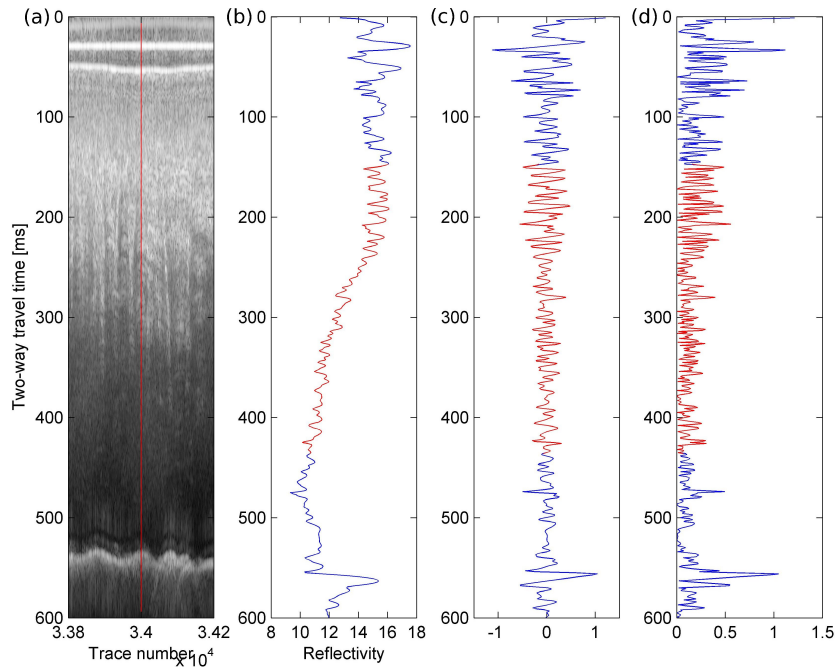


Figure 4.8: (a) Radargram from flightline 12 of length 7.8 km and ice thickness of 1.9 km, (b) wiggle plot corresponding to the red line in (a), (c) the gradient of the wiggle plot and (d) the absolute value of the gradient. The red colours show the part of the wiggle plot that is included in the analysis.

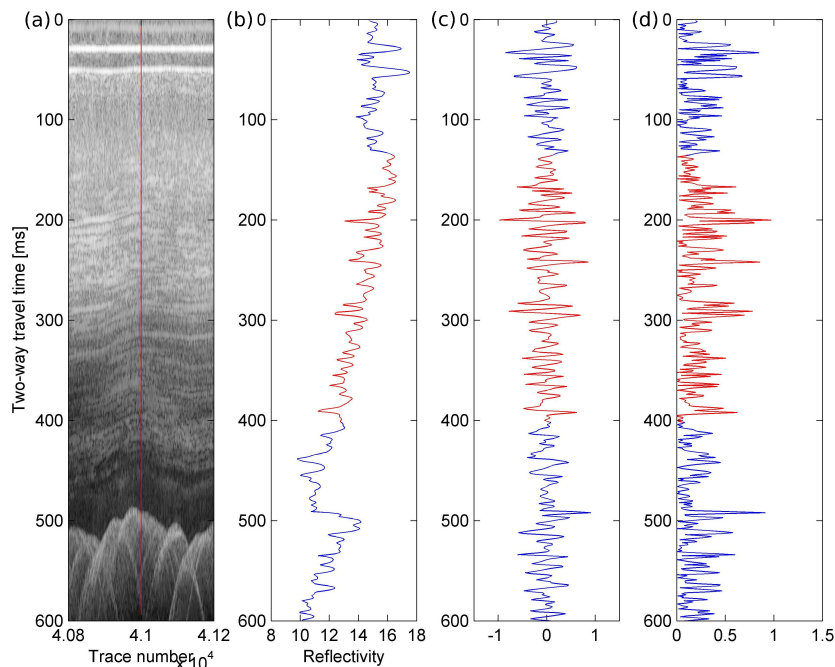


Figure 4.9: (a) Radargram from flightline 12 of length 7.2 km and ice thickness of 1.7 km, (b) wiggle plot corresponding to the red line in (a), (c) the gradient of the wiggle plot and (d) the absolute value of the gradient. The red colours show the part of the wiggle plot that is included in the analysis.

The lacunarity  $\Lambda$  is then defined as

$$\Lambda = \frac{Z_2}{Z_1^2} \quad (4.7)$$

Generally, high lacunarity values indicate clumping in the data on a certain spatial scale. From the nature of the continuous and discontinuous areas the continuous areas are expected to have a higher degree of “clumping” than the discontinuous areas that are dominated to some extent by random noise.

In order to use lacunarity analysis the Z-scope radar data are transformed into an image consisting of pixels of values 0 or 1. The transformation is carried out by calculating the mean and standard deviation of the data, and setting all values in the data to zero if they are below the mean minus the standard deviation or above the mean plus the standard deviation (Figure 4.10). Due to the signal attenuation this has to be done piecewise in boxes moving down in the ice as otherwise the mean of the entire radargram will be lower than the signal in the upper part of the ice, but substantially higher than the signal from the lower part of the ice. The outcome of the transformation is shown in Figure 4.10. The next question is the length of the box  $r$ . In the case of radargrams the spatial scales are known in the sense that the internal layers are hundreds or more traces long (approximately 3 km), but since they are not necessarily horizontal a box of this length might not capture the scale of the layers. Several options for box length were therefore tested to ensure that the spatial scale was correct.

#### 4.2.2.3 Test of Different Methods

The methods presented above have been tested with a section from flightline 12 that displays a significant change in layering from missing to discontinuous to continuous layers. In Figures 4.11 and 4.12 the data from flightline 12 are shown with the results the various methods.

In Figure 4.11b the grey line shows method I, the correlation coefficient, between each individual trace and its neighbour, the red line is the smoothed version of the grey line over a window of 100 samples. There does not appear to be any significant change in correlation coefficient between continuous and discontinuous areas. In fact it seems that areas with discontinuous or missing layers have a better correlation than the area with continuous layers. The largest change in correlation coefficient occurs at traces 37,000 to 39,000 corresponding exactly to a marked change in ice thickness. In order to improve the method the individual wiggle plots are instead correlated with the average value of its 50 neighbouring points on each side. This does increase the overall correlation slightly (blue line

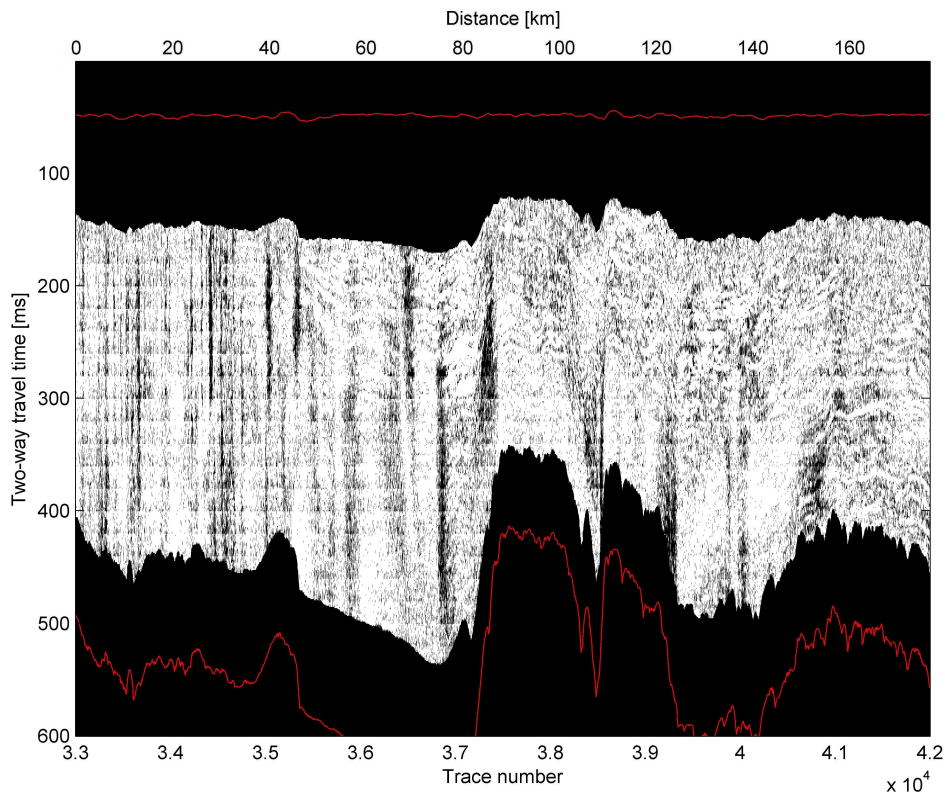


Figure 4.10: Transformation of Figure 4.6 into a binary dataset. White colours denote “occupied” sites *i.e.* sites of high reflectivity. The red lines show the surface and bed topography.

in Figure 4.11b), but the ice thickness variations still dominate the results. One reason why this method does not work very well could be that it is the pixel-wise horizontal correlation that is calculated. In other words, if the internal layer has moved upwards one pixel between two traces, which is likely if the layers are sloping, the correlation between the two wiggle plots is lost. They might even become anti-correlated. This could form part of the explanation why the more or less random noise in the discontinuous area is better correlated.

The results in Figure 4.11c shows the area under the curve (method IIb) of the natural logarithm of each wiggle plot. The difference in value between the left hand side (missing and discontinuous layering) and the right hand side (continuous layering) is insignificant compared to the variations at traces 37,000 to 39,000 (approximately at distance 80 - 120 km) where the method seems to be influenced to a large extent by a change in ice thickness. In this case it is less surprising that the method is influenced by the ice thickness, as an increase in ice thickness increases the part of the wiggle plot that is used in the calculations, thus increasing the total area under the curve.

Figure 4.12b shows the results from the absolute derivative method (method II) with a grey line and the results smoothed over 100 traces (thick red line).

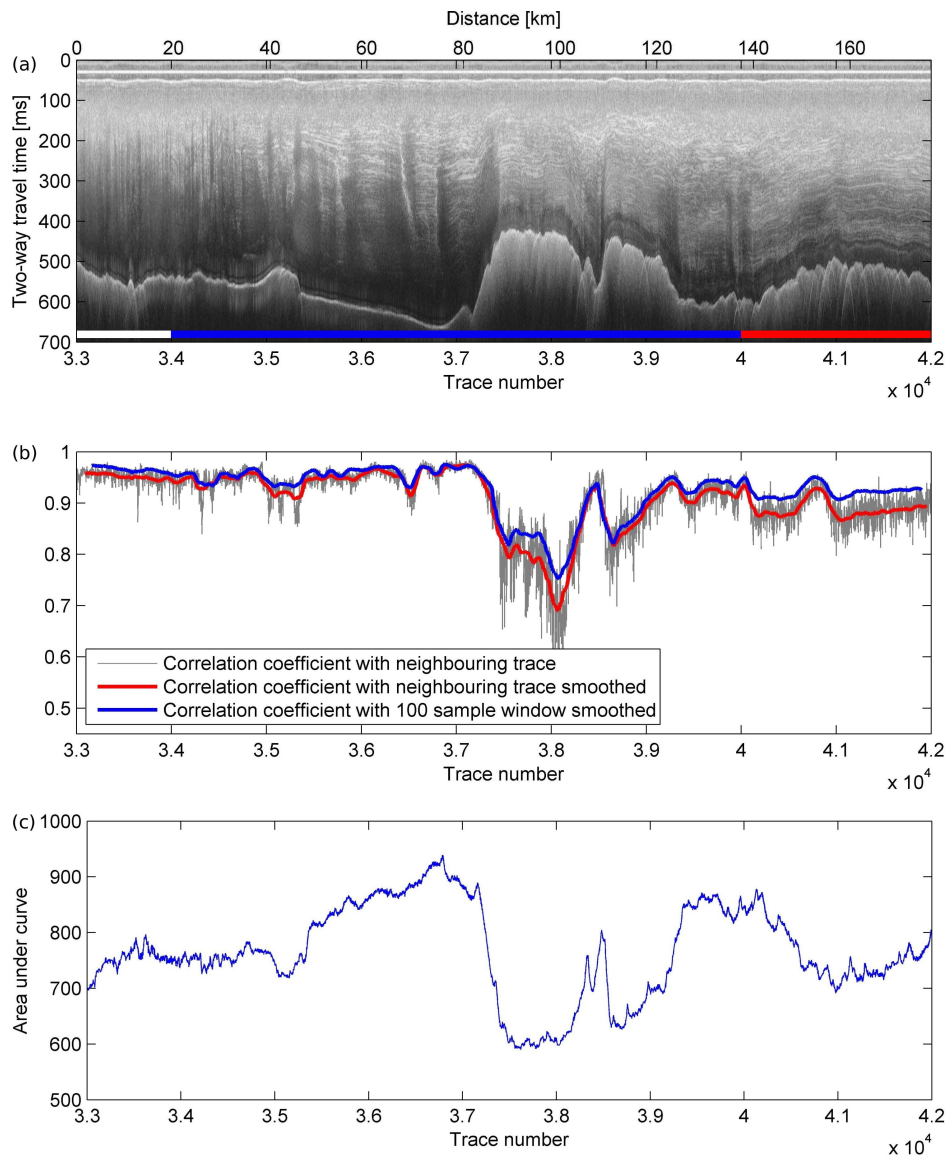


Figure 4.11: (a) Radargram from flightline 12 with a coloured bar showing missing (white), discontinuous (blue) and continuous (red) layering, (b) Correlation coefficient for each trace (grey lines), for each trace and then smoothed over 100 samples (red line) and correlation coefficient for each trace with a running mean over 100 samples and then smoothed (blue line). (c) Area under curve for the natural logarithm of each wiggle plot.

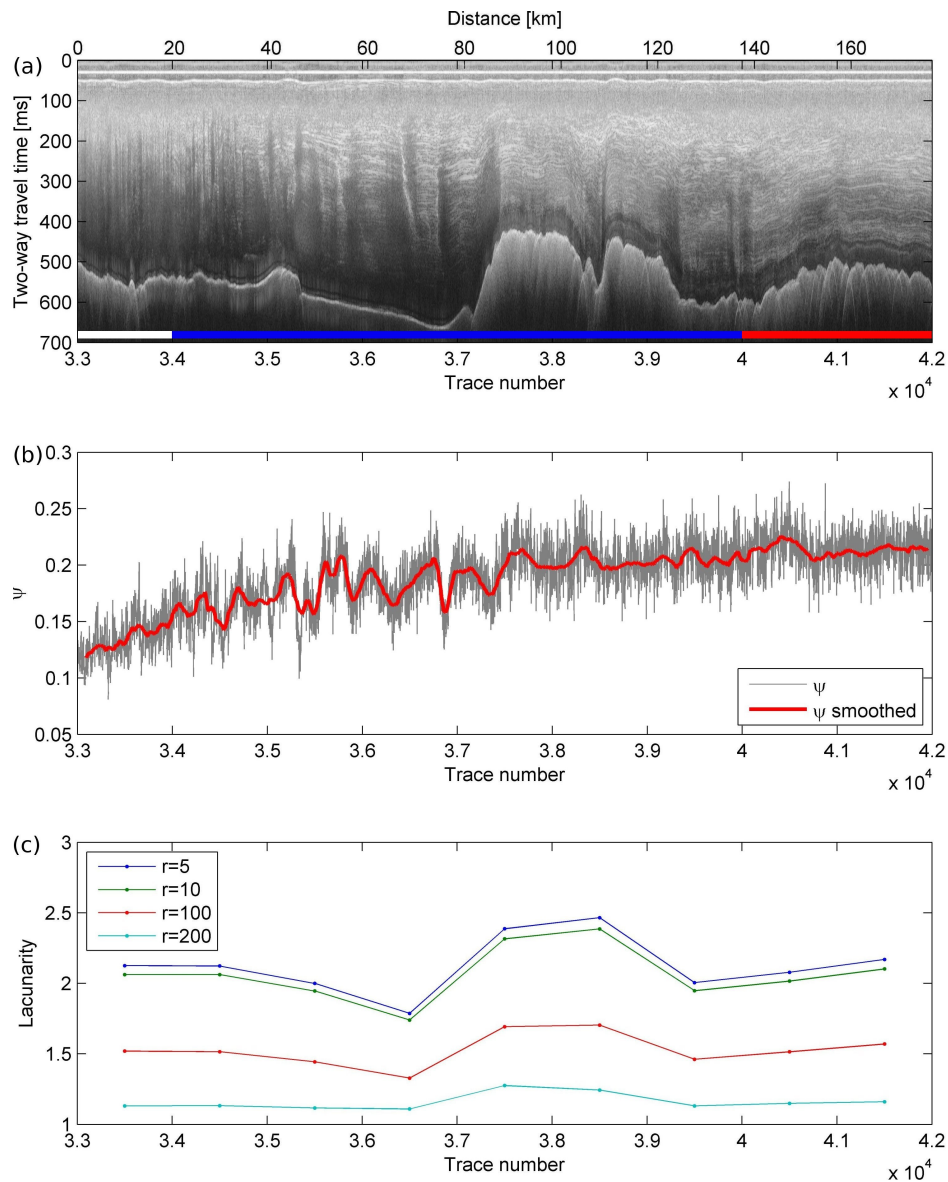


Figure 4.12: (a) Radargram from flightline 12 with a coloured bar showing missing (white), discontinuous (blue) and continuous (red) layering, (b)  $\psi$ -values for each wiggle plot (grey line) and smoothed with a window size of 100 (c) The results of the lacunarity analysis for box size  $r = 5$  (blue line),  $r = 10$  (green line),  $r = 100$  (red line) and  $r = 200$  (turquoise line).

Comparing the  $\psi$ -values with the radargram it appears that on average areas displaying discontinuity have lower  $\psi$ -values than continuous areas. The overall trend of increasing continuity is captured by a corresponding increase in  $\psi$ -value. The areas where no internal reflections are visible, for example around traces 36,800 and 37,500 (at approximately 75 km), correspond well with dips in the  $\psi$ -value. Furthermore, the method seems to be independent of changes in ice thickness.

Figure 4.12c shows the results of the lacunarity analysis for different box sizes. It is evident that the continuity of the layers is not linked to the lacunarity. Instead the lacunarity seems to be influenced by increase or decrease of the ice thickness. Furthermore, there does not appear to be any particular spatial scale that the method captures, as the variations in box size  $r$  do not impact the pattern of the lacunarity values along the flightline.

With these results in mind it appears that out of the four proposed methods for quantifying the continuity of internal layers the method named absolute derivative method is performing best. It is largely independent of ice thickness and captures the overall trend of change in layer type from missing to discontinuous to continuous layering.

One of the criteria listed in the beginning of this section was that a quantitative method should be applicable for other datasets than the Pine Island data investigated here. This was tested on a radargram from a traverse with a 2 MHz frequency collected along the lower reaches of Kamb Ice Stream and Siple Dome (Raymond et al., 2006) using the same procedures. The radargram is shown in Figure 4.13, where blue lines outline the area included in the analysis, with the corresponding  $\psi$ -value below. Since the SEG-Y-profiles were not available this analysis was performed by importing a JPEG image of the data into Matlab. It is clear that the  $\psi$ -value reflects the change in internal layering in this dataset.

### 4.2.3 Further Data Analysis Methods

This section describes further data analysis methods that were employed in order to extract more information from the PASIN dataset. Section 4.2.3.1 describes a layer tracing routine that was an integral part in linking the radar data to the flow models. Section 4.2.3.2 presents a method for measuring observed surface undulations that was constructed in order to gain insight into the influence of the bed topography and ice flow on the surface topography. This section describes further data analysis methods that were employed in order to extract more information from the PASIN dataset. Section 4.2.3.1 describes a layer tracing routine that was an integral part in linking the radar data to the flow models. Section

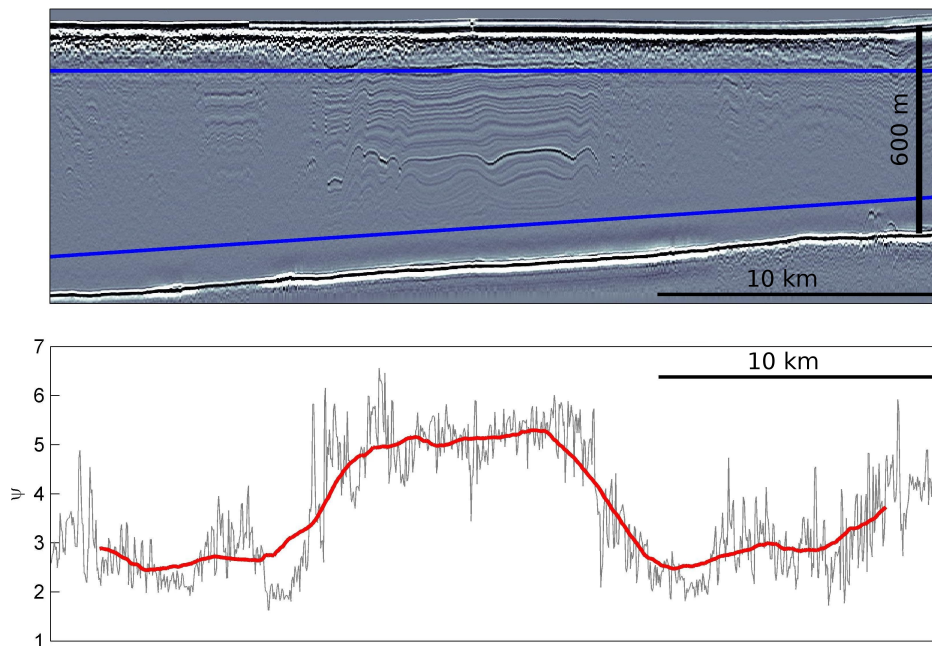


Figure 4.13: (a) Radargram from “Duckfoot” C (see Raymond et al., 2006), the blue lines mark the area that was used in the analysis. (b)  $\psi$ -values for each wiggle plot (grey line) and smoothed with a window size of 100 (red line). Data available from the National Snow and Ice Data Center.

4.2.3.2 presents a method for measuring observed surface undulations that was constructed in order to gain insight into the influence of the bed topography and ice flow on the surface topography.

#### 4.2.3.1 Layer Tracing

The layer tracing routine was partly constructed in order to aid in the layer classification but primarily it was used to provide layer elevations for the ice flow models. (See Chapters 6 and 7). It relies on the SEG-Y data being imported into Matlab and treated as a data array.

The layer tracing routine is based on the observation that even sloping layers appear more or less horizontal within approximately 20 traces. The routine is not able to identify layers unaided but needs a user to specify the start and end points of a layer, it is, in other words, semi-automatic. The routine was constructed to work as follows: after the SEG-Y data have been loaded into Matlab the user must specify  $x$  and  $z$ -coordinates of the start and end points. From the start point the routine calculates nine possible paths in an angle of  $\pm 45^\circ$  looking forward (black lines in Figure 4.14). Based on the nine calculated paths the routine chooses the path that passes through the area with highest reflectivity (blue line in Figure 4.14). The routine then moves forward a few traces to a new point (green circle in Figure 4.14) along this path and calculates nine new paths. This continues

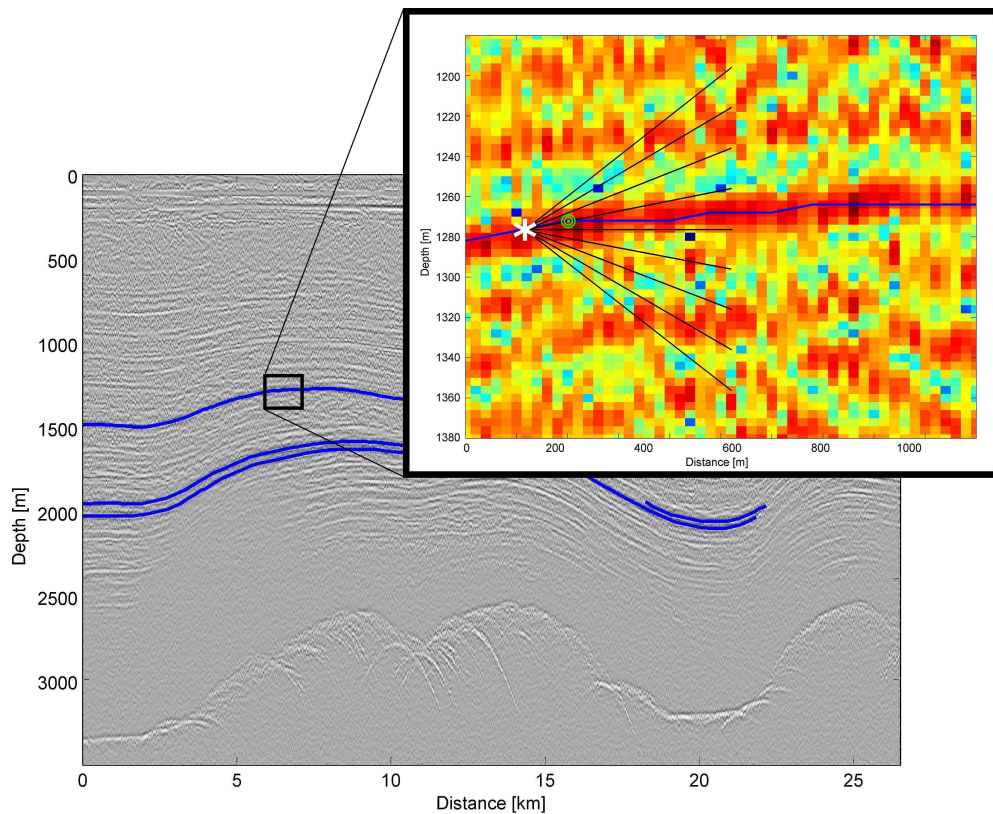


Figure 4.14: Radar data showing internal layers in grey-scale. Inset: Zoom in on radar data (colours) with layers of high reflection in red. The black lines are the directions that the program calculates as possible paths from the point marked with a large white star. The green circle marks the points that the program will assign as next coordinate. The calculated path for this layer is marked with dashed thick blue.

until the routine reaches the end point.

Thus the tracing routine relies on the contrast between highly reflecting layers and the background with no layers. Difficulties mainly occur where gaps appear in the layering or if the layer is obscured. In these cases it can become necessary to define multiple start and end points for a single layer and then stitch the data together afterwards. Another difficulty arises when layers are squeezed close together and then subsequently moves apart. In these cases there might be several paths with high reflectivity for the routine to choose from and it is imperative that the user controls the paths suggested by the routine to make sure the correct layer is followed. The routine also includes the ability to disregard certain paths if, for example, the layer is sloping downwards the routine can be set to disregard all possible paths moving upwards. Overall, where the internal layering is reasonably well-defined and, more importantly, has significantly higher reflectivity than the surrounding background, the routine performs well.

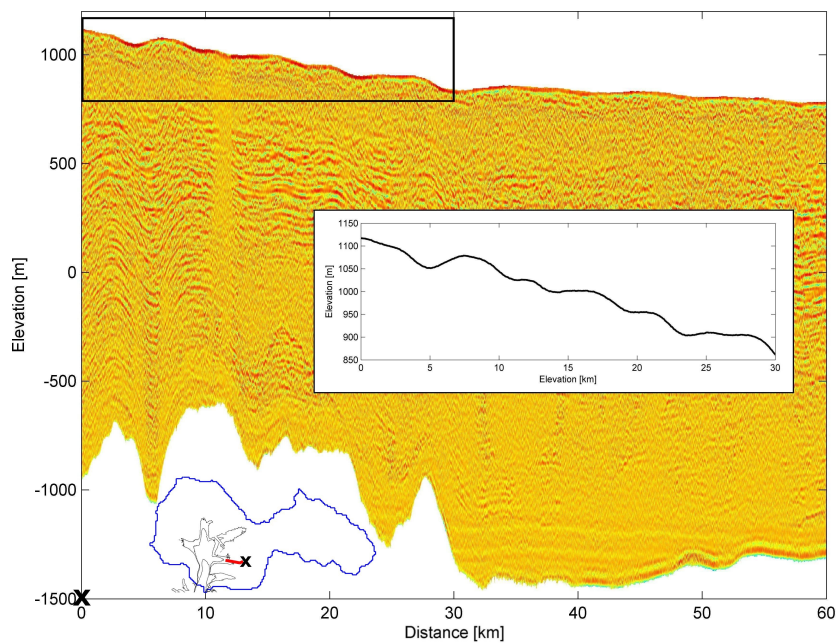


Figure 4.15: *Example of surface undulations in flightline 10. Inset: Surface elevation (black line).*

#### 4.2.3.2 Exploring Surface Roughness

While investigating the internal layers it became evident that information on ice flow and bed topography was also stored in the surface topography. In the PIG dataset several areas displayed an undulating surface with wavelengths of 10 to 20 km. These undulations typically set in at the transition area to enhanced or fast flow and thus might be correlated with the direction of ice flow. An example is shown in Figure 4.15.

Undulations in the surface topography of glaciers are not unknown. For example, flow stripes are often observed in West Antarctic ice streams and have been found to occur in areas of high basal speed where basal undulations are reflected in the surface (e.g. Gudmundsson et al., 1998). Efforts have been made to use the roughness of the surface to extract information on basal conditions such as basal velocity and lubrication (Thorsteinsson et al., 2003). In PIG Joughin et al. (2009) identified an area of undulating surface topography and flow stripes just upstream of the grounding line that is interpreted as indication for a weak bed with low basal shear stress.

In order to quantify the occurrence of the undulations in PIG, the surface roughness is calculated using a method similar to the one employed when considering the basal roughness of a glacier. Following methods from Taylor et al. (2004); Bingham and Siegert (2007a); Bingham et al. (2007) and Rippin et al. (2010) (in press) for studying basal roughness, the surface roughness is calculated

in steps outlined below:

(i) The flightlines are split into sections of across or along the ice flow direction. If the sections are neither they are discarded.

(ii) The data are resampled with a uniform distance of 50 m. The mean sampling interval in the data is 30 m, however, the sampling interval is often larger than 30 m and it is therefore necessary to resample the data to ensure continuity. If the gap between data points is smaller than 1 km the missing data points are filled in using linear interpolation. If the gap between two data points is larger than 1 km the flightline is split into two sections. Since the surface undulations are of the scale of 10 km the interpolation should have little effect on their detection. Furthermore, less than 15% of the points were located further than 50 m apart so little interpolation between points was needed.

(iii) In order to filter out large-scale variations the data were detrended by calculating the best fitting straight line through a moving window of 10 km's width (Figure 4.16b). This introduces a small error in the end points since the best fit for the end points will rely only on points on one side of them.

(iv) The detrended data are passed through a Fast Fourier Transform (FFT). Taylor et al. (2004) recommends using a moving window of  $2^N$  points with the minimum value of  $N = 5$  e.g. 32 points where the central point in the window is used to characterise the roughness.

(v) A single value for the roughness in each point is then calculated by integrating the power density plot from the FFT. The integral is calculated using the trapezoidal rule in Matlab's *trapz* function.

(vi) The roughness value is smoothed with a centralised moving window over 100 points (5 km). During the smoothing of data the end points that are less than 2.5 km from each end are discarded.

When plotting the data it was easier to visualise the results by looking at the natural logarithm of the roughness (Figure 4.16c).

#### 4.2.4 Summary

This section has reviewed several methods for extracting information from a RES dataset. The internal layers, whose geometry are linked to ice flow dynamics, can be classified qualitatively by assessing the type of layering and categorising the data as containing continuous, discontinuous or missing layering. Several more objective and quantitative methods were discussed and the method that was found to perform best utilises the absolute derivative of each wiggle plot. Not only was it largely independent of ice thickness it was also applicable to other datasets than the PIG data.

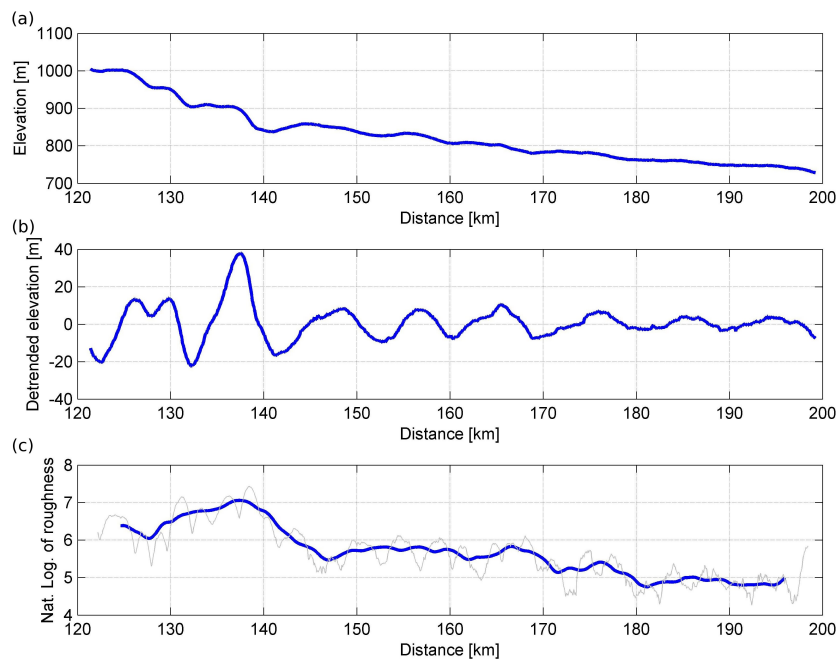


Figure 4.16: (a) Example of surface undulations in flightline 10, (b) Detrended surface topography and (c) The natural logarithm of the surface roughness.

The classification was done partly with the aid of a layer tracing routine, the construction of which was also explained in this section. Finally, a method for measuring the roughness of the surface of the glacier was presented, based on basal roughness studies.

Part of the reason for classifying and tracing internal layering is to compare the observations of internal layering with layering computed by numerical ice flow models. The construction of two ice flow models that have been used for this purpose in this thesis is discussed in the next section.

## 4.3 Ice Flow Models

This section introduces the two ice flow models used in this thesis. (i) “BASISM” - the three-dimensional “British Antarctic Survey Ice Sheet Model” (used recently in, for example, Hindmarsh et al. (2009)) and (ii) a two-dimensional model constructed in this thesis. Both models rely on the age equation (Equation 2.10) described in Chapter 2, but here a more detailed introduction to how the models solve that equation will be given. Some space will be given to describe the background for solving differential equations numerically using finite difference methods, with the two-dimensional model serving as an example. A list of the symbols used in this section can be found in the List of Symbols at the beginning of this thesis.

### 4.3.1 Three-Dimensional Model

Three-dimensional ice flow modelling conducted in this thesis uses BASISM constructed by R. Hindmarsh and recent applications of which are described by Leysinger Vieli et al. (2007) and Hindmarsh et al. (2009). The model is based on the shallow ice approximation (see Section 2.4.5) and uses Glen’s Law (Equation 2.18, Section 2.4.4) to compute the horizontal velocity in three dimensions to compute the age of the internal layers.

The model solves the age equation (Equation 2.10, Section 2.4.2) in three dimensions. It is convenient to change coordinate system and work in normalised coordinates in the vertical direction. This coordinate is denoted  $\zeta$  and defined as

$$\zeta = \zeta(\mathbf{r}, z, t) = \frac{z - b(\mathbf{r})}{H(\mathbf{r}, t)} \quad (4.8)$$

where  $z$  is the elevation,  $\mathbf{r}$  is the coordinate vector,  $t$  is time,  $b(\mathbf{r}, t)$  is the elevation of the bed and  $H(\mathbf{r}, t)$  is the ice thickness. The coordinate change means that the surface elevation is set to 1 and the bed to 0. An illustration of the coordinate change is shown in Figure 4.17. Substituting Equation 4.8 into Equation 2.10 gives:

$$\frac{\partial X}{\partial t} + \mathbf{u} \cdot \nabla_H X + \frac{\nabla_H \Psi - c}{H} \frac{\partial X}{\partial \zeta} = \delta \quad (4.9)$$

where  $\Psi = \zeta \mathbf{Q} - \mathbf{q}$ ,  $c = \zeta a + (1 - \zeta)m$  with  $m$  the basal melt rate,  $a$  the accumulation,  $\mathbf{Q}$  the mass flux and  $\mathbf{q}$  the partial mass flux.  $\nabla_H$  represents the gradient in  $(x, y)$  along surfaces of constant  $\zeta$ . The partial mass flux  $\mathbf{q}(\mathbf{r}, \zeta, t)$  represents the flux in an area from the bed to an elevation  $\zeta$ , thus  $Q(\mathbf{r}, t) =$

$\mathbf{q}(\mathbf{r}, 1, t)$ . The partial flux can be calculated as

$$\mathbf{q}(\mathbf{r}, \zeta, t) = \int_0^\zeta \mathbf{u}(\mathbf{r}, \zeta', t) d\zeta' \quad (4.10)$$

while the flux  $Q$  is given as  $Q(\mathbf{r}, t) = \bar{\mathbf{u}}H$ , where  $\bar{\mathbf{u}}$  is the vertically averaged horizontal velocity.

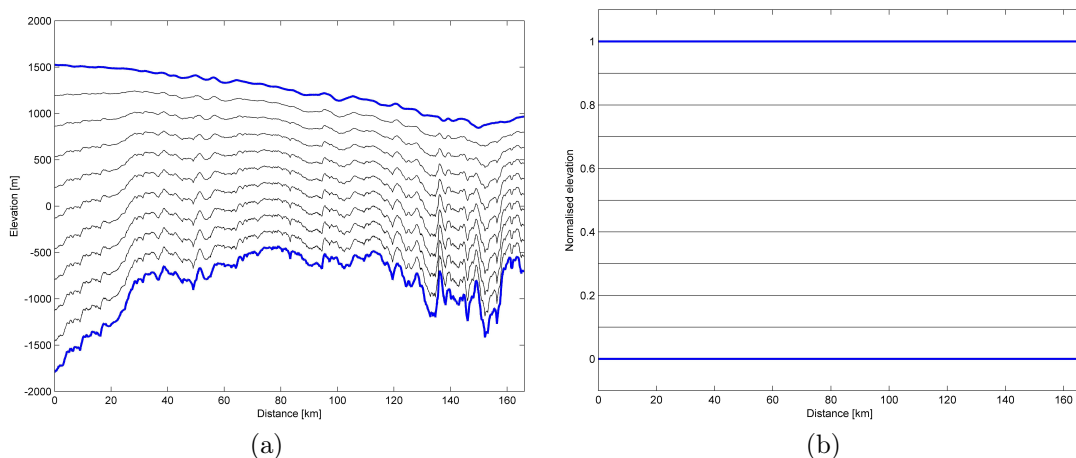


Figure 4.17: (a) Example of surface and bed elevation (blue lines), the black lines show the elevation of ten equidistant vertical points. (b) the elevation and has been changed to normalised elevation and the ten points are now at the same elevation regardless of the ice depth.

In order to calculate the change of the horizontal velocities with depth the model uses the shallow ice flow approximation. The horizontal velocity is set to be either constant with depth (plug flow) or varying due to the internal deformation of the ice. This is expressed by the velocity shape function  $v$ :

$$v(\zeta, \mathbf{r}) = 1, \quad \text{S} \quad (4.11a)$$

$$v(\zeta, \mathbf{r}) = \frac{n+2}{n+1}(1 - (1 - \zeta)^{n+1}), \quad \text{ID} \quad (4.11b)$$

that describes two situations; uniform plug flow (S) and isothermal internal deformation (ID) with flow exponent  $n = 3$ . Plug flow means that the horizontal velocity does not change with depth and it often applies to areas with a high degree of basal melting where the ice moves as one block over the bed topography. Internal deformation is more common in areas with slower flowing ice where the horizontal velocity decreases with depth. In this way the horizontal velocity  $\mathbf{u}$  can be calculated from the expression  $\mathbf{u} = \bar{\mathbf{u}}v(\zeta, \mathbf{r})$  where  $\bar{\mathbf{u}}$  is the vertically averaged velocity.

With a surface and bed topography as input, the model assumes that the

surface velocity of the glacier equals the balance velocities. Balance velocities are calculated from the surface slope and mass balance of a glacier assuming that the glacier is in balance (steady state) and that ice flow takes place following the steepest surface slope (on a horizontal scale of several ice thicknesses). For more information on calculating balance velocities see Budd and Warner (1996). The entire velocity field can then be calculated from the continuity equation (Equation 2.11) and Equations 4.11a or 4.11b.

#### 4.3.1.1 EISMINT Topography

The European Ice Sheet Modelling Initiative (EISMINT, see Huybrechts et al. (1996) and Payne et al. (2000)) included an intercomparison study of ice-sheet models to investigate how well different models capture parameters such as ice thickness, velocity and temperature. The experiment prescribed a number of test cases in order to compare the model outputs including fixed or moving margins and isothermal or fully thermally coupled tests.

In order to illustrate the output of the BASISM model results from a run with the EISMINT test parameters is shown here. The grid in the model set-up is a 31x31 matrix with both  $x$  and  $y$  axes running from 0 to 1500 km. The input surface and bed topography are plotted in Figure 4.18a. The accumulation is kept constant at a rate of  $1 \text{ m yr}^{-1}$ . Figure 4.19 shows the internal layer stratigraphy calculated by BASISM using the above parameters and with the assumption of uniform accumulation and a small basal melt rate. Note how the oldest ice is at the centre of the ice-sheet with the age at the base decreasing towards the margins of the ice. Notice also the difference the location of the cross-section makes for the stratigraphy of the layers. Figure 4.19a goes through the centre of the ice-sheet and shows very symmetrical layers. In contrast, Figure 4.19b shows a cross-section that cuts asymmetrically across the ice (Figure 4.18b green line), leading to a layer stratigraphy in the cross section with bumps and undulations that result solely from the geometry of the layers and the direction of the cross-section rather than any complexities in or changes to ice flow. The fact that apparent undulations in internal layering may result solely from the strike of the profile with respect to the internal flow field of the ice, and not necessarily reflect any change to ice flow, must be kept in mind when using internal layering to help interpret past ice sheet change.

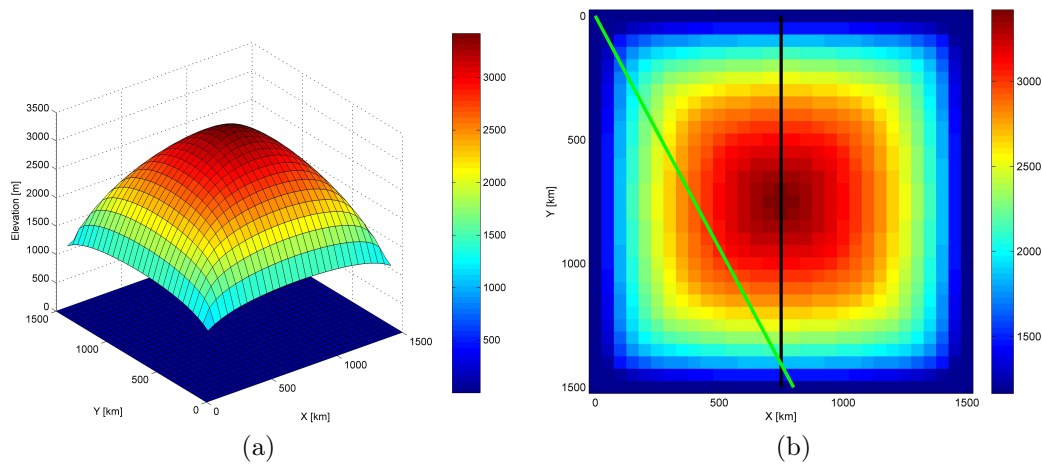


Figure 4.18: (a) Surface and bed topography in metres used in the EISMINT test (Huybrechts et al., 1996; Payne et al., 2000). (b) Surface topography map in metres showing the location of the cross sections show in Figures 4.19a and 4.19b marked with a black and green line respectively.

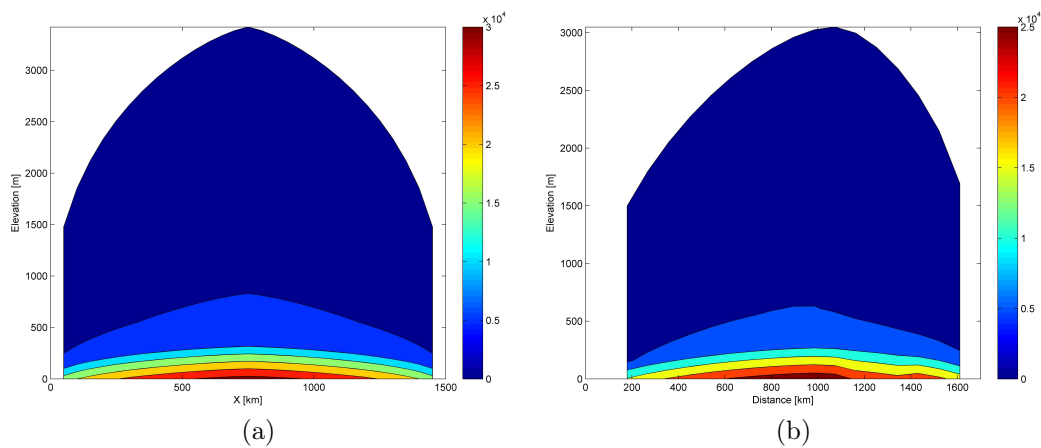


Figure 4.19: Cross section through (a) the centre of the ice-sheet (black line in Figure 4.18b) and (b) through a diagonal cut of the ice sheet (green line in Figure 4.18b). Colours indicate layer age in years.

### 4.3.1.2 Fitting Layers to Model

It is the inclusion of a layer-fitting algorithm within the structure of BASISM that makes it a particularly suitable model for the work presented in this thesis. Since the age of the internal layers is unknown the problem presents itself of finding the modelled isochrone that fits best with the observed layer. This is achieved by a least-square formulation. The fitting is done by interpolating the calculated isochrones to the same points in the horizontal and vertical as the picked points in the data (this is unavoidable due to differences in resolution between data and model). Then the layer in the model that matches most closely to an observed layer is found using an optimisation algorithm (i.e. least-square). This algorithm is described in more detail in Hindmarsh et al. (2009) and can also be used to obtain the optimum estimate of different model parameters.

While conceptually simple, in practice fitting observed layers to modelled layers is far from straight-forward. Problems often occur where the flow model is wrong, which can happen on different length scales. For example, the isochrones are affected by the shortest wavelength of the three-dimensional topography (Hindmarsh et al., 2006, 2009) which may not coincide with the direction of the radargram. Another effect that the model does not necessarily include could be a regional variation in accumulation rate.

The numerical solution of the equations presented above is very involved and includes discretization of the variables on a grid and the use of finite difference methods. Details are presented in Hindmarsh et al. (2009). An example of how to solve the age equation in two dimensions will be discussed below.

## 4.3.2 Two-Dimensional Model

The theory behind ice flow models and the equations governing ice flow have already been discussed in Chapter 2. In this section the set-up of a two-dimensional (flowline) model will be discussed in more detail, including the assumptions the model is based on and its limitations in terms of calculating internal layering that can be compared to radar data.

### 4.3.2.1 Model set-up

The two-dimensional flow model used in this thesis is based on the age equation (Equation 2.10 from Chapter 2). In two dimensions the equation reduces to:

$$\frac{\partial X}{\partial t} + u \frac{\partial X}{\partial x} + w \frac{\partial X}{\partial z} = 1 \quad (4.12)$$

This section contains a description of how a two-dimensional model of the age distribution in flowing ice has been set up by solving the equation above numerically. Only the simple case of plug flow (i.e. the horizontal velocity is unchanged with depth (Equation 4.11a)) is considered, primarily because the model was mainly constructed to investigate higher resolution topography, which will have a significantly larger impact on layer stratigraphy than flow mode (cf. Hindmarsh et al., 2009).

The horizontal velocity is calculated for a given accumulation pattern assuming that the ice is in a steady state, e.g. that the mass influx  $Q$  must equal the mass outflux over a given area:

$$Q = \bar{u}H = (a - m)x \quad (4.13)$$

As in the section above  $H$  is ice thickness,  $a$  accumulation and  $m$  melt rate. This allows for calculation of  $\bar{u}$ , the vertically averaged horizontal velocity, along the  $x$ -axis and since the horizontal velocity does not vary with depth,  $u = \bar{u}$ . Using the continuity equation (Equation 2.11) the vertical velocity can then be found from

$$\frac{\partial u}{\partial x} + \frac{\partial w}{\partial z} = 0 \Rightarrow w(x, z) = - \int_0^z \frac{\partial u}{\partial x} dz' \quad (4.14)$$

with the boundary condition that  $w(x, 0) = m$  this gives  $w(x, z) = m + \frac{a-m}{H}z$ . After the velocity field has been constructed, Equation 4.12 can be solved using the finite difference method that will be described in more detail below.

#### 4.3.2.2 Finite Differences Method

The age equation is a hyperbolic partial differential equation and presents a well-known problem in glaciology. In order to solve the equation trade-offs must often be made between accuracy of the model and a physically correct representation of the age field (Hindmarsh et al., 2009). The outline of the finite difference method below is only meant to serve as a general overview of the method as applied in glaciology. For a more thorough discussion see, for example, Greve et al. (2002) and Hindmarsh et al. (2009). A more general introduction to finite differences solutions to partial differential equations can be found in numerous textbooks, for example, Smith (1985). The following section is based on these sources.

First a brief note on the mathematical notation: the  $i$ th point of  $\phi$ , a function of  $x$ , is written  $\phi(x_i)$  or simply  $\phi_i$ . For the two-dimensional age equation  $i$  denotes the  $x$ -direction and  $j$  the  $z$ -direction, thus the  $i$ th point in  $x$  and the  $j$ th point in  $z$  is written  $\phi(x_i, z_j) = \phi_{ij}$ . Finally, the time dimension introduces the superscript

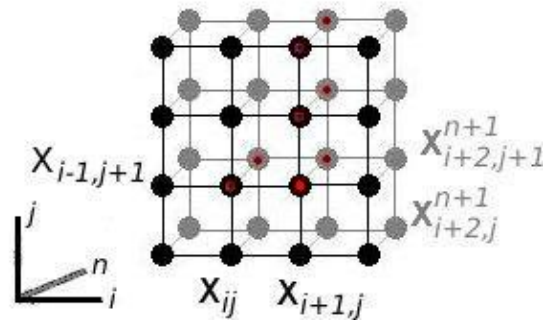


Figure 4.20: Illustration of the grid used in the finite differences method.  $i, j$  denotes the  $x, z$ -direction and  $n$  the time dimension. The point marked with a red dot corresponds to  $X_{i+1,j+1}$ .

$n$ :  $\phi(x_i, z_j, t_n) = \phi_{ij}^n$ . The grid that is produced by this discretization is shown in Figure 4.20.

The finite difference method is based on the general Taylor series, that states that an analytic function  $\phi$  in a point  $x$  can be represented as:

$$\phi(x) = \phi(a) + (x - a) \frac{\partial \phi}{\partial x} + \frac{(x - a)^2}{2!} \frac{\partial^2 \phi}{\partial x^2} + \frac{(x - a)^3}{3!} \frac{\partial^3 \phi}{\partial x^3} + \dots \quad (4.15)$$

However, it can also be regarded as a way of obtaining an estimate of the derivative of a function when two points are known. If all higher order terms are ignored this gives:

$$\begin{aligned} \frac{\partial \phi}{\partial x} &= \frac{\phi(x_i) - \phi(x_{i-1})}{(x_i - x_{i-1})} + O(x^2) \Rightarrow \\ \frac{\partial \phi}{\partial x} &\approx \frac{\phi(x_i) - \phi(x_{i-1})}{(x_i - x_{i-1})} \end{aligned}$$

This approximation is a first-order (since the higher-order terms are ignored), backward or upstream (since it uses the point upstream of  $x_i$ ) difference. Equally a first-order, forward or downstream difference can be written as

$$\frac{\partial \phi}{\partial x} \approx \frac{\phi(x_{i+1}) - \phi(x_i)}{(x_{i+1} - x_i)} \quad (4.16)$$

Strictly speaking the first-order differences approximate the value of  $\frac{\partial \phi}{\partial x}$  at the mid-point between  $x_i$  and  $x_{i\pm 1}$  i.e.  $x_{i\pm 1/2}$ . One problem with first order approximations is that they might lead to instabilities especially at abrupt transitions (e.g. Payne, 2005). It is therefore often advantageous to include an extra point

on the other side of  $x$  to stabilise the expression:

$$\frac{\partial\phi}{\partial x} \approx \frac{\phi(x_{i+1}) - \phi(x_{i-1}))}{x_{i+1} - x_{i-1}} \quad (4.17)$$

This is called a central difference.

When implementing finite differences in order to solve an equation that describes a physical system it is important to consider the physical properties of the system and whether or not these properties are captured correctly. Using central differences means that the age of a point will depend on the age of the points next to it in both directions. However, for a slab of ice moving in one direction information will always travel from upstream (Greve et al., 2002). Thus the use of central differences for the age equation introduces numerical oscillations because of the unphysical centralisation (Greve et al., 2002). It therefore makes sense to use upstream differences.

Using first-order differences introduces another problem. In the  $z$ -direction the age changes rapidly especially at the base of the ice (see Section 4.3.2.2 below for a detailed discussion of solving for the basal point) and the first-order approximation easily becomes unstable. In order to increase the stability of the solution the gradient in the  $z$ -direction is therefore solved using a second-order upstream difference:

$$\frac{\partial\phi}{\partial z} \approx \frac{3\phi(z_i) - 4\phi(z_{i-1}) + \phi(z_{i-2}))}{2\Delta z} \quad (4.18)$$

where  $\Delta z$  is the grid size. In the  $x$ -direction the changes in age are much smaller and a first-order difference is therefore adequate (Hindmarsh et al., 2009). The use of upstream differences is equivalent to introducing a small diffusion term that dampens numerical oscillations. This causes areas with steep gradients to get overly smoothed by the solution (Greve et al., 2002). This is one of the trade-offs that must be considered when constructing a finite difference model.

The spatial components of Equation 4.12 are thus approximated as:

$$u \frac{\partial X}{\partial x} + w \frac{\partial X}{\partial z} = u_{ij} \frac{X(x_i, z_j) - X(x_{i-1}, z_j)}{\Delta x} + w_{ij} \frac{3X(x_i, z_j) - 4X(x, z_{j-1}) + X(x, z_{j-2}))}{2\Delta z} \quad (4.19)$$

introducing  $X_{ij} = X(x_i, z_i)$  for simplification and re-arranging the terms gives:

$$\begin{aligned} u \frac{\partial X}{\partial x} + w \frac{\partial X}{\partial z} &= \left( \frac{u}{\Delta x} + 3/2 \frac{w}{\Delta z} \right) X_{ij} \\ - \frac{u}{\Delta x} X_{i-1,j} - \frac{2w}{\Delta z} X_{i,j-1} + \frac{w}{2\Delta z} X_{i,j-2} \end{aligned} \quad (4.20)$$

Now the time-derivative needs to be included in the equation. Time derivatives can be approximated in the same way as spatial gradients:

$$\frac{\partial X}{\partial t} \approx \frac{X(t_n) - X(t_{n-1})}{\Delta t} \quad (4.21)$$

However, this approximation quickly becomes unstable in the time-dimension. A common approach to stabilise time steps is the Crank-Nicholson method which is second-order in time (e.g. Smith, 1985). In the following  $X(t_n) = X^n$ . The Crank-Nicholson method states that:

$$\frac{X^{n+1} - X^n}{\Delta t} = \frac{1}{2} \left( \left. \frac{\partial X}{\partial t} \right|^{n+1} + \left. \frac{\partial X}{\partial t} \right|^n \right) \quad (4.22)$$

and hence from Equation 4.12

$$\left. \frac{\partial X}{\partial t} \right| = 1 - u \left. \frac{\partial X}{\partial x} \right| - w \left. \frac{\partial X}{\partial z} \right| \quad (4.23)$$

$$\Rightarrow \frac{X^{n+1} - X^n}{\Delta t} = \frac{1}{2} \left( 1 - u \left. \frac{\partial X}{\partial x} \right|^{n+1} - w \left. \frac{\partial X}{\partial z} \right|^{n+1} + 1 - u \left. \frac{\partial X}{\partial x} \right|^n - w \left. \frac{\partial X}{\partial z} \right|^n \right) \quad (4.24)$$

$$\Rightarrow X^{n+1} - \frac{\Delta t}{2} \left( 1 - u \left. \frac{\partial X}{\partial x} \right|^{n+1} - w \left. \frac{\partial X}{\partial z} \right|^{n+1} \right) = X^n + \frac{\Delta t}{2} \left( 1 - u \left. \frac{\partial X}{\partial x} \right|^n - w \left. \frac{\partial X}{\partial z} \right|^n \right) \quad (4.25)$$

Inserting Equation 4.19 into the equation above gives a finite difference solution to Equation 4.12 with the assumption that the velocity field is not changing with time. To solve the equation for the entire system it is re-written in terms of matrix calculations:

$$\bar{\bar{\mathbf{A}}} \mathbf{X}^{n+1} = \Delta t + \bar{\bar{\mathbf{B}}} \mathbf{X}^n \quad (4.26)$$

The matrices  $\bar{\bar{\mathbf{A}}}$  and  $\bar{\bar{\mathbf{B}}}$  are tri-diagonal matrices and contain the terms in front of  $X$ . The full form of the matrices will not be shown here but can be found in Appendix A.

### Analytical Solution

Greve et al. (2002) compared different one-dimensional finite difference schemes with an analytical solution and found that relatively simple upstream methods

(such as that outlined above) compare well with more complicated methods with the largest errors occurring at the base of the ice. The analytical solution was found by considering only the vertical dimension, thus reducing the age equation to

$$w \frac{\partial X}{\partial z} = 1, \quad X(z_s) = 0 \quad (4.27)$$

where  $z_s$  is the surface. Greve et al. (2002) solved the equation analytically by using a Dansgaard-Johnsen type flow model (Dansgaard and Johnsen, 1969). Since only plug flow is considered here the flow type is even simpler and can be considered as a special case of the Dansgaard-Johnsen model where the kink height  $h_k$  is equal to the bed elevation (see Section 2.4.5 for a description of the Dansgaard-Johnsen model). In this case the analytical solution from Greve et al. (2002) simplifies to

$$X(z) = \frac{1}{c_1} \ln \left( \frac{1}{c_1 z - c_2} \right) \quad (4.28)$$

where  $c_1$  and  $c_2$  are

$$\begin{aligned} c_1 &= \frac{2(1 + w_b)}{2 - h_k} \\ c_2 &= \frac{h_k + 2w_b}{2 - h_k} \end{aligned}$$

with  $w_b$  denoting the vertical velocity at the base which is equal to the melt rate. The analytical solution represents a useful comparison against the finite difference solution. Other studies of analytical solutions to the age problem include a study by Hindmarsh et al. (2009) and work by Parrenin et al. (2006) and Parrenin and Hindmarsh (2007), who consider two-dimensional effects of bed topography and velocity.

## Boundary Conditions

When solving Equation 4.12 it is important to set up the correct boundary conditions. In this model the age at the surface is always zero and the vertical velocity at the base is always equal to the melt rate.

The basal point is a particular problem. Firstly, because mathematically the age will go to infinity if there is no basal melting. Secondly, even with a basal melt rate the age increases rapidly at the basal point which can make a numerical solution unstable. Hindmarsh et al. (2009) discussed ways to solve for the basal point including constructing a special finite difference formula and compared their solution to an analytical solution. In this context, however, the age of the layers are of less interest than their overall shape. The age of the basal point is therefore

of less concern and has not been solved for specifically. The model therefore uses the finite-difference method outlined above in the basal point, taking into account that the ages at the base will be inaccurate (most likely underestimating the age).

On a more technical level the finite differences need to be defined at end-points of the grid where the points considered do not have neighbouring upstream points i.e. at  $x = 0$  at the start of the grid and the two most upper points of the ice surface. These points are approximated using a simple upstream difference (in the case of the second points in the  $z$ -direction) or a simple downstream difference (in the case of the first points in the  $z$ -direction and  $x$ -directions). Early experiments showed that the use of a down-stream difference in the  $x$ -direction led to a significant overestimation of the layer depths. This was less evident where the model started at zero horizontal surface velocity but became increasingly a problem later on. It was therefore decided to impose a boundary condition on the starting point and set all points at  $x = 0$  equal to the analytical solution.

#### 4.3.2.3 Layer Fitting

In order to get a quantitative measure of how well the two-dimensional model fits the layers and to compare between the models a simple layer fitting algorithm has been constructed for the two-dimensional model. The layer fitting algorithm uses the elevation of the layer and an initial guess at the layer age to find the best fitting modelled layer. Based on the initial guess the model calculates the elevation of the modelled layer and the difference between the first guess and the observed line. Depending on the sign and magnitude of the difference, the model then improves its guess at a higher or lower elevation, calculates the difference again and so on until the difference in age between the two guesses is less than one year. The model uses the variation of age with depth from the model to determine the increase or decrease in elevation after its first guess.

#### 4.3.2.4 Test of Model Results

In order to test that the model produced reasonable outputs it was run with parameters from Leysinger Vieli et al. (2007), Parrenin et al. (2006) and Hindmarsh et al. (2009) and compared against the results from these studies. The values of the parameters used in the tests are given in Table 4.1.

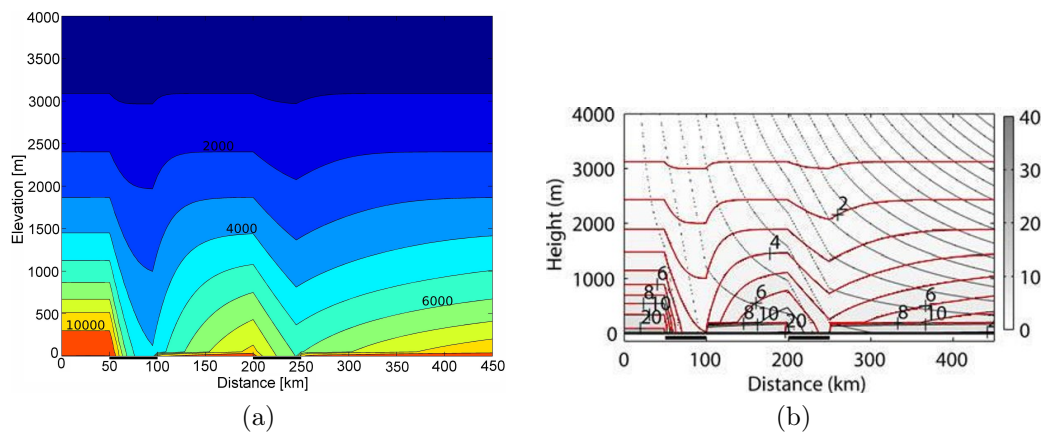


Figure 4.21: (a) Isochrones (colours) in a 2D velocity field with two areas with increased basal melting (black bars). The direction of ice flow is from left to right and numbers indicate age in years. (b) Isochrones (red lines) in a 2D velocity field with two areas of increased basal melting (black bars) (Leysinger Vieli et al., 2007, Fig. 1). The direction of ice flow is from left to right and numbers indicate age in thousand years.

### Increased Basal Melting

First the response of the model to increased basal melting is tested. Here two regions were prescribed of 50 km length each that had an increased basal melt rate of  $1 \text{ myr}^{-1}$ . Using the parameters for accumulation and melt rate in the Table 4.1 the velocities were calculated as described above.

With the velocities known the age equation can now be solved and the result is shown in Figure 4.21. The layers dipped as they entered the areas of increased melting and the dip increased with depth. The oldest layers were found in the area upstream of melting areas. The shape of the layers were very similar to the results from Leysinger Vieli et al. (2007) except from at the very base where the model did not capture the very high ages (cf. Figure 4.21).

### Obstacle in Bed Topography

The second test was to introduce an obstacle in the bed rock. This “bump” caused the layers to drape over the bed topography and partially reproduced the shape of the bed rock with increasing amplitude towards the bed. It is clear that the shape of the layers are affected by the bedrock downstream of it and not just directly over it. Comparing the model output with results obtained by Hindmarsh et al. (2009) gave a good agreement (Figure 4.22) and it can be seen that the two-dimensional model captures the general age distribution with depth. Notice how the numerical solution in Figure 4.22b is smooth compared to the analytical solution (white lines) due to the finite differences method.

| Parameter  | Value          |
|--|----------------|
| Ice Thickness                                      | 4000 m         |
| <i>x</i> -axis                                     |                |
| Leysinger Vieli et al. (2007)                      | 450 km         |
| Parrenin et al. (2006)                             | 300 km         |
| Accumulation                                       |                |
| Leysinger Vieli et al. (2007)                      | 1 m/yr         |
| Parrenin et al. (2006)                             | 0.03 m/yr      |
| Basal melting                                      |                |
| Leysinger Vieli et al. (2007):                     | 0.01 m/yr      |
| for $x \in [50 : 100] \wedge x \in [200 : 250]$ km | 1 m/yr         |
| Parrenin et al. (2006)                             | $10^{-4}$ m/yr |
| Bed topography                                     | 0 m            |
| Parrenin et al. (2006):                            |                |
| for $x \in [30 : 600]$ km                          | 2000 m         |

Table 4.1: Test parameters for the runs described in Section 4.3.2.4.

#### 4.3.2.5 Summary

Overall the two-dimensional model developed here reproduces the results from previous studies well as discussed above. It has a tendency to underestimate the age of the layers at the base of the ice. This is a notoriously difficult problem to solve and it is possible that the boundary conditions at the bedrock does not capture the steep increase in age. It is also possible that the model is not reaching steady state completely (i.e. the number of iterations should be increased) which could lead an underestimation of the layer ages as well. However, this would mean a significant increase in computational time. Even so, the general shape of the layers is very close to results from previous studies and since the age of the basal point is not important in this context the model can be said to capture the layer stratigraphy satisfactorily, under the assumption that the results from the previous studies are representative of layer stratigraphy.

#### 4.3.3 Summary

In this section two models, the three-dimensional model BASISM and a two-dimensional model, for computing internal layering have been introduced. Both models rely on the age equation (Equation 2.10) for describing the age of internal layering. The models use finite differences methods to obtain a numerical solution for the equation. The three-dimensional uses normalised coordinates in the vertical and includes two different flow modes. It also includes a layer fitting algorithm that allows estimates of the best fit of an observed internal layer to

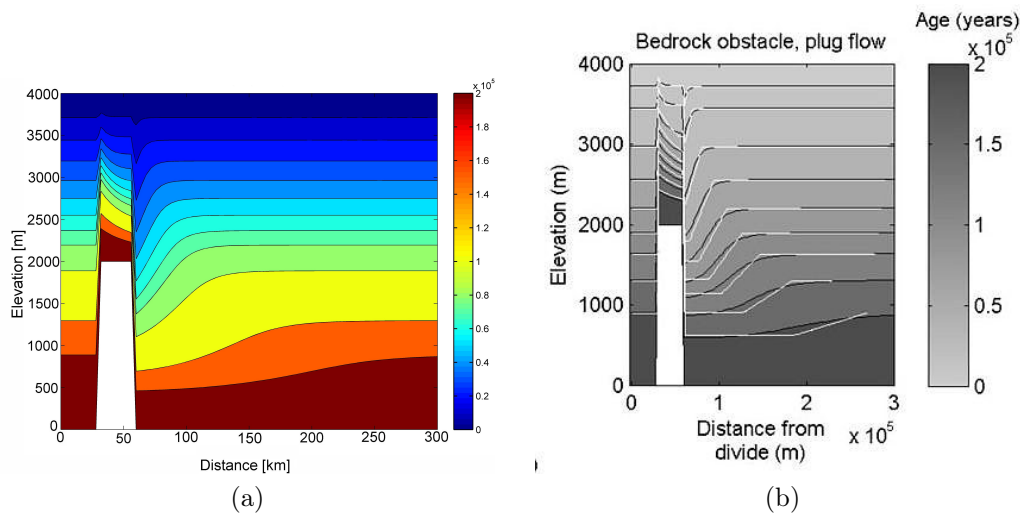


Figure 4.22: (a) Isochrones (colours) in years in a 2D velocity field with a bump in the bedrock (b) Isochrones (grey scale) in years in a 2D velocity field with a bump in the bedrock from (Hindmarsh et al., 2009, Fig. 4). The white lines represent the analytic solutions. The direction of ice flow is from left to right.

a modelled isochrone. The two-dimensional model is a flowline model and only considers plug flow. This model, is a direct result from work on this thesis, compares well to results from other studies, although as expected it is less accurate at the base of the ice.

In this thesis BASISM will be applied to an extensive internal layering dataset in order to assimilate the observed layers. The layer fitting algorithm will be used to estimate the goodness of the fit and thus retrieve the parameters that return the best overall fit to the observations. This will provide indications of the influence of past conditions of PIG. The two-dimensional model will be applied along flowlines to obtain a higher resolution comparison between observed and modelled layers and especially to highlight discrepancies between observations and model that might not be captured by the larger scale BASISM model.

# Chapter 5

## Radar Data Analyses

This chapter contains the results of the analyses of the PIG radar data. The main focus is on the internal layers and their classification. Both the qualitative (Section 5.1) and the quantitative (Section 5.2) methods are discussed. In the last part of this chapter the layer tracing (Section 5.3) and the correlation between internal layering and the stress regime are discussed (Section 5.4). In the last section (Section 5.5) the relationship between surface roughness and basal shear stress is investigated.

For clarity it should be noted that in the sections below the term fast flow will refer to flow velocities above  $200 \text{ m yr}^{-1}$  and the term enhanced flow to velocities above  $50 \text{ m yr}^{-1}$  and less than  $200 \text{ m yr}^{-1}$  in order to distinguish between ice stream flow and flow in the tributaries. Joughin et al. (1999) suggested that a transition to ice stream flow takes place at a surface velocity of around  $100 \text{ m yr}^{-1}$ . However, in this thesis - following (Shepherd et al., 2002) - the  $200 \text{ m yr}^{-1}$  contour will be used as marker for the main trunk and thus outlining ice stream flow, while the tributaries are considered to be delineated by the  $50 \text{ m yr}^{-1}$  contour (green lines in Figure 5.1).

### 5.1 Qualitative Classification of Layers

In this section results from a qualitative classification of the radar-imaged internal layers are presented. Results from this section have been published in Karlsson et al. (2009).

#### 5.1.1 Results

Unless specifically stated otherwise the results are based on the chirped radar data (see Section 4.1.1). Flightlines 10 - 14, that were acquired with constant

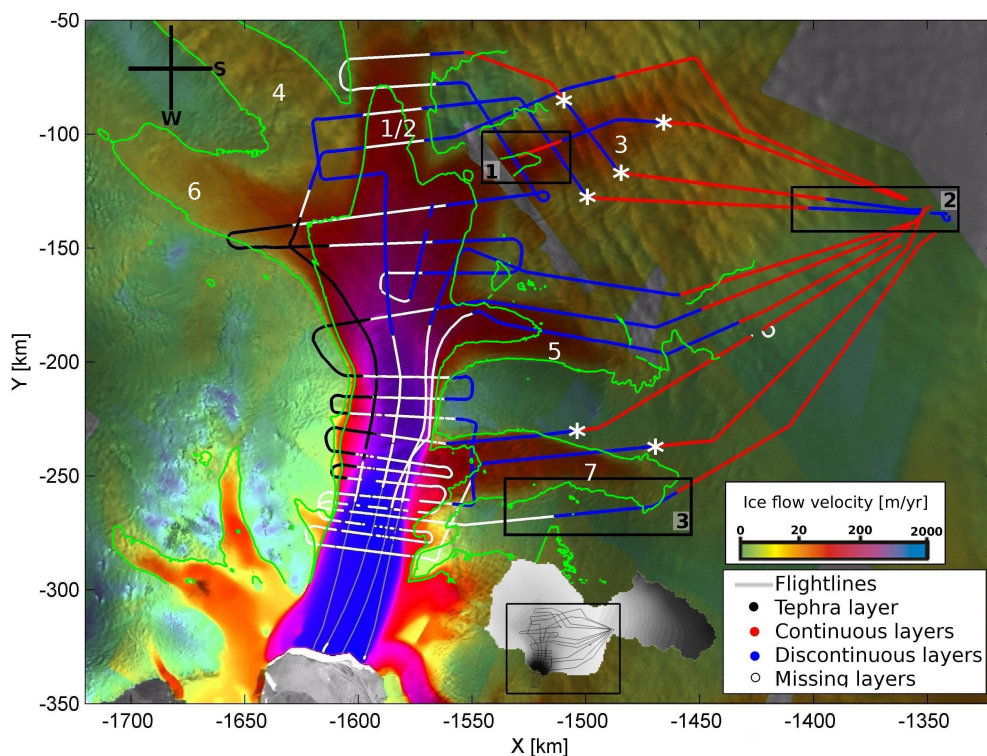


Figure 5.1: Classification of internal layering along flightlines 10-14 showing continuous layers (red lines), discontinuous layers (blue lines) and missing layers (white lines). The black lines mark profiles with one strongly reflecting layer (see Corr and Vaughan, 2008). The classification is superimposed over InSAR velocity data (Rignot, 2006) with the  $50 \text{ m yr}^{-1}$  and  $200 \text{ m yr}^{-1}$  contour in green. White stars denote a sudden change of layer type consistent with an onset of enhanced flow. Numbers in black refer to the number of the box while numbers in white are the numbers of the tributary (following Stenoien and Bentley, 2000).

terrain clearance, will be treated separately and in more detail than the rest of the flightlines.

#### 5.1.1.1 General Layer Classification

The results from the classification of flightlines 10 to 14 are shown on an InSAR surface velocity map in Figure 5.1. Generally, areas of slow flow exhibit continuous layers, while almost all of the enhanced flow areas and their margins have either discontinuous or missing layers. 95% of all continuous layers are found in slow flowing areas with a mean surface velocity in the continuous areas of  $65 \text{ m yr}^{-1}$  (based on InSAR velocity data from Rignot (2006)). The discontinuous layers are primarily, but not exclusively, found in areas with enhanced and fast flow and the mean velocity for the discontinuous areas is  $140 \text{ m yr}^{-1}$ . Most of the discontinuous layers are found in the tributaries, and although a few areas of the main trunk exhibit discontinuous layering, no layers were initially identified

downstream of Tributary 5. Finally, a strongly reflecting layer was identified north of the main trunk (black lines in Figure 5.1). This is the tephra layer that was also identified by Corr and Vaughan (2008) and has been linked to a volcanic eruption dated at  $207\text{ BC} \pm 240\text{ yr}$ . The stratigraphy of the tephra layer will not be discussed further here, but at a later stage in this thesis it will serve as input in the ice flow modelling study (see Section 6.3).

In several flightlines, a transition in internal layering corresponds to a change in ice surface velocity (marked with a white \* in Figure 5.1). For example, in Tributary 7 the change from continuous to discontinuous layering occurs at the onset of enhanced flow. The locations of the margins in Tributary 3 also correspond with a change in layer type from continuous to discontinuous. Assuming that the missing layers in the main trunk are an actual physical feature, the margins of the trunk clearly correlate with a change in layer type from discontinuous to missing layers in several areas.

A few areas display discrepancies from the general pattern outlined above. One exception is the small “island” of continuous layering in Tributary 3 parallel to the flow direction (box 1 in Figure 5.1). Another is the discontinuity that was observed in the otherwise continuous slow-moving area close to the field camp (box 2 in Figure 5.1). Finally, an area with discontinuous and missing layers has been identified in the otherwise slow flowing area west of Tributary 7 (box 3 in Figure 5.1).

Comparing the layer type with the subglacial topography (Figure 5.2) there is a clear correlation between the deep subglacial troughs under tributaries 1/2 and 3 and a change in layering, while there is no obvious change in bed topography under Tributary 7. The location of Tributary 5 also corresponds to a subglacial depression, but the change in layering type takes place some distance from the trough.

The remaining flightlines were not acquired with constant terrain clearance and the risk of misinterpretations is therefore increased due to changes in aircraft elevation during data acquisition. Even so, the results (Figure 5.3) indicate a good agreement with the results from flightlines 10 - 14, with continuous layering in the slow flowing area, discontinuous layers in the tributary and intertributary areas and no internal layering observed in the main trunk downstream of tributary 5. The transitions from continuous to discontinuous layering in Tributaries 3 and 7 are still in good agreement with the surface velocity measurements (white \* in Figure 5.3). The observed changes in layer type south of Tributary 5 are also consistent with what was observed in flightlines 10 - 14.

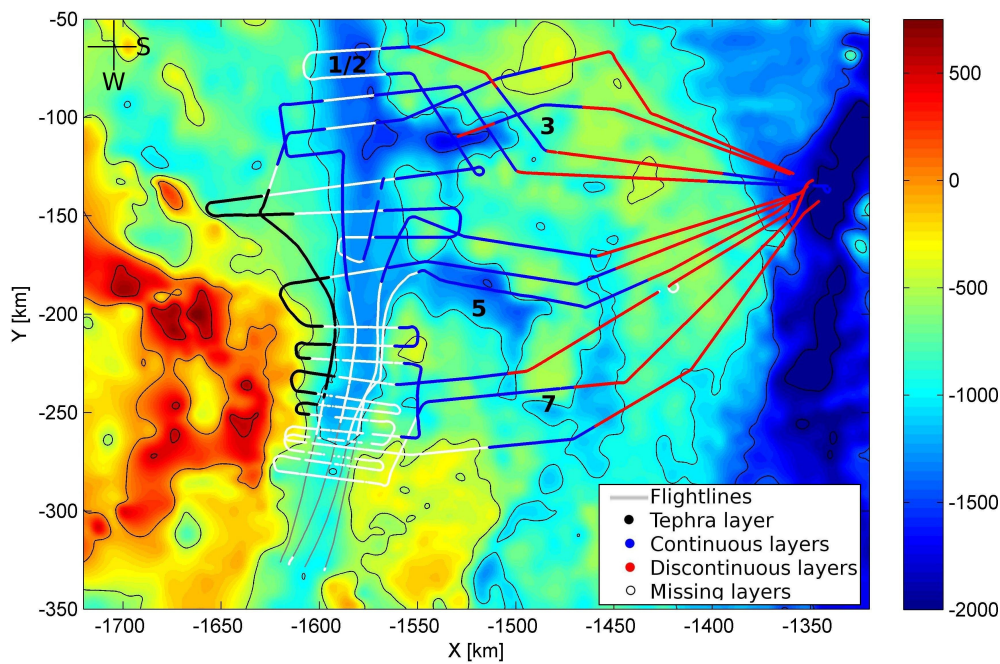


Figure 5.2: Classification of internal layering along flightlines 10 - 14 showing continuous layers (red lines), discontinuous layers (blue lines) and missing layers (white lines). The black lines mark profiles with one strongly reflecting layer (see Corr and Vaughan, 2008). The classification is superimposed over a bed elevation map (metres) in colours (Vaughan et al., 2006).

Considering the entire PIG catchment (Figure 5.4) the area around the field camp PNE (marked with an *X* in Figure 5.4) displayed predominantly continuous layering, while the area west of the field camp outside the catchment basin mainly showed discontinuous layers. As the flightlines enter the enhanced flow area in the northern basin the layering changes to discontinuous layers. In the southern basin the majority of the layering is continuous with a small discontinuous area in the middle of the basin. It is possible that some of the changes in layering in the southern basin are caused by changes in bed relief as most of the discontinuous layering is located on the slope between the Bentley Subglacial Trench and the Ellsworth Subglacial Highlands (see also Figure 3.5).

### 5.1.1.2 Subglacial Lakes

Several features were identified in the radar data that exhibited one or more of the characteristics that were used to identify a basal reflector as a subglacial lake. Following Siegert et al. (1996) a feature was characterised as a subglacial water body if it met the following criteria: (i) stronger reflections than the reflection from the surrounding ice-bedrock interface, (ii) constant reflection strength indicating a smooth surface, and (ii) virtually horizontal reflection. Especially around

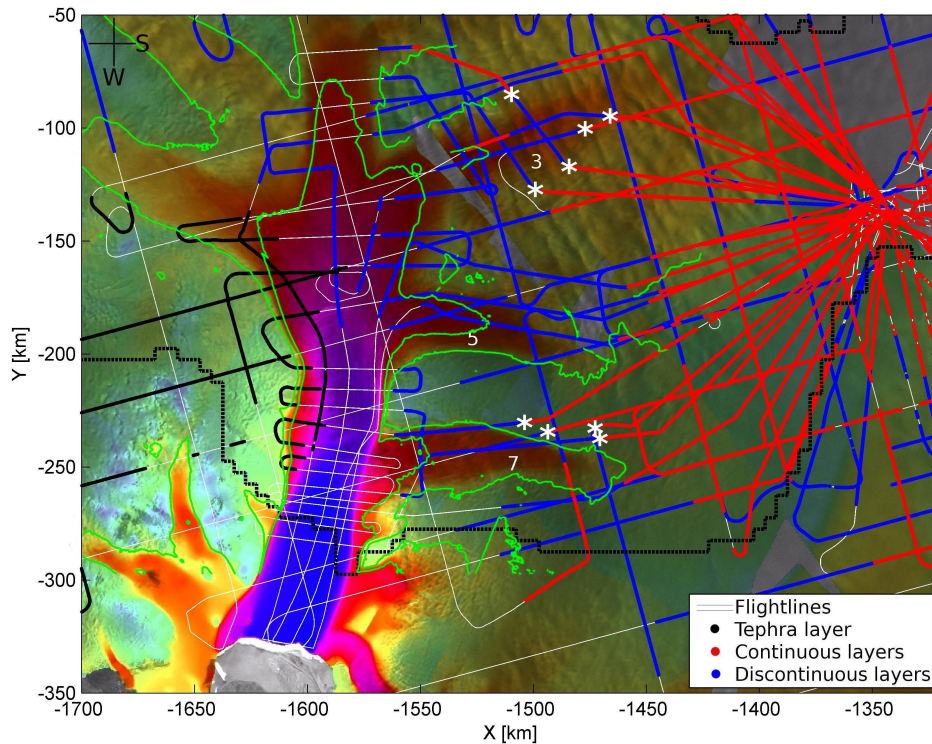


Figure 5.3: *Both figures: Classification of internal layering along all flightlines. The red lines mark continuous layers, the blue lines discontinuous layers and white lines missing layers. The black lines mark profiles with one strongly reflecting layer (see Corr and Vaughan (2008)). The PIG catchment is outlined with a dashed black line. The classification is superimposed over InSAR velocity data (Rignot, 2006) with the  $50 \text{ m yr}^{-1}$  and  $200 \text{ m yr}^{-1}$  contour in green. White stars denote a sudden change of layer type consistent with an onset of enhanced or fast flow.*

the field camp several such features were identified. Figure 5.5 shows the location of lake-like subglacial reflectors close to the field camp (black lines). From the radar data it is difficult to ascertain whether the reflectors are part of subglacial lakes, small localised water-bodies or water-saturated sediments. Similar features were also identified outside the catchment area in the Ellsworth mountains.

### 5.1.1.3 Buckled and Missing Layering

The term buckled is used in this thesis only to describe layering that does not conform to the bed topography. In other words layering that is disrupted but does not exhibit a clearly different slope compared to the bed topography is discontinuous but not buckled. This kind of layering has only been identified in a few locations in PIG and only three times in the flightlines 10 - 14 (yellow lines in Figure 5.6). One such area is located between Tributaries 3 and 5 close to the main trunk. The second area is upstream of Tributary 3 and the last area is close

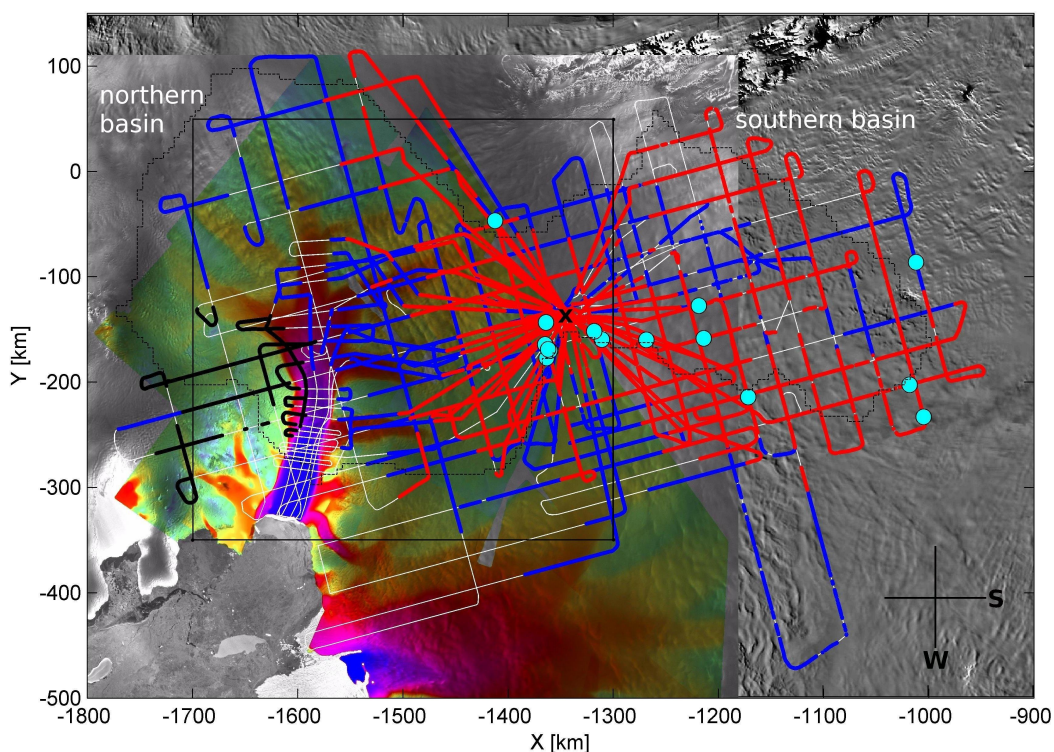


Figure 5.4: *Classification of internal layering in all flightlines. Blue dots denote areas where lake-like reflectors have been identified (see Figure 5.5) and the black box corresponds to Figure 5.3. See Figure 5.1 captions for details.*

to the field camp between the neck of the southern and northern basin. For the flightlines with non-constant terrain clearance it is difficult to identify especially deeper layers and the identification of buckled layering in these flightlines must therefore be done with caution. However, there appear to be at least two more areas that contain buckled layers (dotted yellow lines in Figure 5.6) close to and south of the field camp, marked with an X in Figure 5.6.

Some areas contained layering in the upper part of the ice but no layering in the deeper part (green lines in Figure 5.6). It is difficult to establish whether this is an actual physical feature of the ice or whether it is due to a reduction in echo strength. Again this is especially the case in the flightlines that were not acquired with constant terrain clearance, and therefore only the results from flightlines 10 - 14 are included in the figure. The areas that contain layers only in the upper part are located close to the field camp, in the upper part of the main trunk upstream of Tributary 5, and close to or in Tributary 7.

The above finding raises the possibility that the areas classified above as not containing layers may in reality contain layers in the upper part of the ice that are not visible in the chirped radar data. In order to explore this further an investigation of the pulsed data was undertaken. Since the pulsed radar signal is

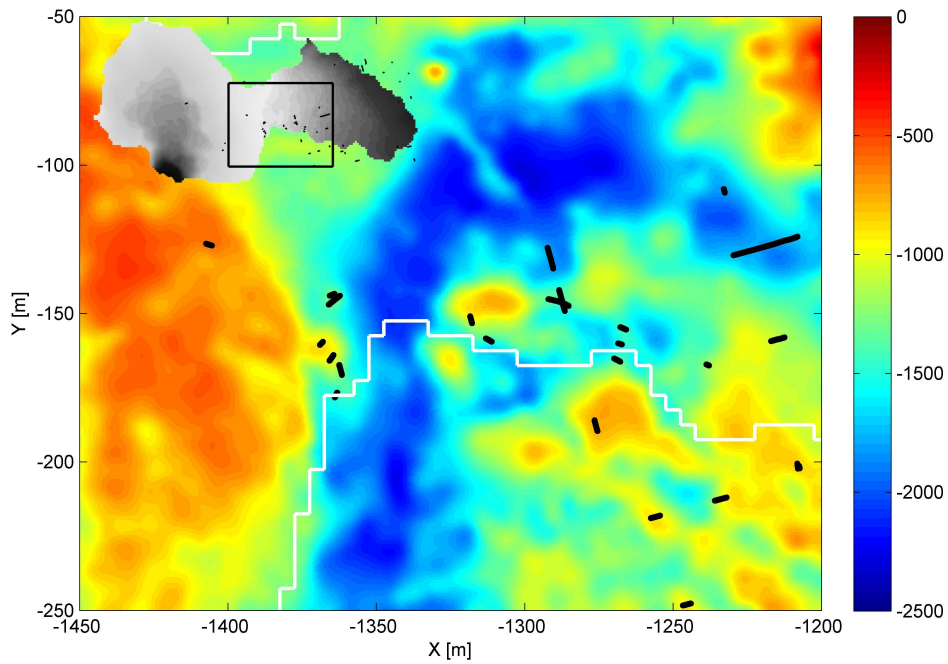


Figure 5.5: *Map of subglacial lakes (black lines) with the subglacial topography (colours) in metres and the PIG catchment outlined with a white line.*

optimised to pick up the surface reflection it is unlikely that this dataset will reveal any extensive deep internal layering. It is, however, likely that more internal layering in the upper part of the ice will be imaged. Focussing on the areas that in the chirped data were classified as containing no internal layering, results showed that in the pulsed data more layering was visible in the upper part of the ice (red lines in Figure 5.6) both in Tributaries 1/2 and in the main trunk as far downstream as past Tributary 5. Close to Tributary 7 two further lines were found to contain visible upper layering.

#### 5.1.1.4 Whirlwind-like Features

As introduced in Section 4.2.1, parts of the flightlines classified as discontinuous layering contain a whirlwind-like structure here referred to as whirlwinds. In Figure 5.7 the locations of the whirlwind-like features are plotted on the surface velocity map. The colours correspond to the example of classification in Figure 4.5; whirlwinds without layers (blue lines), whirlwinds with layers (cyan lines) and whirlwinds with layers and widely spaced vertical structures (magenta lines), where widely-spaced indicates a distance of over 100 traces (approximately 3 km) between each vertical structure.

Figure 5.7 suggests that nearly all of the whirlwind structures are associated with areas of enhanced or fast flow. The whirlwinds with no layers (blue lines) are only found in the main trunk and in the fast flowing part of a tributary. Similarly

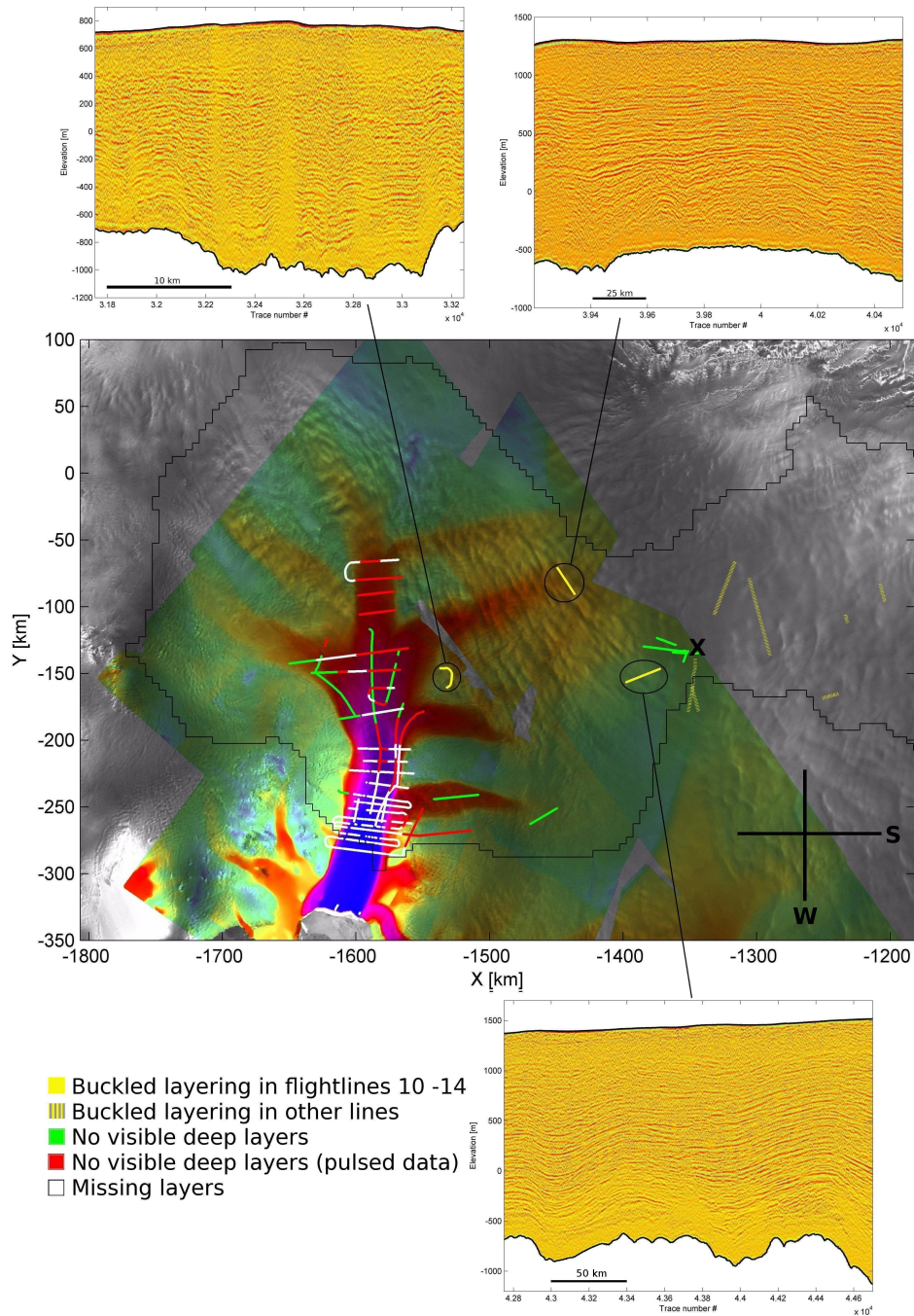


Figure 5.6: Map of buckled layering identified in flightlines 10 - 14 (yellow lines) and other flightlines (dotted yellow lines). The three radargrams correspond to the three lines circled in black. Green lines show areas where no layers could be identified at depth, but some layering was visible at the surface. The red lines show areas that had been classified as no layering, but had visible layering in the upper part of the ice in the pulsed radar data. Areas in flightlines 10 - 14 where neither chirped nor pulsed data show layering are marked with white lines. The PIG catchment is outlined with a thin black line.

more or less all the closely spaced whirlwinds containing layers (cyan lines) are located in the enhanced or fast flow areas but not in the main trunk; in some areas there is a gradual transition from no layers to visible layering, typically where the ice flow is slower than in the main trunk. The widely spaced whirlwinds have only been identified in Tributaries 5 and 7. One interesting feature is the area close to the main trunk in Tributary 7 that displays all three different kinds of whirlwind features (black box in Figure 5.7). The whirlwind features in Figure 5.7 are all classified as “active” since they penetrate the entire depth of the ice and thus influence the stratigraphy of all the internal layers.

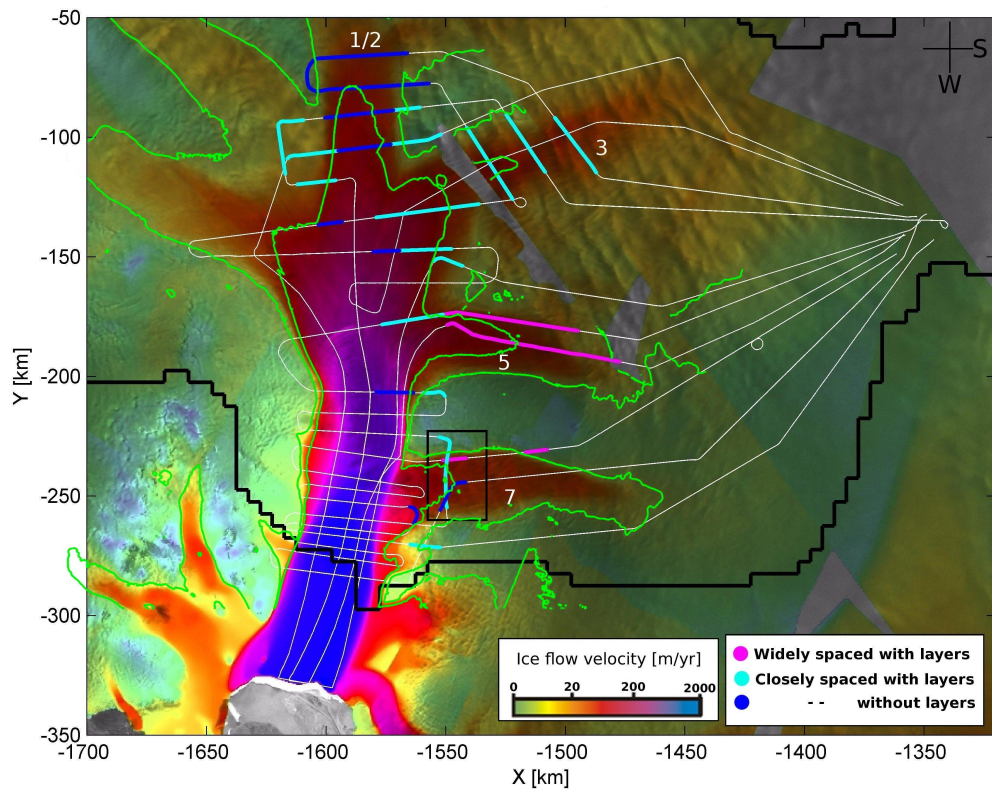


Figure 5.7: Whirlwind features in flightlines 10 - 14 on an InSAR velocity map. The colours correspond to the example in Figure 4.5; whirlwinds without layers (blue lines), whirlwinds with layers (cyan lines) and whirlwinds with layers and widely spaced vertical structures (magenta lines). Background colours show InSAR velocity data (Rignot, 2006) with the  $50 \text{ m yr}^{-1}$  and  $200 \text{ m yr}^{-1}$  contour in green. The black line outlines the PIG catchment basin.

Including the rest of the flightlines produces a more complete picture (Figure 5.8), although it must be kept in mind that due to the variations in aircraft height over the ice surface it is more likely that the radar does not image all internal layering that is present. There seems to be an overall good agreement between Figures 5.7 and 5.8. The whirlwinds without layering are predominantly found in fast flowing areas. One interesting feature is the different types in Tributaries 5

and 7. This could be an indication of a directional dependence on the whirlwind types.

### 5.1.2 Interpretation of Qualitative Layer Classification Results

The majority of the results from the general layer classification - with a few exceptions - can be explained by the current flow regime of PIG. This is interpreted as indicating that no major spatial changes have taken place in the flow pattern of PIG. Furthermore, it seems likely that the absence of layers downstream in the main trunk results from their extinction due to fast flow (cf. Jacobel et al., 1993), since all the flights over the main trunk, including the pulsed radar data (Figure 5.6) and those flown for the acquisition of gravity data (Figure 5.4), do not exhibit any layers downstream of Tributary 7.

The continuous layers identified in this study are almost exclusively located in slow flow areas indicating that since their deposition the flow velocity of the ice has not been sufficient to erase the internal layering. This can be interpreted as a sign that in areas with continuous layering (especially the southern part of the northern basin that is upstream of the onset of enhanced flow), the flow velocities have remained low for a significant amount of time. It also indicates that the enhanced flow of Tributary 7 is unlikely to have extended significantly southwards since the layers were deposited. Only one area, located in the enhanced flow region of Tributary 3, exhibits an “island” of continuous layers. The continuous layering could be a sign that the disruptive processes are not active in that area.

Discontinuous layering has been identified primarily in areas where high longitudinal stresses are expected i.e. areas of enhanced flow or areas close to margins of tributaries or the main trunk of PIG. A notable exception is the flightline parallel to and west of Tributary 7 (box 3 in Figure 5.1) displays discontinuous and missing layers despite this area being some distance from the current margin of the tributary and therefore expected to contain continuous layering. The pulsed radar data from the area further revealed some layering in the upper part of the ice. Assuming that the absence of deep layers in the flightline is not a measurement artifact, the missing layers could indicate that high internal stresses are, or have been, present here. Bed topography (Figure 5.2) reveals that Tributary 7 is not located in a particularly deep basin and it is therefore possible that the position of the tributary has changed and the main flow of the tributary was previously further west of its current position. However, all the flightlines from inter-tributary areas show discontinuous and/or missing layers, even be-

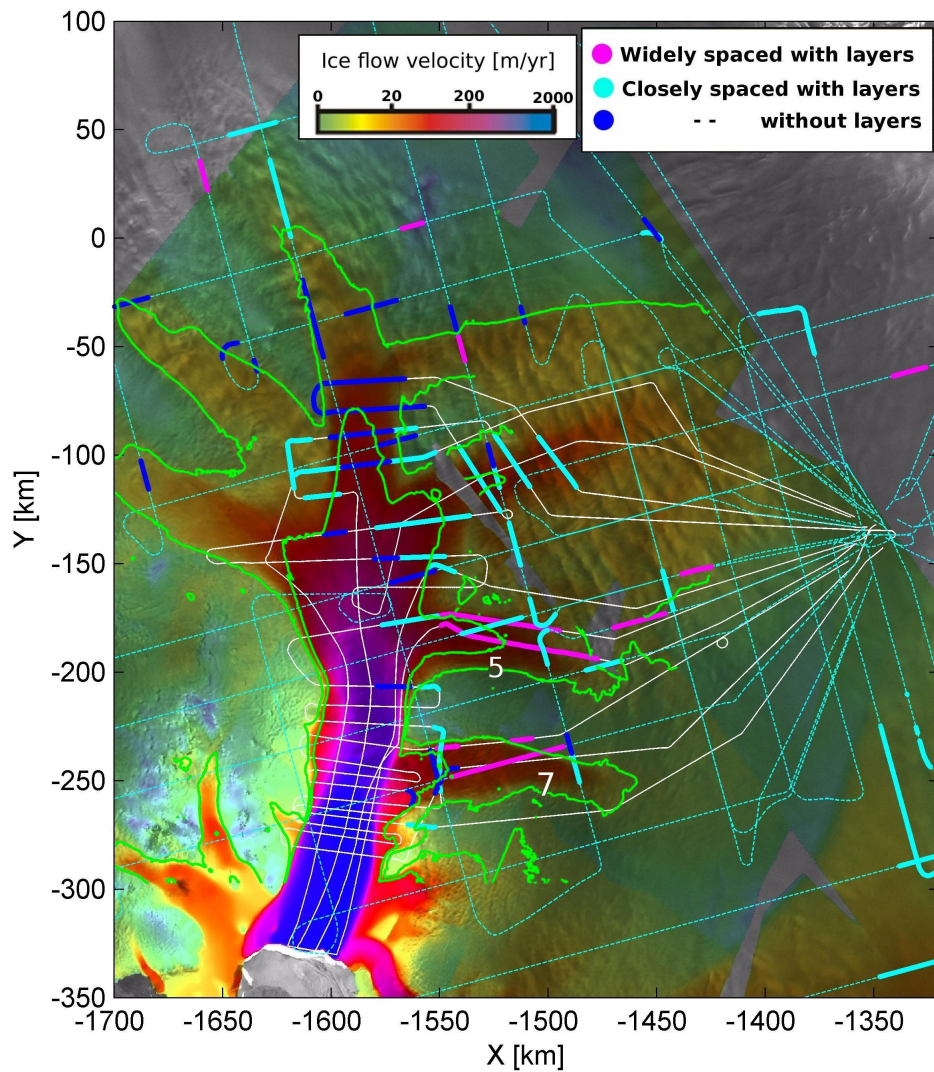


Figure 5.8: Whirlwind features in all flightlines on an InSAR velocity map (Rignot, 2006) with the  $50 \text{ m yr}^{-1}$  and  $200 \text{ m yr}^{-1}$  contour in green. The colours correspond to the example in Figure 4.5; whirlwinds without layers (blue lines), whirlwinds with layers (cyan lines) and whirlwinds with layers and widely spaced vertical structures (magenta lines).

tween Tributaries 3 and 5 that are thought to be topographically constrained. It therefore cannot be excluded that other processes are involved in disrupting the layers although no other area that distance from the main trunk is so clearly devoid of internal layering.

The area close to the field camp is slow flowing and exhibits continuous layering apart from two of the flightlines in which the upper layers are disrupted and layers are absent at depth (box 2 in Figure 5.1). The absence of deeper layers may be a consequence of echo strength reduction with depth, or could reflect the extinction of deeper internal layers due to high stresses. The area is located south of the bed-high in an area where the bed is inclining towards the south while the ice is flowing to the north (as measured by Vaughan et al. (2006)). Thus, a possible explanation for the disrupted layering, with the missing layers at depth, could be that the ice is being subjected to large strain rates due to the slope inclining in the opposite direction of the ice flow. In other words the ice is flowing “uphill” potentially causing a build up of strain rates sufficient to disrupt the layers. That the disruption is not observed to the same extent in the other flightlines could be due to the fact that the two flightlines in question are the only ones parallel to the flow direction i.e. the direction where the disruption is taking place.

The areas that contain visible layering in the upper part of the ice but no deep layers are all located in fast flow areas with only two exceptions. The first exception is the area close to the field camp that has already been discussed above. The second exception is the area around Tributary 7. Two lines contain visible upper layers but no deep layers, and the inclusion of the pulsed radar data added yet another line. If the missing deep layers are an actual feature of the ice then this could indicate a past change in the location of Tributary 7 or an additional area west of Tributary 7 that until recently have been fast flowing. This is in line with what was discussed previously about the less constrained position of Tributary 7.

The layer classification used here depends to some extent on the direction of the flightline. One example of this is the island of continuous layering in Tributary 3 (box 1 in Figure 5.1) where continuous layering is easily identifiable in the flightline parallel to the direction of ice flow while the flightlines perpendicular to the ice flow direction all display discontinuous layering. The same phenomena can be seen in the main trunk where one line parallel to the main trunk (upstream of Tributary 5) contains visible upper layers while the lines from the same area that run perpendicular to the ice flow direction have no deep layers.

### 5.1.2.1 Buckled Layering

Areas where layers in the lower ice column are buckled while those in the upper ice are continuous are thought to be reminiscent of fast flow in the past and have in previous studies been interpreted to represent changes in flow regime i.e. migration of fast/enhanced flow areas or changes in flow path (e.g. Rippin et al., 2003b). In the PIG data none of the areas containing buckled layers in the lower part of the ice column are located in fast flow areas. This could indicate that the extent of the glacier has changed since the deposition of the layers. The location of two of these features, upstream and next to Tributary 3, could be interpreted as evidence that Tributary 3 once extended further upstream than at present and that the main trunk was either wider or its position has changed. In other words, this finding suggests that the location and flow dynamics of Tributary 3 are not as stable as the bed topography might suggest. The third area with buckled layering was located close to the neck between the northern and southern basin. A possible interpretation of this feature could be that enhanced flow has extended much further upstream than at present.

### 5.1.2.2 Whirlwinds

It remains unclear what the whirlwinds, that have been identified in areas of enhanced and fast flow, actually are. They could be real physical features resulting from flow convergence and/or changes in flow mode (cf. Ng and Conway, 2004; Leysinger Vieli et al., 2007) or bedrock conditions that alternate between being smooth and sticky i.e. melting and freezing (H. F. J. Corr, pers. communication, 2008). This would cause the ice flow to alternate between accelerating basal gliding and slower flow potentially dominated by internal deformation, thus disrupting the layers (Parrenin and Hindmarsh, 2007). Another possibility is that they are a result of interference patterns from the radar waves (cf. Harrison, 1971). However, it seems reasonable to suggest that the different types of whirlwinds described here are representing different stages of the transition of internal layers from continuous to discontinuous to missing as the ice moves from slow to fast flowing ice. For example, Tributaries 1/2 contain whirlwinds without layers (or with some layering but only in the upper part of the ice), and the onset of whirlwinds with layers at depth is spatially associated with a change in velocity at the boundary of the tributary (Figure 5.7). Tributary 3 contains whirlwinds with layers, which might indicate that the flow in this tributary is not sufficiently fast to erase the internal layers completely. The fact that the features have only been identified in flightlines perpendicular to the ice flow direction, and not in

flightlines parallel to the ice flow, indicates that their detection is coupled to the ice flow direction.

### 5.1.2.3 Subglacial Water

As described in Section 5.1.1.2, in several locations along the flightlines, especially close to the field camp, basal reflectors were visible that exhibited characteristics usually associated with occurrence of subglacial water. Interestingly, the features were not located in the deepest parts of the ice and their positions did not seem to be strongly linked to subglacial topography. None of the identified locations correspond to lakes identified by Smith et al. (2009) using ICESat data. This could be due to the small spatial scale of the lakes or because they do not display a significant drainage pattern and therefore do not cause surface lowering. The fact that some of the locations are close to each other may indicate that they are part of a connected water-drainage system similar to what has been observed under, for example, Whillans Ice Stream (formerly Ice Stream B) (Fricker et al., 2007).

A study of subglacial water in East Antarctica by Carter et al. (2007) classified subglacial lakes into several subcategories by comparing the echo strength of a potential lake to its immediate surroundings, and by using the specularity of the signal (e.g. its mirror-like qualities) and the absolute strength of the signal. The classification conducted in this thesis is purely qualitative and while the relative reflectivity of the identified lakes were higher than their immediate surroundings, the absolute reflective and the specularity of the signal were not investigated. It is therefore possible that some of the lakes identified in this thesis fall into the categories described as either ‘dim lakes’ or ‘fuzzy lakes’ by Carter et al. (2007). While the cause of dim lakes is uncertain, Carter et al. (2007) interpret fuzzy lakes as corresponding to saturated basal sediments or very shallow lakes. It is therefore possible that at least a part of the reflectors identified in this thesis are due to water-saturated sediments rather than actual lakes.

### 5.1.3 Summary

The qualitative layer classification discussed above draws out a clear association between layer type, and surface velocity, consistent with previous work on classification of englacial layering (Siegert et al., 2003b; Rippin et al., 2003b). Continuous layers have primarily been found in the slow flowing areas and discontinuous layers in regions of enhanced and fast flow, especially in and between tributaries. No layers were identified in the main trunk downstream of Tributary

7. In many cases a change in layer type corresponded to a transition in surface velocity. Several lake-like basal reflectors were also identified and were especially numerous where the ice is deepest in the southern, inland basin of PIG.

Anomalous areas were identified in Tributary 3 (“island” of continuous layers in a fast flowing area), in Tributary 7 (missing and discontinuous layering in a slow flowing area) and close to the field camp (discontinuous area and missing deep layers in a slow flowing area). In the tributaries and in inter-tributary areas several vertical, whirlwind-like, features were observed. The appearance of the features were clearly linked to ice flow direction and velocity. In several areas in the main trunk and tributaries an absence of deep internal layers were observed and the fact that the only slow flowing area to exhibit this characteristic was located just west of Tributary 7 indicates that the onset of enhanced flow Tributary 7 might have migrated.

In three areas layering was found that did not match the bed topography. Two of those areas were located close to Tributary 3 and this observation in combination with the island of continuous layering could indicate that the position of Tributary 3 is less stable than previously assumed based on the subglacial topography.

The results from this section are all based on a manual classification scheme. While this method ensures a high degree of consistency of the results, this kind of data analysis would benefit from a more automated, quantitative approach. Results from such a method will be discussed in the next section.

## 5.2 Quantitative Classification

In Section 4.2.2 several methods for quantifying internal layers were discussed. The method that performed most robustly and proved mainly independent of ice thickness was the absolute derivative method, where the continuity of the layers is represented by a  $\psi$ -value. In this section the results from this quantitative classification are presented for flightlines 10-14 and compared to the qualitative results discussed above.

### 5.2.1 Results

This section presents and discusses the results from the absolute derivative method, hereafter referred to as the quantitative method. Before presenting the results from all five flightlines, the results from flightline 14 compared to the qualitative method in more detail to get better insight into how the  $\psi$ -values reflect the layer type and what potential errors and misinterpretations might occur.

#### 5.2.1.1 A Detailed Study of Flightline 14

Figure 5.9 shows (a) a radargram from flightline 14 and (b) the corresponding  $\psi$ -values. The distinction between layer types for the quantitative method is based on where the dotted blue and black lines intersect the black line representing a smoothing of 1000 traces. Comparison between  $\psi$ -values and radar data indicated two cut-off values to distinguish between continuous and discontinuous layering. Based on this  $\psi$ -values above the dotted blue line ( $\psi \gtrsim 0.19$ ) were taken to indicate continuous layers and  $\psi$ -values below the dotted black line ( $\psi \lesssim 0.13$ ) to indicate missing layers. As a general rule the  $\psi$ -value needed to be below (or above) the threshold value for several hundred traces before it was interpreted as an indication of change in layering type.

The general agreement between the two methods is reasonable. Both methods identify areas of continuity at the beginning and end of the radargram, missing layers at traces 15,000 to 20,000 approximately, and discontinuous layers between the missing layers and the continuous areas. However, there are some discrepancies and especially the transitions from continuous to discontinuous layering are different in several places. Some of the discrepancies can be explained by examining the data more closely. For example, at the beginning of the radargram the qualitative method sets the first approximately 1,000 traces as discontinuous. This is because the layering in the deeper part of the ice is not visible, either due to the signal attenuation of the radar or other effects in the ice. The missing layers in the lower half causes a decrease in  $\psi$ -value.

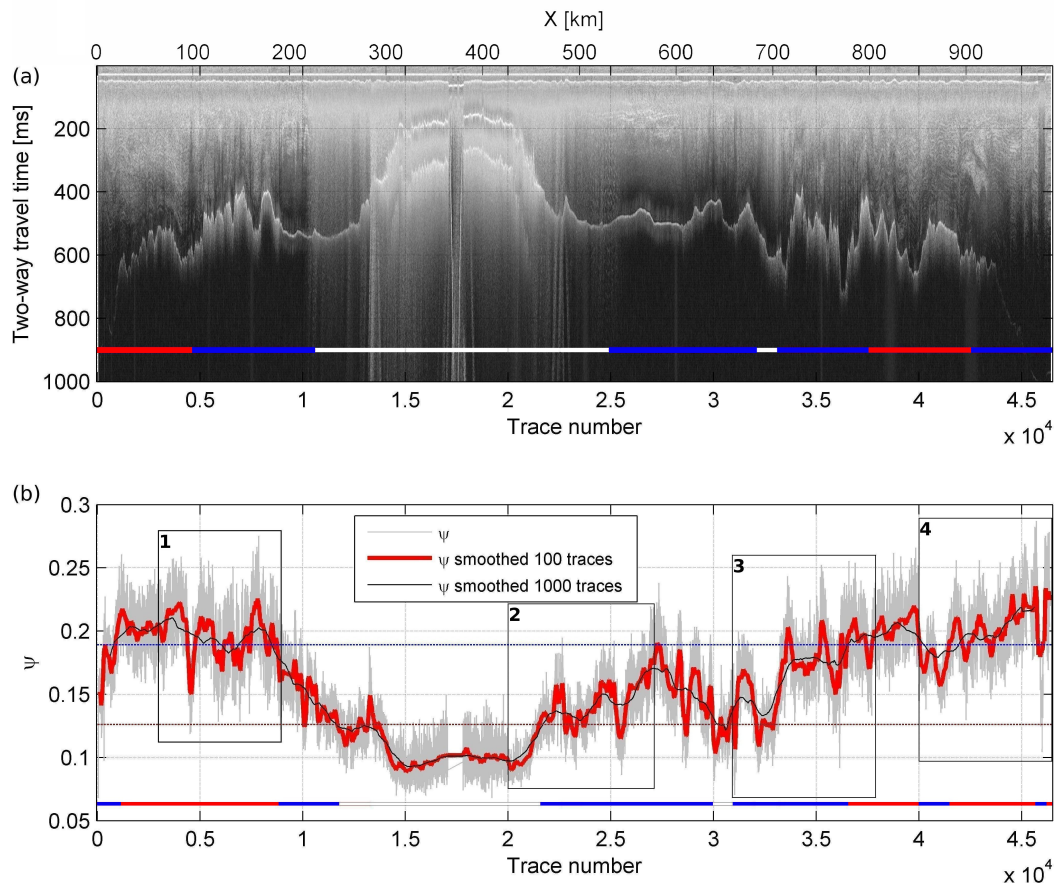


Figure 5.9: (a) Radargram from flightline 14, the coloured line shows continuous (red), discontinuous (blue) and missing (white) layering from the qualitative classification. (b)  $\psi$ -values for flightline 14 (grey line), the  $\psi$ -values smoothed over 100 traces (thick red line) and the  $\psi$ -values smoothed over 1000 traces (thin black line), the coloured line shows continuous (red), discontinuous (blue) and missing (white) layering based on the  $\psi$ -values. The two dotted lines indicate the approximate cut-off values for continuous/discontinuous/missing layers.

Figure 5.10b shows  $\psi$ -values at traces 3,000 to 9,000 (approximately 75 - 210 km) corresponding to box 1 in Figure 5.9. Based on the  $\psi$ -values the entire part of this radargram has been classified as continuous except at the very end, while the qualitative method has identified the majority of the radargram as containing discontinuous layering. The left hand side of the radargram is a fairly continuous area which is reflected in the high  $\psi$ -values. At 4,500 ( $\sim 110$  km), however, a dip in the  $\psi$ -values corresponds precisely with a small section of missing layers. From approximately 5,000 ( $\sim 120$  km) and onwards the layers get a bit more discontinuous but the  $\psi$ -values are only slightly lower. Between traces 7,500 and 8,000 ( $\sim 170 - 190$  km) there is another local maximum in  $\psi$ -value. Close examination of the data reveals that the maximum is caused by an area that indeed has numerous internal layering, but the layers are only traceable for short distances though it could be argued that the layering is close to being continuous.

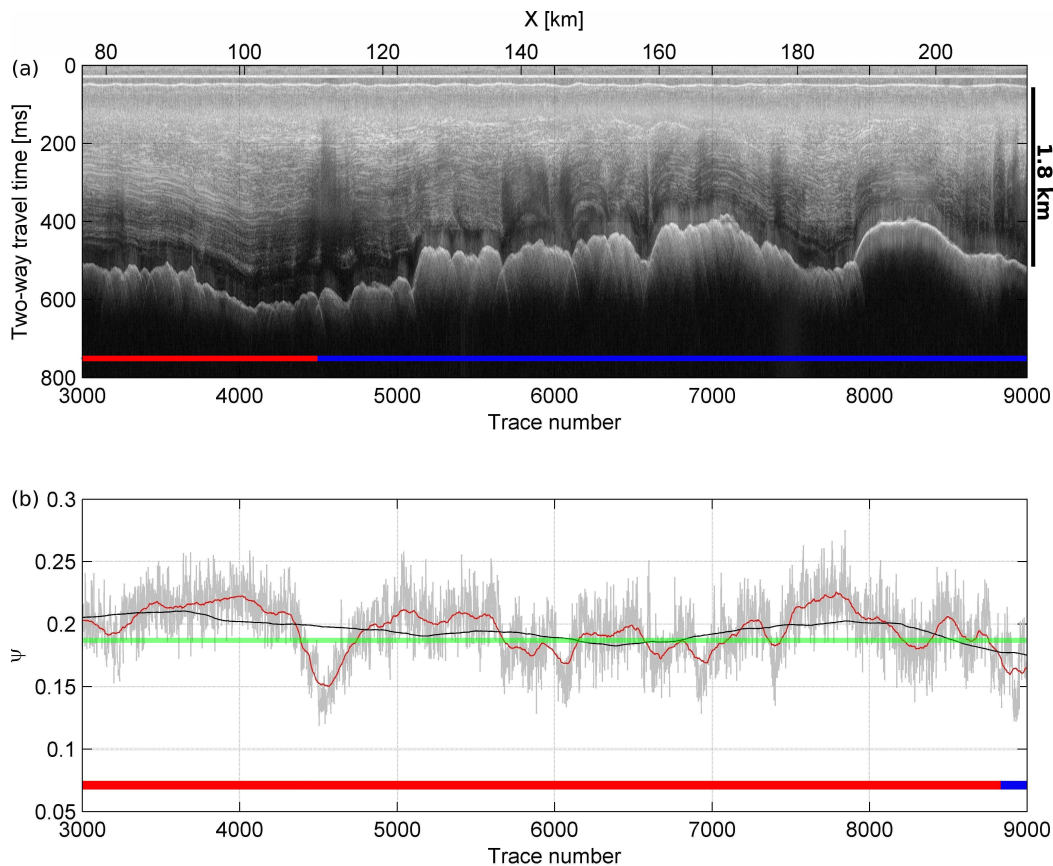


Figure 5.10: (a) Radargram from flightline 14 corresponding to box 1 in Figure 5.9, the coloured line shows continuous (red) and discontinuous (blue) layering. (b)  $\psi$ -values for flightline 14 (grey line), the  $\psi$ -values smoothed over 100 traces (thick red line) and the  $\psi$ -values smoothed over 1000 traces (thin black line). The green line indicates the approximate cut-off at  $\psi \gtrsim 0.19$ .

A zoom in on the second box in Figure 5.9 is shown in Figure 5.11. This part of the flightline contains very few visible layers. The transition between missing and discontinuous layering is set at trace 25,000 ( $\sim 555$  km) in the qualitative method while the quantitative method sets the transition at approximately trace 21,500 ( $\sim 475$  km). Part of the reason for the increase in  $\psi$ -value can be found in the noise in the data that is (incorrectly) interpreted as layers. The method does, however, still reflect the increase in number of layers to the right in the image (mainly visible in the top part). The low at 25,500 ( $\sim 570$  km) is an artefact caused by very little noise combined with very few layers. Interestingly, the top part of the radargram from trace 23,500 ( $\sim 530$  km) displays some internal layering, so it could be argued that the qualitative classification of the area as containing no layering is erroneous supporting the agreement with the quantitative method.

The third box in Figure 5.9 contains traces 31,000 to 38,000 ( $\sim 680 - 830$  km) (Figure 5.12). The qualitative method has identified a section with missing layers, but otherwise the layering is mainly discontinuous with some continuous layers to

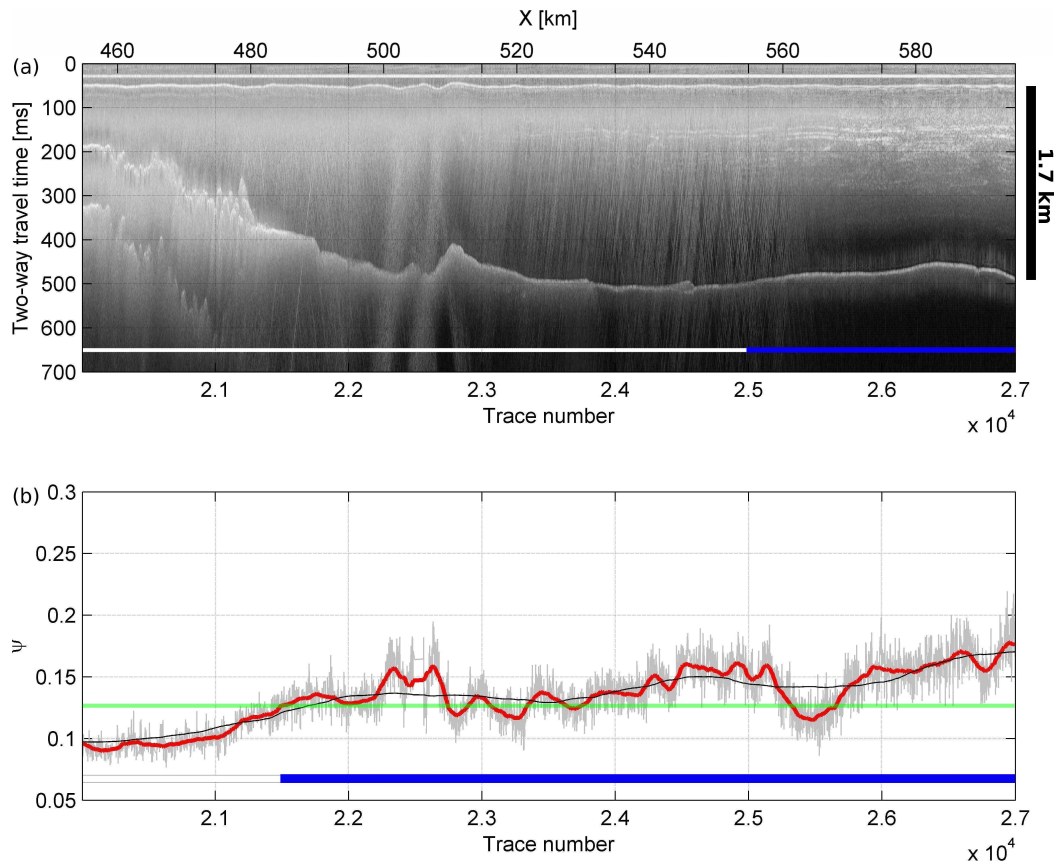


Figure 5.11: (a) Radargram from flightline 14 corresponding to box 2 in Figure 5.9. (b)  $\psi$ -values for flightline 14.

far right of the radargram. The quantitative method classifies the missing layer area as discontinuous and has the transition from discontinuous to continuous layering further to the left at trace 36,200 ( $\sim 780$  km). Closer examination of the data in this area shows a gradual change from discontinuous to continuous layers, although the transition is probably closer to 37,000 than 36,000. In the area that has been classified as containing no layers a few internal reflectors are visible in the top part of the ice, although in this case the term layering might be inappropriate since they do not display any horizontal coherence. Even so it explains the increase in  $\psi$ -value that leads to the area being classified as containing discontinuous layering rather than missing layers.

Finally, the fourth box is from an area of continuous and discontinuous layering. In the right hand side of Figure 5.12 (e.g. traces 40,000 - 42,000,  $\sim 870$ – $990$  km) the method performs less well in terms of predicting continuous layers. Although the layering is clearly continuous the quantitative method classifies this area as discontinuous due to a local minimum in  $\psi$ -value. The discontinuous area on the other hand display increasing  $\psi$ -values in spite of several discontinuities. The increase in  $\psi$ -value can be explained by the abundant layering in the

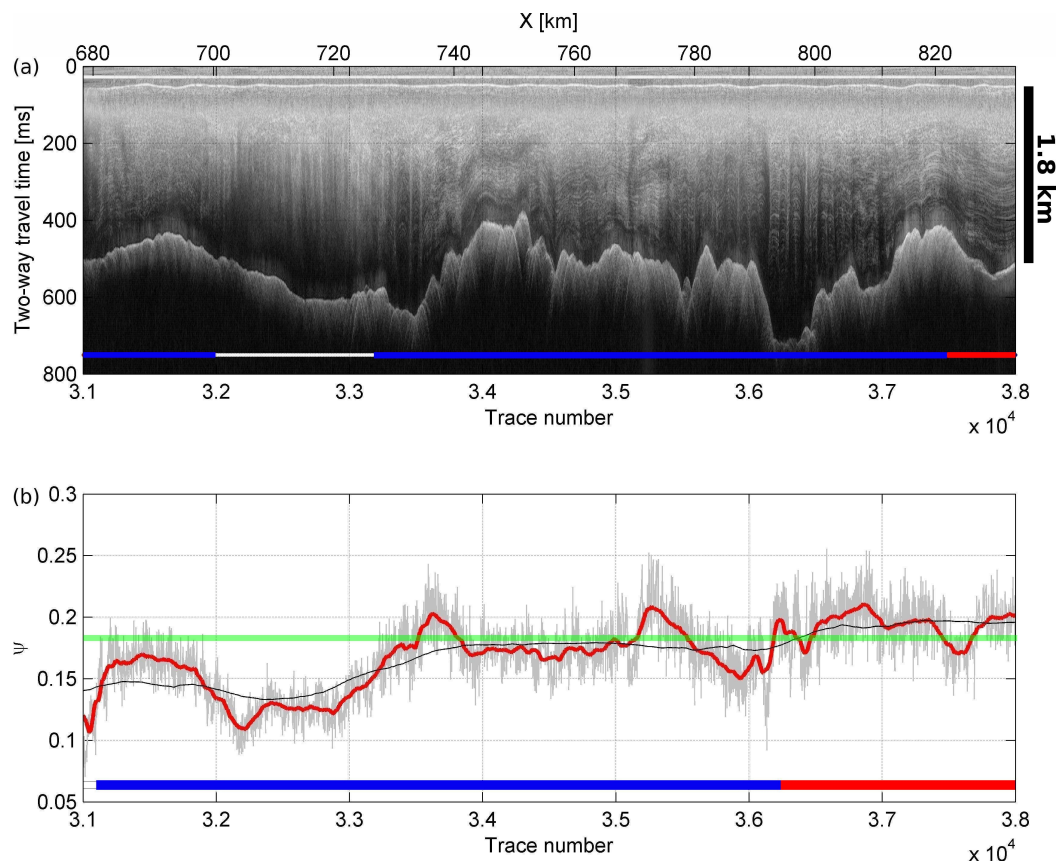


Figure 5.12: (a) Radargram from flightline 14 corresponding to box 3 in Figure 5.9. (b)  $\psi$ -values for flightline 14. The green line indicates the approximate cut-off at  $\psi \gtrsim 0.19$ .

top part that could be argued to be close to being continuous. The decrease in the left hand side of the figure on the other hand is more difficult to explain but could be related to the shallow ice thickness leading to very short wiggle plots and thus increasing the probability of an error.

The quantitative method proposed here performs well in terms of characterising the number of layers in a radargram, but it is not without its limitations. For example, noisy data will to some extent have an increased  $\psi$ -value compared to data with little noise, which could be interpreted incorrectly as layers (e.g. Figure 5.11). Furthermore, the method does not distinguish between areas where the layering is continuous at the top but missing at the bottom and areas where the layering is discontinuous (e.g. Figure 5.13). Finally it should be noted that in terms of the  $\psi$ -value there will be practically no difference between areas with no internal layering and areas where only one continuous layer is visible. More importantly, however, the method does distinguish between continuous layers, discontinuous layers and missing layers.

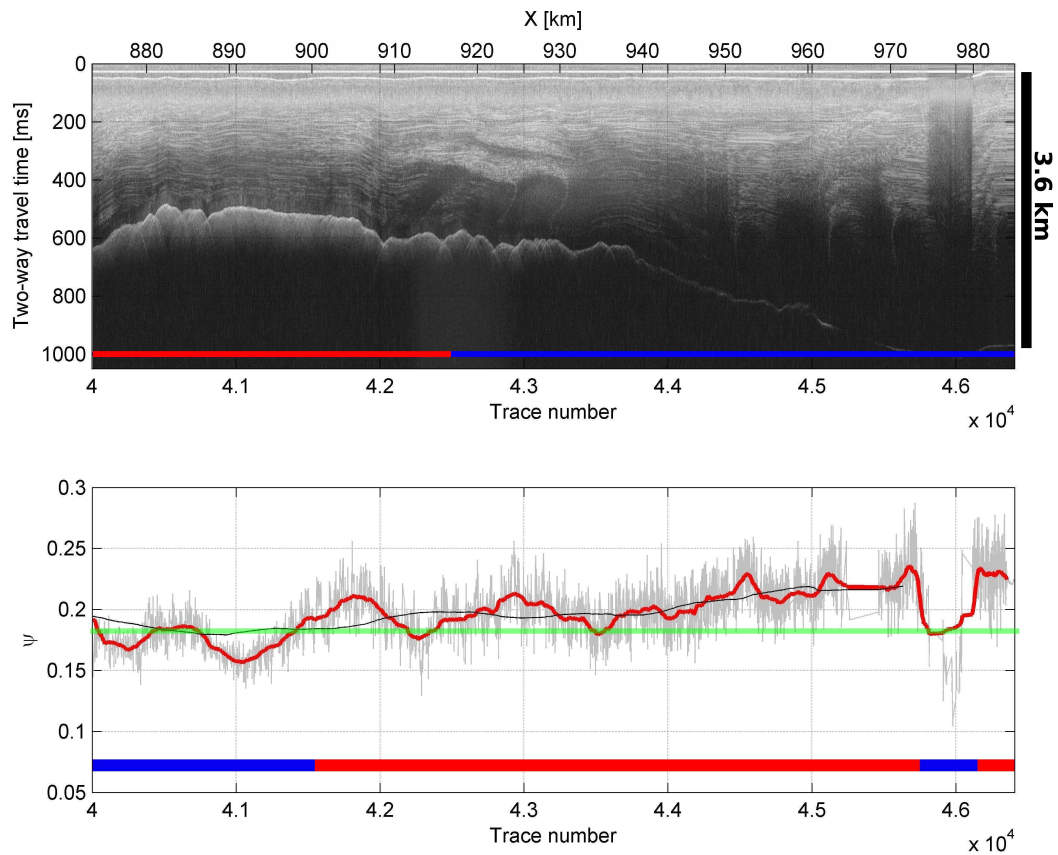


Figure 5.13: (a) Radargram from flightline 14 corresponding to box 4 in Figure 5.9. (b)  $\psi$ -values for flightline 14 (grey line). The green line indicates the approximate cut-off at  $\psi \gtrsim 0.19$ .

### 5.2.1.2 Flightlines 10 - 14

The  $\psi$ -values for flightlines 10-14 are now considered for  $\psi$ -values smoothed over 100 traces (Figure 5.14a) and over 1000 traces (Figure 5.14b). While the smoothing over 100 traces is better for identifying individual anomalies the smoothing over 1000 traces gives a more broad picture and both are therefore included here.

The general pattern is a decrease in  $\psi$ -values as the velocity increases. In some areas this transition is very sharp, for example, in Tributary 7, where there are two obvious transitions from continuous to discontinuous layering, while the flightline below tributary 7 changes from discontinuous to missing layering (black stars in Figure 5.14a). In other areas, for example Tributary 5, the change in  $\psi$ -value is more gradual with a general decrease in  $\psi$ -values as the flightlines enter the faster flowing tributary. For Tributary 3 two of the flightlines that cross the tributary perpendicular to the direction of flow exhibits a sharp change in  $\psi$ -value. The flightline that runs parallel to the flow in Tributary 3 contains a sharp transition from discontinuous to continuous layering (grey stars in Figure 5.14a). In Tributary 1/2 the onset of enhanced and fast flow is clearly reflected

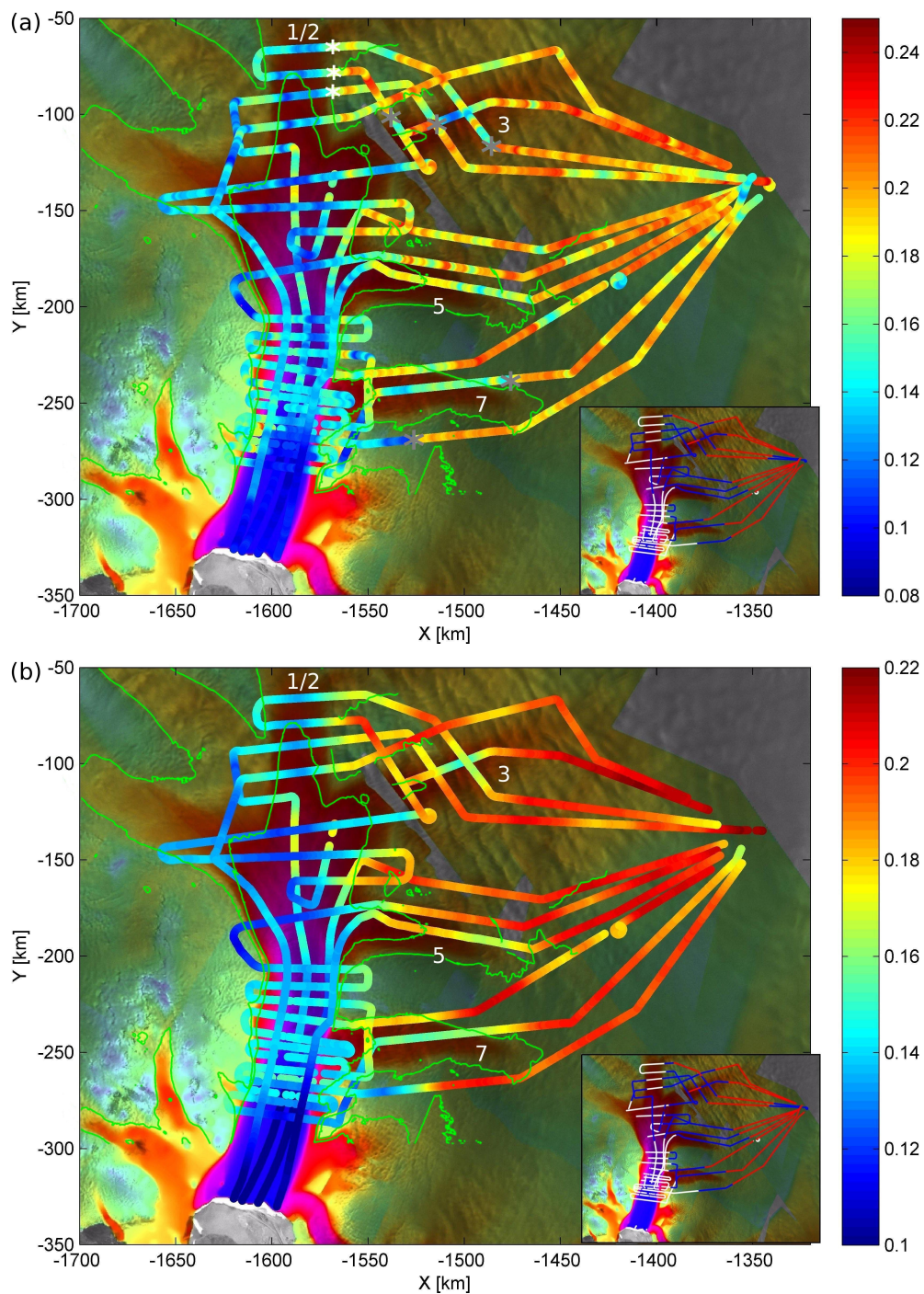


Figure 5.14:  $\psi$ -values for flightlines 10-14 smoothed over (a) 100 traces and (b) 1000 traces with InSAR velocities as background with the  $50 \text{ m yr}^{-1}$  and  $200 \text{ m yr}^{-1}$  contour in green. Notice the different colour scale in the two figures. Grey and white stars in (a) mark transitions in  $\psi$ -value correlating with a change in surface velocity.

in the decrease in  $\psi$ -values (white stars in Figure 5.14a). Along the main trunk the onset of fast flow corresponds with decreasing  $\psi$ -values in several places. The lowest  $\psi$ -values are found in the floating part of the main trunk where the ice is shallow. One interesting feature that occurs in several places is the difference in  $\psi$ -value depending on the angle of the flightline to the direction of the ice flow. This effect was also observed in the qualitative approach.

### 5.2.1.3 Comparison with Qualitative Method

Compared to the qualitative method the quantitative method performs very well in identifying the transition between areas with no layering and areas with some layering. However, the transition between discontinuous and continuous layering is less clear.

In Tributary 7 the two transitions from continuous to discontinuous layering that are identified in the qualitative analysis appear in quantitative method too, the flightline below Tributary 7 that changes from discontinuous to missing layering is also identified in the qualitative method, although the change from discontinuous to continuous layering is not. For Tributary 5 there is no marked onset of change in layer type although both methods indicate a change to discontinuous layering. In Tributary 3 the small “island” of continuous layering corresponds to the results from the qualitative method, as well as the transition to discontinuous layer in the flightlines that are perpendicular to the flow direction. The same can be observed in Tributary 1/2.

### 5.2.1.4 Other Flightlines

Unfortunately the quantitative method is less applicable when used on data that does not have a constant distance to the ice surface. This is due to the changing elevation of the radar instrument that causes the returned signal from the internal reflectors to vary in strength and thus oscillations of the internal layers to appear smaller/larger due to the decrease/increase in signal. An example from this can be seen in flightline 06 (Figure 5.15) where the distance between aircraft and ice surface changes and the layering changes simultaneously. Thus the method described above can be said to be independent of flight height during acquisition but not to *changes* in flight height.

## 5.2.2 Summary

The results from the quantitative method agrees well with changes in surface velocity from slow to fast flow; the main trunk displays very low  $\psi$ -values ( $< 0.13$ )

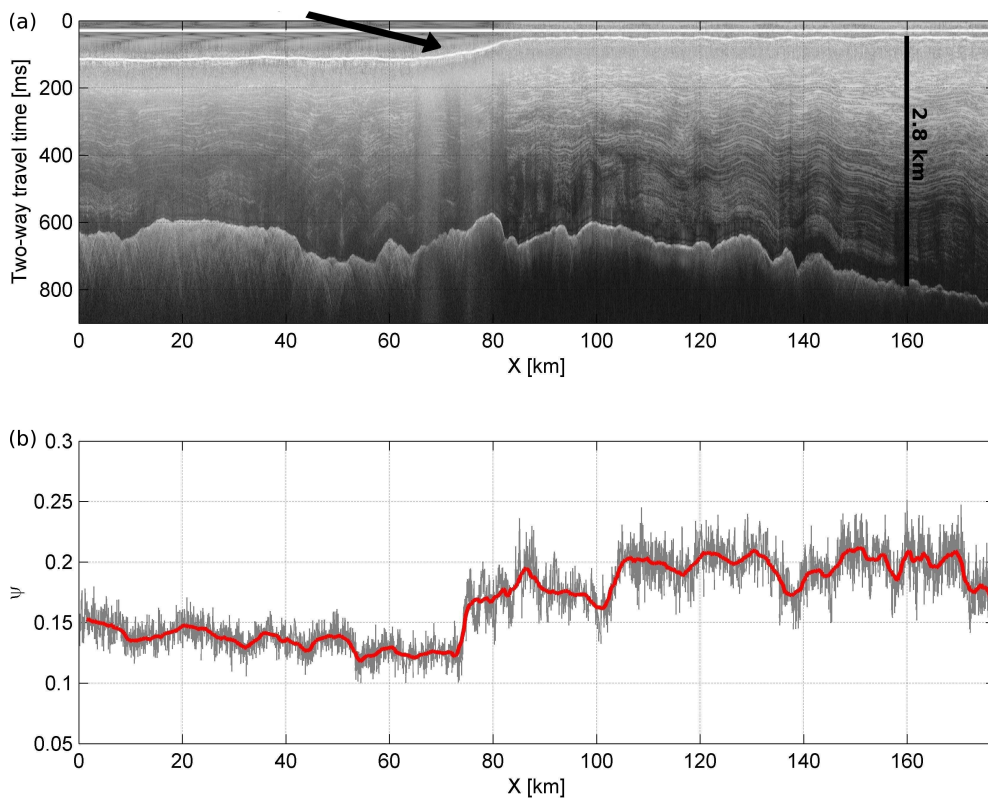


Figure 5.15: (a) Example from flightline 06 of changing acquisition height (black arrow) above ice surface and the impact on internal layering. The internal layering is significantly less clear in the left part of the image compared to the right part. (b) Corresponding  $\psi$ -values (grey lines) and averaged over 100 traces (thick red lines).

and the slow-flowing areas display high  $\psi$ -values ( $> 0.19$ ). Furthermore, the changes in  $\psi$ -values are often very well correlated with onset of enhanced/fast flow. The results further highlight an area of anomalously low  $\psi$ -values west of Tributary 7, where the surface velocity is relatively slow, and an area in Tributary 3, where the  $\psi$ -values are low even though the surface velocity is enhanced. As discussed in Section 5.1.2 this can be interpreted as evidence for a past change in ice flow. Interestingly, the onset of enhanced flow in Tributary 5 is not correlated with any significant change in  $\psi$ -values (most clear in Figure 5.14a), although the  $50 \text{ m yr}^{-1}$  contour for this tributary in the InSAR data is less clear. This could be an indication that the layers in Tributary 5 are experiencing less longitudinal stress or that the onset of enhanced flow is, or has been until recently, much more gradual than in Tributaries 3 and 7.

Inevitably, the quantitative method is limited by the dataset itself. Since the frequency of the radar is such that deep layers are not always resolved, the method will assign low  $\psi$ -values to areas with missing deep layers compared to areas with lower ice thickness. This means that the method to some extent is

dependent on ice thickness via the radar system properties, however, if the radar system had been able to resolve the deeper layers this would most likely not have occurred. Conversely, very shallow ice might lead to an underestimation of the  $\psi$ -value as discussed for Figure 5.13.

The comparison between the qualitative and quantitative classification emphasises the subjectivity of the qualitative approach and also the limitation in only being able to classify three layer types, when in reality there often is a gradual transition. In many cases the layer type could be characterised as a mixture of continuous and discontinuous layers. The quantitative method is particularly powerful used together with a qualitative method as differences in the results will help identify areas of unusual layering and also serve as a check of the qualitative results for areas where the interpretation is less clear. Most importantly, however, the quantitative method is rigorous and significantly faster than the qualitative method providing an easier way to classify radar data independently of the person performing the analysis.

## 5.3 Layer Tracing

With the use of a semi-automated tracing routine numerous internal layers in all flightlines were traced (see Section 4.2.3.1 for a description of the layer tracing routine). In this section the layer statistics are explored further. First by considering the statistics of the entire layer ensemble looking at each traced layer as an individual layer with no correlation between flightlines. Secondly, by exploring a layer pattern that was identified in several flightlines and enabled correlation between flightlines constructing a three-dimensional surface of the internal ice sheet structure.

### 5.3.1 Layer Statistics

Over 300 layers were picked from the parts of the flightlines that were inside the PIG catchment basin. Of these, 95% were shorter than 36 km, and the majority (59%) were shorter than 10 km (Figure 5.16a) with a mean layer length of 11 km. It was only possible to pick 10 layers that exceeded 50 km from the entire dataset.

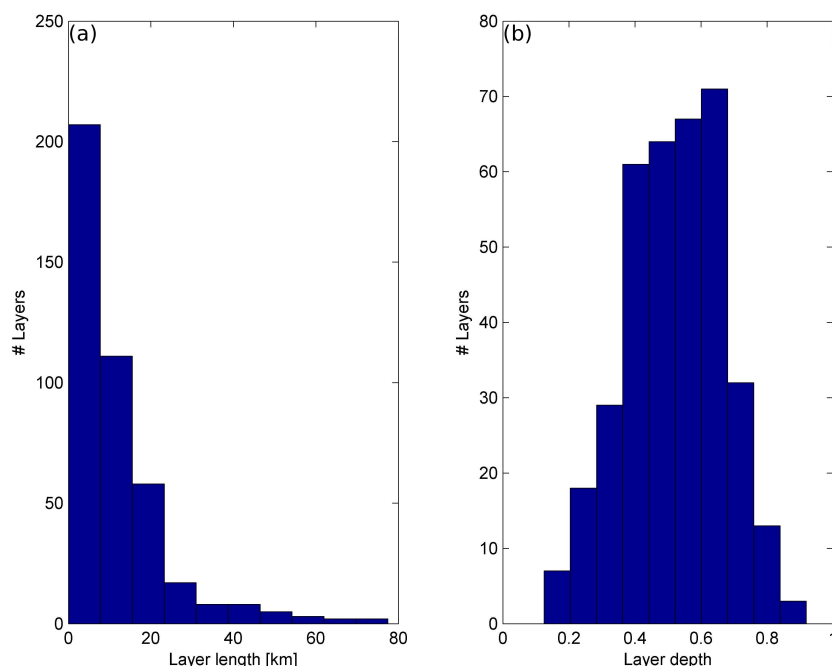


Figure 5.16: *Layer Statistics showing (a) the length of each traced layer and (b) the average normalised elevation of each layer.*

Due to the vast amount of data available not every single layer in the radar data was picked, but rather the most easily identifiable and the ones easiest to trace i.e. the ones that could be traced with the greatest confidence. The picked layers are therefore biased towards layers that occur at depths where the signal attenuation is still not significant enough to obscure them or where the bed relief

has not made tracing difficult. 95% of the layers were found at an elevation between 0.22 and 0.82 (in normalised elevation) and 70% were found within the approximate middle third of the ice (between elevations 0.37 and 0.67). The mean elevation was 0.52. No layers were traced deeper than 0.12 (i.e. in the lower 12% of the ice) or shallower than 0.92 (i.e. in the upper 8% of the ice) (Figure 5.16b).

The number of layers that were traced reflects the successful application of the layer tracing routine. However, the greatest contribution of the layer tracing routine was to provide input to the ice flow models, which will be presented in Chapters 6 and 7.

### 5.3.2 Retrieving Information from a Layer Package

Due to the nature of the radar data it proved difficult to identify the same internal reflector in different flightlines and thus correlate the layers across the flightlines and construct a 3D image of the internal structure. In one area, however, this was possible due to a distinct layer package. In these areas one very strongly reflecting layer was visible with two strongly reflecting layers below it. In between these layers a “diffuse” layer could be seen. In the following the top layer will be referred to as Layer 1 and the upper of the two lower layers will be referred to as Layer 2. Figure 5.17a shows an example of one place where this layer package is visible. The extent of the layer package is shown on the map in Figure 5.17b with white lines.

At first the statistical properties of the layer package are examined (Table 5.1). Keep in mind that for normalised elevation high values denote shallow layers while when referring to the depth of a layer higher values mean closer to the bed. The range in normalised elevation is higher for Layer 2 than for Layer 1 and so is the standard deviation. Hodgkins et al. (2000) interpreted a larger range and standard deviation of a RES layer to indicate a larger degree of cumulative deformation. Thus Layer 2 would be expected to show a larger range in depth and a larger standard deviation, since the layer is deeper than Layer 1, in agreement with the fact that the deeper a layer is, the older it is and the more cumulative deformation it has been subjected to (Hodgkins et al., 2000).

Since the layer package was traced across multiple flightlines it was possible to use it to construct three-dimensional surfaces of the interior of the glacier. The surfaces are constructed using interpolation from the Matlab routine *gridfit*. The routine interpolates between data points by assigning each data point into a triangular cell and linearly interpolating inside the triangles. The routine attempts to ensure that the gradient is as smooth as possible everywhere and that the solution fits a smooth surface.

| Statistics         | Layer 1             | Layer 2             |
|--------------------|---------------------|---------------------|
| X-range (Northing) | -1,472 to -1,236 km | -1,481 to -1,235 km |
| Y-range (Easting)  | -198 to -59 km      | -166 to -58 km      |
| Norm. elevation    |                     |                     |
| Maximum            | 0.74                | 0.64                |
| Minimum            | 0.33                | 0.18                |
| Range              | 0.40                | 0.44                |
| Mean               | 0.55                | 0.44                |
| Standard deviation | 0.06                | 0.07                |

Table 5.1: Statistics for Layer 1 and 2 in a layer package.

The result can be seen in Figure 5.19. The flightlines where the layer package has been identified are shown as thick black lines. From the figures it can be seen that both surfaces dip at the neck between the two catchment basins. The depth decreases towards the north corresponding to the high in the subglacial topography identified by Vaughan et al. (2006). The depth also increases just outside the PIG catchment which is in agreement with the existence of a deep subglacial trench in that area.

### 5.3.3 Summary

Considering the numerous studies where internal layering has been traced for several hundred kilometres (e.g. Welch and Jacobel, 2003; Siegert and Payne, 2004), the fact that the mean traced layer length for all layers was 11 km is a good example of the limitations of the PIG dataset. The small layer lengths mean that the spatial extent of the isochrones is small and provides only limited constraints on internal ice sheet structure. The combination of a radar frequency of 150 MHz and the fact that the flow of PIG is sufficiently fast in areas to disrupt or eradicate layering made the layering more difficult to identify over larger areas compared to, for example, the SPRI datasets.

The results from the statistical properties of the normalised elevation shows that Layer 2 has a larger range and standard deviation in elevation than Layer 1. This implies that Layer 2 has been influenced more by internal deformation than Layer 1 (Hodgkins et al., 2000), in good agreement with the fact that Layer 2 is deeper than Layer 1.

Although the construction of gridded surfaces of the internal structure does not at present add substantial information to our knowledge of PIG, the maps may become very useful in the future if RES surveys were to be conducted in the region, helping to identify the same layer package again.

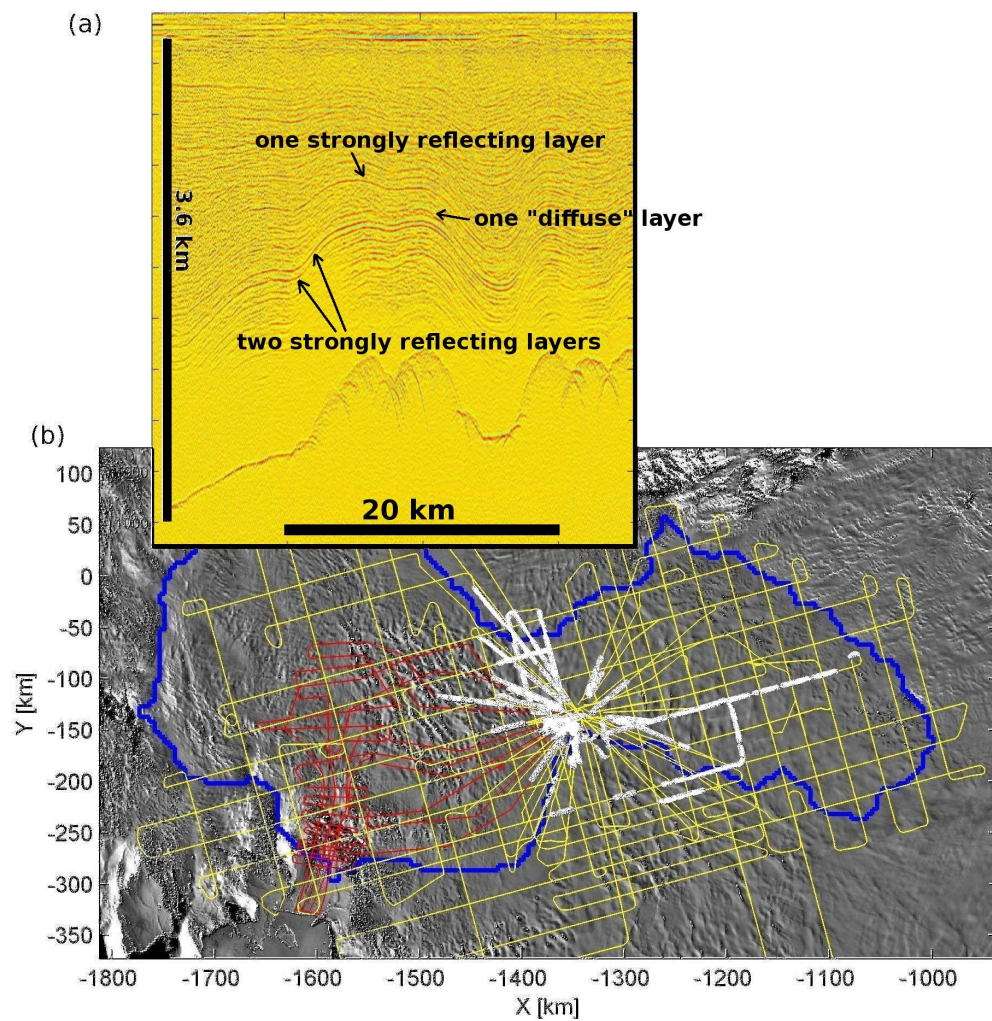


Figure 5.17: (a) Example of the layer package identified in several flightlines: One strongly reflecting layer, followed by a more diffuse layer and then two strongly reflecting layers. (b) Map of the spatial distribution of the layer pattern. The flightlines are shown as yellow (flights with constant elevation) and red lines (flights with constant terrain clearance), the blue line outlines the catchment basin and the white lines are locations where either one or both of the layers have been identified.

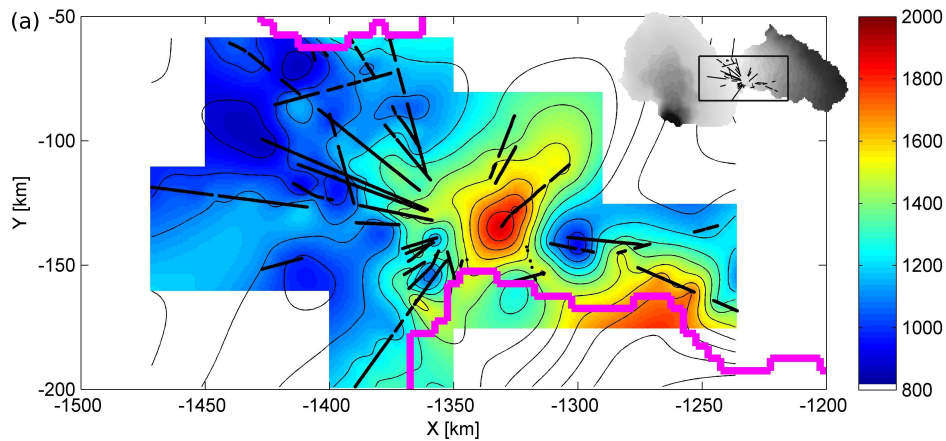


Figure 5.18:

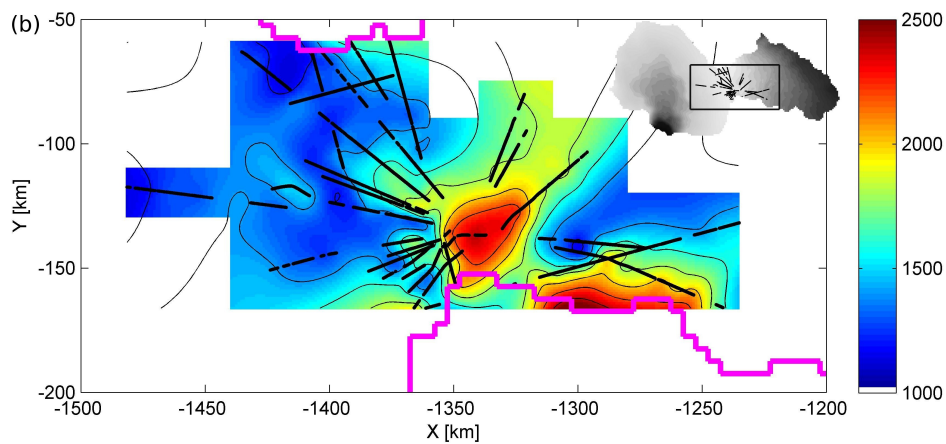


Figure 5.19: *Elevation of the gridded surface (colours and thin black contour lines) in metres constructed from depth measurements of (a) Layer 1 and (b) Layer 2 (thick black lines) and the outline of PIG is in thick magenta lines. Note the different colour scales. Parts of the surfaces have been blanked out if the area was deemed too far from an actual measurement to be accurate. Note the clear dip in layer depth in the neck between the northern and the southern basin.*

## 5.4 Stresses and Internal Layering in PIG

The occurrence (or non-occurrence) of internal layering in a glacier can often be linked to the stresses in the glacier (e.g. Raymond et al., 2001; Conway et al., 2002). This relationship along with the stress regime of the glacier will be explored in more detail in the sections below. First, the role of the driving stress and deformational stress is explored following methods from Stenoien and Bentley (2000) and then the correlation between basal shear stress (calculated by Joughin et al., 2009) and the internal layering is examined.

### 5.4.1 Driving Stress and Deformation

The driving stress of a glacier can be calculated from knowledge of ice thickness and topography (e.g. Paterson, 2002):  $\tau_d = \rho g H \sin \alpha$ , where  $\tau_d$  is the driving stress,  $\rho$  is the density of ice,  $g$  is the gravitational constant,  $H$  is ice thickness and  $\alpha$  is the surface slope averaged over 10 km. Following Stenoien and Bentley (2000) the driving stress can be used to calculate the deformational velocity  $u$ :

$$u = \frac{2H}{n+1} \left( \frac{\tau_d}{B} \right)^n \quad (5.1)$$

where  $n$  is the flow law exponent ( $n = 3$ ) and  $B$  is the viscosity parameter which Stenoien and Bentley (2000) sets to  $B = 0.35 \text{ MPa yr}^{1/3}$  in PIG basin, noting that this value will be accurate within a factor of two.

The deformational velocity is the ice velocity caused by internal deformation and comparison between  $u$  and the observed surface velocity should enable identification of areas where the ice flow is dominated by internal deformation (the deformational velocity is of the same size as the observed velocity) or by sliding (the deformational velocity is significantly smaller than the observed velocity).

#### 5.4.1.1 Results

Figure 5.20 shows (a) the deformational velocity calculated from Equation 5.1 and (b) observed surface velocity from InSAR data (Rignot, 2006). The main trunk and Tributaries 2, 4 and 6 have very low deformational velocity indicating a flow mode dominated by sliding. The deformational velocity was found to be substantially higher in the tributaries south of the main trunk, however, comparison with observed velocities reveal that the observed surface velocity is substantially higher than the deformational velocity (note that the colour scale is logarithmic). Comparison between the deformational velocity and the bed topography (Figure 5.21) on the other hand shows an agreement between the extent of the deep

trough, where the main trunk is located, and a decrease in deformational velocity upstream of Tributary 7. Furthermore, the part of Tributary 5 that has low deformational velocity corresponds to the extent of the deep subglacial bed under the tributary. The figure also shows the continuous and discontinuous layering identified, but there does not appear to be any correlation between the locations for changes in layer type and changes in deformational velocity.

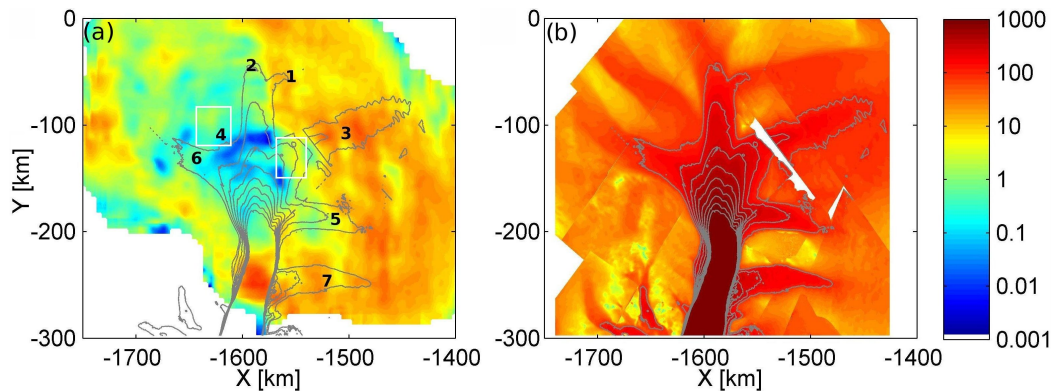


Figure 5.20: (a) Deformational and (b) observed surface velocity ( $m yr^{-1}$ ) on the same logarithmic scale. The observed velocity field is outlined with thin grey contours ( $100 - 900 m yr^{-1}$ ).

#### 5.4.1.2 Interpretation

The results indicate that most of the ice flow in the northern basin of PIG is taking place via some degree of basal sliding. The tributaries that experience the largest degree of deformation are Tributaries 3 and 7. However, when Tributary 3 enters the main trunk this coincide with an area of low deformational velocities, while the deformational velocity of Tributary 7 stays almost unchanged as the tributary enters the main trunk. Stenoien and Bentley (2000) found evidence for areas undergoing rapid acceleration that might be considered onset of fast flow in Tributaries 3 and 4. These two potential areas have been outlined with white boxes in Figure 5.20, however, it is not clear what distinguishes these two areas from, for example, the change in deformational velocity in Tributary 5.

In the study by Stenoien and Bentley (2000), the authors conclude that the onset of fast flow was not correlated with any significant change in surface or bed topography. However, in Figure 5.21 the deformational velocity and the subglacial topography appear to be correlated in several locations, for example, Tributary 5 and the main trunk. This may indicate a change in flow dynamics as the ice enters the main trunk.

While the internal layering did not have any strong correlation with the deformational velocity, the correlation between bed topography and onset of significant

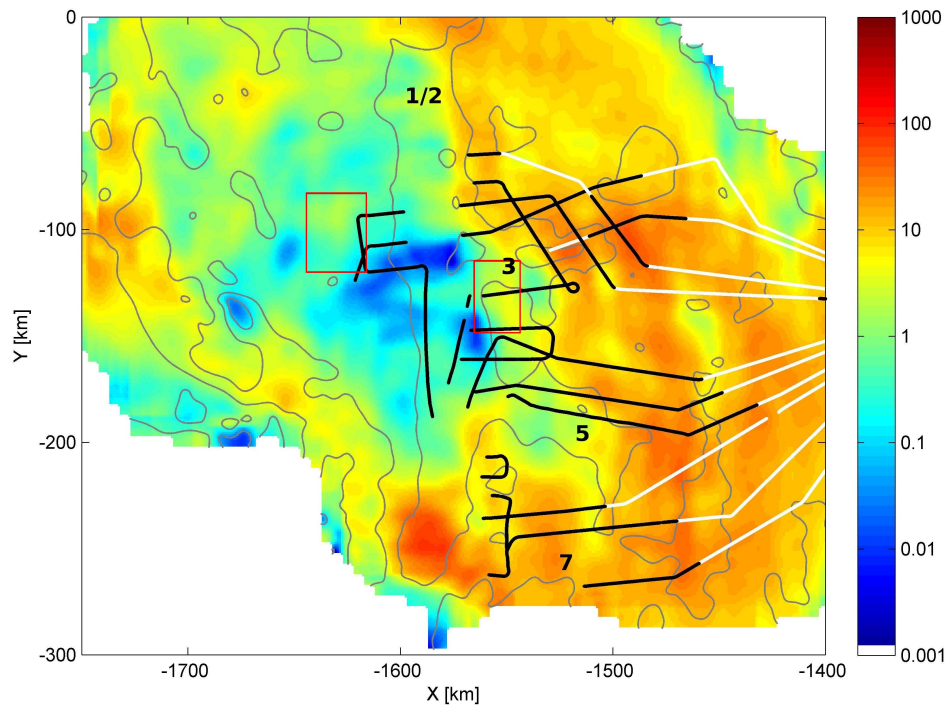


Figure 5.21: *Deformational velocity (colours on a logarithmic scale) and subglacial topography (grey contour lines). The internal layering is indicated with thick black (discontinuous) and white (continuous) lines.*

basal sliding is clear. This is in agreement with previous studies that conclude that flow dynamics of PIG is strongly controlled by its bed topography (Vaughan et al., 2006).

#### 5.4.2 Internal Layering and Basal Shear Stress

In this section the role of basal conditions and the correlation with the internal layering are explored. The basal conditions of glaciers are difficult to observe and often bed properties are inferred from velocity measurements at the surface (e.g. Joughin et al., 2006) or from basal reflectors in RES data (e.g. Catania et al. (2003), see also Section 2.3.2). This section makes use of the basal shear stress from a study by Joughin et al. (2009), who used remote sensing data to constrain an ice-stream model that incorporated basal conditions such as melting and basal shear stress. The study made use of InSAR velocity measurements from 1996 by ERS-1 and ERS-2 and surface and bed topography from Vaughan et al. (2006). The basal shear stress was found by inverting the ice-stream model to find the basal shear stress that produced the smallest misfit between modelled and observed velocities. More information on the methodology of this study can be found in Joughin et al. (2009).

### 5.4.2.1 Results

Figure 5.22 shows (a) the basal shear stress from Joughin et al. (2009) and (b) the result from the internal layering classification. The comparison between the two figures is made difficult by the fact that the velocity contours are not exactly identical due to slightly different velocity dataset. However, the similarities should be obvious enough for a comparison. Three boxes in white (Figure 5.22a) and turquoise (Figure 5.22b) mark the same three locations for ease of comparison. The island of continuous layers in Tributary 3 is remarkably well correlated with an area of low basal shear stress. Also the change in layer type in Tributary 7 fits well with an increase in basal shear stress. Furthermore, the change from visible upper layering to no layering correlates with the increase of basal shear stress in the main trunk. On the other hand the discontinuous line in Tributary 7 is not explained by the basal shear stress and neither is the discontinuous lines in Tributary 5 that coincide with an area of low basal shear stress.

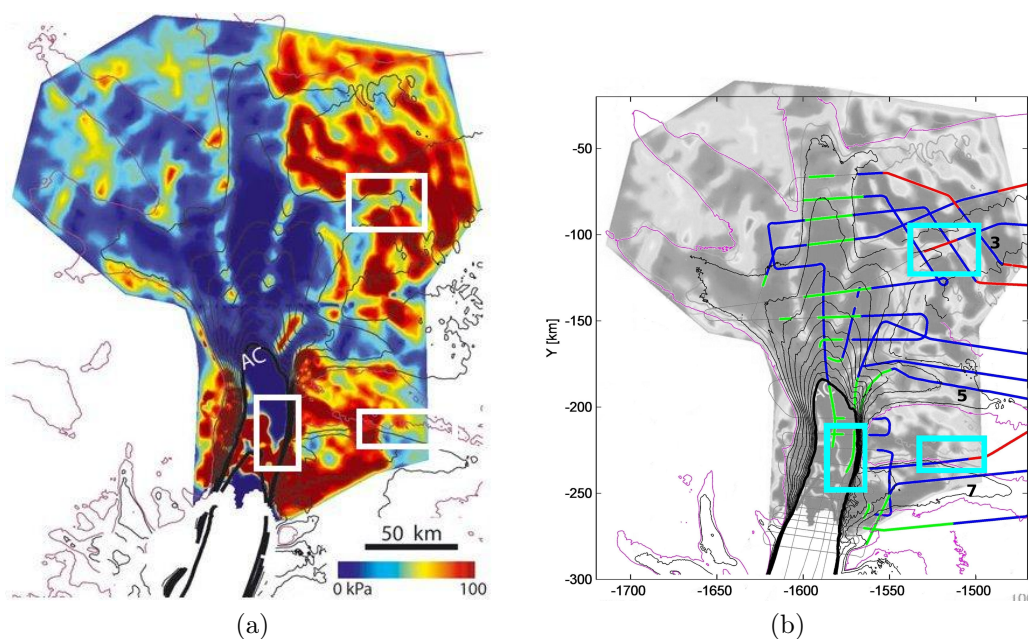


Figure 5.22: (a) Basal shear stress for Pine Island Glacier (Joughin et al., 2009, Figure 5a). Surface velocity is shown with a  $50 \text{ m yr}^{-1}$  contour (purple),  $100 \text{ m yr}^{-1}$  contours up to  $900 \text{ m yr}^{-1}$  (thin black), and  $1000 \text{ m yr}^{-1}$  contours (thick black). (b) Internal layering with surface velocity contours (from Rignot, 2006) with  $50 \text{ m yr}^{-1}$  contour (magenta),  $100 \text{ m yr}^{-1}$  contours up to  $900 \text{ m yr}^{-1}$  (thin black), and  $1000 \text{ m yr}^{-1}$  contours (thick black). Flightlines 10 - 14 are shown as thin grey lines, continuous layering in red, discontinuous in blue and lines where the pulsed radar data showed layering while the chirped data not are plotted as green lines.

Comparison between the basal shear stress and results from the quantitative layer classification is shown in (Figure 5.23). Again the general agreement be-

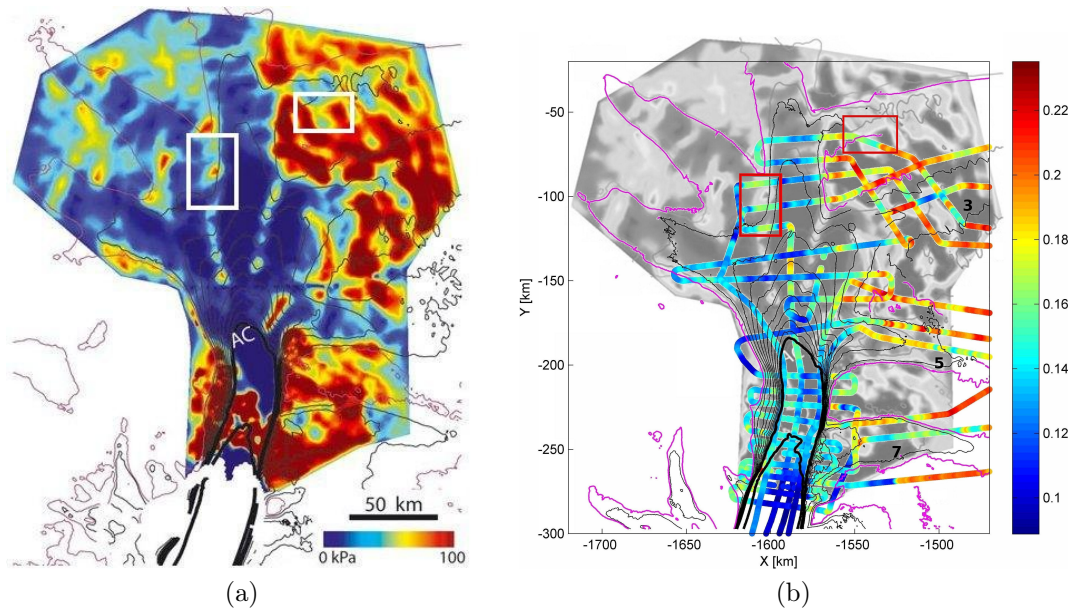


Figure 5.23: (a) Basal shear stress for Pine Island Glacier (Joughin et al., 2009, Figure 5a). Surface velocity is shown with a  $50 \text{ m yr}^{-1}$  contour (purple),  $100 \text{ m yr}^{-1}$  contours up to  $900 \text{ m yr}^{-1}$  (thin black), and  $1000 \text{ m yr}^{-1}$  contours (thick black). (b) Results from the quantitative classification of the internal layering in flightlines 10 - 14. High  $\psi$ -values (colours) indicate areas of continuous layering. Surface velocity contours (from Rignot, 2006) are shown with  $50 \text{ m yr}^{-1}$  contour (magenta),  $100 \text{ m yr}^{-1}$  contours up to  $900 \text{ m yr}^{-1}$  (thin black), and  $1000 \text{ m yr}^{-1}$  contours (thick black).

tween the two figures is very good and especially two areas are highlighted here. The small area of increased basal shear stress between Tributary 4 and the main trunk and between Tributaries 1 and 3 where an area of low basal shear stress correlates with an area of low  $\psi$ -values (grey boxes in Figure 5.23bc).

#### 5.4.2.2 Interpretation

The correlation between the continuity of the internal layering and the basal shear stress suggests that the internal layering reflects stress regimes in the ice. It also indicates that the anomalous island of continuous layering in Tributary 3 might be due to basal conditions such as low basal shear stress rather than change and/or migration of fast flow behaviour. Interestingly, Tributary 5 on the other hand has an area of decreased basal shear stress although all flightlines show discontinuous layers. It is therefore possible that a potential onset of higher shear stresses are occurring outside the area covered in the results. This in conjunction with the low deformational velocity (e.g. Figure 5.21) indicates that the disruption of the internal layering in this tributary is controlled by other factors, potentially a gradual change in velocity or high bed relief closer to the slow flowing areas.

## 5.5 Surface Roughness

In several flightlines the surface appeared to undulate with a wavelength of the scale tens of km and an amplitude of less than 10 m. The quantification of these undulations as surface roughness has been discussed in Section 4.2.3.

### 5.5.1 Results

The results of the quantification are shown in Figure 5.24. Figure 5.25 shows a zoom in on Tributaries 5 and 7 with a corresponding LIMA imagery (Landsat Image Mosaic Of Antarctica, data available from US Geological Survey), demonstrating that the method captures the overall surface undulations.

From Figure 5.24, the surface roughness is generally low in the main trunk except for an area just upstream of the grounding line. Some of the tributaries have areas of fairly high surface roughness (e.g. Tributaries 7 and 3) while other tributaries appear to have a very smooth surface topography on the spatial scales considered here (e.g. Tributary 5).

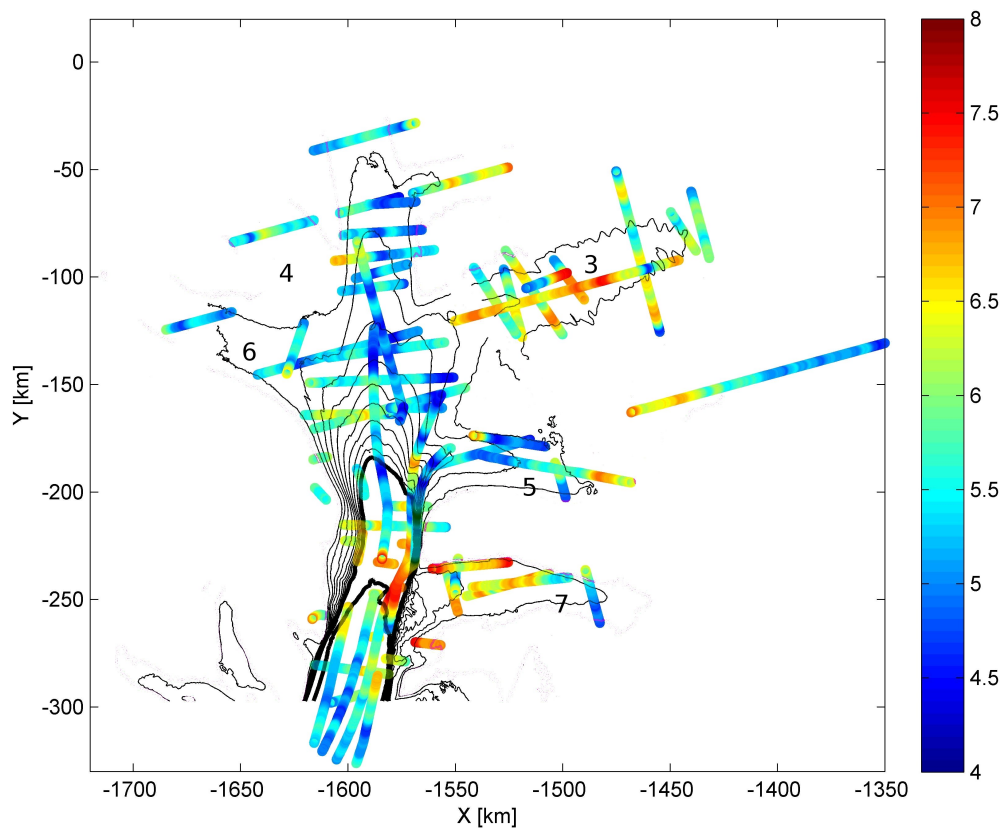


Figure 5.24: *Surface roughness on a logarithmic scale. The observed surface velocity contours are shown in black lines.*

Compared to the deformational velocity (Figure 5.20a) there are several similarities. Low surface roughness and low deformational velocity in Tributary 5, high surface roughness values in Tributaries 3 and 7 correspond to high deformational velocity and the area in the main trunk, just upstream of the grounding line, with high deformational velocity corresponds to the surface roughness increase as well.

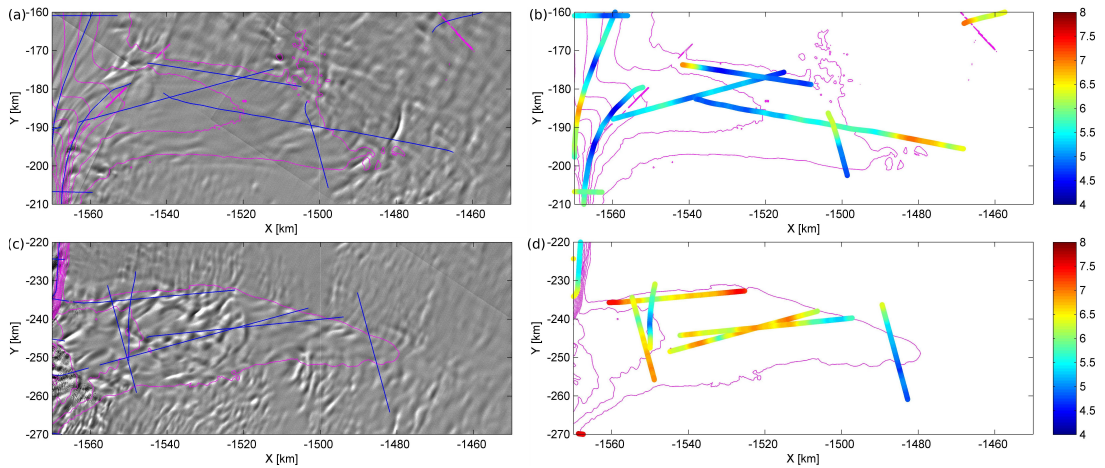


Figure 5.25: (a) and (c) LIMA data showing Tributaries 5 and 7 with surface velocity contours in magenta. (b) and (d) Surface roughness in Tributaries 5 and 7 on a logarithmic scale. The observed surface velocity contours are shown in magenta lines.

### 5.5.2 Comparison with Basal Roughness and Shear Stress

Although the mechanism behind the surface undulations is unknown, a comparison with basal roughness (Rippin et al., 2010, in press) and basal shear stress (Joughin et al., 2009) shows numerous similarities.

The basal roughness exhibits a very similar pattern as the surface roughness (Figure 5.26). A large part of the main trunk has low basal roughness and low surface roughness and the area close to the grounding line with high basal roughness corresponds to the area with high surface roughness as well. Tributary 5 that exhibited low surface roughness has a corresponding low basal roughness while Tributaries 3 and 7 have high basal and surface roughness. Interestingly the line that continues furthest to the south has decreasing surface roughness but that trend is not found in the basal roughness map.

Figure 5.27a shows the surface roughness with grey boxes highlighting areas of high correlation with the basal shear stress map (green boxes in Figure 5.27b). Box number 1 in Figure 5.27b shows an area close to the grounding line where the basal shear stress increases abruptly. The extent of the area of increased

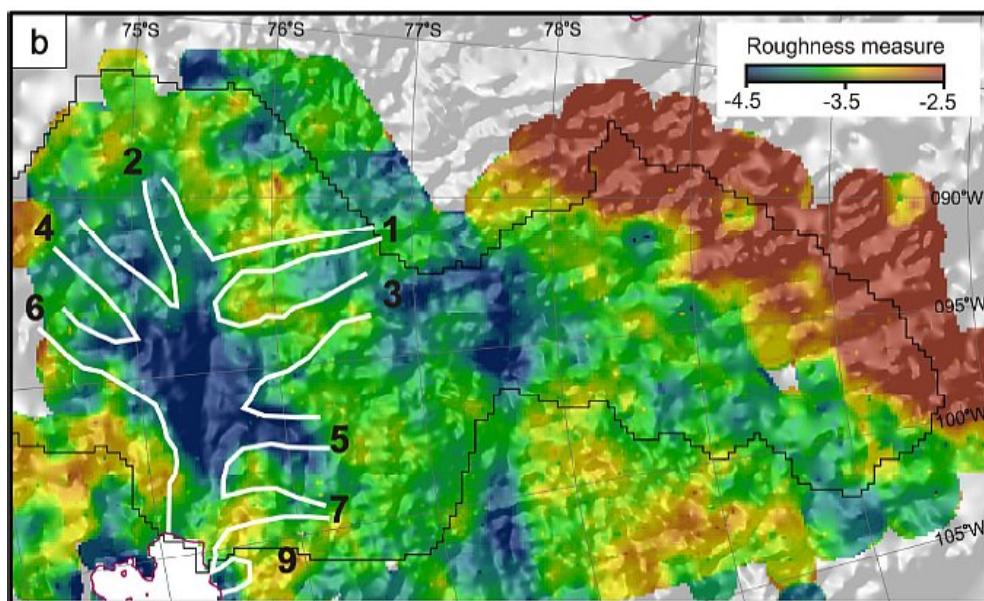


Figure 5.26: Basal roughness from (Figure 4b Rippin et al., 2010, in press).

basal shear stress corresponds well with the change in surface roughness. In Tributary 7 (box number 2) an area of low basal shear stress close to the main trunk surrounded by high basal shear stress fits with a small area of low surface roughness. In box number 3 (upstream of box number 1) a small area of localised high basal shear stress in the main trunk corresponds to an increase in surface roughness. The same can be observed in at the margin of Tributary 5 (box number 4). Tributary 3 displays a more complex pattern of changing basal shear stress (box number 5), this is mirrored by changing areas of high and low surface roughness values, however, comparison is made difficult by the difference in velocity contour plots. In Tributary 1 the transition from high to low surface roughness values correspond to the decrease in basal shear stress as the tributary enters the main trunk (box number 6). Finally, box number 7 between Tributaries 2 and 4 contains a small area of increased basal shear stress that corresponds to a localised increase in basal shear stress.

### 5.5.3 Interpretation

The comparisons between the surface roughness, deformational velocity, basal roughness and basal shear stress indicate that the surface roughness is linked in some way to ice flow mode and basal conditions. Although there is a correspondence between high surface roughness and deformational velocity, it is worth emphasising that the observed surface velocity exceeds the deformational velocities in all the areas discussed here. This is in agreement with studies that have

found that undulations in subglacial topography are most prominently reflected in the surface topography when the basal motion is large compared to the motion caused by internal deformation (Thorsteinsson et al., 2003; Gudmundsson, 2003). Thus areas of high surface roughness likely correspond to areas where the basal motion is high.

The transition in flow velocity might take place as a change from ice flow dominated by internal deformation, to a combination of deformation and basal sliding, to a flow mode where the motion is purely basal sliding. This explains the low surface roughness values in the single line furthest to the south in Figure 5.24 where velocity would be low enough for ice flow mode to be dominated by internal deformation. An increase in basal sliding in the tributaries would lead to an increase in surface roughness if the bed is rough and then a decreasing surface roughness when the bed topography becomes smooth causing the glacier to speed up significantly. The transition to very high basal motion corresponds to the low basal shear stresses. To summarise, areas of very fast flow and low basal roughness (e.g. the main trunk) correspond to low surface roughness, areas of fast/enhanced flow and high basal roughness exhibit a high surface roughness and slower flowing areas have low surface roughness.

Unfortunately due to the limited InSAR velocity coverage it was very difficult to establish whether flightlines were perpendicular or parallel to the ice flow in the area away from the main trunk. No further data analysis could therefore be carried out closer to the slow flow areas.

This analysis also highlighted the difference in flow mode and basal conditions between Tributaries 3 and 7 and Tributary 5. While Tributaries 3 and 7 exhibit high basal shear stress and high surface roughness, Tributary 5 has low basal shear stress and low surface roughness values. Surface roughness measurements south of Tributary 5 indicate that a potential increase in basal shear stress is taking place further towards the slow flowing area. This could indicate that Tributary 5 provides a smooth, fast flowing transport system on an easily deformable bed for ice originating further upstream.

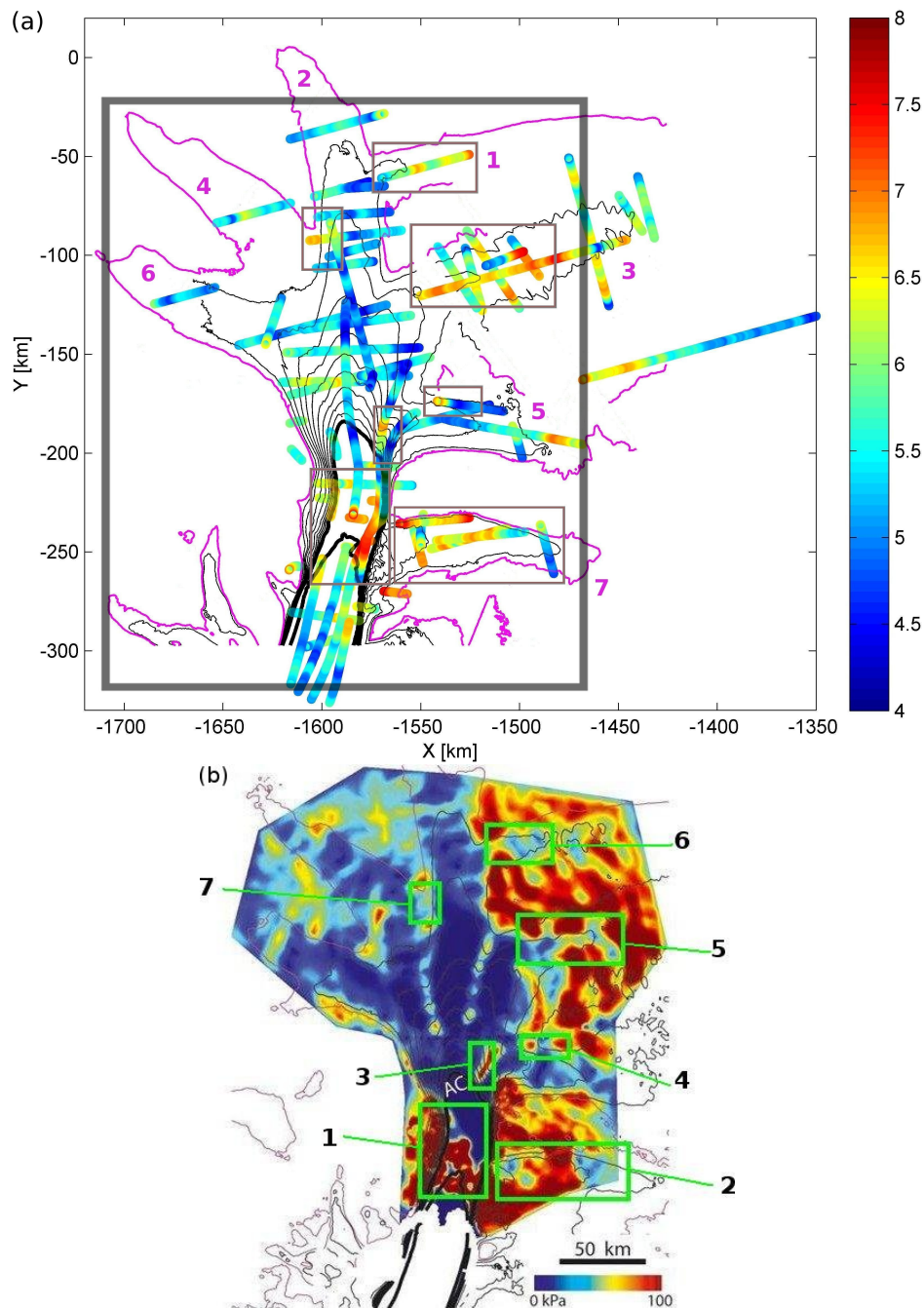


Figure 5.27: (a) Surface roughness values (colours). The surface velocity contours are similar to Figure 5.23. Thin grey boxes correspond to boxes outlined with green in Figure (b) and numbers in purple refer the tributaries. The large thick grey box corresponds roughly to extent of (b). (b) Basal shear stress for Pine Island Glacier (Joughin et al., 2009, Figure 5a). Green boxes correspond to boxes outlined with thin grey in (a).

## 5.6 Discussion

The flightlines in the main trunk and in the tributaries north and east of the main trunk (Tributaries 1, 2, 4 and 6) were either completely devoid of internal layering or contained discontinuous layers. Considering the fast flow of the ice in conjunction with the low deformational velocity, low basal shear stress and low basal roughness it is likely that the flow in these areas is dominated by basal sliding and streaming flow (Joughin et al., 2009). This is in agreement with the fact that necessary conditions for streaming flow often are coupled to the presence of sediments with low shear strength (Bindschadler et al., 2001a). Thus the findings of this thesis agree with the proposed link between disruption of internal layers and the occurrence of streaming ice flow (e.g. Jacobel et al., 2000; Rippin et al., 2003b), which has been observed in numerous other ice streams, for example, the Siple Coast ice streams (e.g. Siegert et al., 2003b).

Similarly the occurrence of continuous layers in primarily slow flowing areas also agrees with this hypothesis. Their presence indicates that since the time of their deposition the ice flow has not been sufficiently fast to disrupt the layers (e.g. Conway et al., 2002; Siegert et al., 2003b). Thus while one part of the northern basin of PIG exhibits highly dynamic behaviour, the part that is furthest to the south has not experienced any significant changes in spatial pattern of ice flow. Other studies have found similar continuous layering in slow flow areas next to areas with faster flow (e.g. Rippin et al., 2006) emphasising the basal control on ice flow patterns (e.g. Vaughan et al., 2003; Peters et al., 2006).

Only one slow flowing area exhibited disrupted and missing layering, which was interpreted to potentially be due to a build up of stresses caused by the fact that the ice is flowing over a bed high. Whether or not such a build up of stress is possible is uncertain, however, the decrease in ice thickness must cause the internal layers to be “squeezed” together, which may account for some of the disruption (Ng and Conway, 2004). A study by Ng and Conway (2004) identified disrupted layering in Kamb Ice Stream due to compression and longitudinal stretching as ice thickness decreased along flow. A study of Rutford Ice Stream found disrupted layering associated with a build up of stresses due to the ice flowing around a sharp bend (King, 2009). However, in both studies ice flow velocities were significantly higher than in the area considered here.

Comparing the location of the disrupted layering with modelled balance velocities (black box in Figure 5.28) does not shed further light on their origin since the balance velocities also indicate a slow flow area. Thus the cause of the disrupted layering might only be resolved by modelling the complete stress regime

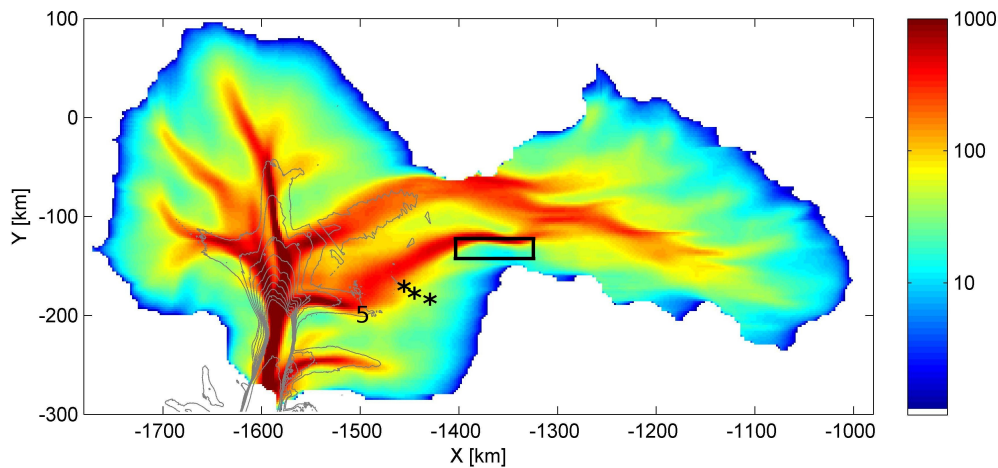


Figure 5.28: Balance velocities ( $m\,yr^{-1}$ ) on a logarithmic scale calculated by the BASISM model (See Chapter 6). Observed surface velocities have been contoured as grey lines. The black box indicates the area with disrupted layering with depth and the black stars show the location of the transition from continuous to discontinuous layering.

of the area, an undertaking that is beyond the scope of this thesis.

In Tributary 3 the qualitative analysis identified an anomalous island of continuous layering in a slow flowing area, this was supported by the low  $\psi$ -values in the quantitative results for the area. Similar islands of continuous layers in enhanced flow regions have been identified in a study of Wilkes Land by Rippin et al. (2003b), but the islands in that study were found to correlate with shallower ice thicknesses compared to the surrounding disrupted areas. The island observed in the PIG dataset, however, is located in an area with relatively deep ice, and it therefore seems unlikely that the anomalous layering found here can be attributed to the same process. Previous studies have also suggested that this kind of layering could be evidence of migration of the onset of fast flow (Whillans et al., 1987; Bindschadler et al., 2001b). The anomalous layering in Tributary 3 could therefore indicate a change in the location of the tributary over the period within which the layering formed. This is supported by the identification of an area of buckled layering upstream in the tributary. The presence of buckled layering at depth has also been found in Whillans Ice Stream and interpreted as an indication of a change in flow direction, potentially even a shutdown, of enhanced ice flow (Conway et al., 2002). It has also been observed in, for example, the neighbouring Kamb Ice Stream, indicating a change in flow direction (Conway et al., 2002). Thus the buckled layering indicates that the onset of enhanced flow in Tributary 3 once have extended further upstream than at present.

Further studies showed, however, that the location of the continuous island in

Tributary 3 corresponds to an area of low deformational velocity and decreased basal shear stress (Joughin et al., 2009) indicating that the continuous layering in Tributary 3 could be tied with basal conditions as well. It is possible that at the time of deposition of the layers, the flow of Tributary 3 was sufficiently slow to preserve the internal layer stratigraphy. Later, when the flow velocity increased, the ice flow had transported the layers downstream to an area of low basal shear stress where the layering was not disturbed significantly due to negligible ice deformation.

These seemingly contradictory results highlight the complexity of the flow regime in Tributary 3. Some of the contradictions in the results may be resolved if a time-scale was available for the PIG basin. For example, since the buckled layering was identified in relatively deep ice it could be a relict of a past enhanced flow feature that shut down before the continuous layering was formed in Tributary 3.

Like Tributary 3, Tributary 5 appears very well constrained by the deep subglacial trough under the tributary. However, Tributary 5 exhibits other characteristics that sets it apart from Tributary 3. The qualitative method identified the transition from continuous to discontinuous layering to be further away from the onset of enhanced flow in Tributary 5 than for the other tributaries, although it is worth noting that the  $50 \text{ m yr}^{-1}$  velocity contour is less clear for this tributary obscuring the location of the onset of tributary flow. Simultaneously the quantitative method did not show any clear transition in layer type indicating that for the layers in Tributary 5 the onset of enhanced flow is, or has been until recently, too gradual to cause a sharp transition in layer type.

The area with discontinuous layers in Tributary 5 coincides with an area of low deformational velocity and low basal roughness and shear stress (Joughin et al., 2009; Rippin et al., 2010, in press). This indicates that Tributary 5 may provide a smooth, fast flowing transport system on an easily deformable bed for ice originating further upstream. When compared to the balance velocities (Figure 5.28) this hypothesis is supported by the fact that high velocities are predicted far upstream of Tributary 5, indicating that this tributary could act as the main channel for transporting ice from the interior of the southern basin.

The observation of discontinuous layering coinciding with low basal roughness in and upstream of Tributary 5 agrees with studies of the ice streams on Siple Coast. In the studies continuous layering was mainly found in areas of slow flow and high basal roughness, while discontinuous layers were more likely to be situated in areas of enhanced flow, which often coincided with low basal roughness

(Siegert et al., 2003b, 2004a).

The location of the discontinuous layering indicates that the onset of the layer disruption is occurring towards the south (i.e. close to the neck between the northern and the southern basin). Unfortunately measurements of basal shear stress (Joughin et al., 2009) did not extend far enough south to identify a potential location for the onset of layer disruption while the basal roughness study (Rippin et al., 2010, in press) did not display any significant change. The single measurement of surface roughness that extends towards the south displays an increase in surface roughness just upstream of the tributary which might indicate that internal stresses are high enough that significant layer disruption could take place.

Another interesting area with discontinuous and missing layers, and exhibiting anomalously low  $\psi$ -values, was identified west of Tributary 7. This area is currently relatively slow flowing and the occurrence of discontinuous and missing layers may indicate that the flow has been faster in the past and/or the margin of the tributary has migrated as has been observed in, for example, Kamb Ice Stream (Raymond et al., 2001). The deformational velocity in the area is uniformly high underlining the fact that the location of Tributary 7 appears less constrained than, for example, Tributaries 3 and 5, and has no well-defined subglacial topography. Work by Bindschadler et al. (2001a) showed that the onset of fast flow is controlled to a large extent by basal conditions, and they argued that in a region with no obvious optimum site for onset of fast flow, the onset is more likely to jump to a new location if conditions such as accumulation rates or the presence of subglacial water change. It might be possible that there is no such optimum site for onset of enhanced/fast flow in Tributary 7, making migration of the margin possible.

If Tributary 7 indeed has migrated in the past then it would seem likely that a change in flow dynamics in the future is possible. It also indicates that there is a possibility for a much more dynamic flow pattern in this area of PIG, with enhanced flow features shutting down or re-appearing, similar to that observed on, for example, the Siple Coast (Siegert et al., 2003b).

Thus while the subglacial topography controls the location of the main trunk and some of the tributaries, at least one tributary (Tributary 7) has the potential to migrate and both Tributaries 3 and 5 exhibit signs that the possibility exists for enhanced flow to take place further upstream than at present.

## 5.7 Conclusion

This chapter has presented and discussed the results from the radar data analysis. In the internal layer classification it was found that the current flow regime could explain the majority of the observed internal layers. This conclusion was supported by results from both the qualitative and the quantitative classifications.

A few findings suggest changes in the onset of enhanced flow in Tributary 3 although the basal conditions of the tributary also is likely to influence the layer stratigraphy. The identification of an area of buckled layering upstream of Tributary 3 further indicated that the onset of enhanced flow have extended further upstream in the past. Other observations indicated the possibility for migration of Tributary 7. Furthermore, Tributary 5 was found to have widespread discontinuous layering which in combination with significantly lower basal shear stress indicates that the tributary provides a smooth tunnel for ice flowing from further upstream.

The quantitative method showed good agreement with the results from the qualitative method. The transition in layer type was captured for most of the areas and a gradual decrease in  $\psi$ -value was found to correspond to gradual changes in layering. The results also highlighted areas where the results from the qualitative method could be interpreted differently.

Finally, a comparison between the stress regime and the internal layering showed a clear correlation between changes in layering in several areas and basal shear stress. The same was found to be true between the surface roughness and the basal shear stress indicating a potential method for a first indication of areas of weak or strong beds.

Although the results above have returned several interesting insights into the dynamics of PIG, most of the insights have been qualitative but have not yielded any information of, for example, the time scale of the layering or the past processes that have influenced. This will be addressed in the following chapters with the help of ice flow modelling.



## Chapter 6

# Investigating Internal Layering with a Three-Dimensional Model

The primary aim of modelling internal layers in PIG is to retrieve information on the parameters that control the geometry of the layers. These parameters will have had an important impact on the past and present evolution of PIG, thus leading to a better understanding of the glacier.

The BASISM model, that is the focus of this chapter, has been described in more detail in Section 4.3.1. This chapter contains the results from applying the model to the internal layers observed in the PIG dataset. Section 6.1 describes the modelling approach. Section 6.2 contains the results from fitting the observed layers to the model individually, Section 6.3 contains the results from fitting the tephra layer and in Section 6.4 a layer package is used to estimate the patterns of accumulation and basal melt. The question of estimating accumulation values and thus the age of the layers is addressed in Section 6.5. Finally the results are discussed in Section 6.6.

### 6.1 Modelling Approach

Several approaches were taken in order to fit the modelled layers with observations. The layers were both fitted individually to the output or, where it was possible, correlated across flightlines to increase the spatial extent of the internal horizon. This section contains a description of the layer data that have been used in the study, the parameters that are investigated and how the fit of the model has been quantified.

### 6.1.1 Layer Fitting

As discussed in Chapter 5 the BAS-UTIG dataset from PIG displays different kinds of internal layers, some are continuous and can be traced over some distance while in other areas the layers are very discontinuous and can hardly be traced at all. All layers that were traced using the semi-automatic tracing routine (see Section 4.2.3.1) were later converted to normalised elevation to use as input in the BASISM model. Using the built in layer fitting algorithm the best fitting modelled layer was then calculated. Due to the nature of the radar data it proved difficult to identify the same internal reflector in different flightlines and thus correlate layer elevations between flightlines. The layers were therefore initially fitted individually to the model output. In two areas, however, it was possible to identify the same layers in multiple flightlines providing a better constraint on the flow model. This was the case for the tephra layer (see Section 5.1) north of the main trunk that could easily be identified in several flightlines (Figure 6.1, red lines). Furthermore, close to the field camp a distinct package of layers (green lines in Figure 6.1) was identified and a three-dimensional map of the layer elevations in that area could be constructed (cf. Section 5.3.2). This provided a better constraint on the layer fitting in the model, since the spatial extent of the layers was thus no longer limited to one single flightline.

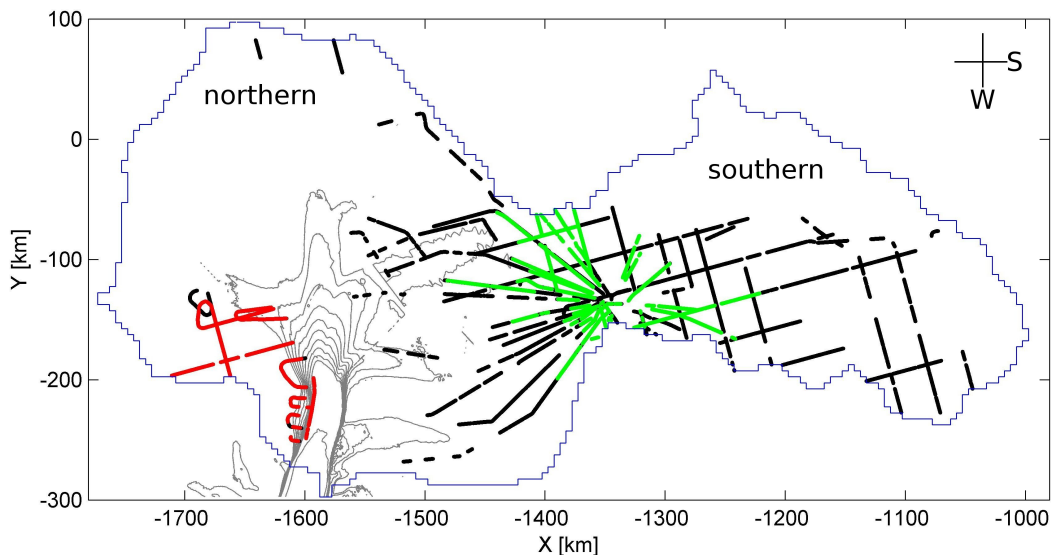


Figure 6.1: Map of all layers traced in the PIG basins (black lines), the layers that are part of the layer package (green lines) and the tephra layer (red lines). The catchment basin is outlined in blue and surface velocity contours in grey ( $100 - 1000 \text{ m yr}^{-1}$ ,  $2000 \text{ m yr}^{-1}$  and  $3000 \text{ m yr}^{-1}$ ).

### 6.1.1.1 General Layer Fitting

First the overall goodness of the model fit to the observed layers was considered. Over 300 layers were picked from 11 different flightlines (Figure 6.1). Although internal layering was to some extent visible in all flightlines a lot of those flightlines were outside the PIG catchment basin and were therefore not considered here. Not every single internal layer was picked in every radargram but rather the most easily identifiable and the ones easiest to trace. Also the longest traceable layer was always consistently picked. In some areas, however, no layers have been traced; This applies to the main trunk, where generally no layers were observed, and in the parts where only short layer fragments were visible, often due to high bed relief (see Section 5.1).

### 6.1.1.2 Tephra Layer

In one area in the PIG dataset one internal layer, identified by Corr and Vaughan (2008) as a highly-reflecting tephra layer, could be correlated between flightlines (see Section 5.1). Based on the depth of the tephra layer its age was estimated to coincide with a strong acidic signal in the Siple Dome ice core dated to 325 BC. The tephra layer is situated north of the main trunk (red lines in Figure 6.1) but disappears as the flightlines enter the very fast flowing areas. Where present the layer was easy to identify and thus allowed for a correlation of the layer depth between flightlines.

### 6.1.1.3 Layer Package

In several flightlines it was possible to identify a layer package consisting of one strongly reflecting layer with a “diffuse” layer below it and then two more strongly reflecting layers below that layer (see Section 5.3.2). The layer package was mainly observed in the neck between the southern and the northern basin (Figure 6.1, green lines). In the following the top layer will be referred to as Layer 1 and the upper of the two lower layers will be referred to as Layer 2 (as per Section 5.3.2). Figure 5.17a in Section 5.3.2 shows an example of a radargram where this layer package is visible. Since the layer package was identified in multiple flightlines it was possible to correlate the layer elevations and construct three-dimensional gridded surfaces of the internal ice sheet structure. Compared to the tephra layer, the layer package is likely to be older due to its lower elevation and thus represents not just a different part of the catchment basin but also a different depositional and deformational history.

## 6.1.2 Parameter Choices

The aim of the layer fitting is to obtain a good fit for the layer stratigraphy not the age of the layers, mainly because very little information concerning the age-depth relationship for the PIG basin is available. The model was run using different model parameters and in the following each run with a different parameter will be referred to as a scenario. A summary of the different scenarios can be found in Table 6.1.

### 6.1.2.1 Surface and Bed Topography

The model uses surface and bed topography from Vaughan et al. (2006) that have been resampled to a resolution of 2 km from the original resolution of 1 km due to computational limitations. The surface topography was further smoothed by an order of several ice thicknesses (e.g. approximately 10 km) to ensure that the gradient of the surface elevation is smooth (Figure 6.2). This was necessary because the model relies on the surface to calculate the balance velocities. If the gradient is not smooth this may lead to areas where the ice is flowing into but not out of the area.

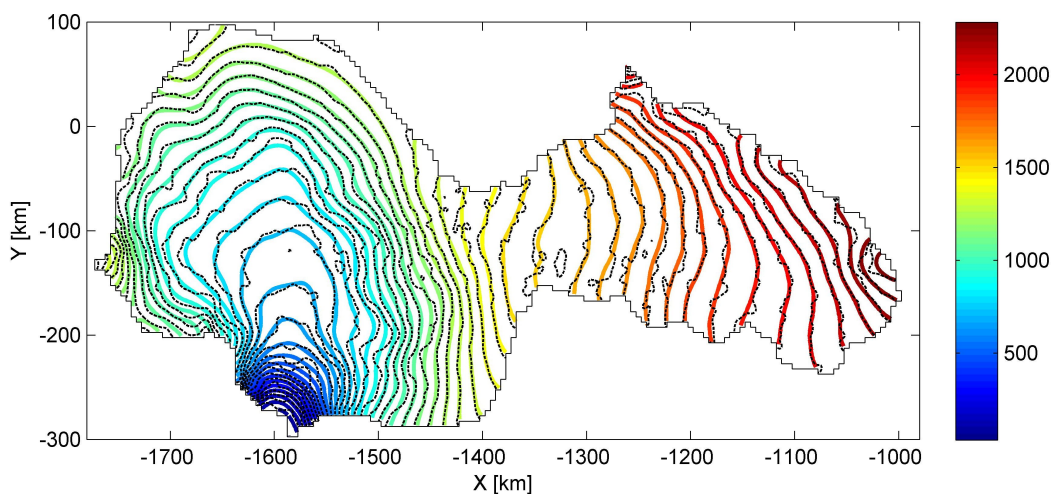


Figure 6.2: *Surface topography map in metres showing the 1 km resolution from Vaughan et al. (2006) (dashed black lines) and the smoothed, resampled topography used in the model (coloured lines).*

The shape of the internal layers is influenced by both large- and small-scale variations in the bed topography. The difference in resolution is approximately two orders of magnitude between the smoothed, gridded bed topography used in the model ( $\Delta_{xy} = 2$  km) and the picked bed topography in the radar data ( $\Delta_{xy} = 30$  m). In other words, the model will be unable to fit the small-scale variations of the layers. This is difficult to avoid due to the fact that the resolution

of the bed topography will be very high along the flightlines but significantly lower between flightlines. The aim was therefore to get the large-scale variations and the overall slope of the layers correct. In order to minimise the signal from the small-scale and large-scale differences between the smoothed, gridded bed topography and the picked radar bed topography a new bed topography map is constructed. First a gridded bed map was constructed based on the radar data that passed through all the data points. The new bed topography map was constructed such that points were assigned values from the gridded radar data if they were closer than 15 km to a flightline, points further away than 30 km from a flightline were assigned values from the gridded bed topography map by Vaughan et al. (2006), and points in between were assigned the mean of the two maps. The new map was then smoothed by a 6 km x 6 km smoothing matrix.

All scenarios described below use this surface and bed topography.

#### 6.1.2.2 Control Scenario

First a control scenario was set up against which subsequent scenarios were tested. The control scenario is based on the following inputs: uniform accumulation of  $1 \text{ myr}^{-1}$ , uniform basal melting of  $0.01 \text{ myr}^{-1}$  (1% of accumulation rate), plug flow, horizontal resolution of 2 km and a vertical resolution of 11 points.

#### 6.1.2.3 Accumulation Pattern

While the age of the layers depend on the value of the mass balance, their stratigraphy depends on the geometry of the ice sheet and the spatial pattern of the mass balance (e.g. Parrenin et al., 2006; Leysinger Vieli et al., 2007). Since the accumulation value works as a scaling factor without influencing the stratigraphy of the layers, the actual value of the accumulation is of less significance than the accumulation pattern (Leysinger Vieli et al., 2007). The scenarios with variation in accumulation are therefore aimed at investigating different plausible accumulation patterns not the value of the accumulation rate.

Two scenarios were tested where the accumulation pattern was changed to reflect a more realistic scenario than uniform accumulation. The first scenario used the modern day accumulation pattern (shown in Figure 6.3a) calculated by Arthern et al. (2006). It is important to note that the modern day accumulation map taken from Arthern et al. (2006) represents a heavily averaged value on the scale of 60 km but Arthern et al. (2006) emphasise that small scale variations of the accumulation might be misrepresented in their accumulation map, and that individual point measurements may have variations up to 30%. It was therefore

| Scenario      | Parameters   | Notes  |
|---------------|--|--|
| Control       | $a = 1 \text{ m yr}^{-1}$ , $m = 0.01 \text{ m yr}^{-1}$ ,<br>$\Delta_{xy} = 2 \text{ km}$ , $\Delta_{\zeta} = 11$ , plug flow | all uniform  |
| Accumulation  | $a$ from Artlorn et al. (2006)<br>$a$ linearly decreasing with surface elevation   | remaining parameters as control  |
| Basal melting | $m = 0.1 \text{ m yr}^{-1}$ (10%) for $H > 2500 \text{ m}$   | remaining parameters as control  |
|               | $m = 0.1 \text{ m yr}^{-1}$ (10%) for $H > 2750 \text{ m}$   | remaining parameters as control  |
|               | $m = 0.1 \text{ m yr}^{-1}$ (10%) for $H > 3000 \text{ m}$   | remaining parameters as control  |
|               | $m = 0.5 \text{ m yr}^{-1}$ (50%) for $H > 2500 \text{ m}$   | remaining parameters as control  |
|               | $m = 0.5 \text{ m yr}^{-1}$ (50%) for $H > 2750 \text{ m}$   | remaining parameters as control  |
|               | $m = 0.5 \text{ m yr}^{-1}$ (50%) for $H > 3000 \text{ m}$   | remaining parameters as control  |
| Ice flow mode | Plug flow<br>Internal deformation  | (corresponds to the control scenario)<br>remaining parameters as control |
| Resolution    | $\Delta_{xy} = 4 \text{ km}$   | remaining parameters as control  |
|               | $\Delta_{\zeta} = 21$  | remaining parameters as control  |
|               | $\Delta_{\zeta} = 31$  | remaining parameters as control  |

Table 6.1: Model scenarios with varying accumulation ( $a$ ), basal melt ( $m$ ), horizontal and vertical resolution ( $\Delta_{xy}$  and  $\Delta_{\zeta}$ ).  $H$  denote ice thickness.

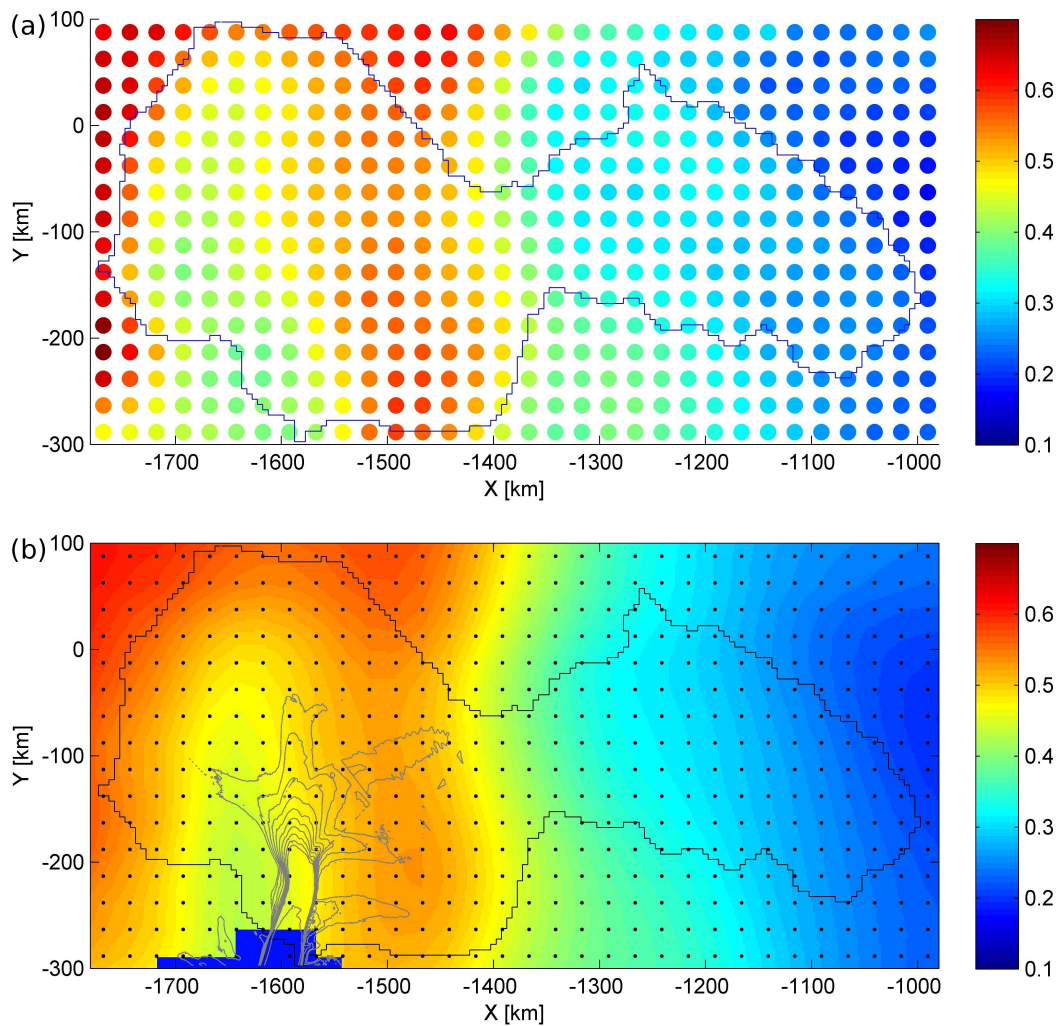


Figure 6.3: *Accumulation in  $\text{myr}^{-1}$  of ice (assuming a density of ice of  $918 \text{ kg m}^{-3}$ ). (a) shows the original dataset from Arthern et al. (2006) with the PIG catchment basin in blue and (b) the smoothed, gridded version of the data from Arthern et al. (2006) with the original data points as black dots, the surface velocity in grey contours.*

the overall spatial variation of the accumulation pattern, and not the individual point values, that was considered. The accumulation values were interpolated and smoothed on to a grid of the same resolution as the surface and bed topography (see Figure 6.3b).

A second method for constructing a plausible accumulation pattern is to assume that the accumulation decreases with increasing surface elevation. This was included in the model method very simply by letting the accumulation decrease linearly with surface elevation (Figure 6.4). A more correct approach would have been to use the correlation between saturation vapor pressure and temperature described by Robin (1977) and the Clausius-Clapeyron equation to get an exponential relation between accumulation  $a$  and temperature  $T$ :  $a \propto \exp(1/T)$

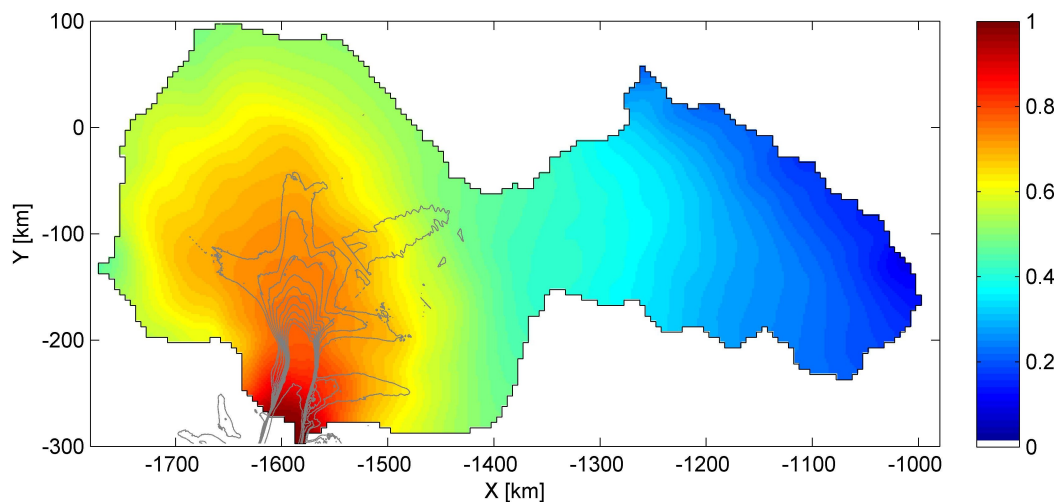


Figure 6.4: Accumulation in  $\text{m yr}^{-1}$  of ice (assuming a density of ice of  $918 \text{ kg m}^{-3}$ ) based on linearly decreasing accumulation with increasing surface elevation.

(Arthern et al., 2006). However, compared to measurements (e.g. Figure 6.3) the assumption of a linearly decreasing accumulation was deemed to be representing actual conditions accurately enough. In the scenario the accumulation is scaled such that it has its maximum value ( $1 \text{ m yr}^{-1}$ ) at minimum elevation and its minimum value ( $0 \text{ m yr}^{-1}$ ) at maximum elevation. Compared to the accumulation values from Arthern et al. (2006), where the accumulation ranges from  $0.1 \text{ m yr}^{-1}$  to  $0.6 \text{ m yr}^{-1}$ , these values are slightly higher, however of the same magnitude as that of the control scenario with a uniform accumulation of  $1 \text{ m yr}^{-1}$ .

#### 6.1.2.4 Basal melting

In the control scenario the basal melting is assumed to be uniform, however, it seems likely that melting at the base would have a spatial variation. Since ice works as an insulating material the geothermal heat flux at the base of the ice causes the temperature in a glacier to increase with ice depth (e.g. Figure 2.7a in Section 2.3.3). This, in combination with a decrease in melting point due to high pressure, leads to basal melting (see Sections 2.3.2 and 2.3.3). At the same time, the geothermal heat flux could be higher in some areas than others. This is supported by evidence that suggests that volcanic activity has been and still is occurring under the West Antarctic Ice Sheet (e.g. Blankenship et al., 1993; Behrendt et al., 1998). The observation of several lake-type reflectors in the PIG basin further supports this (Figure 5.5, Section 5.1.1).

The temperature at the bed of the ice can be estimated using the heat equation (Equation 2.14 from Chapter 2.4). For simplicity the heat generated by

deformation and friction of the ice is disregarded and the equation is re-written into a one-dimensional problem describing the distribution of temperature with ice thickness. This provides an estimate of the possible temperature ranges in the ice (e.g. Hindmarsh, 1999). The equation then reads:

$$\frac{\partial \theta}{\partial t} = \frac{k_i}{\rho c_p} \frac{\partial^2 \theta}{\partial z^2} \quad (6.1)$$

Where  $c_p$  is the heat capacity of ice,  $\theta$  is the ice temperature and  $k_i$  is the thermal conductivity. Note that the heat conductivity and the heat capacity are assumed to be constant in time and with depth. For this purpose the temperature is assumed not to vary with time. This leads to a straightforward, second order, differential equation that can easily be solved using the boundary conditions:

$$\frac{\partial \theta}{\partial z} = -\frac{Q}{k_i} \quad (6.2)$$

Where  $Q$  is the geothermal heat flux, thus the boundary condition represents the heat gradient. The second boundary equation is:

$$\theta(z = H) = \theta_s \quad (6.3)$$

Where  $\theta_s$  denotes the surface temperature. This leads to a linear relation between the temperature and the depth  $z$

$$\theta(z) = \theta_s + \frac{Q}{k_i}(H - z) \quad (6.4)$$

where  $H$  denotes ice thickness. More information on calculating the distribution of temperature in ice can be found in, for example, Hindmarsh (1999) and Larsen and Dahl-Jensen (2000). The thermal conductivity of pure ice is  $k_i = 2 \text{ W m}^{-1}\text{K}^{-1}$  (Paterson, 2002). Studies have suggested that the geothermal heat flux  $Q$  is likely to be between 80 and 125  $\text{mW m}^{-2}$  (Shapiro and Ritzwoller, 2004) for West Antarctica. Using the lower value of that range returns a geothermal gradient  $Q/k_i = 0.04 \text{ K m}^{-1}$ . With an average surface temperature of  $-30^\circ\text{C}$  (cf. Comiso, 2000) ice thicknesses only needs to be close to 1 km for the temperature to rise above zero. However, the ice does not need to reach zero degrees to melt, since the pressure melting point of ice decreases by  $8.7 * 10^{-4}$  degrees per metre ice, corresponding to melting at approximately  $-0.9^\circ\text{C}$  for ice thicknesses over 1 km (Paterson, 2002). It is in other words very likely that melting is taking place at the base of the ice as has been observed in numerous locations across Antarctica (e.g. Bell, 2008; Smith et al., 2009).

Note: in the model the geothermal gradient is set equal to  $Q/k_i = 0.021 \text{ K m}^{-1}$  corresponding to a geothermal heat flux of  $Q = 0.042 \text{ W m}^{-2}$ . This value, however, does not influence the basal melting.

Assuming that basal melting is caused by insulation due to large ice thicknesses, six different model scenarios were tested assuming increased basal melting of 10% and 50% of the accumulation rate respectively, for three different spatial distributions: areas with an ice thickness above 2500 m, 2750 m and 3000 m.

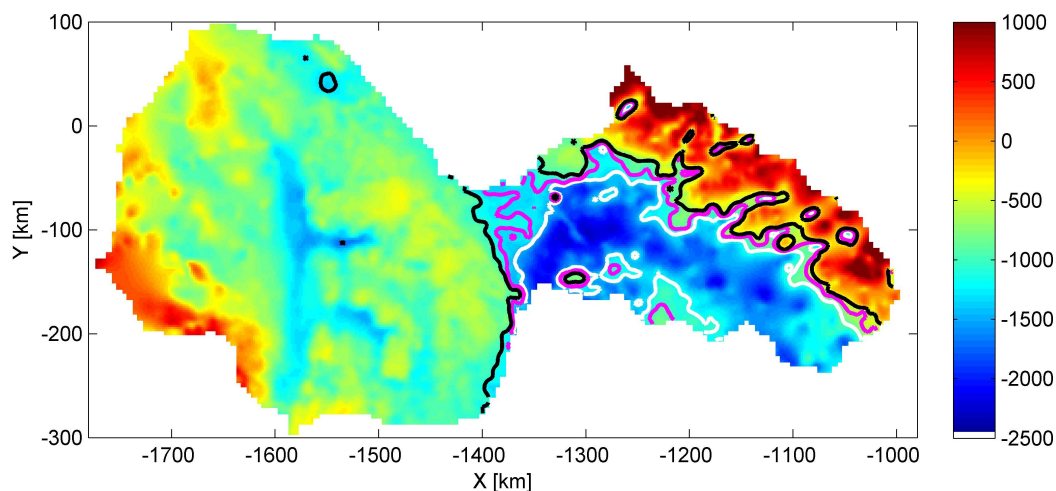


Figure 6.5: *Bed topography with lines contouring potential areas of increased melting for ice thicknesses above 2500 m (black lines), 2750 m (magenta lines) and 3000 m (white lines).*

### 6.1.2.5 Flow Mode

In order to test if a change in flow mode from plug flow (i.e. sliding over the bed) to internal deformation will affect the modelled layers (e.g. Hindmarsh et al., 2009) a scenario was run with internal deformation in the entire basin (in contrast to the control scenario with plug flow in the entire basin).

### 6.1.2.6 Vertical and Horizontal Resolution

Three scenarios were compared to test the impact of the vertical resolution on the model fit and thus the robustness of the results. The runs were made with number of vertical points changing from 11 to 21 to 31, corresponding to each vertical grid cell covering 10%, 5% and 2.5% of the ice column. Similarly the sensitivity to horizontal resolution was tested by changing the resolution from a 2 km to a 4 km grid.

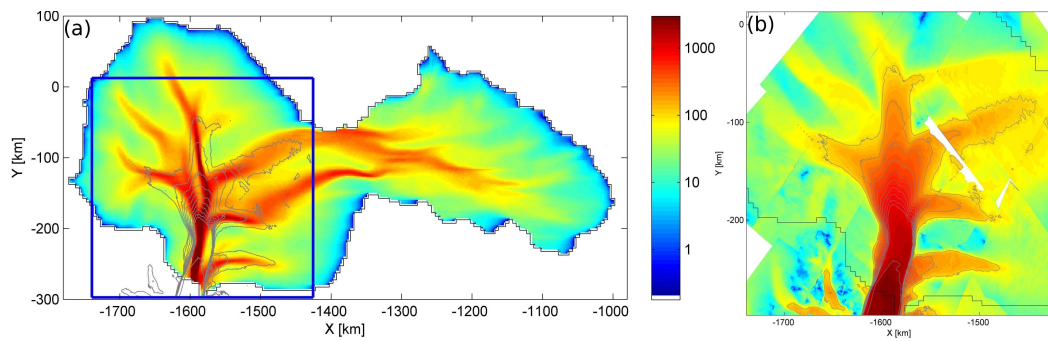


Figure 6.6: (a) Balance velocities calculated by the BASISM model, the blue box outlines (b) InSAR velocities from Rignot (2006). Both images are on the same logarithmic scale.

### 6.1.2.7 Estimating Optimum Parameters

The BASISM model does not include a formal way of optimising parameters in order to improve the fit. Some attempts were therefore made at estimating the optimum value of a parameter in order to decrease the misfit between observations and model. As these “estimates” will depend on the results from the previous scenarios, the estimates will be discussed together with the results from the scenarios.

### 6.1.3 Calculating the Surface Velocity

In order to model the internal layers the model needs to know the surface velocity. In BASISM the surface velocity is assumed to be equal to the balance velocity of the glacier (as discussed in Section 4.3.1) based on a known mass balance and the assumption that the glacier is in steady state. However, this is most likely not the case (e.g. Rignot et al., 2008; Wingham et al., 2009) and from a comparison between the balance velocities calculated by BASISM (Figure 6.6a) and the velocities measured by InSAR (Figure 6.6b) it is clear that the balance velocities underestimate the width of the main trunk and of some of the tributaries. On the other hand, the general spatial pattern of the velocity including the tributary system is very similar. Unfortunately the InSAR velocities only cover the main trunk and tributaries and it is therefore unknown if the discrepancy also applies to areas in, for example, the southern basin that are much slower flowing. It is, however, likely that the differences will be substantially smaller in these areas since the acceleration of PIG only very recently was observed to have spread beyond the main trunk (Wingham et al., 2009).

It is expected that the fact that the balance velocities differ from observed velocities will lead to some discrepancies between model and observations. How-

ever, since the difference should be most pronounced in the fast flow areas, where only a small part of the internal layers were observed, the difference should be of less significance than other parameters such as mass balance and ice flow mode.

### 6.1.4 Quantifying the Fit

The goodness of a fit was quantified by considering the “difference” and the “distance” between modelled and observed layers. The difference takes into account the direction of the misfit whereas the distance is the absolute value of the difference (concept illustrated in Figure 6.7). In other words, the distance is always a positive number that describes the magnitude of the misfit, while the difference is either positive or negative depending on whether or not the model is over- or underestimating the layer elevations. When the difference between observed and modelled layers is above zero the model is overestimating the layer depth and when the difference is below zero the model is underestimating the layer depths. In areas where several layers occur at the same coordinates the mean was used.

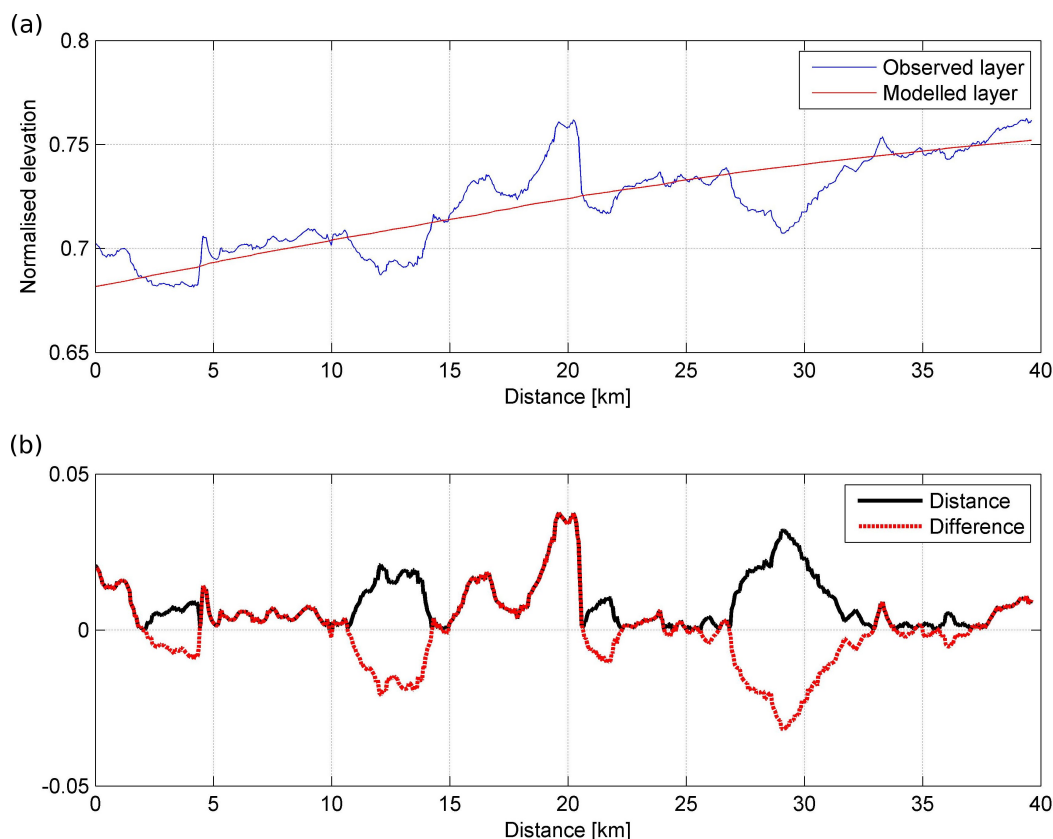


Figure 6.7: (a) Example of observed (blue line) and modelled (red line) layer. (b) Illustration of the terms difference (red dashed line) and distance (black line). The median of the distance for this layer is 0.006.

The goodness of a fit for one single layer was represented by the median value of the *distance* between the observed layer and the modelled isochrone. The reason for using the median of the distance rather than the mean was to take into account cases where the modelled layers might achieve an overall good fit but have one localised large misfit due to, for example, small-scale variations that are not captured in the model. This would influence the mean value significantly but the median value less so. For all layers in a scenario the mean of the median distance was taken as an indication of the goodness of the overall fit for the scenario. This value will henceforth be termed the median misfit.

## 6.2 Individual Layer Fitting

This section considers the fitting of the individual layers where no attempts were made to correlate between flightlines. In summary, the model achieved a good fit to the observed layers. In most of the scenarios over 80% of the layers had a median layer misfit of less 0.05. For none of the scenarios there appeared to be any pattern in terms of spatial variation of the difference between observations and model results or goodness of the fit. Layers that obtained a good fit could be found next to, or overlapping with, layers that had a significantly less good fit.

The differences between the observed and the modelled layers were typically between -0.15 to 0.15 (in normalised elevation) with an overall mean median misfit of 0.016 for all layers for the control scenario. For this scenario the difference between the observed and the modelled layers is shown in Figure 6.8a and the median of the distance between the observed and the modelled layer for each of the layers is shown in Figure 6.8b. From the figure there is no obvious difference in misfit between areas of fast flow and areas of slow flow.

| Scenario                     | Mean median misfit |
|------------------------------|--------------------|
| Control                      | 0.016              |
| Modern day accumulation      | 0.017 (-5%)        |
| Linear accumulation          | 0.017 (-4%)        |
| Basal melting, 50%           |                    |
| $H > 2500$ m                 | 0.017 (-1%)        |
| $H > 2750$ m                 | 0.016 (1%)         |
| $H > 3000$ m                 | 0.016 (3%)         |
| Basal melting, 10%           |                    |
| $H > 2500$ m                 | 0.016 (1%)         |
| $H > 2750$ m                 | 0.016 (0%)         |
| $H > 3000$ m                 | 0.016 (1%)         |
| $\Delta_{\zeta} = 21$ points | 0.016 (5%)         |
| $\Delta_{\zeta} = 31$ points | 0.016 (5%)         |
| $\Delta_{xy} = 4$ km         | 0.017 (-4%)        |
| Internal deformation         | 0.016 (5%)         |
| $\Delta_{\zeta} = 21$ points | 0.015 (7%)         |
| $\Delta_{\zeta} = 31$ points | 0.015 (8%)         |

Table 6.2: Results from individual layer fitting

### 6.2.1 Effects of Varying Parameters

When comparing results from different scenarios with the observations and the control scenario, it is useful to keep the following in mind: Since all elevations have been converted to normalised elevation, an elevation of 1 corresponds to

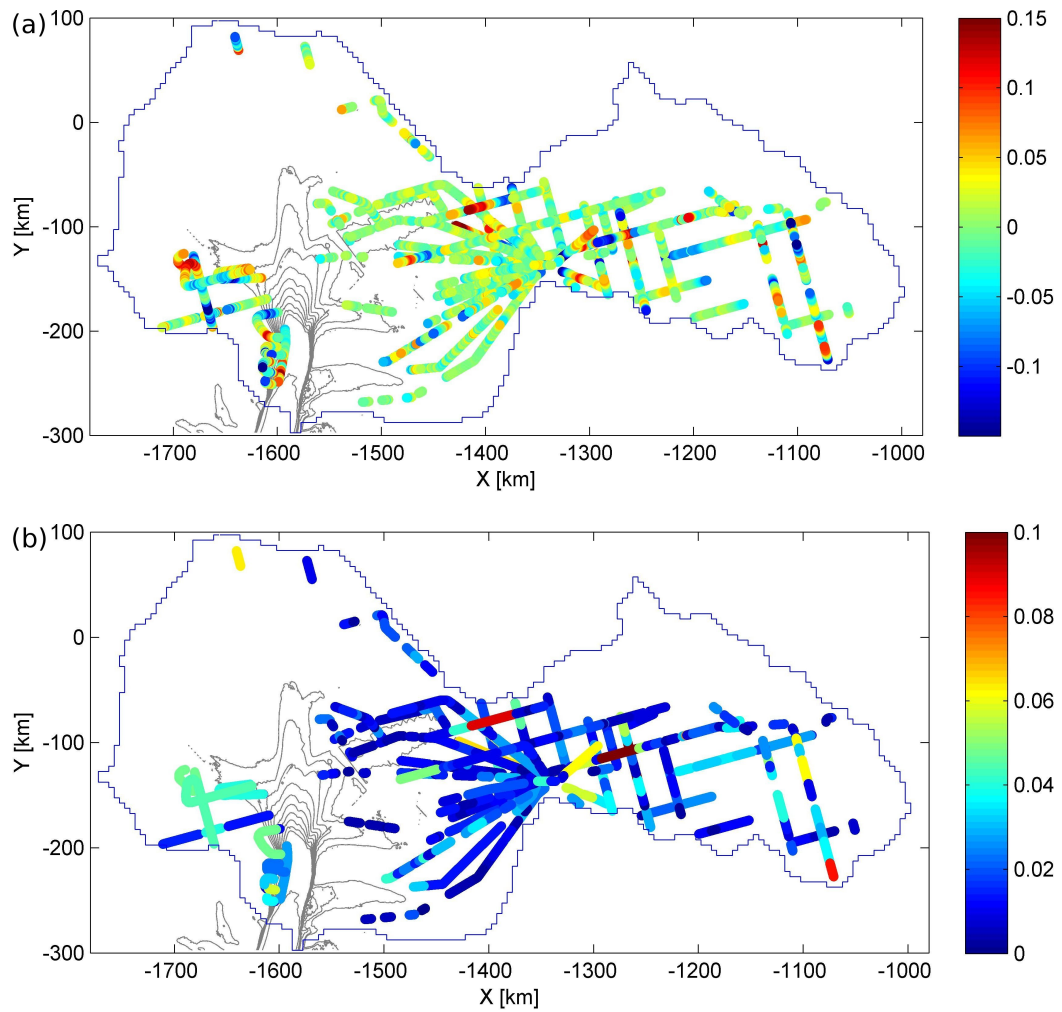


Figure 6.8: (a) Difference in normalised elevation between observed and modelled layers for the control scenario. (b) Median of the difference in normalised elevation between modelled and observed layers for the control scenario. The blue line outlines the PIG catchment basin.

the thickness of the ice. Thus a difference between observations and modelled layers of the order of  $10^{-1}$  implies a misfit of 10% of the ice thickness, a difference of  $10^{-2}$  implies a misfit of 1% of the ice thickness and so on. The results are summarised in Table 6.2.

### 6.2.1.1 Accumulation Pattern

With a modern day accumulation pattern the overall fit of the model (0.017) is almost equal to that for uniform accumulation (0.016) with the biggest differences between the two scenarios occurring in the neck between the northern and southern basin (see Figure 6.9). The scenario with decreasing accumulation for increased surface elevation achieves a mean median distance of 0.017 and again the biggest differences between the two scenarios occur in the neck between the northern and southern basin. The difference between the modelled layers for uniform and non-uniform scenarios is of the order of  $10^{-2}$ , which is an order of magnitude smaller than the difference between observations and model results.

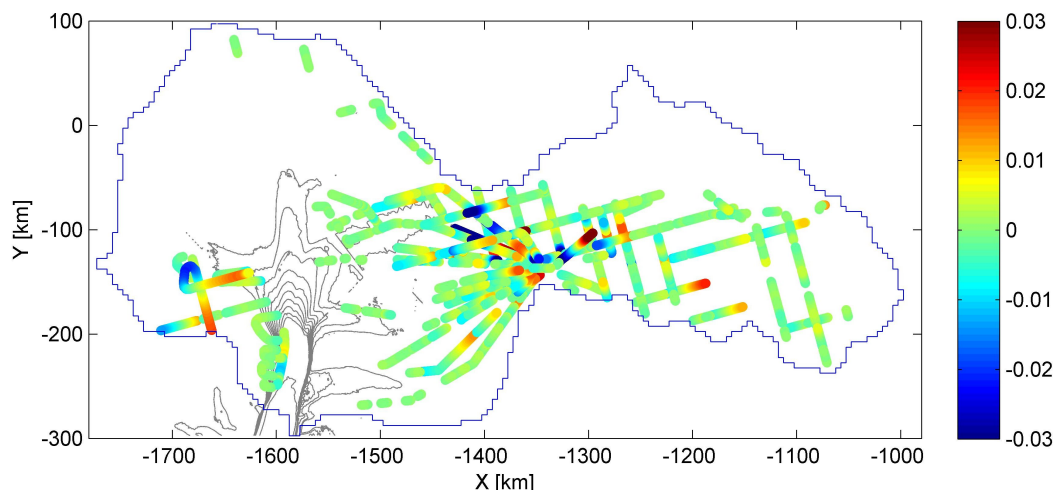


Figure 6.9: *Difference between modelled layers with modern day accumulation pattern and a uniform accumulation pattern.*

### 6.2.1.2 Basal melting

All six scenarios had a mean median distance of 0.016, except the scenario with 50% basal melting for thicknesses larger than 2500 m that had a mean median misfit of 0.017. Differences between the scenario with uniform basal melting and the scenarios with localised increased basal melting are, not surprisingly, largest at areas of large ice thicknesses i.e. where the basal melting was set to increase. The difference between the scenario with uniform basal melting and the scenario where the basal melt rate is increased to 10% of the accumulation

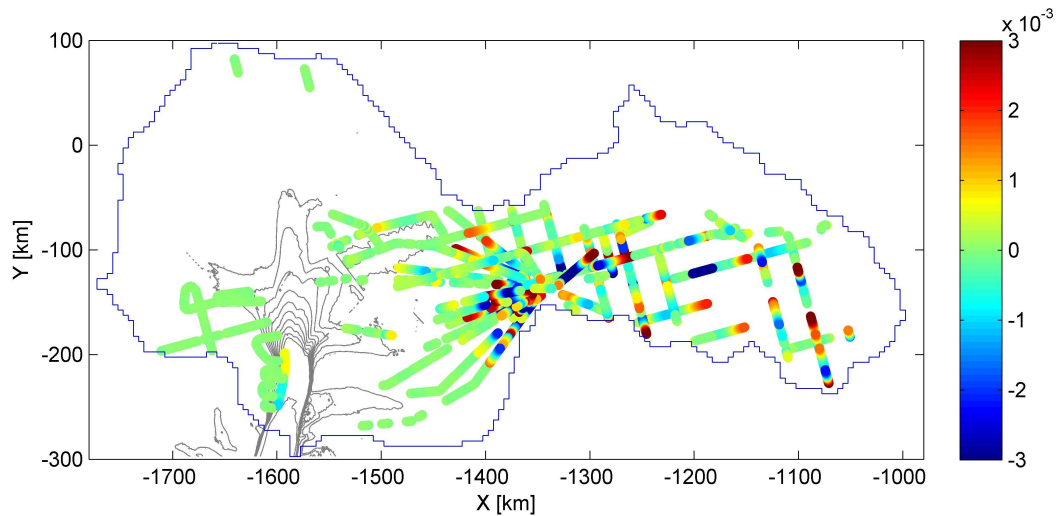


Figure 6.10: *Difference between modelled layers for increased basal melting of 10% of the accumulation rate for ice thicknesses larger than 2750 m and for uniform basal melting.*

in areas of ice thicknesses larger than 2750 m can be seen in Figure 6.10. The differences compared to the control scenario are of the order of  $10^{-3}$  with the largest differences occurring in the southern basin where the basal melt rate has been increased. An example of a radargram with traced layers and the results from the control scenario and a basal melt scenario is shown in Figure 6.11. It is clear how the modelled layers are dragged down for the scenario with basal melt in the right and left hand side of the figure.

### 6.2.1.3 Vertical and Horizontal Resolution

An increase in vertical resolution significantly reduced the computational speed of the model while the pay-off in terms of increase in the goodness of the fit turned out to be very small. All three scenarios with 11, 21 and 31 vertical grid points achieved a mean median distance of 0.016. The spatial pattern of the misfit was unchanged between each run. The difference between the modelled layers for 31 vertical points and 11 vertical points is shown in Figure 6.12a. The difference is of the order  $10^{-3}$  with the largest differences occurring in the area with the tephra layer and in the neck between the southern and northern basin.

A change in horizontal resolution from a 2 km grid to a 4 km grid did not change the spatial pattern of the misfit. Figure 6.12b shows the difference between observed and modelled layers for a 4 km grid and in comparison to Figure 6.8 there is very little difference between this scenario and the control scenario. Areas that had large differences between observations and model for the lower resolution were the same areas that had large differences in the higher resolution scenario.

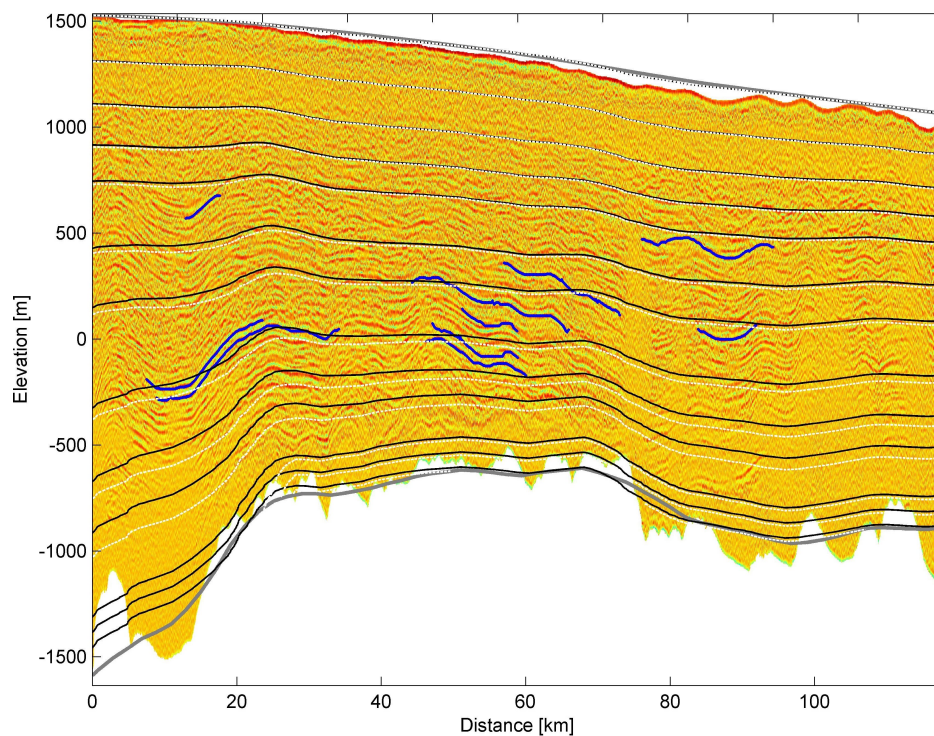


Figure 6.11: Radargram showing internal layers (blue lines) with the results from the control scenario (black lines) and a scenario with increased basal melt (dashed white lines). Surface and bed topography used in the model are shown as grey lines.

The mean median misfit also stayed almost unchanged at 0.017.

#### 6.2.1.4 Flow Mode

The scenarios with plug flow (control scenario) and internal deformation both produced the same mean median distance: 0.016. The difference between the modelled layers for internal deformation and for plug flow is shown in Figure 6.13. The difference is on the scale of  $10^{-2}$ . The largest differences occurred in the area where the tephra layer was identified and in the neck between the two basins. As an extra test two extra scenarios were run with internal deformation but with 21 and 31 vertical points. The reason for increasing the vertical resolution is the fact that internal deformation of ice means a change in the horizontal velocity with depth. This gradient is particularly steep close to the bed of the ice and therefore the vertical resolution is likely to have an impact as the gradient is resolved in more detail for higher resolution. These two scenarios produced the same median misfit of 0.015, a slight improvement compared to the control scenario, but with no difference in the spatial pattern.

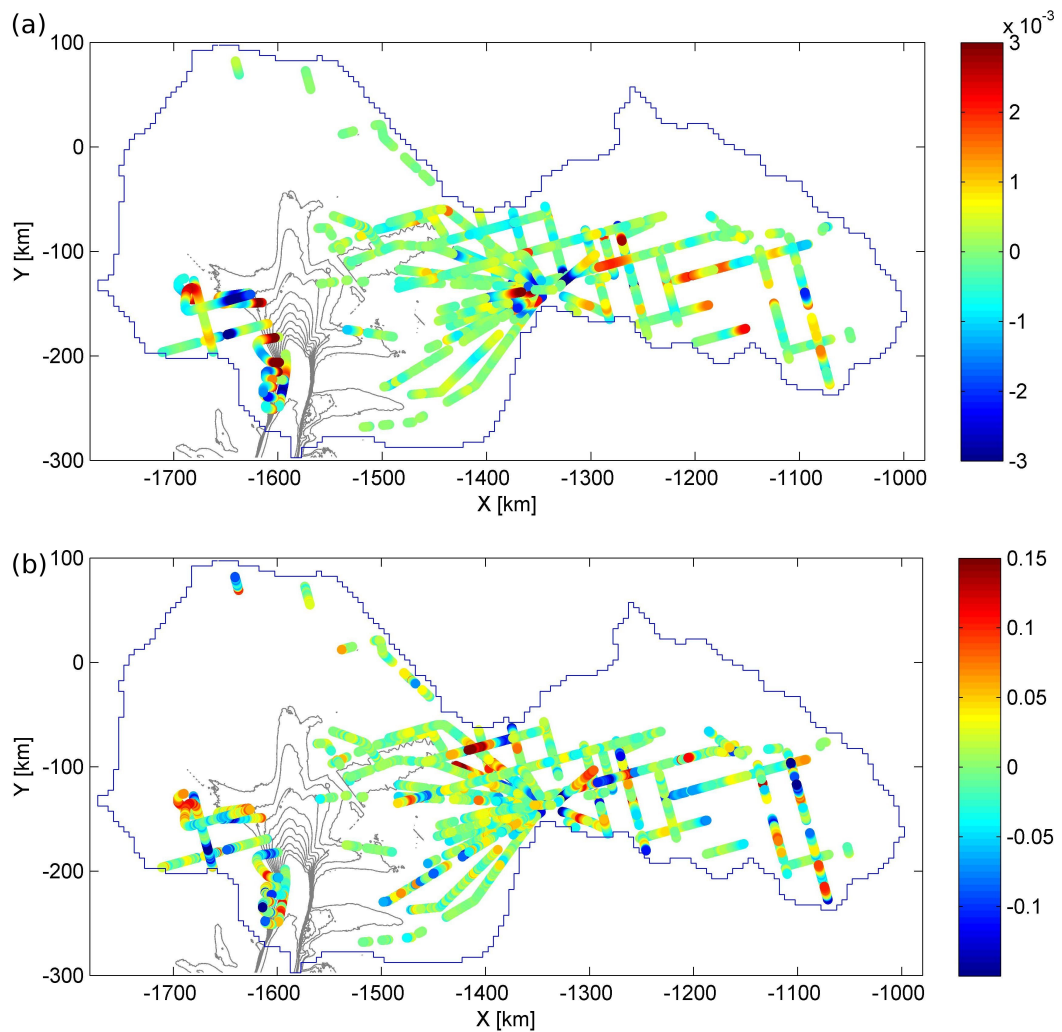


Figure 6.12: (a) Difference between model results for 31 vertical points and 11 vertical points. (b) Difference between observed and modelled layers for a horizontal resolution of 4 km. Compared to the spatial pattern in Figure 6.8 there is no visible difference. The blue line is the PIG catchment basin

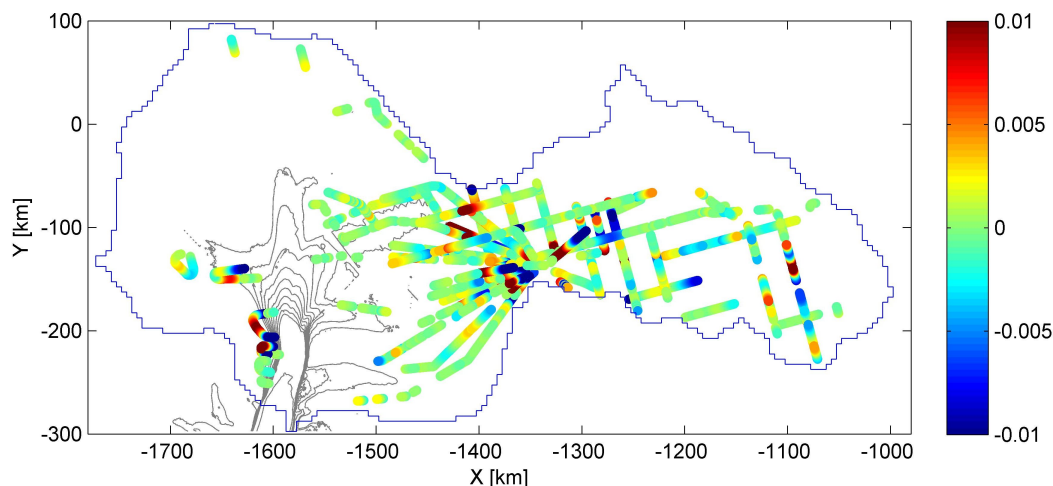


Figure 6.13: *Difference between modelled layers for internal deformation and plug flow.*

### 6.2.1.5 Additional Considerations

As an additional consideration the relationship between the layer properties and the misfits was investigated. Since the depth of a layer reflects its age this naturally gave rise to the question if some scenarios fit shallow (younger) layers better than deep (older) layers and if this relationship reflects the fact that the scenario represent older/younger conditions better. Figure 6.14 shows the median of the misfits for each layer with (average normalised) elevation for the case of uniform accumulation (blue dots) and for modern accumulation pattern (red stars). The reason for investigating this particular scenario is that the upper layers, that are mainly influenced by the accumulation pattern, might be captured better by a modern accumulation pattern. Note that in normalised elevation 0 denotes the bed and 1 the surface. Although some points differ between the two scenarios there is no obvious pattern as to where the scenario with uniform accumulation performs better or worse. Both scenarios have slightly more points that have a high misfit in the lower part of the ice between elevations 0.1-0.5. There does not appear to be any obvious relationship between the average elevation of a layer and the misfit between the layer and the model.

Figure 6.15 shows the median layer misfit for each layer with (average normalised) elevation for uniform basal melt (blue dots) and localised increased basal melt (green circles) of 10% of the accumulation in areas of ice thicknesses larger than 2750 m. Since the deep layers are more influenced by the basal melting than the upper layers, the deep layers might exhibit a change in misfit between the control scenario and the scenario with changes in basal melting. However, again there does not appear to be any obvious relationship between the average eleva-

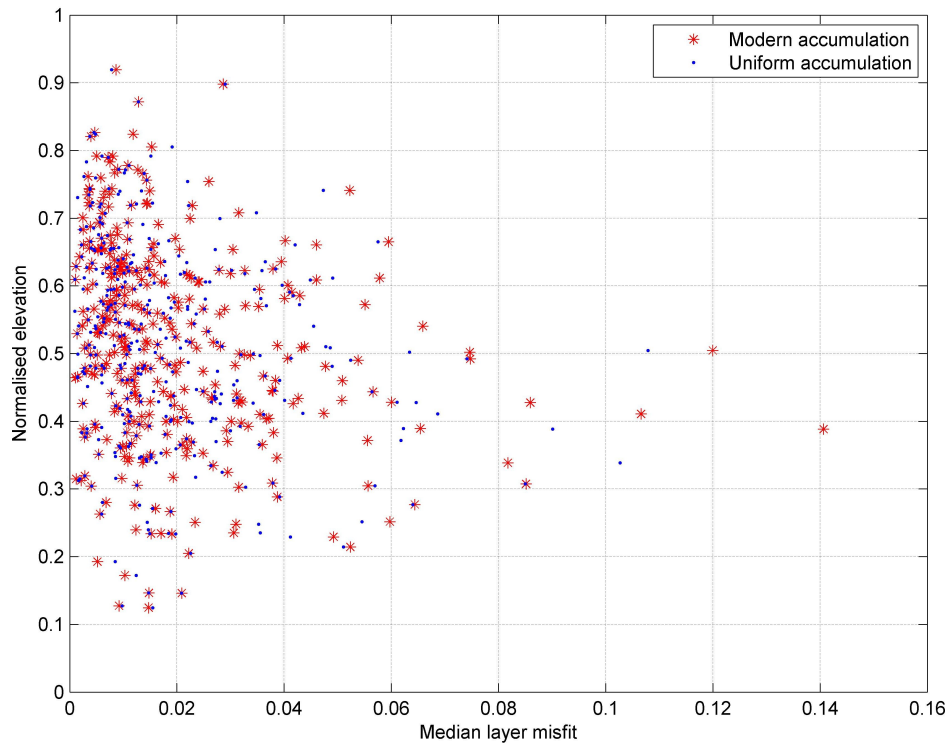


Figure 6.14: *Median layer misfit with depth for uniform accumulation (blue dots) and modern accumulation pattern (red stars).*

tion of a layer and the misfit and there is no obvious pattern where the uniform basal melting is better or worse than the scenario with localised basal melt.

Finally the impact of the lengths of the layers on the goodness of the fit is investigated. Figure 6.16 shows the (logarithm of the) lengths of the layers as a function of their respective median misfit for three cases: control case (blue dots), modern day accumulation (red stars) and localised increased basal melting (green circles). As can be seen from the figure it is mainly layers that are longer than 10 km that return large misfits. There also appears to be a general increase in misfit with layer length.

### 6.2.2 Interpretation

The median misfit changed less than 10% between each scenario which can be considered to be practically insignificant. This is most likely because most of the layers are relatively short thus making it comparatively easy for the model to fit an isochrone to a layer since the fit is not very well constrained in time or in space. This indicates that the spatial scale of the accumulation pattern and basal melting for PIG is larger than the length of most of the individual layers considered here. In other words the accumulation pattern and basal melting probably varies over distances larger than approximately 10 km.

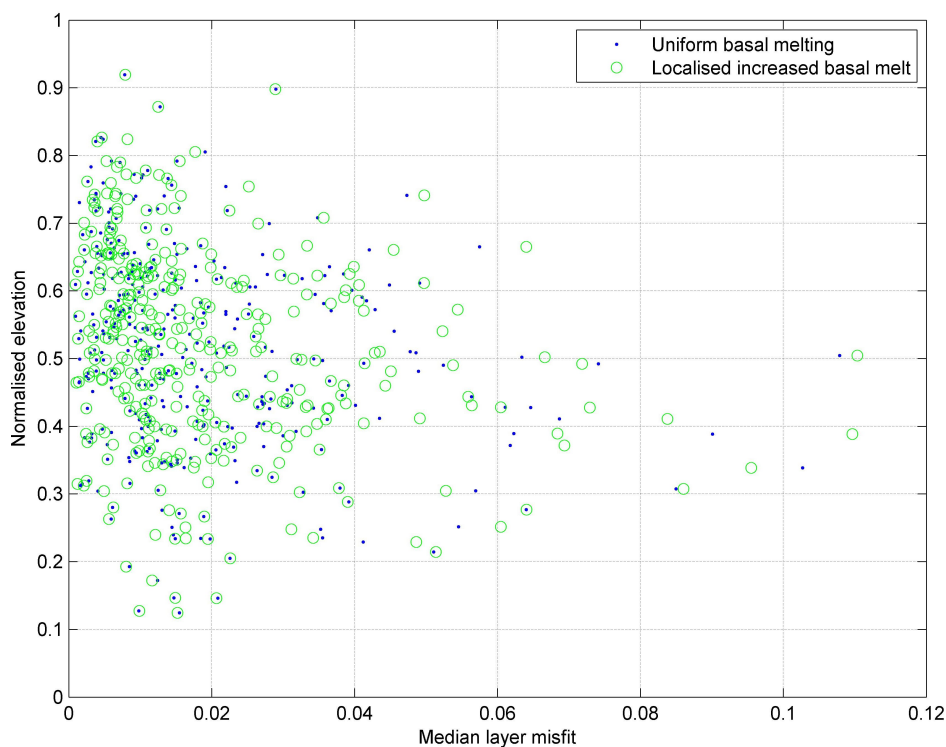


Figure 6.15: Median layer misfit with depth for uniform basal melt (blue dots) and localised increased basal melt (green circles).

In terms of the changes in basal melt it should be noted that, just like for the accumulation pattern, the actual value of the basal melt rate will not impact the fit of the model to the layer shape. Thus changes in basal melt pattern will only influence the layers that are located in the areas where there is a gradient in basal melt rate. This also explains why there was very little change observed in the northern basin.

The largest differences compared to the control scenario occurred in the neck between the northern and southern basin. This could indicate that the area is particularly sensitive to changes in parameters of the model. Another area that returns large differences between each scenario is the area south of the main trunk where the tephra layer is located (see also Section 6.3 below). A change in flow mode in particular had an impact on this area, which could indicate that deformation or sliding over the bed takes place over relatively short spatial scales. This is consistent with the high bed relief and generally rough subglacial topography in this area that would influence layer geometry over short spatial scales.

Considering the model performance, it was reassuring that changes in vertical and horizontal resolution had little if any impact on the modelling result (two orders of magnitude smaller than the difference between observations and

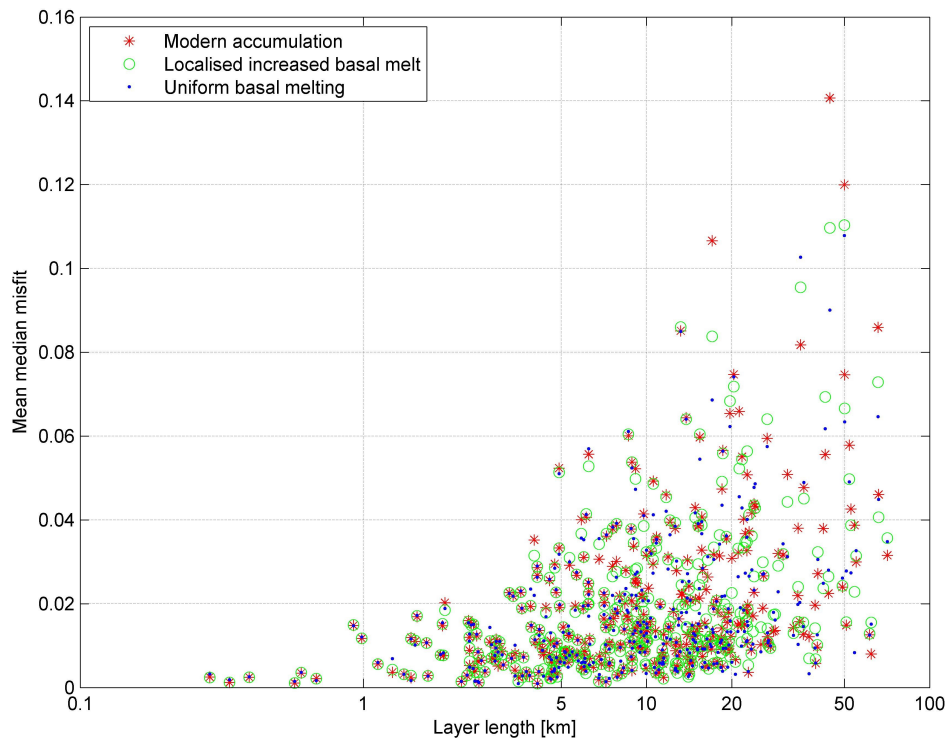


Figure 6.16: Median layer misfit as a function of layer length for uniform accumulation and basal melt (blue dots), modern accumulation pattern (red stars) and localised increased basal melt (green circles).

model results). In order to test how well the model favoured large-scale layer undulations, an additional experiments was set up using layer data that had been smoothed over several ice thicknesses. In spite of the filtering no significant change in the spatial pattern of the misfit was observed. This supports confidence in the model fitting the large scale undulations of the layers.

There are some obvious problems with this method; The fact that not every single layer in the radar data has been picked means that the picked layers are biased towards layers that occur at depths where the layers are the most visible. Secondly, since the majority of the layers have a very low median misfit it is possible that it is in fact a very few layers that determine how well a scenario performs. The mean median distance might reflect how well each scenario fits a subset of layers rather than the goodness of the overall fit.

All of these considerations point to the conclusion that it might not be possible to retrieve meaningful estimates of parameters that influence the stratigraphy of the larger over spatial scales larger than the average layer length (i.e. approximately 10 km) unless the model can be better constrained.

In summary, the model achieved a good fit of the layers for each different scenario. The difference between modelled and observed layers was generally on the scale of  $10^{-1}$ , the difference between the control scenario and the scenarios

with variation in accumulation or flow mode was of the order of  $10^{-2}$ , while the difference between the control scenario with 11 vertical points and the scenarios with 21 and 31 points was of the order of  $10^{-3}$ , the same was the case for the scenarios with changes in basal melting. This indicates that the model is generally less sensitive to changes in vertical resolution than to changes in other parameters.

## 6.3 Tephra Layer

The tephra layer is located to the north of the main trunk where no other internal layering was visible. The mean normalised elevation of the tephra layer is 0.57, in other words just above the mid-point of the ice. In the scenarios described below the tephra layer was used as input in BASISM not as a collection of layers but as one single internal horizon. This means that BASISM will fit a surface of the same age that has the optimum fit with all points in all lines containing the tephra layers thus constraining the model better.

The difference between observed and modelled layers for the tephra layer is for most areas between -0.2 and 0.2. For the control scenario the median of the misfit for the tephra layer is 0.041. This is a significantly higher misfit than the results discussed above, however, that is expected considering the new constraint on the model. The spatial pattern of the difference between observed and modelled layers for the control scenario can be seen in Figure 6.17. Generally the model appears to be underestimating the layer depths in the lines close to the main trunk, and overestimating the depths further away (red box in Figure 6.17) with the exception of the layers located furthest to the east (grey box in Figure 6.17). All the results from fitting the tephra layer are summarised in Table 6.3.

| Scenario                         | Mean median misfit |
|----------------------------------|--------------------|
| Control scenario                 | 0.041              |
| Modern accumulation pattern      | 0.043 (-3%)        |
| Linear accumulation pattern      | 0.049 (-19%)       |
| $\Delta_{\zeta} = 21$            | 0.042 (-1%)        |
| $\Delta_{\zeta} = 31$            | 0.042 (-1%)        |
| $\Delta_{xy} = 4$ km             | 0.042 (-2%)        |
| Internal deformation             | 0.040 (3%)         |
| $\Delta_{\zeta} = 21$            | 0.039 (5%)         |
| modern accumulation              | 0.040 (2%)         |
| $\Delta_{\zeta} = 31$            | 0.039 (5%)         |
| modern accumulation              | 0.041 (2%)         |
| Localised decrease in basal melt | 0.041 (0%)         |

Table 6.3: Results for fitting of the tephra layer.

### 6.3.1 Effects of Varying Parameters

#### 6.3.1.1 Accumulation Pattern

In the scenario with modern day accumulation pattern the model achieved a slightly worse fit compared to the control scenario with a median misfit of 0.043

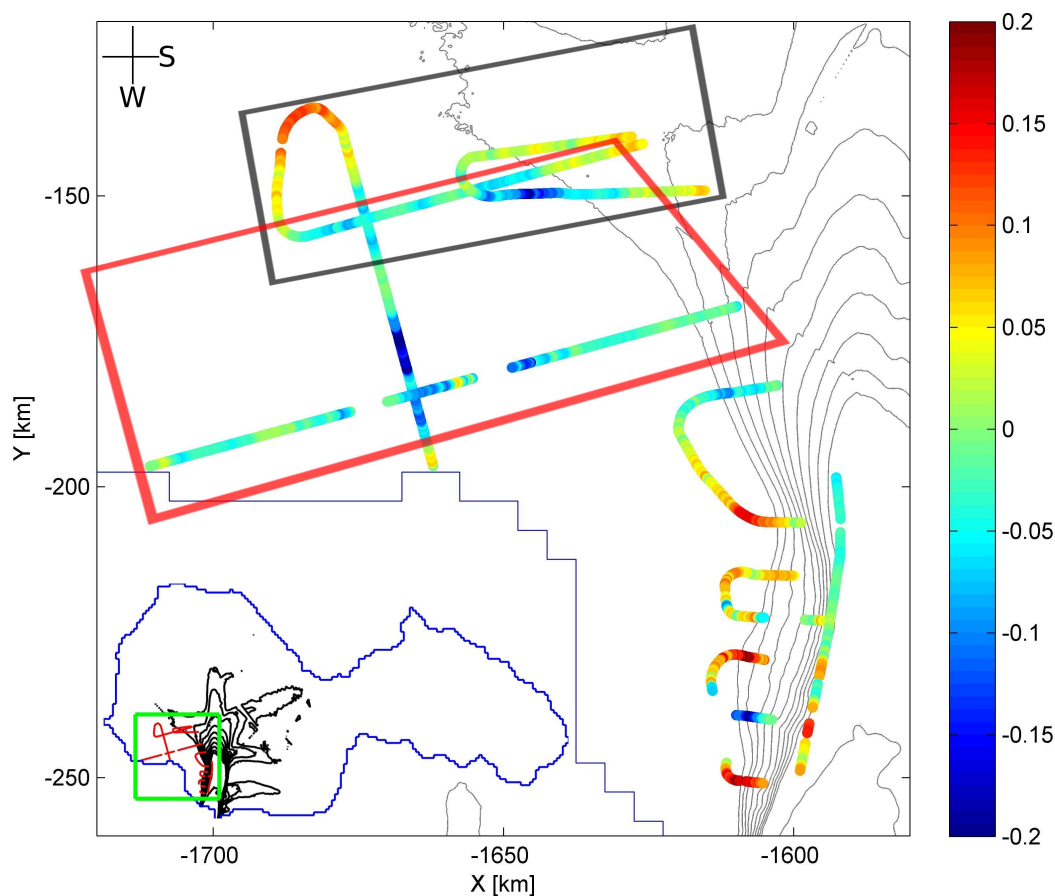


Figure 6.17: *Difference between observed and modelled layers for the control scenario for the tephra layer. The grey contours outline the surface velocity in  $100 \text{ m yr}^{-1}$  intervals.*

while the linearly dependent accumulation pattern had a significantly worse fit with a median misfit of 0.049. The spatial pattern of the misfit stayed unchanged and the differences were of the order of  $10^{-2}$ . Figure 6.18 shows clearly how with a linear accumulation pattern the model is overestimating layer depths close to the main trunk and underestimating them further away.

### 6.3.1.2 Basal Melting

In Section 6.1.2 the basal melting was defined based on ice thicknesses larger than 2500 m, 2750 m and 3000 m respectively. However, the tephra layer was only identified in the area north of the main trunk where ice thicknesses were significantly lower than that. Thus since the tephra layer is not present in any of the areas where basal melting was defined the changes had no impact on the fitting of the layer.

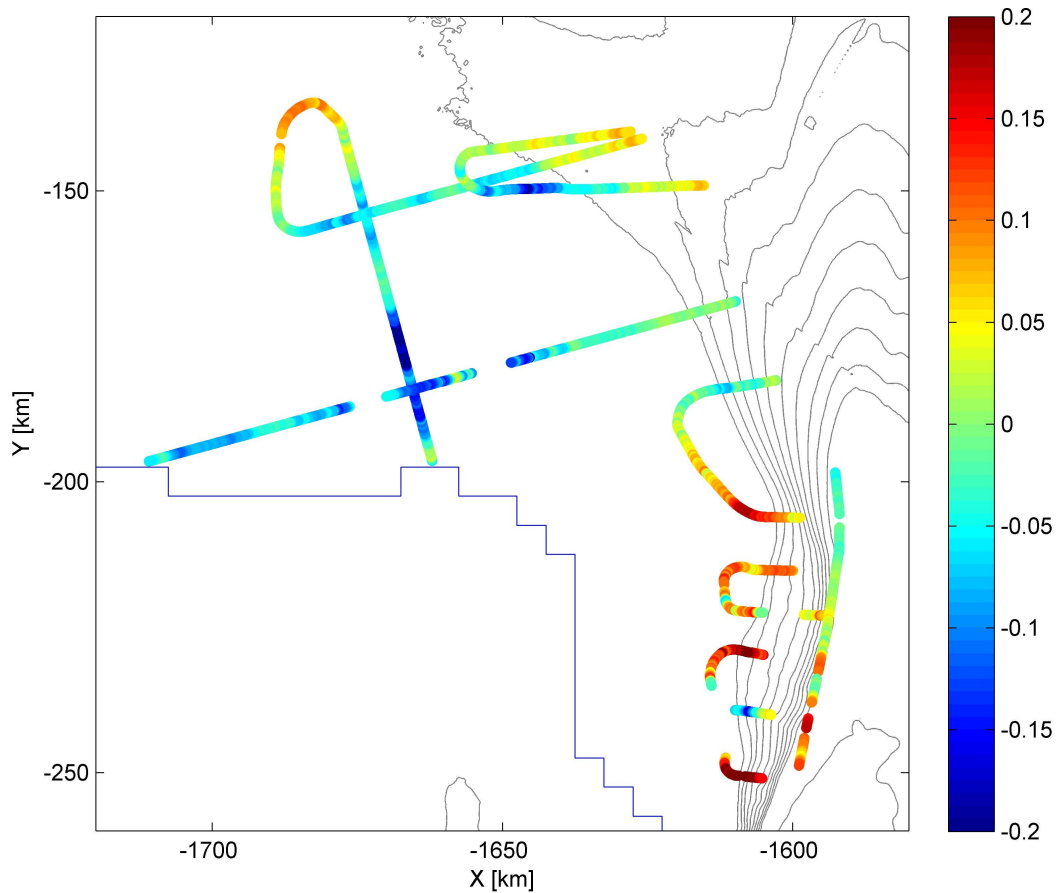


Figure 6.18: *Difference between observed and modelled layers for the scenario with linear accumulation. The grey contours outline the surface velocity in  $100 \text{ m yr}^{-1}$  intervals.*

### 6.3.1.3 Horizontal and Vertical Resolution

The vertical resolution was increased to 21 and 31 points but the impact of the changes in resolution was minimal. While the control case with 11 vertical points had a median misfit of 0.041, an increase in vertical resolution lead to a median misfit of 0.042 for both 21 and 31 points. The change in horizontal resolution returned a median misfit of 0.042. Again the spatial pattern was unchanged.

### 6.3.1.4 Flow Mode

Changing the flow mode to internal deformation the median misfit changed from 0.041 to 0.040. Increasing the vertical resolution to 21 points the median misfit was 0.040 (compared to 0.042 for plug flow). Increasing the resolution yet again to 31 points gave misfits of 0.042 and 0.039 for plug flow and internal deformation respectively. The difference between the control case (e.i. plug flow) and internal deformation for a vertical resolution of 21 points is shown in Figure 6.19. The difference is of the order of  $10^{-2}$  e.g. an order of magnitude smaller than the

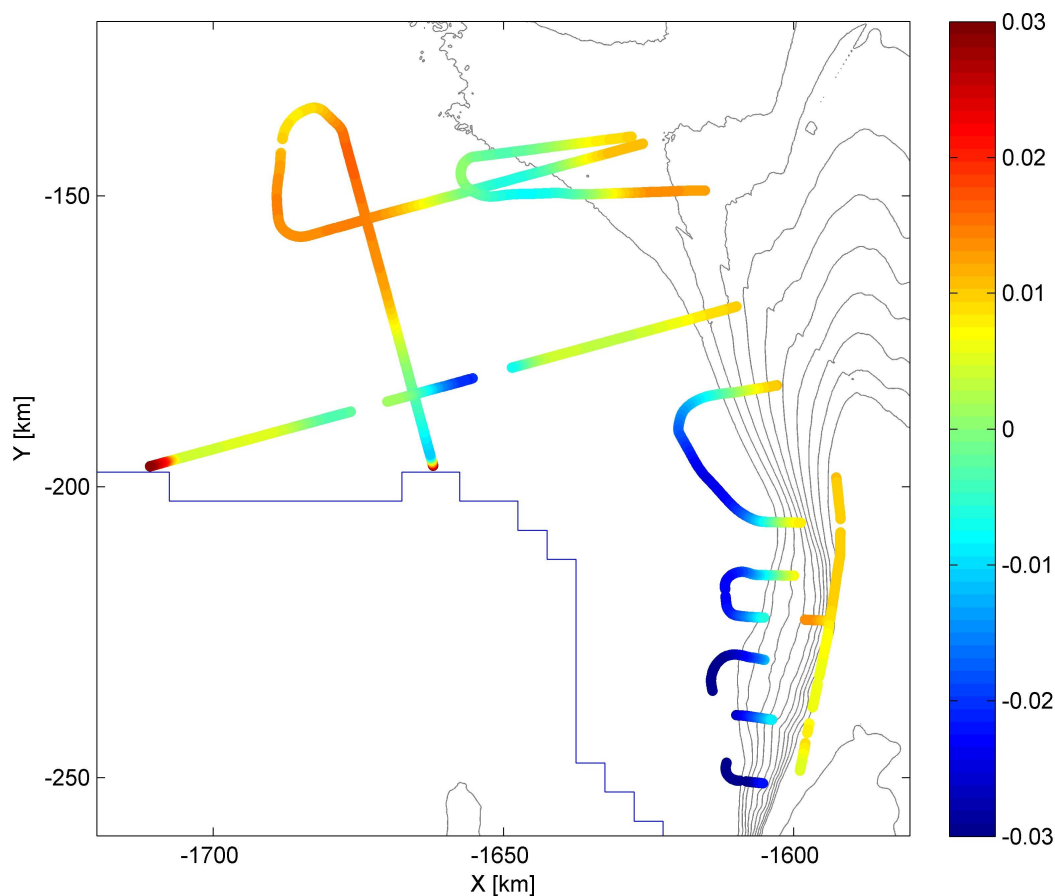


Figure 6.19: *Difference in normalised elevation between plug flow and internal deformation for the tephra layer. The grey contours outline the surface velocity in  $100 \text{ m yr}^{-1}$  intervals.*

difference between observations and model results.

### 6.3.2 Estimating Optimum Parameters

The combined influence of several of the parameters were also investigated. Firstly, since the tephra layer is a relatively recent deposition it is plausible that the accumulation pattern at the time of its deposition was similar to modern day accumulation pattern. Thus in an attempt to improve the fit for a modern day accumulation pattern, a scenario was constructed that included internal deformation and a vertical resolution of 21 points. This scenario achieved the same misfit and the overall spatial pattern stayed the same compared to the control case. Increasing the vertical resolution to 31 points returned a median misfit of 0.041 i.e. practically unchanged.

Considering the spatial pattern of the misfit for the control scenario shown in Figure 6.17 there did not appear to be any significant spatial pattern except for a large area in the centre of the plot where the model overestimates the depth of

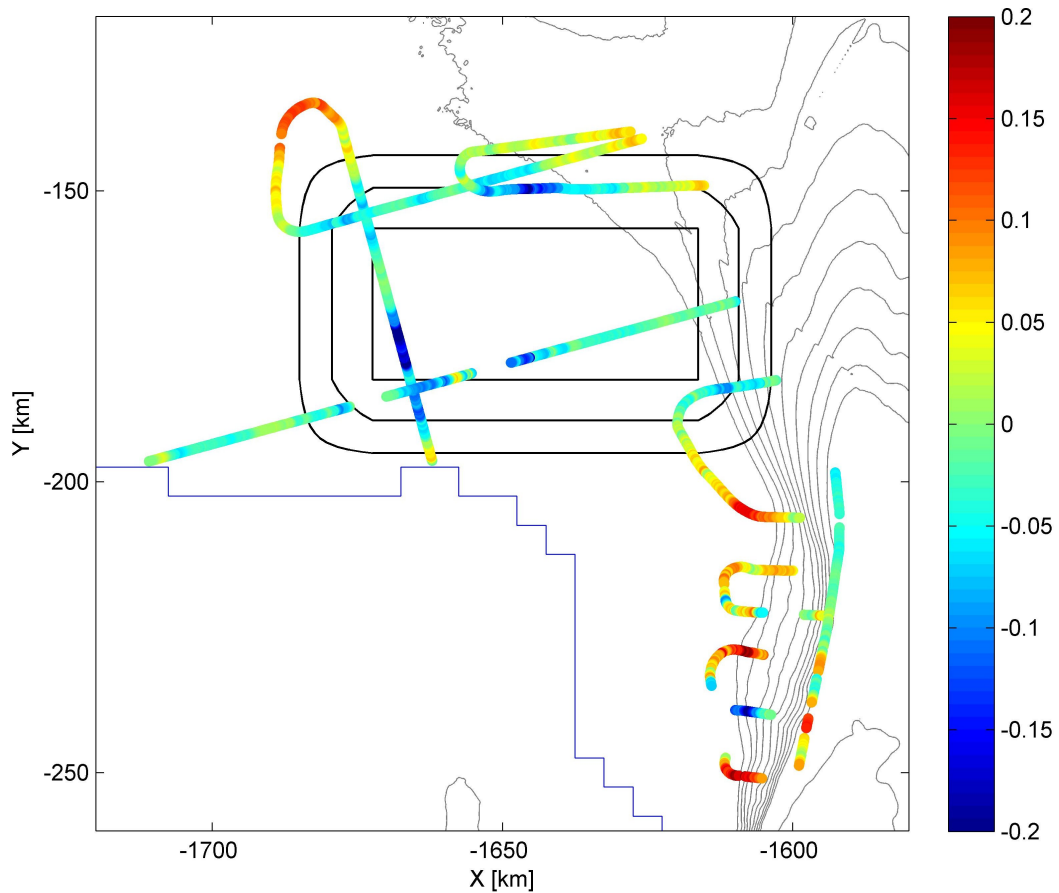


Figure 6.20: *Difference in normalised elevation between observed and modelled layers for localised basal melting accumulation (outlined with black contour lines). The grey contours outline the surface velocity in  $100 \text{ m yr}^{-1}$  intervals.*

the layers. This could indicate that an effect is increasing the depth of the layers such as localised lower accumulation rates than the neighbouring areas or less basal melting (or a combination of the two). Since this area for the modern day accumulation pattern has a higher accumulation than the rest of the area this does not explain the decrease in misfit for the modern accumulation scenario. In order to improve the fit a low basal melting of 0.5% of the accumulation rate was defined in the area where the model is overestimating the layer depths. The result can be seen in Figure 6.20 where the area of decreased basal melt is contoured with black lines. However, this did not appear to have any significant effect on the spatial pattern of the misfit and the median also stays the same of 0.041.

### 6.3.3 Interpretation

The changes in misfit for the tephra layer were, with one exception, less than 10% and thus considered to be insignificant. The scenario with the linearly changing accumulation pattern produced a significantly worse fit than the control scenario

indicating that this accumulation pattern is less likely to represent the actual accumulation pattern in this area. The fact that the tephra layer has been dated to be approximately 2.3 kyr (Corr and Vaughan, 2008) should mean that a modern accumulation pattern would improve the fit, however, this does not appear to be the case. It is thus possible that the accumulation pattern has changed since the deposition of the layer, but as the difference in mean median misfit between each scenario is only small this might also indicate that the spatial extent of the layering is not large enough to represent the wavelength of accumulation. It is also possible that the tephra layer, with its location close to the main trunk, has experienced more complicated flow dynamics that are not captured in this model.

Finally, it is also possible that the ice thickness in the area close to the main trunk has changed significantly, which would also introduce errors in the results from the flow model, that is based on an assumption of constant ice thickness. Thus it is only possible to conclude from modelling the tephra layer that it looks unlikely that the accumulation pattern in this area has been similar to a linearly increasing accumulation pattern.

## 6.4 Layer Package

The discovery of a layer package occurring in several flightlines has already been discussed in Section 5.3.2. An example of two radargrams containing the layer package is shown in Figure 6.21 in two-way travel time with the elevation of the layers shown below in Figure 6.21.

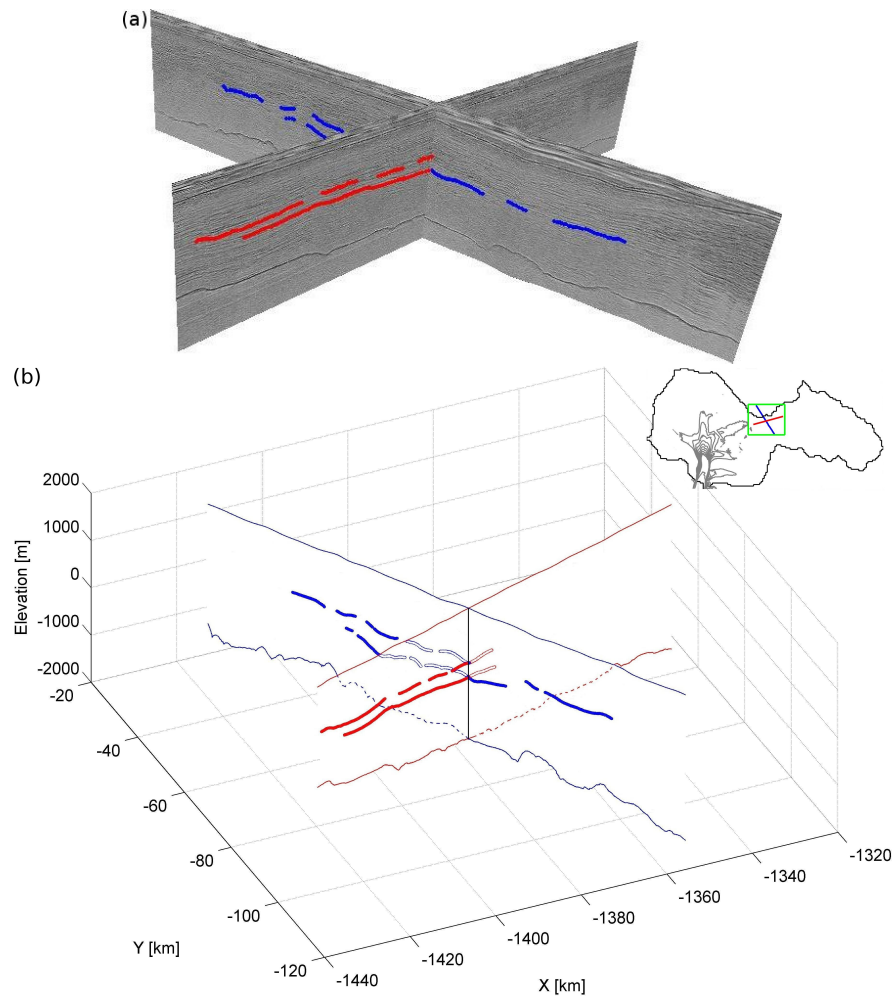


Figure 6.21: 3D view of intersection of two flightlines (shown in red and blue respectively) containing the layer package. (a) Radargram in two-way traveltime. (b) Elevation of Layer 1, Layer 2 and surface and bed topography.

Generally the difference between observed and modelled layers was in the range of -0.1 to 0.1 in normalised elevation. The difference for the control scenario between observed and modelled layers is shown in Figure 6.22 for Layer 1 and in Figure 6.22 for Layer 2. To reiterate; when the difference between observed and modelled layers is above zero the model is overestimating the layer depth and when the difference is negative the model is underestimating the layer depths. The control scenario fits the layer package with a median of 0.026 for Layer 1 and 0.034 for Layer 2. All results are summarised in Table 6.4.

| Scenario              | Layer 1 | %      | Layer 2 | %      |
|-----------------------|---------|--------|---------|--------|
| Control scenario      | 0.026   |        | 0.034   |        |
| Modern accumulation   | 0.036   | (-35%) | 0.031   | (9%)   |
| Linear accumulation   | 0.033   | (-26%) | 0.030   | (12%)  |
| Basal melting of 50%  |         |        |         |        |
| $H > 2500$ m          | 0.029   | (-12%) | 0.037   | (-8%)  |
| $H > 2750$ m          | 0.024   | (-6%)  | 0.032   | (1%)   |
| $H > 3000$ m          | 0.024   | (3%)   | 0.033   | (1%)   |
| Basal melting of 10%  |         |        |         |        |
| $H > 2500$ m          | 0.026   | (-2%)  | 0.033   | (3%)   |
| $H > 2750$ m          | 0.025   | (-1%)  | 0.031   | (3%)   |
| $H > 3000$ m          | 0.025   | (-1%)  | 0.032   | (2%)   |
| Internal deformation  |         |        |         |        |
| $\Delta_{\zeta} = 11$ | 0.030   | (-13%) | 0.029   | (14%)  |
| $\Delta_{\zeta} = 21$ | 0.028   | (-7%)  | 0.039   | (-17%) |
| $\Delta_{\zeta} = 31$ | 0.028   | (-7%)  | 0.039   | (-17%) |
| $\Delta_{\zeta} = 21$ | 0.026   | (2%)   | 0.033   | (4%)   |
| $\Delta_{\zeta} = 31$ | 0.026   | (3%)   | 0.032   | (4%)   |
| $\Delta_{xy} = 4$ km  | 0.026   | (2%)   | 0.031   | (7%)   |

Table 6.4: Results for different scenarios for fitting the layer package.

From Figure 6.22 a few obvious misfits can be seen immediately. For example, the layer that extends furthest out to the left hand side in Figure 6.22 (marked with a red circle) is in an area where the surface slope of the smoothed surface topography is significantly steeper than the actual topography leading to a substantial overestimation of the layer slope in the model. This layer will therefore be disregarded in the further analysis, as will the layer in the middle of Figure 6.22a that has a much larger negative difference and the layer in Figure 6.22b that has a much larger positive difference than surrounding layers (both marked with red circles) since the difference for these layers is anomalously large.

One interesting feature that can be observed in Figure 6.22 is that the model is underestimating the slope of the layers particularly in the areas marked with grey boxes. This is an indication that something that is not captured in the model is causing the layers to be dragged down such as, for example, increased basal melting or changes in accumulation rates. An example of this effect is shown in Figure 6.23 where the observed layers (blue lines) have a different slope than the modelled layers (black lines) in the right hand side of the radargram. The median values of the misfit can be found in Table 6.4.

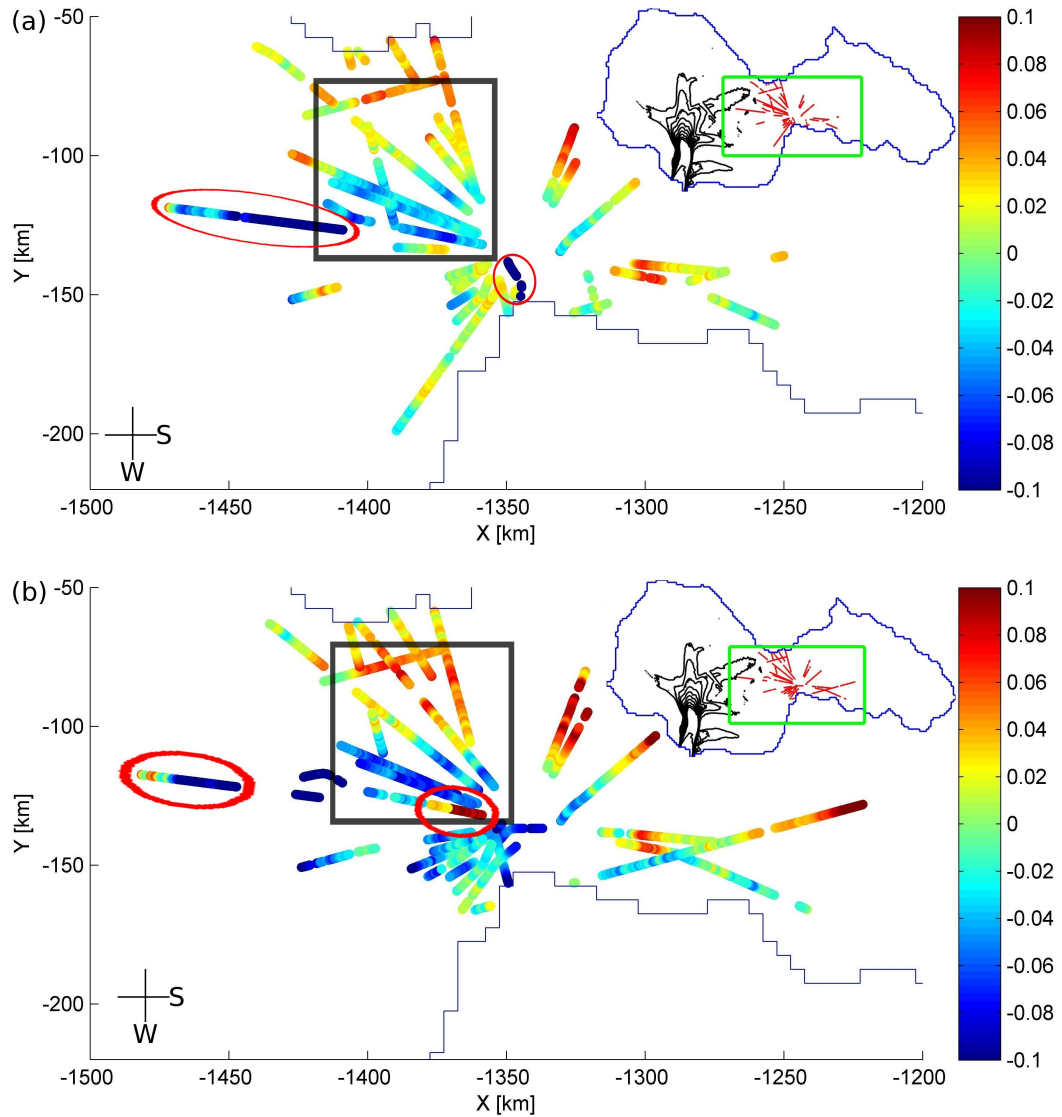


Figure 6.22: *Difference in normalised elevation between observed and modelled layers for layer 1 and 2 for the control case. The blue line is the outline of the PIG catchment basin, the red circles note lines that will be disregarded in the further analysis and the grey box marks an area where the slope of the layers is underestimated by the model.*

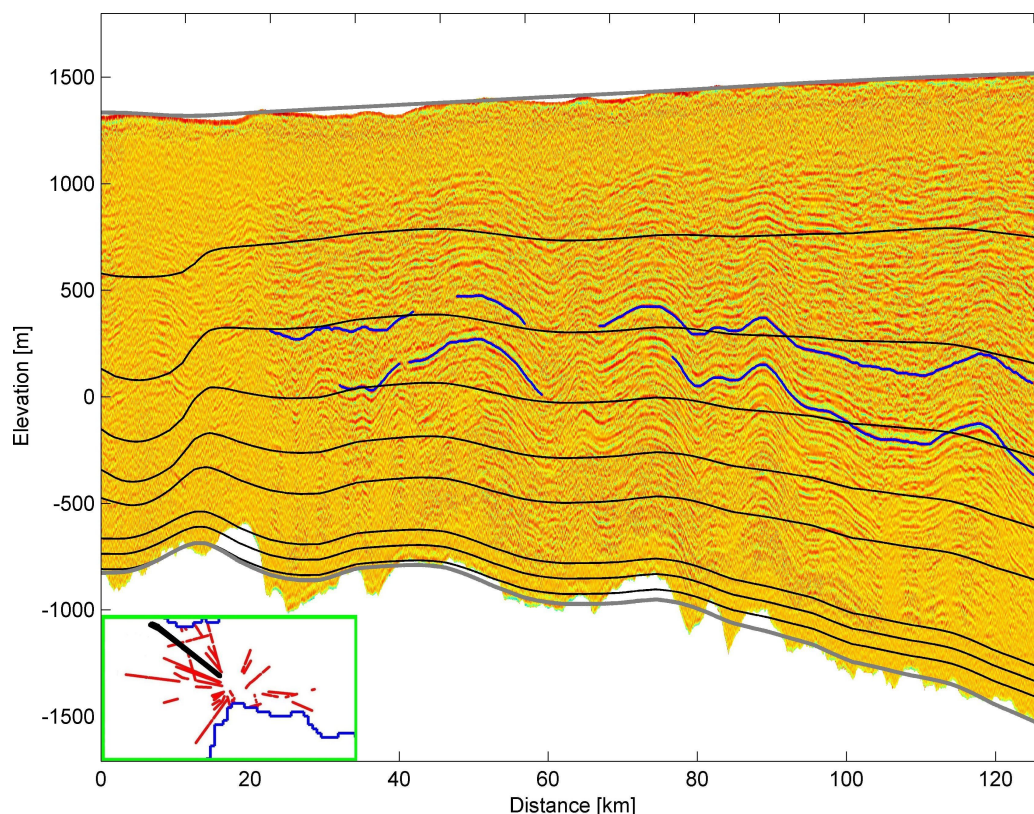


Figure 6.23: *Radargram with internal layering from the control scenario shown as black contours. The surface and bed topography used in the model are shown as grey lines and some internal layers are marked for clarity with blue lines. Inset: Context map with the radargram marked with a red line.*

## 6.4.1 Effects of Varying Parameters

### 6.4.1.1 Accumulation Pattern

Surprisingly, the pattern corresponding to a modern accumulation pattern produces a significantly worse fit than that for a uniform accumulation for Layer 1 (median of 0.036) but slightly improved for Layer 2 (median of 0.031). For Layer 1 (Figure 6.24a) the fit is worse for almost all the lines except for the number of short lines starting at the neck, while for Layer 2 (Figure 6.24b) the fit is especially bad for the layers where the model is already underestimating the slope and for the lines furthest to the south in the basin. An example of the worsening of the fit in this area is shown in Figure 6.25. The black contour lines show the modelled internal layers and the blue lines the observed layers. For comparison the control scenario is shown with white lines. The difference between observations and model is of the order of  $10^{-1}$ , and so is the difference between this scenario and the control scenario.

For the scenario where the accumulation is made linearly dependent on the

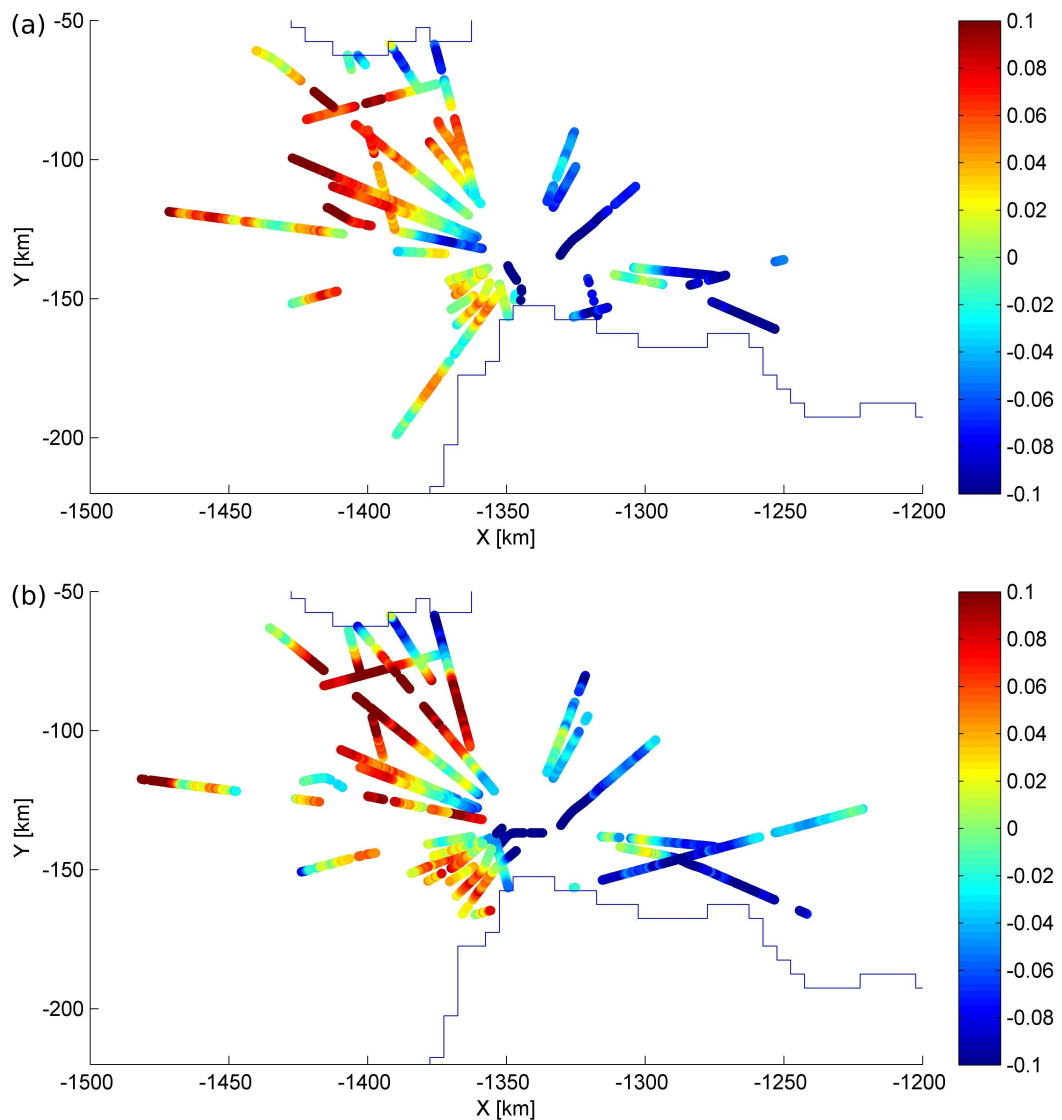


Figure 6.24: *Difference between observed and modelled layers for modern accumulation for (a) Layer 1 and (b) Layer 2.*

surface elevation the fit is worse for the Layer 1 (median of 0.033) but better for Layer 2 (median of 0.030). For both Layer 1 and Layer 2 (Figure 6.26) all lines in the southern part of the basin achieve a better fit compared to the control case while all the short lines in the lower middle part of the figure have a worse fit. The rest of the lines are practically unchanged. The difference between modelled and observed layers is of the order of  $10^{-1}$  and so is the difference between the results from this scenario and the control scenario

#### 6.4.1.2 Basal Melting

Assuming that basal melting is taking place due to large ice thicknesses, six different model runs were made assuming increased basal melting of 10% and

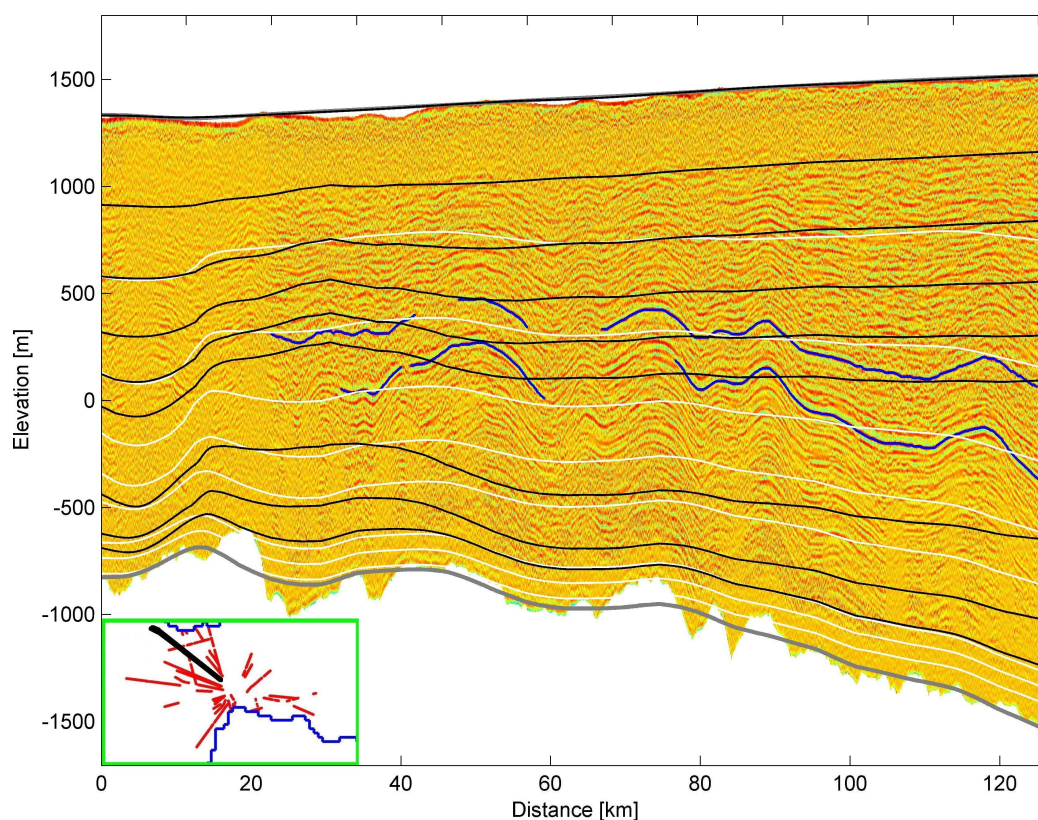


Figure 6.25: *Radargram with internal layering from the scenario with modern accumulation shown as black contours. The results from control scenario are shown with white lines. The surface and bed topography used in the model are shown as grey lines and some internal layers are marked for clarity with blue lines. Inset: context map with the position of the radargram marked with a red line.*

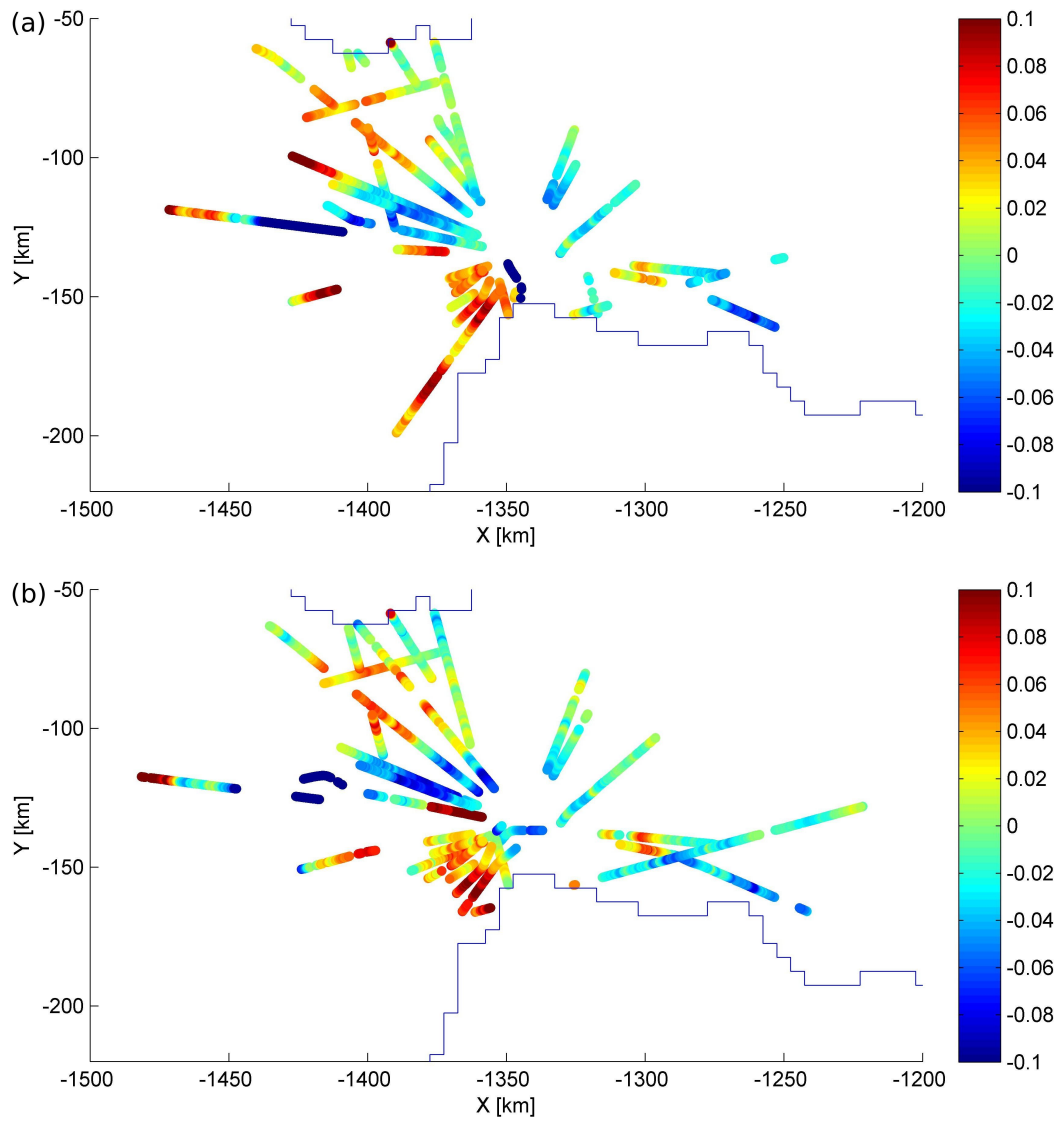


Figure 6.26: *Difference between observed and modelled layers for accumulation decreasing linearly with surface elevation for (a) Layer 1 and (b) Layer 2.*

50% of the accumulation rate respectively for areas with an ice thickness above 2500 m, 2750 m and 3000 m. Generally, for all the fits with non-uniform basal melt the spatial pattern of the fit only changed slightly with the biggest change in the scenario with 50% basal melting for ice thicknesses above 2500 m. The line furthest to the north (marked with a red circle in Figure 6.22) obtain a slightly better fit for both Layer 1 and Layer 2. For Layer 1 the fit of the layers left of the neck (starting at approximate  $x = -1300$ ) also display a slightly improved fit, while the introduction of a non-uniform basal melting rate does improve the overall fit in some cases. The order of the misfit does not change significantly but is still of the order of  $10^{-1}$  (Figure 6.27).

The scenarios where basal melting is occurring in areas with ice thicknesses above 2.5 km obtain a slightly worse fit compared to the control run while the scenarios with increased basal melting in areas with ice thicknesses above 2750 m and 3000 m have a slightly better fit. The best fit for Layer 1 is obtained in the scenario with basal melting at ice thicknesses above 2750 and 3000 m with 50% of the accumulation rate (median of 0.025). For Layer 2 the best fit was obtained with basal melting of 10% of the accumulation rate for ice thicknesses larger than 2750 m (median of 0.031).

### 6.4.1.3 Flow Mode

A change in flow mode from internal deformation to plug flow changed the misfit for Layer 1 from 0.026 for plug flow to 0.030 for internal deformation. For Layer 2 the median misfit is 0.034 for plug flow and 0.029 for internal deformation. As in the previous sections the impact of internal deformation is also tested for different vertical resolutions. For 21 vertical points the change in flow mode has almost no effect on Layer 1: 0.026 for plug flow and 0.028 for internal deformation. For Layer 2 the same change for 21 vertical points gives 0.033 for plug flow but a worse fit for internal deformation: 0.039. Furthermore, the spatial pattern of the misfit changes and it appears that two distinct areas appear (Figure 6.28): an area where the model underestimates the layer elevations (red colours) and an area where the model overestimates the layer elevations (blue colours, marked with a black circle). The line marked with a red circle is disregarded as explained above. Further increasing the vertical resolution to 31 vertical points in the case for internal deformation returns a median misfit of 0.039 for Layer 2 while Layer 1 achieved a slightly better fit with a median misfit of 0.028.

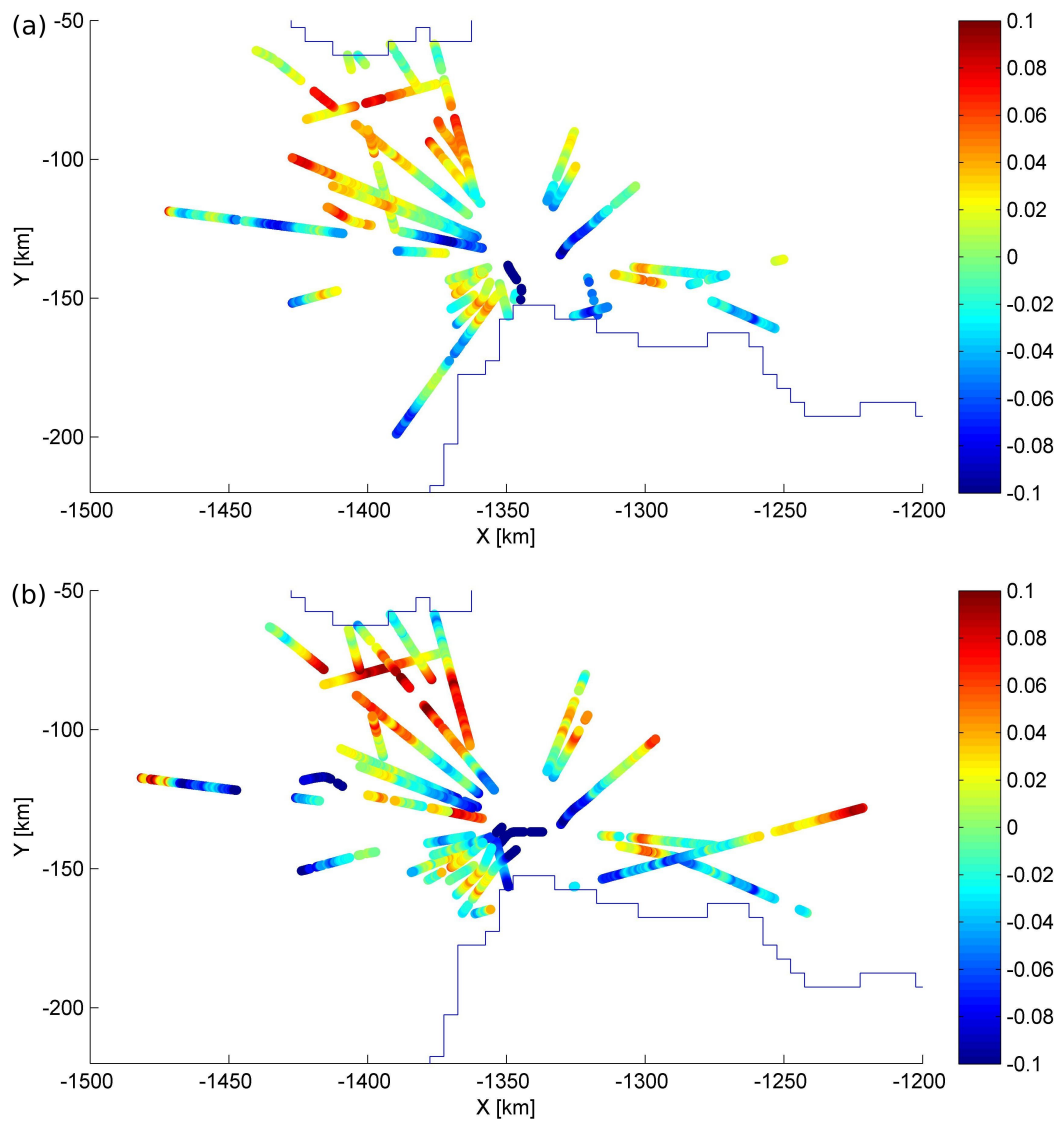


Figure 6.27: *Difference between observed and modelled layers for non-uniform basal melting for (a) Layer 1 and (b) Layer 2. The basal melt rate has been set to 10% of the accumulation rate in areas where the ice thickness is above 2750 m.*

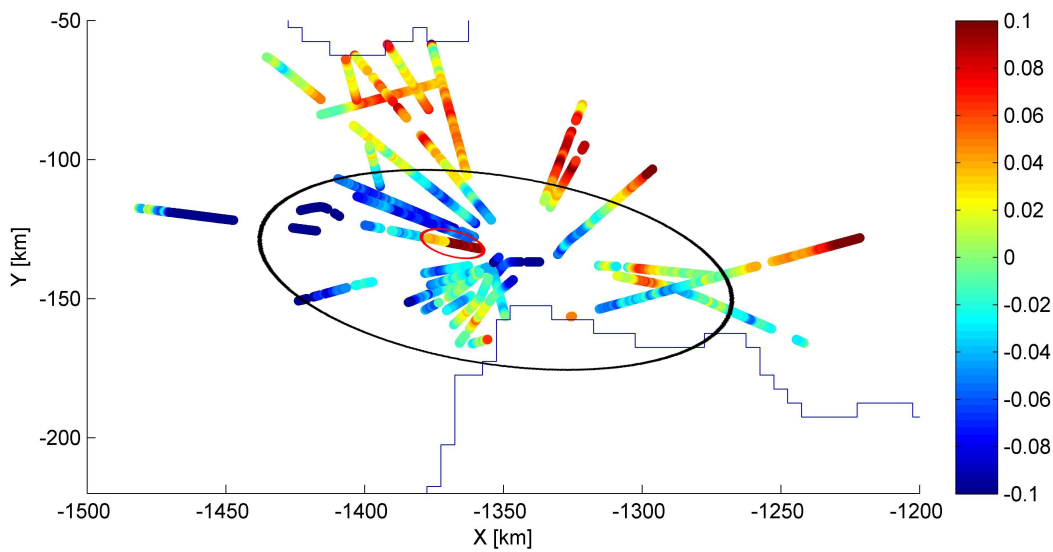


Figure 6.28: *Difference in normalised elevation between observed and modelled layers for the scenario with Layer 2 for internal deformation.*

#### 6.4.1.4 Horizontal and Vertical Resolution

The sensitivity of the model to changes in resolution was also tested for the layer package for a vertical resolution of 11 , 21 and 31. For changes in vertical resolution Layer 1 achieved the same median misfit of 0.026 for all three scenarios. For Layer 2 the median misfit changes from 0.034 for 11 vertical points, to 0.033 for 21 vertical points to 0.032 for 31 vertical points.

By reducing the horizontal resolution to a 4 km grid size the median misfit for Layer 1 stays unchanged at 0.026 and for Layer 2 the median misfit is 0.031. A possible explanation for the slightly lower median misfit for Layer 2 will be discussed later. For both layers the spatial pattern is practically unchanged. In the area marked with grey circles in Figure 6.22 the underestimation of the layer slopes is slightly more pronounced for this scenario than for the control scenario.

#### 6.4.2 Estimating Optimum Parameters

In reality the geometry of the internal layers is determined by the combined effect of basal melting, flow mode and accumulation pattern, while the sections above have considered each effect separately. This section explores the combined effect of the parameters in order to reflect a more realistic scenario. Results from each of the scenarios are shown in Table 6.5.

### 6.4.2.1 Localised Melting or Accumulation

The introduction of areas of spatially varying basal melting or accumulation did not have a significant impact on how well the model captured the slope of the internal layers. This could point towards a more localised area of either increased basal melt or accumulation. To test the hypothesis of more localised changes, two scenarios were constructed with changing accumulation or melt rate based on the area where the model is underestimating the elevation of Layer 1 by more than 0.01 (black lines in Figures 6.29). In the first scenario the basal melt is set to 10% of the accumulation rate, in the second scenario the accumulation is increased by 50%. Both areas were smoothed by a 6 km x 6 km matrix to avoid unrealistically sharp gradients. In general this area coincides with the deepest part of the basin.

Compared to the control scenario (median misfit of 0.026) the fit is improved for Layer 1 both for the scenario with increased basal melt (median misfit of 0.021) and local accumulation high (0.020). For Layer 2, however, the improvement is less than 10% (median misfit of 0.031 for increased basal melt and 0.033 for local accumulation high). The difference between the observed layers and the modelled layers for the increased basal melt case is shown in Figure 6.29. The misfit is improved for Layer 1 (from a median misfit of 0.026 to 0.021) but for Layer 2 the improvement is less than 10% and the spatial pattern of the misfit did not change significantly for Layer 1 nor for Layer 2.

Since a localised basal melt improved the fit of Layer 1, it might be possible to achieve a better fit for a modern accumulation scenario using this basal melt pattern. However, this turned out not to be the case with a median misfit of 0.035 for Layer 1 and 0.034 for Layer 2.

### 6.4.2.2 Internal Deformation and Increased Vertical Resolution

While the results were practically unchanged for changes in vertical resolution in the scenarios with plug flow, Layer 2 especially displayed a sensitivity to changes in vertical resolution for internal deformation. Here it is explored how this sensitivity affects other scenarios by increasing vertical resolution, changing the flow mode to internal deformation and employing the different accumulation pattern and basal melt scenarios discussed above.

When comparing the results from the different scenarios a distinct pattern emerged; while the changes for Layer 1 were fairly small and almost exclusively obtained a slightly worse misfit than the control scenario, Layer 2 changed dramatically.

Comparing the different scenarios with modern accumulation pattern for Layer

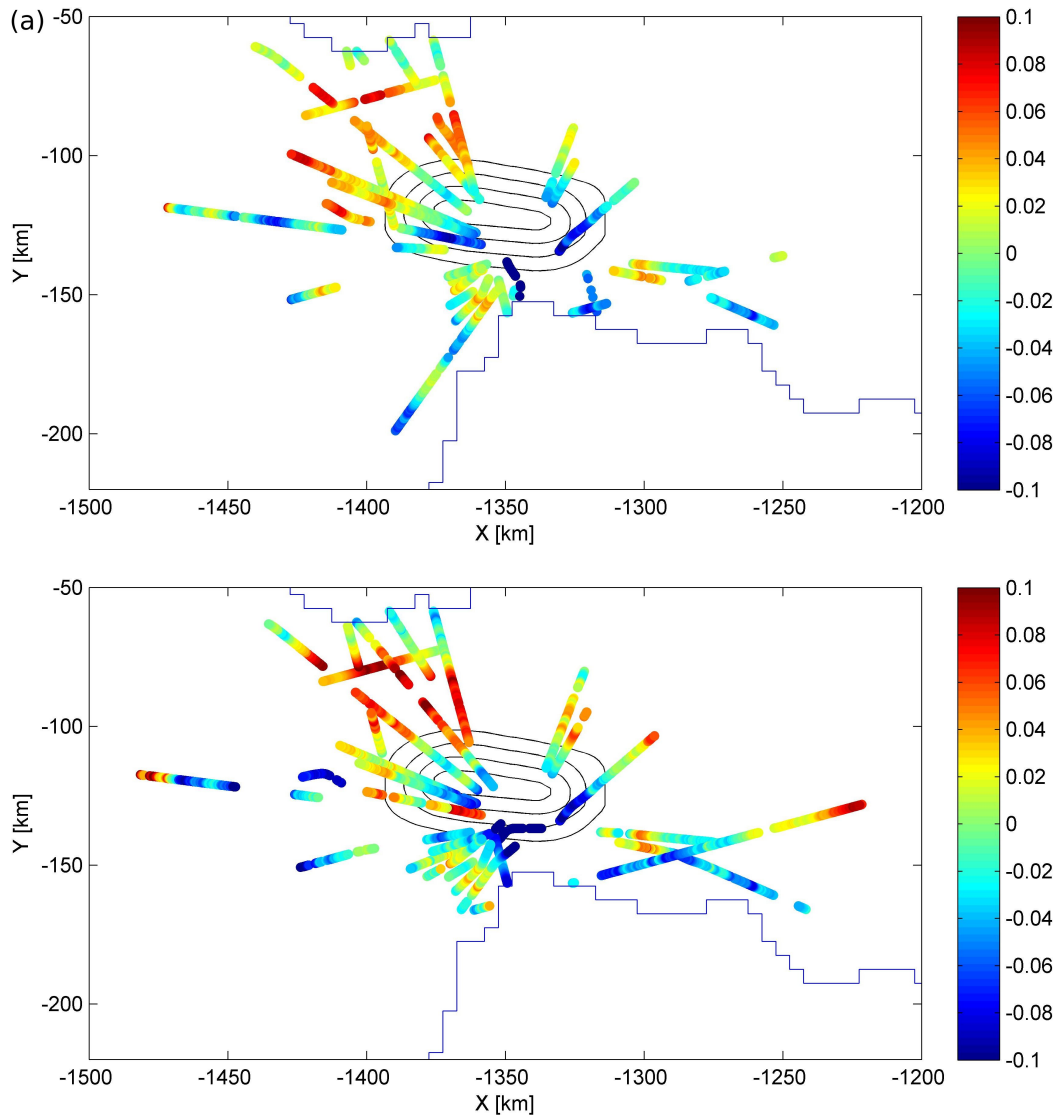


Figure 6.29: *Difference in normalised elevation between observed and modelled layers for non-uniform basal melting for (a) Layer 1 and (b) Layer 2. The blue line is the outline of the PIG catchment basin. The basal melt rate has been set to 10% of the accumulation rate in areas where the distance between modelled and observed layers is larger than 0.01 in normalised elevation (black lines).*

| Scenario                           | Layer 1 | %      | Layer 2 | %      |
|------------------------------------|---------|--------|---------|--------|
| Control                            | 0.026   |        | 0.034   |        |
| Local basal melt area              | 0.021   | (19%)  | 0.031   | (7%)   |
| modern accumulation                | 0.035   | (-32%) | 0.034   | (-1%)  |
| Local accumulation high            | 0.020   | (23%)  | 0.033   | (2%)   |
| 10% basal melting for $H > 2750$ m | 0.027   | (-1%)  | 0.033   | (3%)   |
| $\Delta_\zeta = 21$                | 0.026   | (3%)   | 0.032   | (14%)  |
| modern accumulation                | 0.034   | (-27%) | 0.026   | (22%)  |
| linear accumulation                | 0.030   | (-12%) | 0.026   | (23%)  |
| local accumulation high            | 0.020   | (24%)  | 0.037   | (-10%) |
| Internal deformation               |         |        |         |        |
| $\Delta_\zeta = 11$                | 0.030   | (-13%) | 0.029   | (14%)  |
| modern accumulation                | 0.030   | (-13%) | 0.030   | (14%)  |
| linear accumulation                | 0.030   | (-14%) | 0.027   | (19%)  |
| local accumulation high            | 0.024   | (8%)   | 0.040   | (-18%) |
| $\Delta_\zeta = 21$                | 0.028   | (-7%)  | 0.039   | (-17%) |
| modern accumulation                | 0.030   | (-11%) | 0.028   | (16%)  |
| linear accumulation                | 0.030   | (-13%) | 0.027   | (21%)  |
| local accumulation high            | 0.023   | (13%)  | 0.038   | (-14%) |
| 50% basal melting for $H > 2750$ m | 0.027   | (-3%)  | 0.035   | (-3%)  |
| 10% basal melting for $H > 2750$ m | 0.028   | (-5%)  | 0.037   | (-10%) |
| $\Delta_\zeta = 31$                | 0.028   | (-7%)  | 0.039   | (-17%) |
| modern accumulation                | 0.029   | (-12%) | 0.028   | (17%)  |

Table 6.5: Median values of the misfit for different combined scenarios.

1 the misfit was somewhat improved by changing to internal deformation and increasing the vertical resolution. However, in none of the cases was the fit better than for the control scenario. The same is true for the scenarios with linear accumulation. While the local accumulation high had a significantly better fit, the change to internal deformation reduced the improvement (from an improvement of 20% to less than 10%).

The opposite was true for Layer 2. While a flow mode with internal deformation alone had a significantly worse fit, the introduction of a modern accumulation or a linearly varying accumulation changed the fit to a significant improvement e.g. for internal deformation and  $\Delta_\zeta = 21$  to misfit changed from -17% for uniform accumulation to 16% for modern accumulation pattern and 21% for linear accumulation. However, this improvement was also seen in the case for plug flow and a vertical resolution of  $\Delta_\zeta = 21$ .

For the local accumulation high the misfits continue to be better than the control scenario for Layer 1, although less pronounced, while Layer 2 obtains a worse misfit. In the case of changes in basal melting the corresponding changes in misfit were equal to or less than -10%.

### 6.4.2.3 Summary of Parameter Estimation

When estimating the optimum combination of parameters, the best fit for Layer 1 was obtained by introducing a localised accumulation maximum with the flow mode set to plug flow. If the flow mode was changed to internal deformation the improvement in fit was lost. In contrast Layer 2 obtained the best fits for scenarios with increased vertical resolution and either modern accumulation pattern or linear accumulation, regardless of flow mode. The scenario that achieved the best fit for both layers combined is the scenario with local basal melting or local accumulation high.

Results indicate a complex flow regime but with no clear trend in terms of misfit improvements. A few facts are therefore pointed out here

- Neither Layer 1 nor Layer 2 produced any significantly different misfit in the scenarios with basal melting based on ice thickness regardless of changes in flow mode or increase in vertical resolution.
- It was not possible to improve the fit of Layer 1 using a modern or linear accumulation pattern regardless of vertical resolution, flow mode and basal melt variation.
- A change in flow mode and vertical resolution caused Layer 2 to be a lot more sensitive to changes in accumulation pattern. This was evident when a spatially varying accumulation pattern was introduced in scenarios with internal deformation and increased vertical resolution causing the misfit to decrease significantly.

It could be argued that the most interesting result is that Layer 1 and Layer 2 do not improve simultaneously with changing scenarios. This indicates that the accumulation pattern has changed since the deposition of Layer 1, but also potentially in the time between the deposition of Layer 1 and 2. It also indicates that Layer 2 is likely to be influenced more by internal deformation than Layer 1.

### 6.4.3 Interpretation

Generally, the model does a reasonably good job of fitting the layers even with the simplified data inputs in the control scenario. Compared to the tephra layer, for example, the fit for Layer 1 and Layer 2 was significantly better, which could also be because the tephra layer has had a much more complicated flow history than Layer 1 and Layer 2 since it is located in a faster flowing area. Even so several

of the possible scenarios with spatially varying parameters achieved better fits than the control scenario, but not all the improvements were significant. For example, the overall difference between the control scenario and the scenarios with different basal melting is not very large. Thus the model does not rule out the presence of areas of increased basal melt, but the results indicate that it is unlikely that the location of areas of increased basal melt are controlled by ice thickness. Considering the evidence for areas of increased basal melt in PIG this indicates that they are due to spatial variations in the geothermal heat flux rather than ice thickness.

The two scenarios with changes in accumulation pattern did not achieve a better fit than the control scenario for Layer 1. Indeed, the modern day accumulation pattern had a significantly worse fit than most other scenarios. This is interpreted as an indication that the mean accumulation pattern of PIG has changed since the deposition of Layer 1.

One of the most interesting results is the fact that the misfit for Layer 1 and 2 did not improve simultaneously with changes in model parameters. Since the elevation of Layer 2 is deeper than Layer 1, it is expected that Layer 2 is more influenced by internal deformation. However, the distance between Layer 1 and Layer 2 is not very large and it is surprising that changes in parameters lead to significantly different changes in misfit. This could indicate that while Layer 1 exists in ice that is shallow enough not to be influenced significantly by internal deformation, Layer 2 might be located close to a threshold elevation below which internal layer deformation is far more pronounced. In other words, the transition in the ice where the horizontal velocity decreases, the so-called *kink height* (Dansgaard and Johnsen, 1969), is likely to be located at an elevation close to Layer 2. Furthermore, considering that the misfit changed significantly between the layers for different accumulation patterns there is an indication that while the accumulation pattern has changed since the time of deposition of Layer 1, there might also be a change in accumulation between the time of deposition of Layer 2 and the deposition of Layer 1.

In summary, the results discussed in this section have provided some important insights into the parameters that control the flow of PIG. However, the layers themselves do unfortunately not provide any means of estimating an age range for the parameters discussed here. This problem will be addressed in the following section.

## 6.5 Estimating Age and Accumulation Values

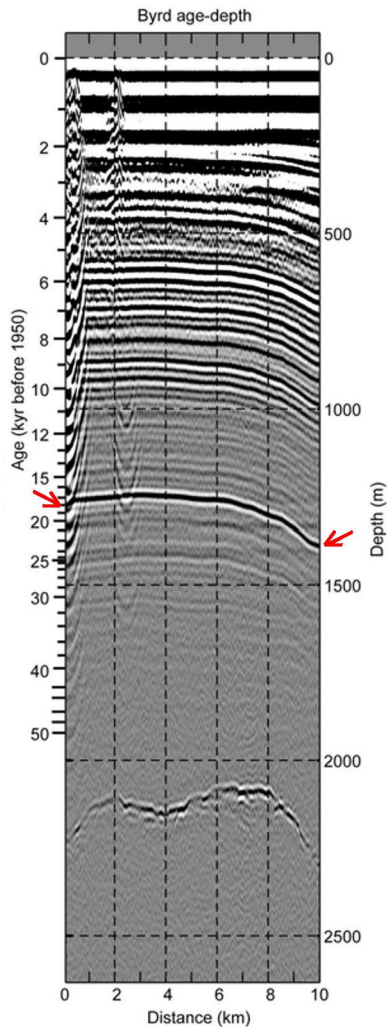


Figure 6.30: *Figure 4 from Jacobel and Welch (2005) showing the radar profile near Byrd Station. The 17.5kyr horizon is clearly visible as a strongly reflecting layer (marked with red arrows).*

The sections above have discussed accumulation values in relative terms. In order to retrieve an absolute value for the accumulation, the age-depth relationship for PIG must be established. However, since no deep ice cores have been drilled in the PIG basin, it is difficult to obtain an estimate of the age of the observed internal layers.

One area of the basin where the age-depth relationship is known is the area that contains the tephra layer. Since the tephra layer represents a relatively recent deposition (Corr and Vaughan, 2008) it is expected that the accumulation values resemble modern day values.

Another area where the age-depth relationship can be inferred is the neck between the northern and southern basin. This relies on radar data from a ground-based radar survey carried out by the United States in years 1999-2002 as part of the International Trans-Antarctic Scientific Expedition (ITASE). The surveys (named US-ITASE) used Byrd Station as starting point and each year travelled in a different direction. The survey of interest here was conducted in 2001 (Welch and Jacobel, 2003; Jacobel and Welch, 2005) and crosses the PIG catchment basin very close to the bottleneck between the northern and southern basin and thus the centre of the layer package described in the section above.

The survey was carried out with a 3 MHz centre frequency radar system and numerous internal layering was identified. For more information on the radar system and the results from the surveys see Welch and Jacobel (2003) and Jacobel and Welch (2005).

One strongly reflecting layer was identified in the radar data acquired over the area around Byrd Station with reflection strengths of the same magnitude

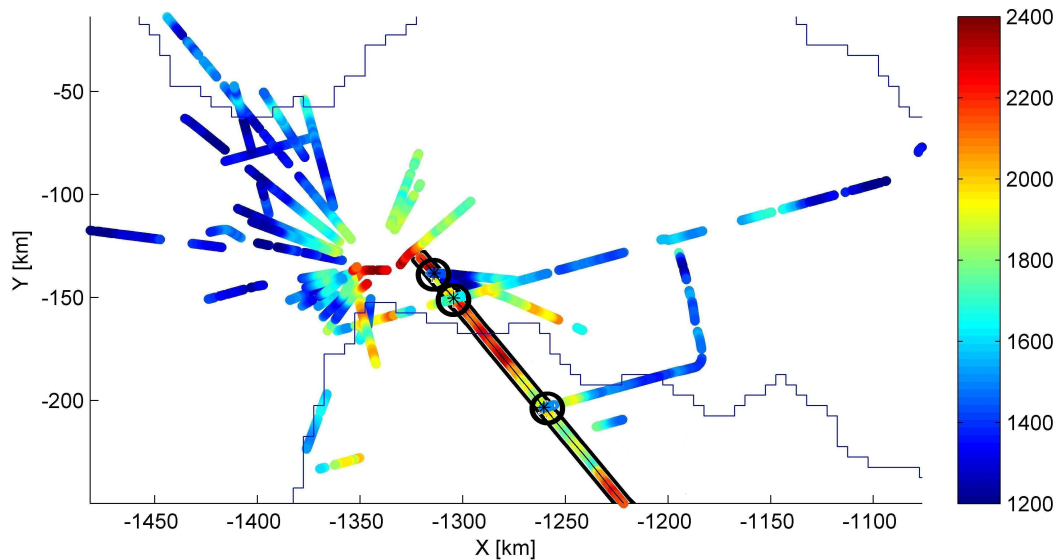


Figure 6.31: *Depth in metres of Layer 2 (colour) and depth of layer traced in the US-ITASE radar survey (colour with black lines). Three locations where Layer 2 and the 17.5 kyr horizon intersect have been marked with black circles.*

as the bed rock (Figure 6.30). This layer was found to correspond to an acidity anomaly first identified by Hammer et al. (1997) and was dated using the ice core chronology by Blunier and Brook (2001) to an age of 17.5kyr old. The layer can be traced all the way to the PIG basin (Jacobel and Welch, 2005) (Figure 6.31).

### 6.5.1 Methods

The tephra layer was easily identifiable in several radargrams and has already been traced as described in Chapter 5 and used as input in BASISM. For the 17.5kyr horizon, however, it proved impossible to identify this one particular layer in the PIG dataset. This could be due to a number of factors. For example, the frequency of the radar used by US-ITASE is lower than that of the PASIN radar used by BAS thus the resolution of the layers will be less. The strong acidity signal measured in the Byrd ice core represents a multiple pulsed acidity variation that stretches over 170 yr (Hammer et al., 1997) thus given the higher frequency of the PASIN radar it is possible that the layer in fact shows up in the PIG dataset as multiple reflecting lines rather than one single line (pers. communication, R. Jacobel, 2010). Furthermore, since the strength of the line decreased with distance from Byrd Station (Jacobel and Welch, 2005) it is also possible that the anomaly is too weak to be picked up by the PASIN radar especially considering the depth of the layer.

Comparing the elevation of Layer 1 and Layer 2 with the elevation of the 17.5kyr layer (data is available from the National Snow and Ice Data Center

| $(x, y)$ [km] | Layer 2 | 17.5kyr horizon | Distance between layers |
|---------------|---------|-----------------|-------------------------|
| (-1260,-200)  | 1.5 km  | 1.9 km          | 0.4 km                  |
| (-1300,-150)  | 1.7 km  | 2.0 km          | 0.3 km                  |
| (-1314,-138)  | 1.4 km  | 2.3 km          | 0.9 km                  |

Table 6.6: Depths of Layer 2 and the 17.5kyr horizon and the distance between the two layers at the three locations where they overlap.

(2010)) it is clear that the 17.5kyr is deeper than Layer 2 (Figure 6.31). This provided an indirect age constraint on the observed layer package since both layers therefore must be younger than 17.5kyr. Three locations were identified where the 17.5kyr horizon intersected with lines containing Layer 2. Most of the US-ITASE line was outside the PIG catchment basin, but the part of the US-ITASE line that was inside the basin provided a small area where the age at a certain depth is known. The depth of the horizon was converted to normalised elevation and used as input in BASISM model. In the absence of knowledge of surface and bed topography measured directly from the radar survey, the gridded surface and bed maps from the PIG dataset were used.

In order to get an estimate of the mean accumulation values since the time of deposition of a layer, a relation between depth and accumulation rate based on the Dansgaard-Johnsen model (Dansgaard and Johnsen, 1969) can be obtained from:

$$a = \frac{2H - h}{2t} \ln\left(\frac{2H - h}{2z - h}\right) \quad , \quad h \leq z \leq H \quad (6.5)$$

where  $a$  is the accumulation value from the time the layer was deposited until present time,  $H$  is ice thickness,  $z$  is elevation above the bed and  $t$  is the age of the layer. The precision of Equation 6.5 depends amongst other things on a good approximation of the value of  $h$  which is generally not known. Previous studies have used the value of  $h = 400$  m for Greenland (Siegert and Payne, 2004) and West Antarctica (Siegert and Payne, 2004). For want of better estimates of  $h$  in the PIG catchment this value will also be used here. Siegert and Payne (2004) note that the equation is thought to be fairly accurate in the upper 80% of the ice. The mean normalised elevation of the 17.5kyr horizon is 0.25 i.e. in the upper 75% of the ice. The accumulation estimate from Equation 6.5 for this horizon is therefore not expected to be more than a guideline. Even so this method has been applied in other studies of WAIS accumulation rates (e.g. Siegert and Payne, 2004; Jacobel and Welch, 2005) with good results.

The model was now run with different scenarios with accumulation rates in the range of what was predicted from Equation 6.5 in order to achieve a prediction of the age for the layers and thus an estimate of past accumulation rates.

### 6.5.2 Results

The mean distance between Layer 2 and the 17.5 kyr horizon is 500 m (see Table 6.6) based on the three locations where they intersect. Since the age of the layers increases exponentially towards the bed Layer 2 might be substantially younger than the 17.5 kyr horizon.

Based on the control scenario, that has an accumulation value of  $1 \text{ m yr}^{-1}$ , the model returns an age for the 17.5 kyr horizon of 4.8 kyr. This is substantially younger than the actual age of the layer indicating that the accumulation value must be significantly lower. Equation 6.5 returns a mean accumulation rate of  $0.25 \text{ m yr}^{-1}$ . The model is therefore run with different scenarios with accumulation ranging from  $0.1 \text{ m yr}^{-1}$  to  $0.35 \text{ m yr}^{-1}$  and constant basal melt of 1% of the accumulation rate. The scenario that obtains the age closest to 17.5 kyr turned out to be the scenario with an accumulation of  $0.25 \text{ m yr}^{-1}$ . In this scenario the age of Layer 2 is 10.7 kyr and the age of Layer 1 is 7.9 kyr.

For the tephra layer Equation 6.5 returns an average accumulation rate of  $0.33 \text{ m yr}^{-1}$  which is almost one-third higher than the accumulation values estimated from the 17.5 kyr horizon. If this value is used as the input for a uniform accumulation pattern the model returns an estimate of the age of the tephra layer as 2.0 kyr which is reasonably close to the date from the Siple Dome ice core (2.3 kyr). Using this accumulation value the model returns ages for Layer 1 of 6.0 kyr and 8.1 kyr for Layer 2 (see also Table 6.7).

|  | Layer 1 | Layer 2  |
|--|---------|----------|
| $a = 0.33 \text{ m yr}^{-1}$<br>(tephra layer)     | 6.0 kyr | 8.1 kyr  |
| $a = 0.25 \text{ m yr}^{-1}$<br>(17.5 kyr horizon) | 7.9 kyr | 10.7 kyr |

Table 6.7: Estimated ages of Layer 1 and 2 where  $a$  denotes accumulation value based on either the tephra layer or the 17.5 kyr horizon.

### 6.5.3 Interpretation

It should be noted that the estimate of age and accumulation values is based on a simple trial and error, by changing the accumulation value to obtain the correct age of the 17.5 kyr horizon. The value of the accumulation of  $0.25 \text{ m yr}^{-1}$  is lower than modern day values of approximately  $0.35 \text{ m yr}^{-1}$  (Arthern et al., 2006), and somewhat lower than estimates by Jacobel and Welch (2005) from the US-ITASE data ( $0.3 \text{ m yr} - 0.35 \text{ m yr}$ ). Furthermore, previous studies that have found evidence for accumulation values being half of modern day values

over the WAIS for the past 6.4 kyr - 16 kyr years (Siegert and Payne, 2004). The results presented here are only approximately 70% of modern day accumulation values but this might be due to the fact that the study by Siegert and Payne (2004) penetrates into the interior of the WAIS across the main ice divide where accumulation rates are likely to be lower than for PIG due to the higher elevation.

The calculation of the accumulation rates from the tephra layer is in a way redundant. The age estimate of the tephra layer from Corr and Vaughan (2008) is based on the Dansgaard-Johnsen model (i.e. Equation 6.5) using modern day accumulation values as input. It is therefore not surprising that the accumulation rate retrieved here is similar to modern values. It is, however, reassuring that the BASISM model returns a reasonable age estimate of the tephra layer for this accumulation value.

The obtained age-depth relationship allows for a return to previously investigated but undated areas of PIG. Assuming that the accumulation rate of  $0.25 \text{ m yr}^{-1}$  adequately represents past conditions, the accumulation rate can then be used to date the buckled layering identified upstream of Tributary 3 (see Section 5.1.1.3). Thus with an accumulation rate of  $0.25 \text{ m yr}^{-1}$  the age of the transition to buckled layering is estimated to be 10 kyr old (Figure 6.32). If the age estimate is correct this implies that the onset of enhanced flow in Tributary 3 changed location approximately 10 kyr ago.

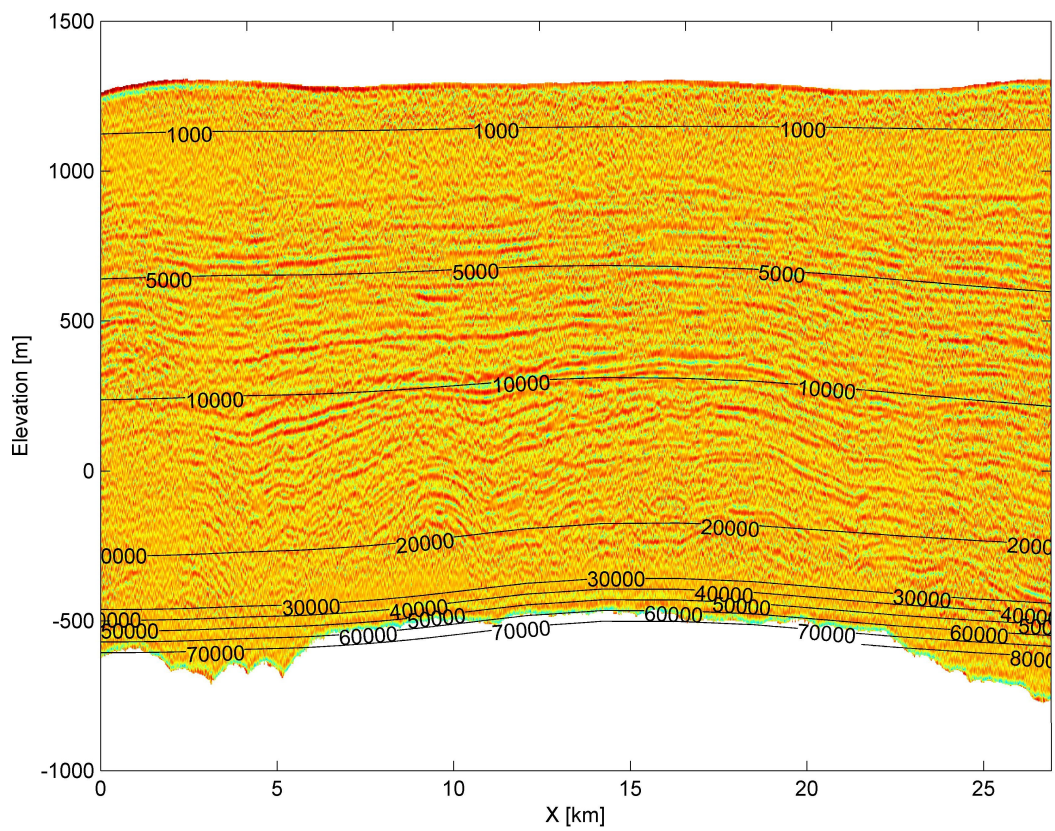


Figure 6.32: Age distribution (black contour lines) in flightline 10, upstream of Tributary 3 using an accumulation rate of  $0.25 \text{ m yr}^{-1}$ . The onset of buckled layering with depth corresponds to the 10 kyr horizon.

## 6.6 Discussion

The individual layer fitting showed that accumulation rates and basal melt are likely to be taking place over spatial scales that are longer than the average layer length i.e.  $\sim 10$  km. This compares well with results from several studies that reconstructed accumulation rates over West Antarctica from RES data (e.g. Nereson et al., 2000; Siegert and Payne, 2004; Neumann et al., 2008). The accumulation pattern was often found to vary over wavelengths from several tens to several hundreds of km.

On a smaller scale variations in accumulation are often observed in the near-surface layers as exemplified in a study by (Vaughan et al., 1999) (see Figure 2.5 in Section 2.2.4). However, these anomalies only affect the near-surface layers that were not considered in this thesis.

Modelling of the layer package, that was identified in the neck between the northern and southern basin, indicated that the accumulation pattern is likely to have been different since the deposition of Layer 1. Previous studies have found evidence for past changes in accumulation rates over the WAIS (based on the Byrd ice core and RES data) (Siegert and Payne, 2004). Is it possible then that a change in accumulation values have coincided with a potential change in accumulation pattern?

The variation in climate in Antarctica is controlled by the Antarctic Oscillation (Thompson and Wallace, 2000) and studies have shown that the accumulation pattern is strongly controlled by surface topography leading to high accumulation rates in coastal areas with decreasing rates inland (van den Broeke et al., 2006). This explains why the scenario with a linear accumulation pattern obtains equally good fits compared to the scenario with modern day accumulation, however, it does not explain why the modern day scenario in general performs less well than the scenario with uniform accumulation for Layer 1. Studies of past accumulation from RES data over the Siple Dome area indicated a change in accumulation rate but returned inconclusive results with regards to a change in accumulation pattern (Nereson et al., 2000). Neumann et al. (2008) calculated accumulation rates across the WAIS ice divide and found evidence for changes in accumulation rate during the past 8 kyr but concluded that the spatial pattern of accumulation is unlikely to have changed significantly. However, it should be noted that both studies have a more limited spatial extent than the data investigated here and it is therefore possible that the dataset considered in this thesis is capturing changes that previous datasets would not necessarily reflect.

The fact that the optimum parameters for fitting Layer 1 and Layer 2 are not identical indicates a time dependence in the parameters. This is most likely due to changes in accumulation pattern between the deposition of the two layers but complicating flow dynamics might also impact the layer geometry (R. C. A. Hindmarsh, pers. communication, 2010). This can also be illustrated by considering the difference in normalised elevation between the two layers. If the accumulation pattern had remained unchanged in the time between their deposition the difference in normalised elevation between the layers would have been more or less uniform. However, in Figure 6.33 it is clear that there is a spatial variation in the difference in elevation. This observation further supports the results indicating one or several past changes in accumulation pattern.

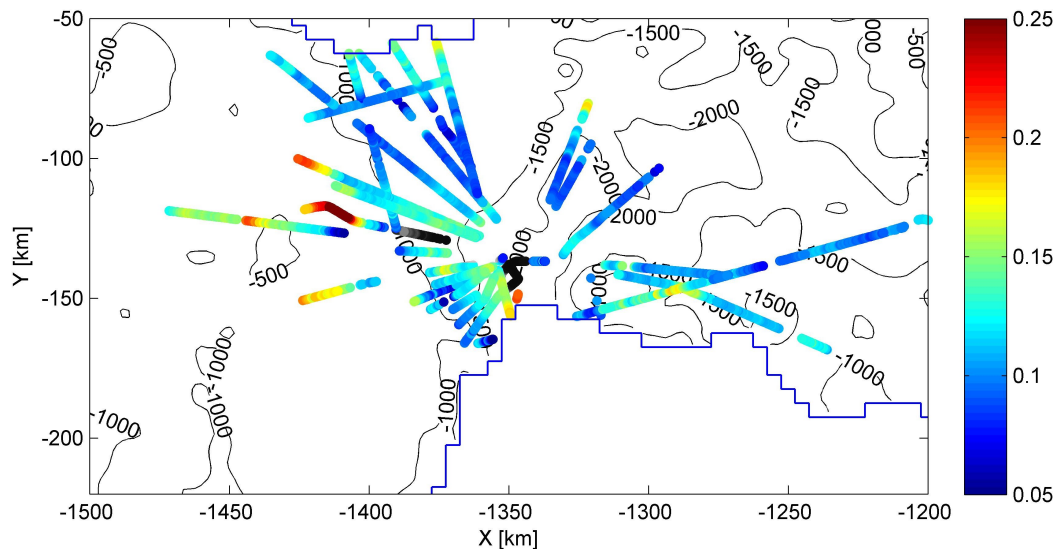


Figure 6.33: *Distance between Layer 1 and Layer 2 in normalised elevation. The black contours outline the bed topography in metres elevation. The two areas in grey scale are disregarded due to anomalous values. They are also identical to the flightlines that were disregarded in the analyses above.*

Two age-depth relationships were obtained indirectly by calculating accumulation rates based on the known ages of the tephra layer and the 17.5 kyr horizon. Considering that the tephra layer is located in a different part of PIG than the layer package it seems more likely that the ages obtained from fitting the 17.5 kyr horizon are representing age and accumulation values better. Thus the accumulation rate averaged over the past 17.5 kyr is estimated to be approximately  $0.25 \text{ m yr}^{-1}$ . With this in mind it is tempting to link the obtained age of Layer 1 of 7.9 kyr to a tephra layer identified in the Byrd ice core of the age of approximately 7.5 kyr thought to originate from an eruption of Mount Takahē (Wilch et al., 1999). An equally interesting link between the two strongly reflecting

lower layers (where Layer 2 is the upper of the two) emerges when comparing the age of Layer 2 with acidity measurements of the Byrd ice core by Hammer et al. (1997). In the interval between 9.7 kyr and the start of the acidity high that characterises the 17.5 kyr horizon (no measurements were made of the ages between 2.4 kyr and 9.7 kyr), two peaks stand out with twice as high acidities as the other measurements. The two peaks correspond to an age of 10.2 kyr and 11.4 kyr i.e. reasonably close to the estimated age of Layer 2 of 10.7 kyr. However, in order to justify both these links the spatial extent and reflectivity of the layers would need to be investigated and the layers traced from the Byrd ice core to PIG. That is beyond the scope of this work.

The estimated accumulation rate is lower than present day rates in agreement with other studies of West Antarctica (e.g. Siegert and Payne, 2004). Regional climate models show that accumulation decreases by up to 30% in West Antarctica when the circumpolar vortex is strong (van den Broeke and van Lipzig, 2004). The results thus indicate that the circumpolar vortex was in a strong mode before the beginning of the Holocene, however, the climate variability of Antarctica is not fully understood and this link needs to be explored more fully before drawing any final conclusions (Neumann et al., 2008).

The suggested change in the onset of enhanced flow in Tributary 3 was dated to be approximately 10 kyr old. This is reasonably close to the estimated transition to Holocene climate, where the elevation of WAIS is thought to have been higher by several hundred metres (e.g. Huybrechts, 2002). It is also within the same time period that PIG most likely experienced considerable changes at its margin with at least one rapid retreat occurring (Anderson et al., 2002). This retreat could have affected flow patterns upstream of the grounding line. Thus even if accumulation rates and ice thickness had stayed the same the dynamics of the glacier could have changed in response to downstream forcings. If as suggested a large amount of ice was lost (Lowe and Anderson, 2002) this would significantly have impacted the mass balance of the glacier as well. Thus the results indicate that the flow pattern of PIG may have changed in response to a climate transition. However, predicting the paleaeo-flow pattern would require a much more detailed knowledge of past elevation and accumulation rates than is available at present and would be beyond the scope of this thesis.

## 6.7 Conclusion

In this section modelled internal layers calculated by the three-dimensional flow model BASISM have been fitted to observed layers that have been traced in several flightlines. A range of different parameters, including vertical resolution, accumulation, basal melting and flow mode, have been used as input in the three-dimensional BASISM model to investigate the influence on the model fit. The goodness of the fit of the modelled layers was used as a proxy for how well the model parameters captured the real physical system.

For the individually fitted layers only an insignificant change in value and spatial distribution of the misfit was observed between each scenario. This most likely indicate that since the layers are fitted individually the misfit will only capture influences from parameters on the same spatial scale as the length of the layers. Changes in accumulation patterns and basal melt are therefore most likely occurring over larger spatial scales.

For the layer package the model proved a lot more sensitive to changes in parameters. Results showed that while Layer 2 was most sensitive to changes in flow mode, Layer 1 was more sensitive to changes in accumulation pattern. The best fit for Layer 2 was obtained with a change to internal deformation and non-uniform accumulation pattern with either linearly varying or modern day accumulation. As a contrast Layer 1 never achieved a fit with a modern accumulation pattern that was better than the simple uniform accumulation. This was interpreted as an indication that the accumulation pattern has changed since the deposition of Layer 1. Finally, the fact that Layer 1 and Layer 2 did not achieve an improved fit for the same scenarios is taking as indication of difference between the depositional history of the layers. For example, Layer 2 is likely to have been affected more by internal deformation due to its lower elevation. It is also possible that the accumulation pattern has changed between the deposition of the two layers.

Using data from a US-ITASE survey and an age-depth chronology from the Byrd ice core (Jacobel and Welch, 2005) an age-depth relationships were established for the PIG basin. The US-ITASE data contained a 17.5 kyr horizon and using the depth of this layer an accumulation estimate of  $0.25 \text{ m yr}^{-1}$  was found. This corresponds to an approximate age for Layer 1 and Layer 2 of 7.9 kyr and 10.7 kyr respectively. The ages fit with a tephra layer identified in the Byrd ice core of the age of 7.5 kyr and a peak in acidity at 10.2 kyr. The age of Layer 2 thus might correlate with the transition to and/or beginning of the Holocene climate.

Assuming that the age estimates are correct this implies that the accumulation pattern over PIG has changed during the past approximately 7 kyr and that accumulation rates have been approximately 30% lower than present day values averaged over 17.5 kyr. Results also indicate that a second change in accumulation pattern could have taken place in the period between 10 kyr to 7 kyr before present.

Finally, based on this accumulation rate the change in location for onset of fast flow in Tributary 3, that was identified in Section 5.1.1.3, was dated to be approximately 10 kyr old. Indicating that the flow pattern of PIG could have changed in connection with the transition to Holocene climate.

# Chapter 7

## Two-Dimensional Flow Model

In order to investigate the stratigraphy of the data in more details a two-dimensional model has been set up as described in Section 4.3.2. The two-dimensional model is in some respects a special case of a three-dimensional model, in the sense that the two-dimensional model only works along flowlines, but in those locations the results from the two models should be identical. Although the fact that the model is two-dimensional imposes some restraints on the model results, the reduction to two dimensions means that it is possible to use topography with a significantly higher resolution than in the three-dimensional model. This is due to a significant reduction in computational time.

This chapter contains results from and discussion of the two-dimensional model. Section 7.1 contains an overview of the approach used for the two-dimensional model including a discussion of the model parameters. In Section 7.2 the two-dimensional model is first tested by comparing the output with results from BASISM using the same input parameters and resolution. The parameters are then changed to the high resolution topography from the picked radar data and compared against the observed radar and the results from BASISM. Finally, Section 7.3 discusses the results further along with the advantages and disadvantages of the two models.

### 7.1 Modelling Approach

A two dimensional model can only simulate ice flow along flowlines i.e. along lines where the ice is assumed to move only in the  $(x, z)$ -plane (see Section 4.3.2). A number of flowlines in the PIG catchment basin were therefore calculated. This was done using a program made available by Julian B. T. Scott, British Antarctic Survey (see Section 4.3.1).

In order to use topography from the radar data in the two-dimensional model,

the flightlines must coincide with flowlines. If a flightline is coinciding with a flowline it is reasonable to assume that the bed topography from the radar data is directly transferable as bed topography under a flowline. Using these flightlines will therefore give a very high resolution insight into the influence of bed topography on the layers.

Since the PIG dataset was acquired with the main purpose of mapping subglacial topography very few of the flightlines coincide with flowlines in the ice. Fortunately three flowlines have been identified that are close to flightlines. Figure 7.1 shows the location of the three flowlines. The flowlines will be referred to as flowline 1 (red line), 2 (blue line) and 3 (green line). Flowline 1 is very close to flightline 11, and flightlines 24 and 14 almost coincide with flowlines 2 and 3. Running the two-dimensional model with surface and bed topography from these three flowlines enable a comparison with the observed data as well as the results from the three-dimensional model.

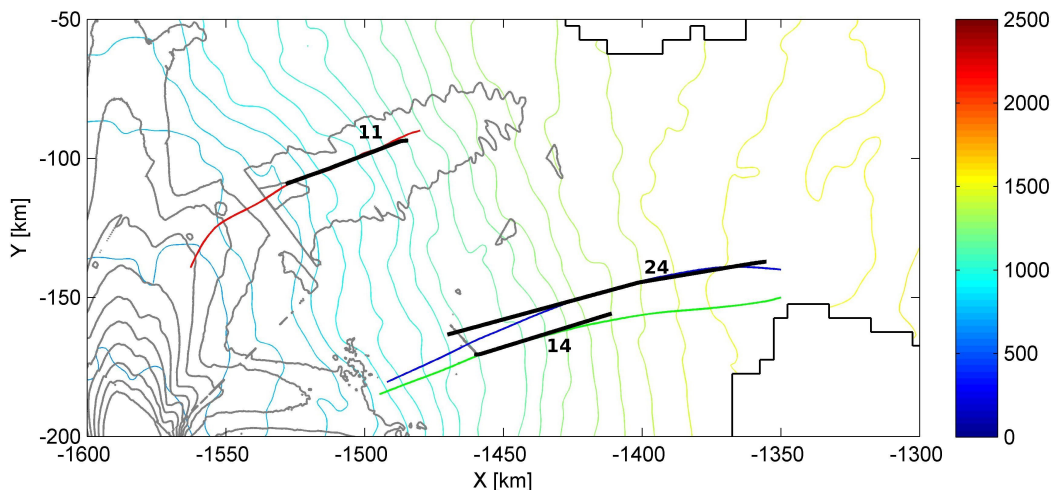


Figure 7.1: Location of flowline 1 (red line), flowline 2 (green line) and flowline 3 (blue line) with surface elevation in metres as coloured lines, surface velocity (grey contour lines) and flightlines 11, 24 and 14 (thick black lines).

## 7.1.1 Model Parameters

### 7.1.1.1 Surface and Bed Topography Input

The sampling rate of the radar and thus the resolution of the imaged bed is on the scale of 30 m. This resolution generated too many data points to be handled by the model and the resolution was therefore reduced to approximately 1 km before the observed topography were used as model input. Studies have shown that if the wavelength of the bed rock undulations is smaller than the ice thickness then the ice will simply override the topography with little impact on the overall

layer stratigraphy (Hindmarsh et al., 2006). The radar bed topography was first resampled with an even spacing equal to the mean spacing between data points (typically about 30 m). The data were then smoothed with a moving filter using a window size that gave a smoothing of the same scale as the average ice thickness (e.g. 1 - 2 km) and finally the horizontal resolution of the data was reduced to the same scale as the average ice thickness.

#### 7.1.1.2 Surface Velocity

In order to generate internal layers the two-dimensional model needs a velocity field. The surface velocity can be assessed in several ways, one of which is to assume zero mass influx at the start of the flowline and then calculate the velocity based on the input mass balance assuming steady state (see Equation 4.13, Section 4.3.2). However, since all three flowlines originated at positions where mass is being added from further upstream this led to significant errors in the surface velocity calculation. The horizontal velocity in the two-dimensional model was therefore calculated assuming steady state but using the balance velocity from the three-dimensional model at the starting point. The vertical velocity is then found using the continuity equation (Equation 2.11).

This way of implementing the velocity field means that the two-dimensional model forces an assumption of no net mass gain or loss. Thus the velocity is tied to the mass input and the ice thickness. If the horizontal velocity was independent on mass input this would lead to an increase or decrease in mass and in the real world the system would respond with a change in surface elevation. However, implementing surface elevation changes in the model introduces a whole new set of problems since this requires knowledge of past accumulation rates. This would significantly complicate the model and most likely not lead to any improvement in the layer calculations since the unknowns associated with estimating the past mass input and surface elevations are significant.

#### 7.1.1.3 Boundary Condition

During the initial model tests it became clear that using the analytical, one-dimensional, solution of the age equation as a boundary condition was insufficient. This is most likely due to the fact that the one-dimensional solution is based on no influx of mass, thus the model will perform well close to an ice divide but significantly less well when there is an influx of mass. All the flowlines considered here have a non-zero influx of mass at the starting point. This problem was solved by using the age calculated by BASISM as boundary condition at the starting

point of  $x = 0$ .

## 7.2 Results

In order to test the two-dimensional model, the model results were first compared to results from BASISM qualitatively along the three flowlines with the same surface and bed topography in both models. Then the results from the two-dimensional model with increased resolution topography were compared qualitatively to the radar data along the flowlines. Finally, the fit of the layers were quantified and compared to the fit obtained with BASISM.

### 7.2.1 Test of Two-Dimensional Model

The two-dimensional model is compared with results from the three-dimensional model in order to test the model results. The models have therefore been initiated with the same surface and bed topography, accumulation and melt rate.

In Figure 7.2a the results from the two-dimensional model (black lines) for flowline 1 in Tributary 3 are shown with the results from the three-dimensional model (red lines). The models agree very well at distances 0 - 80 km but less well further downstream. Notice how the layers calculated with the three-dimensional model undulates more than the two-dimensional model downstream of distances of approximately 100 km. In flowline 2 the difference between the two models was largest at the middle of the flowline (at distances between approximately 30 km to 80 km) and smallest at the beginning and end (Figure 7.2b). The best agreement between the two models is reached in flowline 3 (Figure 7.2). In spite of the differences between the models, the agreement was generally quite good. A possible reason for the differences is discussed in Section 7.3.

### 7.2.2 Comparison with Radar Data

The model input is now changed to the picked bed topography from flightlines 11, 14 and 24. Except from a smoothing of the scale of the ice thickness as mentioned above the topography corresponds to that observed in the radar data. The results are shown with radargrams and with the results from the two-dimensional as black lines and results from BASISM as red lines. This comparison focuses on the qualitative agreement between observations and model results, the goodness of the fit will be quantified in the next section. The fit between observations and model for the two-dimensional model will be presented first and then compared to the three-dimensional results afterwards.

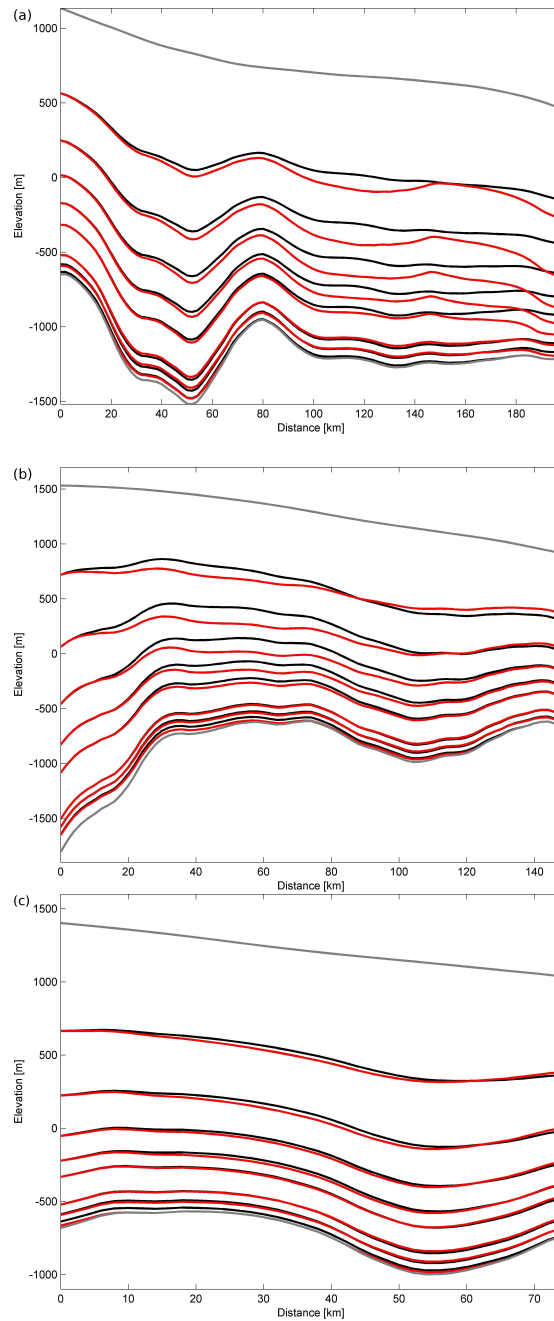


Figure 7.2: Result from the two-dimensional model (black lines) along (a) flowline 1 and (b) flowline 2 and (c) flowline 3 and results along the same flowline from the BASISM model as red lines. The gridded surface and bed topography are marked with thick grey lines.

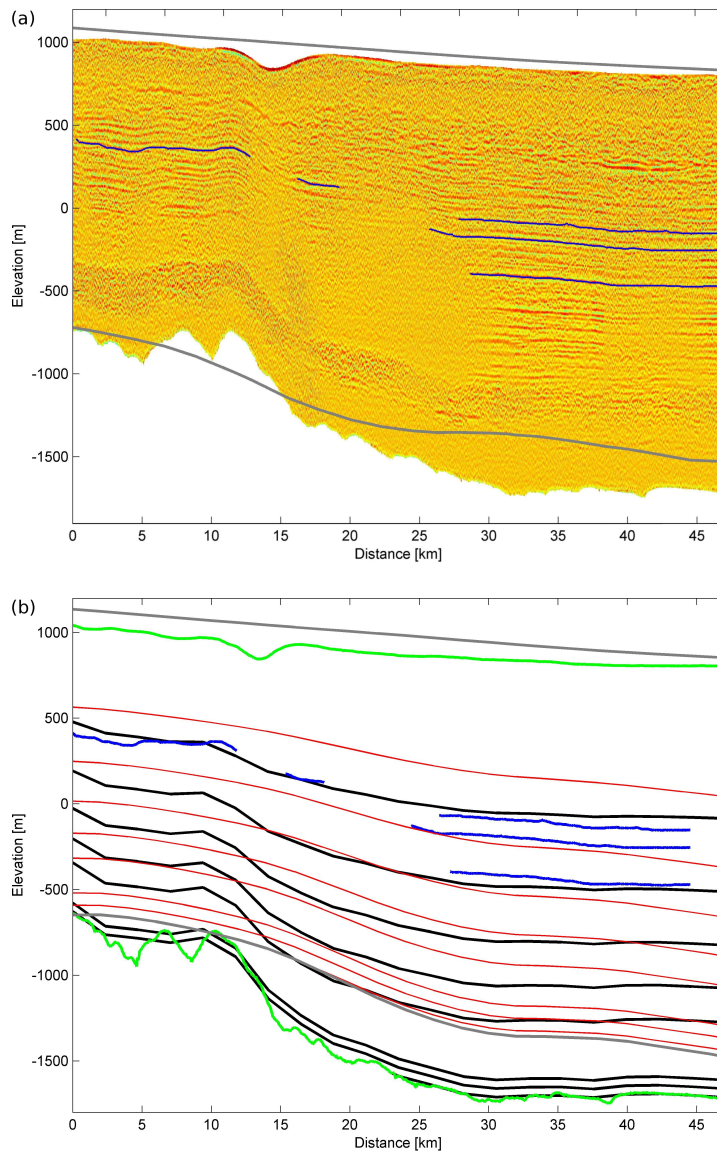


Figure 7.3: (a) Radar data from flightline 11. Some internal layers have been picked with blue line to emphasise their stratigraphy. The thick grey lines are gridded surface and bed topography. (b) Modelled layers in flightline 11 in contours. For comparison the results from the three-dimensional model are plotted in red lines and a few of the observed layers have been added with blue lines. The surface and bed topography from the radar data are shown in green lines.

Figure 7.3a shows the radar data from flightline 11 with a few of the internal layers picked out in blue. Figure 7.3b shows the internal layers calculated for the control scenario. Most of the layers are represented quite well by the model and the general shape and the flatness of the layers correspond well with observations. The first internal layer situated at distances 0 - 10 km is captured well by the model, the shape of the layer reflects the bed topography and the slope is close to that of the observed layer. For the layers furthest to the right in Figure 7.3 the shape of the modelled layers is quite similar to the observed layers, although the slope of the modelled layers is less steep than the observed layers.

The data and results for flightline 14 (flowline 2) are shown in Figure 7.4a (radar data) and Figure 7.4b (model results). Generally, the two-dimensional model is able to capture a lot of the layer stratigraphy correctly. There is especially good agreement between the model and observations in the left hand side of the figure. The radar data at distances 20 - 35 km have a slightly steeper slope than the model, but the general agreement is quite good.

In Figure 7.5 the radar data from flightline 24 are shown with the modelled results. The flow direction is downslope (e.g. from left to right). Again the fit is best in the beginning of the flowline (distances 0 - 30 km), while further downstream the modelled layers have a significantly different slope than the observations (distances 50 - 70 km). For the two layers furthest downstream the fit improves again.

For comparison the results from the three-dimensional model are plotted as red lines in Figures 7.3b, 7.4b and 7.5b. Notice how the small-scale undulations of the bed are not captured by the three-dimensional model and in one case (Figure 7.3) due to the gridded bed topography, the three-dimensional model considerably underestimates the ice thickness. Generally, with the higher resolution bed topography the two-dimensional model performs better in terms of capturing the layer stratigraphy correctly. Even so the agreement between the models is quite good when it comes to the general layer slope.

### 7.2.3 Layer Fitting

In order to compare the model and layers more quantitatively the fit of the layers from the two-dimensional model is calculated using a layer fitting routine (see Section 4.3.2.3). Results from the layer fitting are given in Table 7.1. An example of the layer elevations (green lines) and modelled elevations (red lines) is shown in Figure 7.6 for the layers in flightlines 24. The mean median misfit for all layers is 0.010 (with a maximum misfit of 0.022 and a minimum of 0.002). For flightlines 11 and 14 the mean median misfits are 0.009 and 0.007 respectively .

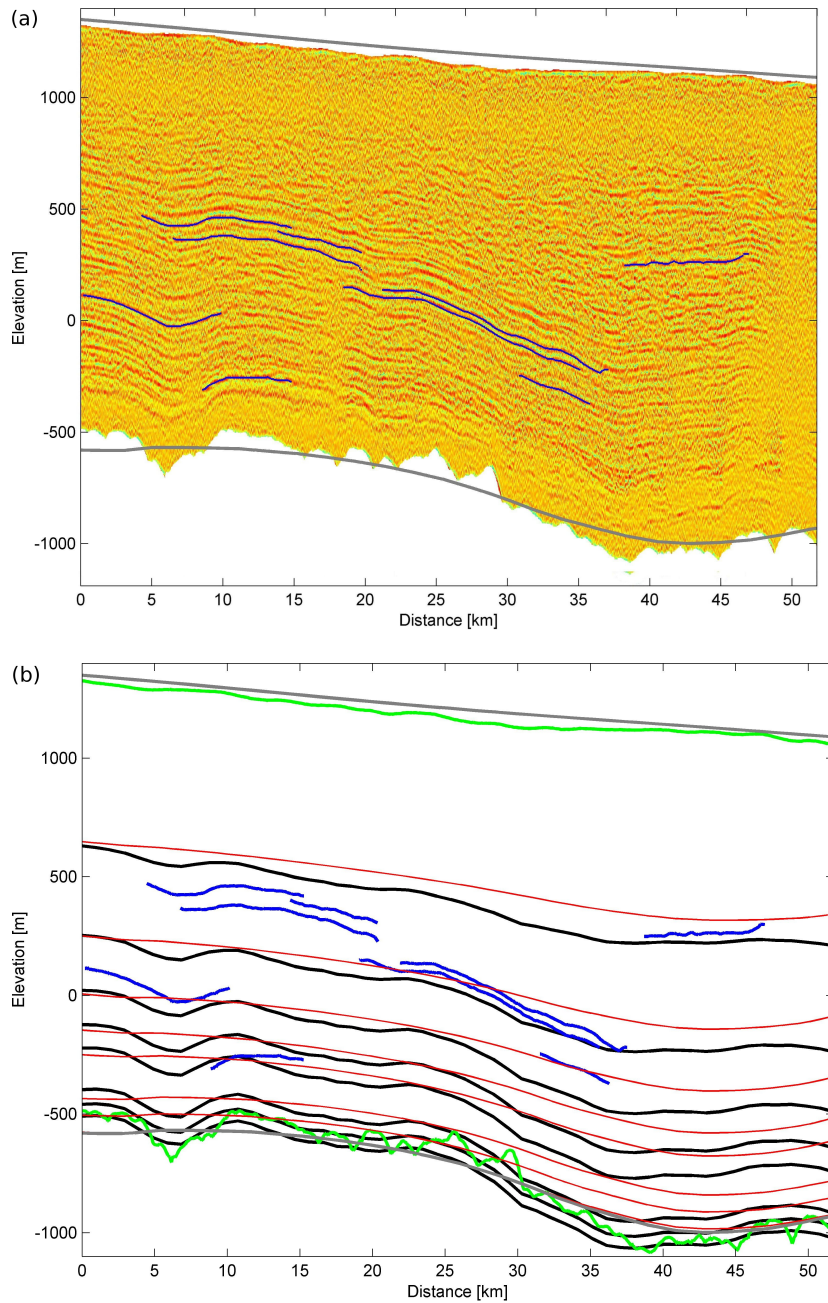


Figure 7.4: (a) Radar data from flightline 14. Some internal layers have been picked with blue line to emphasise their stratigraphy. The grey lines are gridded surface and bed topography. (b) Modelled layers in flightline 14 in contours. For comparison the results from the three-dimensional model are plotted in red lines and a few of the observed layers have been added with blue lines. The surface and bed topography from the radar data are shown in green lines.

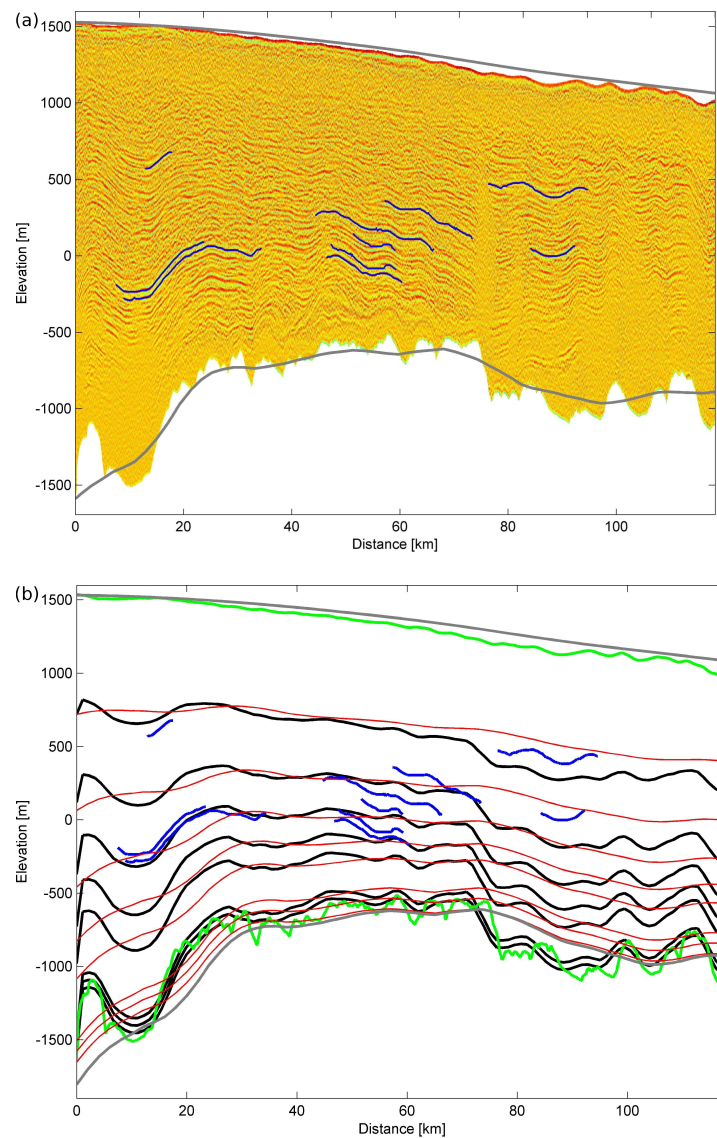


Figure 7.5: (a) Radar data from flightline 24. Some internal layers have been picked with blue line to emphasise their stratigraphy. The grey lines are gridded surface and bed topography. (b) Modelled layers in flightline 24 in contours. For comparison the results from the three-dimensional model are plotted in red lines and a few of the observed layers have been added with blue lines. The surface and bed topography from the radar data are shown in green lines.

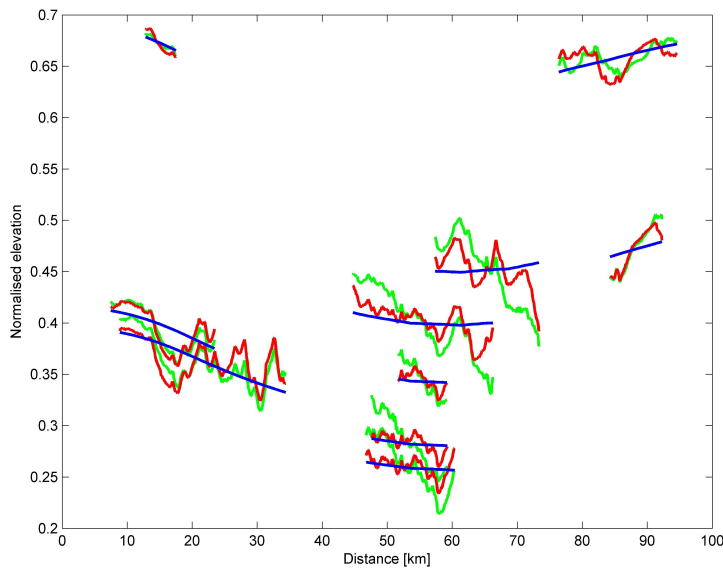


Figure 7.6: Observed radar layers (green lines) from flightline 24 (Figure 7.5) with the best fitting layers from the two-dimensional model (red lines) and the three-dimensional model (blue lines).

| Flightline             | Two-dimensional model | Three-dimensional model |
|------------------------|-----------------------|-------------------------|
| #24 mean median misfit | 0.010                 | 0.015                   |
| max. median misfit     | 0.022                 | 0.036                   |
| min. median misfit     | 0.002                 | 0.002                   |
| #11 mean median misfit | 0.009                 | 0.004                   |
| max. median misfit     | 0.018                 | 0.007                   |
| min. median misfit     | 0.001                 | 0.003                   |
| #14 mean median misfit | 0.007                 | 0.005                   |
| max. median misfit     | 0.018                 | 0.017                   |
| min. median misfit     | 0.002                 | 0.002                   |

Table 7.1: Results from fitting layers with the two-dimensional model

Figure 7.6 also shows the results from the three-dimensional model (blue lines). The results from this model are much smoother due to the lower resolution, however, the general slope of the layers is captured in most of the lines. The mean median misfit for flightline 24 is 0.015, (with a maximum misfit of 0.036 and a minimum of 0.002). For flightlines 11 and 14 the mean median misfits are 0.004 and 0.005. In other words the misfits the two models achieve are all of the same magnitude with especially flightline 14 obtaining very similar results.

## 7.3 Interpretation

In spite of its relative simplicity the two-dimensional model performs well in terms of calculating internal layering. Compared to the radar data the modelled layers are very similar and obtains overall small misfits indicating that the parameters included in the model are the ones that has the largest influence on layer stratigraphy, namely, surface and bed topography. It is expected that on this spatial scale the accumulation pattern and basal melt will have much less influence (this was also discussed in Section 6.2.2).

One very interesting feature appeared in flightline 24 where it was evident that the slope of some of the observed layers was significantly different from the modelled layers with no evidence that the sloping was caused by the bed rock, that was almost flat with only small-scale undulations. Several processes can alter the slope of internal layering, for example, a local anomaly in accumulation will cause an increase in undulations close to the surface decreasing with depth, while a local increase in basal melt rate will cause an undulation increasing with depth (e.g. Vaughan et al., 1999; Leysinger Vieli et al., 2007; Hindmarsh et al., 2009). The fact that the slope of the layers does not appear to change with depth indicates that it is less likely to have been caused by variations in accumulation or basal melting. It is also possible that the slope is caused by a three-dimensional effect where the layers reflect the largest amplitude in the bed topography, that may not necessarily be along the direction of sight. However, considering that the three-dimensional model also failed to capture the slope of the layers indicates that a three-dimensional effect is less likely. Finally, the feature might indicate a change in flow mode, such as a relict fast flow area or a change in flow direction, which could mean that the position of the flowline has changed.

The two-dimensional model is considerably simpler than the three-dimensional model. The primary reason for the difference between the two models is most likely due to the way the horizontal velocity is calculated. While the three-dimensional model obviously can include fluxes from further upstream and give a more realistic picture of the velocity, the two-dimensional model is limited to assuming that the horizontal velocity increases along the flowline in response to mass input and ice thickness. Thus the increase in velocity will be close to linear. An example from this effect can be seen in Figure 7.7 where horizontal surface velocities along flowline 2 are plotted for the three-dimensional model (blue line) and the two-dimensional model (red line). Notice the difference between the velocities increases with distance along the flowline. This might explain to the difference between the results.

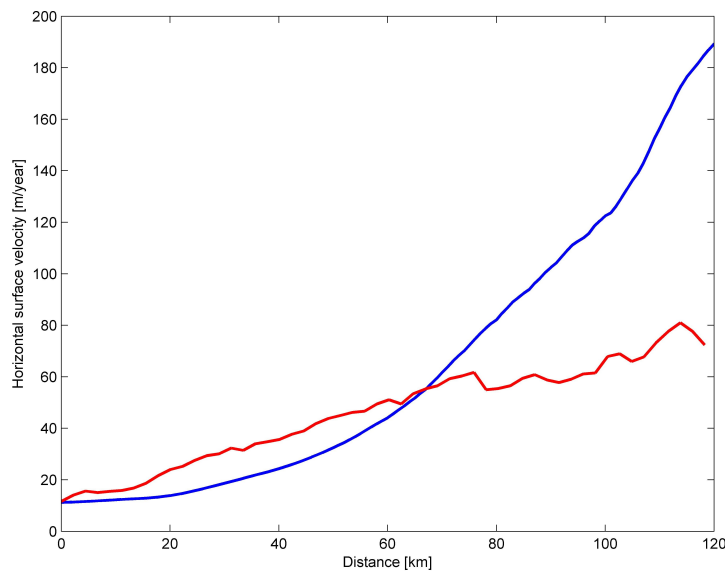


Figure 7.7: *Horizontal surface velocities along flowline 2 from the three-dimensional model (blue line) and the two-dimensional model (red line).*

Although the model satisfactorily produces the internal layering it has at least one substantial problem: it only works along flowlines and hardly any flightlines overlap with flowlines. This makes it very difficult to compare model with observations. On the other hand the greatest strength of the model is the improved resolution that enables a better estimate of the difference between observed layers and model. If it was possible to achieve this level of resolution with a three-dimensional model it might eliminate some of the misfits and thus to a larger extent highlight where the ice is influenced by other properties.

The construction of a two-dimensional model such as this one might be considered the next best approach. For example, in flightline 24 the two-dimensional model fit the layers better than BASISM indicating that the layers are influenced by undulations in the bed rock at a smaller scale than captured in the three-dimensional model. Even so both the two- and three-dimensional model obtains a worse fit for this flightline than the other flightlines in agreement with what was discussed above relating to changes in flow. In flightline 11 the three-dimensional model captured the layer slopes better than the two-dimensional model. Closer inspection of the data reveals that the slope of the bed is different from the slope of the layers indicating that other processes are influencing the layer geometry, for example, three-dimensional effects or flow mode. This also agrees with the location of flightline 11 in the area of anomalous continuous layering identified in Tributary 3 (see Section 5.1). Thus comparison between the two model outputs often makes it more clear where different ice processes are prevalent.

## 7.4 Discussion

The location of flightline 24 is close to the area shown in Figure 5.6 containing buckled layering (Section 5.1.1.3). This indicates that the anomalous layer slopes, that the models failed to capture fully, could indeed be due to changes in flow mode.

With the use of BASISM and an accumulation rate of  $0.25 \text{ m yr}^{-1}$  (see Section 6.5.3) an age for the upper buckled layer (located at distances 60 - 80 km) was estimated to be 6 kyr. This indicates that a possible change in flow direction has taken place within the past approximately 6 kyr, which curiously coincides with a change in accumulation rates. Results from Siegert and Payne (2004) and Neumann et al. (2008) conclude that accumulation rates have been higher between 3 - 5 kyr ago, while Siegert and Payne (2004) also conclude that accumulation rates over WAIS at 6.4-16 kyr ago have been lower than present day rates. However, it seems unlikely that a change in accumulation could have triggered a significant change in flow direction within such a short timespan. Alternatively, the change in flow could be a reaction to changes in climate at the end of the Holocene and, for example, relate to the second rapid retreat that Lowe and Anderson (2002) found evidence for in their study of the sea floor in Pine Island Bay. It is thought that this retreat caused a large amount of ice to be lost to the sea within a comparatively short timespan (2 - 4 kyr) which would significantly have influenced the mass balance of the glacier and potentially its flow pattern. The ungrounding of a large ice-shelf in Pine Island Bay could have led to surface elevation lowering, which in turn could cause higher accumulation rates due to decrease in altitude.

Finally, it must be noted that this part of flightline 24 is close to the bed high in the southernmost part of the northern basin, and thus part of the disruption of the internal layering might be caused by a build up of stress as the ice is flowing uphill (see also discussion in Section 6.6).

## 7.5 Conclusion

A two-dimensional model was used to model internal layers in three flowlines that were chosen so that they followed three observed flightlines. The model was first tested to match the results from the three-dimensional model and was found to reproduce layering from that model satisfactorily, with the biggest difference being due to the difference in the way the horizontal surface velocity was included. The two-dimensional model was then used to assimilate the observed layers in three flightlines. The increased resolution meant that the internal layering could

be reproduced more clearly, and the difference in fit between the two-dimensional model and BASISM highlighted areas where different parameters influenced the layer stratigraphy. For example, in flightline 24 an area of buckled layering was identified in a location close to an area containing buckled layering previously identified (see Section 5.1). Thus the two-dimensional model highlighted areas that might have a more complicated flow history.

# Chapter 8

## Discussion and Conclusion

The overall aim of this thesis was to investigate past flow dynamics of Pine Island Glacier, West Antarctica, using radar-imaged internal layering in the ice and the information it contains. The specific objectives of the research were established in Chapter 1, Section 1.3:

- (i) to classify and interpret the internal layering imaged by radar
- (ii) to construct an objective classification system for internal layering
- (iii) to explore other properties of the radar dataset that can yield information on current or past flow patterns
- (iv) to compare observed internal layering to modelled layering from numerical ice flow models
- (v) to retrieve information on past flow parameters such as accumulation, basal melting and ice deformation using observations and numerical ice flow models

These objectives were addressed using an extensive airborne radio-echo sounding dataset acquired during a survey of PIG in the austral summer 2004/2005 by the British Antarctic Survey and Institute for Geophysics, University of Texas (see Chapter 4). The first stage in the research involved tracing the internal layers imaged in the radar data, and analysing and interpreting these layers with respect to the information they contain on past variations in accumulation, basal conditions and ice flow mechanics. In order to achieve this methods were developed to classify and trace the internal layers. The relationship between the layer geometries and past conditions of PIG then formed the basis for modelling the past ice flow of PIG using both two- and three-dimensional models. A major focus for the modelling was making use of the opportunity to compare modelled results

with the comprehensive radar dataset. Comparisons between model results and the observed data returned information on past ice flow and snowfall rates.

In this chapter the main findings from the thesis are summarised and discussed (Section 8.1) and the implications of the findings are discussed (Section 8.2). The conclusion of this thesis is then outlined (Section 8.3) and several venues for future work are then proposed along with suggestions for further development of the methods (Section 8.4).

## 8.1 Summary and Discussion

### 8.1.1 Classification of Internal Layering

The internal layering of PIG has been extensively classified according to layering type: continuous, discontinuous or missing layers. The analyses of the internal layers used both quantitative and qualitative classification schemes and provided strong evidence that most of the catchment basin has not experienced major spatial changes in its flow regime over recent centuries (see Chapter 5, Section 5.1.2 and 5.2.2). The current flow pattern is in close agreement with the location of several deep subglacial troughs (Vaughan et al., 2006) which are likely to exert a strong topographic control on the main flow features. Thus the findings support other observations demonstrating strong basal control on ice flow patterns (e.g. Vaughan et al., 2003; Peters et al., 2006).

However, some regions in the northern basin of PIG represent exceptions to this overall result (see Figure 5.6). For example, in Tributary 3 an island of continuous layering was identified in a fast flow area that might have been caused by migration of the onset of fast flow (Whillans et al., 1987) or could be related to the basal conditions of the tributary, that is located on a relatively weak bed (Joughin et al., 2009). Slightly upstream of Tributary 3 an area with buckled layering was found indicating that the tributary might have extended further upstream than at present (cf. Conway et al., 2002). Tributary 5 exhibited discontinuous layering significantly further upstream than the other tributaries, which might be related to a combination of fast flow and a weak bed (Joughin et al., 2009) indicating a smooth channel for ice transported from the interior of the basin. It is also possible that the weak bed under Tributary 5 would make the tributary more sensitive to external forcing thus enhancing ice transport into the sea.

Tributaries 3 and 5 are also most likely the largest contributors in terms of mass transport from the interior of the southern basin (cf. Figure 5.28) and

changes in their flow dynamics might therefore have significant impact on the overall stability of PIG. While Tributary 3 has a relatively strong bed, Tributary 5 has low basal roughness and shear stress, implying that the response of the tributaries to further acceleration and surface lowering of the main trunk is likely to be different. This is supported by studies of PIG basal roughness by Rippin et al. (2010) (in press) who conclude that it is likely that the tributaries will transmit forcings from downstream into the interior of PIG at different rates.

Finally, in Tributary 7 layering indicated that the tributary might have migrated in the past from a position further towards the west. This indicates that the possibility exists for a very dynamic flow pattern in this part of PIG, where enhanced flow features might be shutting down or re-appearing in response to internal or external forcings as observed at, for example, the Siple Coast (Conway et al., 2002; Siegert et al., 2003b).

Another important outcome of the thesis was the development of a new method for quantifying the continuity of the internal layers, which proved to be a significantly faster approach to classifying internal layering. Comparisons between the qualitative and quantitative classification further emphasised the subjectivity and limitations of the qualitative approach. The quantitative method is particularly powerful used together with a qualitative method as differences in the results will help identify areas of unusual layering and highlight areas where the interpretation is less clear. Finally, a semi-automatic layer tracing routine was constructed that proved instrumental in providing the necessary layer elevations for the ice flow models.

### 8.1.2 Flow Patterns from Other Properties

While the internal layer classification was the main product retrieved from the radar data analyses, other properties of the dataset were also explored and the internal layering was compared to the calculated deformational velocity to gain further insight into the cause of the disrupted layering.

The deformational velocity showed that the tributaries that experience the largest degree of deformation are Tributaries 3 and 7 (see Section 5.4 and Figure 5.20), while the deformational velocity is particularly low in the main trunk and in the tributaries north and east of the main trunk (e.g. Tributaries 2, 4 and 6). However, even in areas where the basal shear stress and roughness were found to be higher (Joughin et al., 2009; Rippin et al., 2010, in press) the observed surface velocity was still higher than the deformational velocity. This is a clear indication that the flow of the northern basin of PIG is dominated by basal sliding.

Comparing the deformational velocity to the internal layering, however, yielded no clear correlation. This could most likely be because that even in areas where deformational velocity is present the basal sliding is still the dominant effect.

Investigations of the RES data indicated that the surface elevation often undulated close to the onset of fast and/or enhanced flow. This was investigated further by quantifying the surface roughness focussing on undulations of a length scale of 10 - 20 km. Previous studies of surface undulations of glaciers have concluded that they reflect the subglacial topography and are most prominent in areas where the basal motion is large compared to the motion caused by internal deformation (Thorsteinsson et al., 2003; Gudmundsson, 2003). The findings of this thesis support this hypothesis, showing that the surface roughness correlate with surface velocity, basal shear stress and basal roughness in the following manner: in areas of very fast flow and low basal roughness (e.g. the main trunk) surface roughness was low, while areas of fast/enhanced flow and high basal roughness exhibited a high surface roughness, and slower flowing areas had generally low surface roughness. This implies that high surface roughness indicates rough basal topography and basal sliding. Thus the findings imply that surface roughness can serve as a parameter for indicating the dominant ice flow mechanism when the basal roughness is known.

### 8.1.3 Comparison between Modelled and Observed Layering

By employing the three-dimensional model BASISM and a two-dimensional model to several traced internal layers, information was retrieved on past conditions of the ice (full details are given in Chapters 6 and 7).

Firstly, layers were fitted individually with BASISM, which showed that accumulation and basal melting are likely to vary over larger spatial scales than the average length of the layers. This is in agreement with observations of modern day accumulation pattern (Arthern et al., 2006) and reconstructions of past accumulation patterns (Siegert and Payne, 2004; Neumann et al., 2008).

Using a layer package identified in the neck between the northern and southern basin several model scenarios in BASISM were tested with different parameters (see Section 6.4 and Figure 6.21). This indicated that a change in accumulation pattern has taken place since the deposition of Layer 1 (the upper layer). It also showed that the parameters that achieved the optimum fit were different for Layer 1 and Layer 2 (the lower layer) indicating a time-dependence in some of

the parameters. This can most likely be attributed to either a second change in accumulation, complicated flow dynamics or a combination of both.

The two-dimensional model enabled an increase in horizontal resolution and this led to the internal layering being reproduced more clearly. The difference in fit between the two-dimensional model and BASISM highlighted areas where different parameters influenced the layer stratigraphy and thus areas that might have a more complicated flow history. It supported the finding from the layer classification that an area upstream of Tributary 5 exhibits disrupted layering and supported the hypothesis that the area has undergone changes in flow direction in the past, similar to what has been observed in other ice streams (e.g. Conway et al., 2002; Rippin et al., 2006).

#### 8.1.4 Paleo-flow conditions of PIG

From an independent survey conducted in 2001 by the US-ITASE program an age-depth relationship was obtained. This indicated an average accumulation rate of  $0.25 \text{ m yr}^{-1}$  over the past 17.5 kyr. The inferred accumulation rate is lower than the observed modern accumulation rate (Arthern et al., 2006), but higher than the rate estimated by Siegert and Payne (2004) from internal layers of the age range 6.4 kyr to 16 kyr. Studies have found evidence for an overall trend of increased accumulation across the West Antarctic Ice Divide from west to east in recent times (Neumann et al., 2008), and if this trend was prevalent then it can explain the higher accumulation rates in this thesis compared to Siegert and Payne (2004).

Using an accumulation rate of  $0.25 \text{ m yr}^{-1}$  BASISM returned an approximate age for Layer 1 and Layer 2 of 7.9 kyr and 10.7 kyr respectively. The age of Layer 1 is close to that of a tephra layer identified in the Byrd ice core of the age of 7.5 kyr from Mount Takahe, while the age of Layer 2 is close to a peak in acidity at 10.2 kyr. Thus Layer 2 might correlate with the transition to and/or the beginning of the Holocene climate. Thus if the above age estimates are correct this indicates that the accumulation rate and pattern has changed in approximately the past 7 kyr. Results also indicate that a second change in accumulation pattern could have taken place in the period between 10 kyr to 7 kyr before present. Similar changes have been reconstructed from other parts of the WAIS on these time scales (e.g. Siegert and Payne, 2004; Neumann et al., 2008), however, more detailed studies of the US-ITASE data are necessary to confirm the ages.

In the northern basin of PIG two possible relict enhanced flow areas were dated to be of an approximate age of 10 kyr and 6 kyr respectively. These timescales

are entirely likely as changes in flow pattern have been found to have taken place as recently as 200 yr ago (Joughin and Tulaczyk, 2002) and 1.3 kyr ago (Jacobel et al., 1996) for Kamb Ice Stream and up to 20 kyr ago for Slessor Glacier (Rippin et al., 2006). It should furthermore be noted that the age of the 10 kyr feature is calculated with the same accumulation rate as that of the 6 kyr. In the modern day accumulation pattern (Arthern et al., 2006) the two sites experience different accumulation rates, with higher accumulation rates at the site of the 10 kyr feature. It is therefore possible that the age of the 10 kyr feature is slightly overestimated and that the two features are in fact closer in age.

The flow modelling studies indicated that accumulation pattern and rate are likely to have changed since the deposition of Layer 1 at approximately 7 kyr ago and potentially changed again between that and the deposition of Layer 2 approximately 10 kyr ago. These ages are close to the estimated ages of the two relict enhanced flow areas. However, assuming that the changes in accumulation pattern and rate are directly related to, or the cause of, the observed anomalous layering would be to adopt a far too simplified view of the glacial processes of PIG. Even so, the elevation of the WAIS is thought to have been several hundred metres higher approximately 7 kyr ago (Huybrechts, 2002). The change in elevation could have caused a change in accumulation rate (Siegert and Payne, 2004) and it might have caused the observed changes in flow pattern. Thus the cause of the disrupted areas and the change in accumulation rate could very well be the same.

To test this hypothesis fully the response time of PIG would need to be known along with paleo ice surface elevation and accumulation rates. That is beyond the scope of this thesis, and here the likely connection between changes in elevation, accumulation and in flow pattern is merely noted.

## 8.2 Impacts of the Research

The work presented in this thesis and the findings that have resulted from the work have a number of significant implications for (i) radar data processing techniques, (ii) our understanding of the dynamics of PIG, and (iii) for the reconstruction of the past of the WAIS.

This thesis has made significant advances in the processing of radio-echo sounding data. The quantitative classification represents a relatively easy and fast way of assessing the occurrence of internal layering and the continuity of the layers. The layer tracing routine makes tracing layers much more efficient and

significantly less time consuming. The techniques developed are applicable to other RES datasets and will greatly aid in the processing of new datasets as well as open up scope for revisiting older datasets.

Extensive surveys of PIG indicated that the flow of the catchment basin is strongly controlled by the bed topography (Vaughan et al., 2006). While this is in general agreement with the results presented here, indications of several smaller changes that are likely to have taken place in the flow pattern were found. Thus the northern basin of PIG is likely to be more dynamic than previously assumed which might have consequences for its response to changes at its margins or to increased mass flux. Modelling studies of the WAIS for projecting future sea-level rise should keep in mind that the flow pattern of PIG has potential to change and that different parts of PIG might respond differently to forcing.

Finally, reconstruction of past accumulation rates and patterns of the WAIS revealed that a likely change has occurred in average accumulation rate during the past 17.5 kyr with overall lower accumulation than at present. Furthermore, results indicated that a change in accumulation pattern have taken place during the past approximately 7 kyr. This kind of information can feed into current efforts to understand the past dynamics of WAIS in order to establish its response to future climate change. This is particularly important when considering the potential instability of the ice sheet.

### 8.3 Conclusion

This thesis has presented the results of an extensive analysis of an airborne radar dataset from Pine Island Glacier and a modelling comparison study of the internal layering. The internal layering classification showed that the flow pattern is controlled by the subglacial topography to a large extent, but also identified two areas where the internal layering indicated a change in flow pattern from enhanced to slow flow. Modelling results estimated the age of change in onset of enhanced flow to be of the scale of 6 kyr to 10 kyr, indicating that the changes could be a response to changes in climate after the transition to the Holocene.

The modelling studies further indicated a possible change in accumulation pattern during the past approximately 7 kyr and potentially another change in accumulation pattern between approximately 7 kyr and 10 kyr. The accumulation rates are also likely to have been lower than at present. The ages were based on data from the US-ITASE program and a better link between these data and the PASIN dataset would allow for a more accurate age estimate.

The results of this thesis have highlighted the dynamic nature of the flow

pattern of the Pine Island Glacier catchment basin. The northern part of the basin was found to be particularly dynamic which may impact the overall stability and flow pattern of PIG and thus eventually the flow dynamics of the WAIS.

## 8.4 Future Work

This thesis has made use of internal layers acquired over much of PIG using a radar system - PASIN - and a collection method that were mainly optimised for imaging the bed topography and acquiring gravity measurements. Though numerous internal layers were acquired, and have been analysed here, several areas apparently devoid of internal layers in the PASIN data may have internal layering if investigated with other radar systems. Valuable insights can be gained by comparing the PASIN data with data from the ground-based survey conducted using the BAS DEep-LOoking Radar Echo Sounder (DELORES) radar (1 MHz) (Bingham et al., 2008), or with the flightlines between PIG and Thwaites Glacier flown by the Institute of Geophysics, University of Texas with a radar of 60 MHz frequency (Holt et al., 2006). At present few of the existing radar tracks overlap, but future applications of PASIN, DELORES or other systems might be directed to do so, and could then provide information on recent changes in the ice flow regime and accumulation.

On a more general note a more thorough investigation into the directionality of the data could be launched. This would especially highlight the propagation of radar waves in the ice and the non-trivial effects that occur when imaging glacial flow, that is a four-dimensional problem, in two dimensions (e.g. Harrison, 1973).

There is plenty of scope for further developing the methods constructed for RES data processing. In fact considering the importance of radar layers in glaciology very little concerted effort has gone into constructing automated processing of radar data. Firstly, the semi-automatic layer tracing routine could be expanded to a more automatic approach that needs less interaction with a user and, for example, includes the ability to identify the layers automatically. This could lead to a further application identifying areas with changing basal melting or extensive buckling of the layers. This kind of automated radar data analysis would have a big impact on the way the glaciological community approach RES data and might add value to already existing datasets.

Finally, the relationship between surface roughness, internal layering and basal conditions was found to hold the potential to impart information on ice flow mechanisms. A further investigation and comparison between these parameters might reveal more about this relationship and would also be applicable to datasets other

than the one investigated here.

One venue for further use of the BASISM model could be to include a calculation of temperature with depth instead of the isothermal solution. This would also affect the degree of internal deformation the ice is experiencing. Expanding on this several values for the geothermal gradient and surface temperature might be tested.

Even if the ice is kept isothermal the list of different parameters to change separately or in combination is almost endless. For example, several other scenarios could be constructed with different accumulation patterns or basal melting or spatial change in flow mode. However, in order to get added insights into the dynamics of the glacier more layers need to be correlated between flightlines. Based on the PASIN dataset alone the observed layering is unfortunately insufficient to allow for additional layer correlation. This highlights the need to acquire further radar data over PIG, preferably with a specific focus on the optimal conditions for imaging internal layers in key areas such as the dynamic northern basin.

The two-dimensional model could be extended to include cases for internal deformation and to include a variation of temperature with depth. However, this is expected to have less impact than the change in resolution compared to BASISM. If reasonable estimates of past elevation of WAIS could be obtained it would also be possible to include a time-dependence in the ice thickness and investigate the impact on the internal layers.

With the current dataset from PIG it was not possible in this study to use the two-dimensional model in more than three locations, where an overlap between flightlines and flowlines provided high resolution information of the bed topography. As a proof of concept, however, the model is applicable for more comprehensive use across PIG if appropriate data are acquired in the future. Furthermore, the model is not limited to PIG and can be used as a tool for understanding internal layering in ice flow in a wide variety of glaciological settings.



# Bibliography

- Ó Cofaigh, C., Dowdeswell, J. A., Allen, C. S., Hiemstra, J. F., Pudsey, C. J., Evans, J., and Evans, D. J. (2005). Flow dynamics and till genesis associated with a marine-based antarctic palaeo-ice stream. *Quaternary Science Reviews*, 24:709–740.
- Abyzov, S. S., Mitskevich, I. N., Poglazova, M. N., Barkov, N. I., Lipenkov, V. Y., Bobin, N. E., Koudryashov, B. B., Pashkevich, V. M., and Ivanov, M. V. (2001). Microflora in the basal strata at antarctic ice core above the vostok lake. *Advances in Space Research*, 28(4):701 – 706.
- Ackert, R. P., Barclay, D. J., Borns, H. W., Calkin, P. E., Kurz, M. D., Fastook, J. L., and Steig, E. J. (1999). Measurements of Past Ice Sheet Elevations in Interior West Antarctica. *Science*, 276:276–280.
- Anderson, J. B., Shipp, S. S., Lowe, A. L., Wellner, J. S., and Mosola, A. B. (2002). The Antarctic Ice Sheet during the Last Glacial Maximum and its subsequent retreat history: a review. *Quaternary Science Reviews*, 21:49–70.
- Arthern, R. and Hindmarsh, R. (2003). Optimal estimation of changes in the mass of ice sheets. *Journal of Geophysical Research*, 108:6007.
- Arthern, R. J., Winebrenner, D. P., and Vaughan, D. G. (2006). Antarctic snow accumulation mapped using polarization of 4.3-cm wavelength microwave emission. *Journal of Geophysical Research*, 111:D06107.
- Bailey, J. T., Evans, S., and Robin, G. (1964). Radio-echo sounding of polar ice sheets. *Nature*, 204:420–423.
- Bamber, J. and Gomez-Dans, J. L. (2005). The accuracy of digital elevation models of the Antarctic continent. *Earth and Planetary Science Letters*, 237:516–523.
- Bamber, J. L., Gomez-Dans, J. L., and Griggs, J. A. (2009a). A new 1 km digital

- elevation model of the Antarctic derived from combined satellite radar and laser data - Part 1: Data and methods. *The Cryosphere*, 3:101–111.
- Bamber, J. L., Riva, R. E. M., Vermeersen, B. L. A., and LeBrocq, A. M. (2009b). Reassessment of the Potential Sea-Level Rise from a Collapse of the West Antarctic Ice Sheet. *Science*, 324:901–903.
- Barnes, P., Tabor, D., and Walker, J. C. F. (1971). The Friction and Creep of Polycrystalline Ice. *Proceedings of the Royal Society of London. A*, 324(1557):127–155.
- Behrendt, J. C. (2005). *Ninth Circle: A Memoir of Life and Death in Antarctica, 1960-1962*. University of New Mexico Press.
- Behrendt, J. C., Finn, C. A., Blankenship, D., and Bell, R. E. (1998). Aeromagnetic evidence for a volcanic caldera(?) complex beneath the divide of the West Antarctic Ice Sheet. *Geophysical Research Letters*, 25(23):4385–4388.
- Bell, R. E. (2008). The role of subglacial water in ice-sheet mass balance. *Nature Geoscience*, 1:297–304.
- Bell, R. E., Blankenship, D. D., Finn, C. A., Morse, D. L., Scambos, T. A., Brozenak, J. M., and Hodge, S. M. (1998). Influence of subglacial geology on the onset of a West Antarctic ice stream from aerogeophysical observations. *Nature*, 394:58–62.
- Bentley, C. R., Lord, N., and Liu, C. (1998). Radar reflections reveal a wet bed beneath stagnant Ice Stream C and a frozen bed beneath ridge BC, West Antarctica. *Journal of Glaciology*, 44:149–156.
- Bindschadler, R. (1998). Future of the West Antarctic Ice Sheet. *Science*, 282:428–429.
- Bindschadler, R., Bamber, J., and Anandakrishnan, S. (2001a). Onset of Streaming Flow in the Siple Coast Region, West Antarctica. In Alley, R. B. and Bindschadler, R. A., editors, *The West Antarctic ice sheet: behavior and environment*, volume 77 of *Antarctic Research Series*, pages 123–136.
- Bindschadler, R. and Vornberger, P. (1998). Changes in the west antarctic ice sheet since 1963 from declassified satellite photography. *Science*, 279:689–692.
- Bindschadler, R. A., Bamber, J., and Anandakrishnan, S. (2001b). *The West Antarctic ice sheet: behaviour and environment*, chapter Onset of streaming

- flow in the Siple Coast region, West Antarctica, pages 123–136. Antarctic Research Series. American Geophysical Union, Washington DC.
- Bingham, R. G., Scott, J. B., Smith, A. M., and Hindmarsh, R. C. (2008). Basal conditions at Pine Island Glacier imaged using deep-looking radar. *EGU General Assembly*, 10:EGU2008–A–05496.
- Bingham, R. G. and Siegert, M. J. (2007a). Radar-derived bed roughness characterization of Institute and Möller ice streams, West Antarctica, and comparison with Siple Coast ice streams. *Geophysical Research Letters*, 34.
- Bingham, R. G. and Siegert, M. J. (2007b). Radio-echo sounding over polar ice masses. *Journal of Environmental and Engineering Geophysics*, 12(1):47–62.
- Bingham, R. G., Siegert, M. J., Young, D. A., and Blankenship, D. D. (2007). Organized flow from the South Pole to the Filchner-Ronne ice shelf: An assessment of balance velocities in interior East Antarctica using radio echo sounding data. *Journal of Geophysical Research*, 112.
- Blankenship, D. D., Bell, R. E., Hodge, S. M., Brozena, J. M., Behrendt, J. C., and Finn, C. A. (1993). Active volcanism beneath the West Antarctic ice sheet and implications for ice-sheet stability. *Nature*, 361:526–529.
- Blunier, T. and Brook, E. J. (2001). Timing of Millennial-Scale Climate Change in Antarctica and Greenland During the Last Glacial Period. *Science*, 291(5501):109–112.
- Bogorodsky, V. V., Bentley, C. R., and Gudmandsen, P. E. (1985). *Radioglaciology*. D. Reidel Publishing Company.
- Buchardt, S. L. and Dahl-Jensen, D. (2007). Estimating the basal melt rate at NorthGRIP using a Monte Carlo technique. *Annals of Glaciology*, 45:137–142.
- Budd, W. F. and Warner, R. C. (1996). A computer scheme for rapid calculations of balance-flux distributions. *Annals of Glaciology*, 23:21–27.
- Carter, S. P., Blankenship, D. D., Peters, M. E., Young, D. A., Holt, J. W., and Morse, D. L. (2007). Radar-based subglacial lake classification in Antarctica. *Geochemistry Geophysics Geosystems*, 8.
- Castello, J. D. and Rogers, S. O., editors (2005). *Life in Ancient Ice*. Princeton University Press.

- Catania, G., Conway, H., Gades, A., Raymond, C., and Engelhardt, H. (2003). Bed reflectivity beneath inactive ice streams in West Antarctica. *Annals of Glaciology*, 36:287–291.
- Catania, G., Conway, H., Raymond, C., and Scambos, T. (2005). Surface morphology and internal layer stratigraphy in the downstream end of Kamb Ice Stream, West Antarctica. *Journal of Glaciology*, 51:423–431.
- Comiso, J. (2000). Variability and trends in Antarctic surface temperatures from in situ and satellite infrared measurements. *Journal of Climate*, 13:1674–1696.
- Conway, H., Catania, G., Raymond, C. F., Gades, A. M., and Scambos, T. A. and Engelhardt, H. (2002). Switch of flow direction in an Antarctic ice stream. *Nature*, 419:465–467.
- Conway, H., Hall, B. L., Denton, G. H., Gades, A. M., and Waddington, E. D. (1999). Past and Future Grounding-Line Retreat of the West Antarctic Ice Sheet. *Science*, 286:280–283.
- Corr, H., Ferraccioli, F., Frearson, N., Jordan, T., Robinson, C., Armadillo, E., Caneva, G., Bozzo, E., and Tabacco, I. (2007). Airborne radio-echo sounding of the Wilkes Subglacial Basin, the Transantarctic Mountains, and the Dome C region. *Terra Antartica Reports*, 13:55–64.
- Corr, H., Moore, J. C., and Nicholls, K. W. (1993). Radar absorption due to impurities in Antarctic ice. *Geophysical Research Letters*, 20:1071–1074.
- Corr, H. F. J., Doake, C. S. M., Jenkins, A., and Vaughan, D. G. (2001). Investigations of an “ice plain” in the mouth of Pine Island Glacier, Antarctica. *Journal of Glaciology*, 47(156):51–57.
- Corr, H. F. J. and Vaughan, D. G. (2008). A recent volcanic eruption beneath the West Antarctic ice sheet. *Nature Geoscience*, 1:122 – 125.
- Crabtree, R. and Doake, C. (1982). Pine Island Glacier and its drainage basin: results from radio-echo sounding. *Annals of Glaciology*, 3:65–70.
- Dansgaard, W. and Johnsen, S. (1969). A flow model and a time scale for the ice core from Camp Century, Greenland. *Journal of Glaciology*, 8(53):215–223.
- Dean, K., Naylor, S., Turchetti, S., and Siegert, M. (2008). Data in Antarctic Science and Politics. *Social Studies of Science*, 38:571–604.

- Dowdeswell, J. A. and Evans, S. (2004). Investigations of the form and flow of ice sheets and glaciers using radio-sounding. *Reports on Progress in Physics*, 67:1821–1861.
- Dowdeswell, J. A., Ottesen, D., Rise, L., and Craig, J. (2007). Identification and preservation of landforms diagnostic of past ice-sheet activity on continental shelves from three-dimensional seismic evidence. *Geology*, 35:359–362.
- Dowdeswell, J. A. and Siegert, M. J. (1999). The dimensions and topographic setting of Antarctic subglacial lakes and implications for large-scale water storage beneath continental ice sheets. *Geological Society of America Bulletin*, 111:254–263.
- Drewry, D. J. (1975). Radio echo sounding map of Antarctica, ( $\sim 90^\circ\text{E} - 180^\circ$ ). *Polar Record*, 17:359–374.
- Drewry, D. J. (1983). Antarctica: Glaciological and Geophysical Folio. Technical report, University of Cambridge, Scott Polar Research Institute.
- Drewry, D. J., Jordan, S. R., and Jankowski, E. (1982). Measured properties of the Antarctic ice sheet: surface configuration, ice thickness, volume and bedrock characteristics. *Annals of Glaciology*, 3:83–91.
- Eisen, O., Nixdorf, U., Wilhelms, F., and Miller, H. (2004). Age estimates of isochronous reflection horizons by combining ice core, survey, and synthetic radar data. *Journal of Geophysical Research*, 109.
- Eisen, O., Wilhelms, F., Steinhage, D., and Schwander, J. (2006). Instruments and Methods: Improved method to determine radio-echo sounding reflector depths from ice-core profiles of permittivity and conductivity. *Journal of Glaciology*, 52:299–310.
- Evans, J., Dowdeswell, J. A., Ó Cofaigh, C., Benham, T. J., and Anderson, J. B. (2006). Extent and dynamics of the West Antarctic Ice Sheet on the outer continental shelf of Pine Island Bay during the last glaciation. *Marine Geology*, 230:53–72.
- Evans, S. (1961). Polar Ionospheric Spread Echoes and Radio Frequency Properties of Ice Shelves. *Journal of Geophysical Research*, 66:4137–4141.
- Evans, S. (1963). International co-operative field experiments in glacier sounding: Greenland, 1963. *Polar Record*, 11:725–726.

- Evans, S. (1967). "progress report on radio echo sounding". *Polar Record*, 13:413–420.
- Evans, S. and Robin, G. (1966). Glacier depth-sounding from the air. *Nature*, 210:883–885.
- Fahnestock, M., Abdalati, W., Joughin, I., Brozena, J., and Gogineni, P. (2001a). High Geothermal Heat Flow, Basal Melt, and the Origin of Rapid Ice Flow in Central Greenland. *Science*, 294:2338–2342.
- Fahnestock, M., Abdalati, W., Luo, S., and Gogineni, S. (2001b). Internal layer tracing and age-depth-accumulation relationships for the northern Greenland ice sheet. *Journal of Geophysical Research*, 106(D24):33789–33797.
- Forieri, A., Zuccoli, L., Bini, A., Zirizzotti, A., Rémy, F., and Tabacco, I. E. (2004). New bedrock map of Dome C, Antarctica, and morphostructural interpretation of the area. *Annals of Glaciology*, 39(1):321–325.
- Fricker, H. A. and Padman, L. (2006). Ice shelf grounding zone structure from ICESat laser altimetry. *Geophysical Research Letters*, 33.
- Fricker, H. A., Scambos, T., Bindschadler, R. A., and Padman, L. (2007). An Active Subglacial Water System in West Antarctica Mapped from Space. *Science*, 315:1544–1548.
- Fujita, S., Maeno, H., Uratsuka, S., Furukawa, T., Mae, S., Fujii, Y., and Watanabe, O. (1999). Nature of radio echo layering in the Antarctic ice sheet detected by a two-frequency experiment. *Journal of Geophysical Research*, 104(B6):13013–13024.
- Gades, A. M., Raymond, C. F., Conway, H., and Jacobel, R. W. (2000). Bed properties of Siple Dome and adjacent ice streams, West Antarctica, inferred from radio-echo sounding measurements. *Journal of Glaciology*, 46(152):88–94.
- Gillet-Chaulet, F., Gagliardini, O., Meyssonier, J., Montagnat, M., and Castelnau, O. (2005). A user-friendly anisotropic flow law for ice-sheet modelling. *Journal of Glaciology*, 51:3–14.
- Glen, J. W. (1955). The creep of polycrystalline ice. *Proceedings of the Royal Society of London A*, 228:519–538.
- Gogineni, S., Chuah, T., Allen, C., Jezek, K., and Moore, R. K. (1998). An improved coherent radar sounder. *Journal of Glaciology*, 44(148):659–669.

- Goldstein, R. M., Engelhardt, H., Kamb, B., and Frolich, R. M. (1993). Satellite Radar Interferometry for Monitoring Ice Sheet Motion: Application to an Antarctic Ice Stream. *Science*, 262(5139):1525 – 1530.
- Graham, A. G. C., Larter, R. D., Gohl, K., Dowdeswell, J. A., Hillenbrand, C.-D., Smith, J. A., Evans, J., Kuhn, G., and Deen, T. (2010). Flow and retreat of the Late Quaternary Pine Island-Thwaites palaeo-ice stream, West Antarctica. *Journal of Geophysical Research*, 115.
- Graham, A. G. C., Larter, R. D., Gohl, K., Hillenbrand, C.-D., Smith, J. A., and Kuhn, G. (2009). Bedform signature of a West Antarctic palaeo-ice stream reveals a multi-temporal record of flow and substrate control. *Quaternary Science Reviews*, 28:2774–2793.
- Greve, R. (1997). Application of a polythermal three-dimensional ice sheet model to the Greenland ice sheet: Response to steady-state and transient climate scenarios. *Journal of Climate*, 10:901–918.
- Greve, R., Placidi, L., and Seddik, H. (2009). A Continuum-Mechanical Model for the Flow of Anisotropic Polar Ice. *Low Temperature Science*, 68:137–148.
- Greve, R., Wang, Y., and Mugge, B. (2002). Comparison of numerical schemes for the solution of the advective age equation in ice sheets. *Annals of Glaciology*, 35:487–494.
- Gudmundsson, G., Raymond, C. F., and Bindshadler, R. (1998). The origin and longevity of flow-stripes on Antarctic ice streams. *Ann*, 27:145–152.
- Gudmundsson, G. H. (2003). Transmission of basal variability to a glacier surface. *Journal of Geophysical Research*, 108.
- Hammer, C. U., Clausen, H. B., and Langway Jr., C. C. (1997). 50,000 years of recorded global volcanism. *Climatic Change*, 35(1):1–15.
- Haran, T., Bohlander, J., Scambos, T., and Fahnestock, M. (2006). MODIS Mosaic of Antarctica (MOA) Image Map. National Snow and Ice Data Center, Boulder, Colorado: <http://nsidc.org/data/nsidc-0280.html>.
- Harrison, C. H. (1971). Radio-Echo Sounding: Focusing Effects in Wavy Strata. *Geophysical Journal of the Royal Astronomical Society*, 24:383–400.
- Harrison, C. H. (1973). Radio echo sounding of horizontal layers in ice. *Journal of Glaciology*, 12:383–397.

- Hays, J. D., Imbrie, J., and Shackleton, N. J. (1976). Variations in the Earth's Orbit: Pacemaker of the Ice Ages. *Science*, 194(4270):1121–1132.
- Hemming, S. R. (2004). Heinrich events: Massive late Pleistocene detritus layers of the North Atlantic and their global climate imprint. *Reviews of Geophysics*, 42.
- Hempel, L., Thyssen, F., Gundestrup, N., Clausen, H. B., and Miller, H. (2000). A comparison of radio-echo sounding data and electrical conductivity of the GRIP ice core. *Journal of Glaciology*, 46(154):369–374.
- Hillenbrand, C.-D., Kuhn, G., and Frederichs, T. (2009). Record of a Mid-Pleistocene depositional anomaly in West Antarctic continental margin sediments: an indicator for ice-sheet collapse? *Quaternary Science Reviews*, 28:1147–1159.
- Hillenbrand, C.-D., tterer, D. K. F., Grobe, H., and Frederichs, T. (2002). No evidence for a Pleistocene collapse of the West Antarctic Ice Sheet from continental margin sediments recovered in the amundsen sea. *Geo-Marine Letters*, 22:51–59.
- Hindmarsh, R. C. A. (1999). On the numerical computation of temperature in an ice sheet. *Journal of Glaciology*, 151:568–574.
- Hindmarsh, R. C. A. (2001). *Continuum Mechanics and applications in geophysics and the environment*, chapter Notes on basic glaciological computational methods and algorithms, pages 222–249. Springer-Verlag.
- Hindmarsh, R. C. A. (2004). A numerical comparison of approximations to the Stokes equations used in ice sheet and glacier modeling. *Journal of Geophysical Research*, 109:F01012.
- Hindmarsh, R. C. A., Leysinger Vieli, G. J.-M., and Parrenin, F. (2009). A large-scale numerical model for computing isochrone geometry. *Annals of Glaciology*, 50(51):130–140.
- Hindmarsh, R. C. A., Leysinger Vieli, G. J.-M. C., Raymond, M. J., and Gudmundsson, G. H. (2006). Draping or overriding: The effect of horizontal stress gradients on internal layer architecture in ice sheets. *Journal of Geophysical Research*, 111:F02018.
- Hodgkins, R., Siegert, M. J., and Dowdeswell, J. A. (2000). Geophysical investigations of ice-sheet internal layering and deformation in the Dome C region of central East Antarctica. *Journal of Glaciology*, 46:161–166.

- Holt, J. W., Blankenship, D. D., Morse, D. L., Young, D. A., Peters, M. E., Kempf, S. D., Richter, T. G., Vaughan, D. G., and Corr, H. F. J. (2006). New boundary conditions for the West Antarctic ice sheet: Subglacial topography beneath Thwaites and Smith glaciers. *Geophysical Research Letters*, 33.
- Hughes, T. J. (1982). The weak underbelly of the West Antarctic ice sheet. *Journal of Glaciology*, 27:518–525.
- Hutter, K. (1983). *Theoretical Glaciology. Material Science of Ice and the Mechanics of Glaciers and Ice Sheets*. D. Reidel Publishing Company.
- Huybrechts, P. (1990). A 3-D model for the Antarctic ice sheet: a sensitivity study on the glacial-interglacial contrast. *Climate Dynamics*, 5:79–92.
- Huybrechts, P. (2002). Sea-level changes at the LGM from ice-dynamic reconstructions of the Greenland and Antarctic ice sheets during the glacial cycles. *Quaternary Science Reviews*, 21:203–231.
- Huybrechts, P., Gregory, J., Janssens, I., and Wild, M. (2004). Modelling Antarctic and Greenland volume changes during the 20th and 21st centuries forced by GCM time slice integrations. *Global and Planetary Change*, 42(1-4):83 – 105. Ice sheets and neotectonics.
- Huybrechts, P., Payne, T., and The-Eimint-Intercomparison-Group (1996). The EISMINT benchmark for testing ice-sheet models. *Annals of Glaciology*, 23:1–12.
- Jacobel, R. W., Gades, A. M., Gottschling, D. L., Hodge, S. M., and Wright, D. L. (1993). Interpretation of radar-detected internal layer folding in West Antarctic ice streams. *Journal of Glaciology*, 39(133):528–537.
- Jacobel, R. W., Scambos, T. A., Nereson, N. A., and Raymond, C. F. (2000). Changes in the margin of Ice Stream C, Antarctica. *Journal of Glaciology*, 46(152):102–109.
- Jacobel, R. W., Scambos, T. A., Raymond, C. F., and Gades, A. M. (1996). Changes in the configuration of ice stream flow from the West Antarctic ice sheet. *Journal of Geophysical Research*, 101:5499–5504.
- Jacobel, R. W. and Welch, B. C. (2005). A time marker at 17.5 kyr BP detected throughout West Antarctica. *Annals of Glaciology*, 41:47–51.

- Jacobel, R. W., Welch, B. C., Osterhouse, D., Pettersson, R., and MacGregor, J. A. (2009). Spatial variation of radar-derived basal conditions on Kamb Ice Stream, West Antarctica. *Annals of Glaciology*, 50:10–16.
- Jacobs, S. S., Hellmer, H. H., and Jenkins, A. (1996). Antarctic ice sheet melting in the Southeast Pacific. *Geophysical Research Letters*, 23(9):957–960.
- Jankowski, E. J. and Drewry, D. J. (1981). The structure of West Antarctica from geophysical studies. *Nature*, 291:17–21.
- Jenkins, A., Dutrieux, P., Jacobs, S. S., McPhail, S. D., Perrett, J. R., T. Webb, A., and White, D. (2010). Observations beneath Pine Island Glacier in West Antarctica and implications for its retreat. *Nature Geoscience*, 3:468–472.
- Jenkins, A., Vaughan, D. G., Jacobs, S. S., Hellmer, H. H., and Keys, J. R. (1997). Glaciological and oceanographic evidence of high melt rates beneath Pine Island Glacier. *Journal of Glaciology*, 43(143):114–121.
- Johnsen, S. J., Dahl-Jensen, D., Gundestrup, N., Steffensen, J. P., Clausen, H. B., Miller, H., Masson-Delmotte, V., Sveinbjörnsdóttir, A. E., and White, J. (2001). Oxygen isotope and palaeotemperature records from six Greenland ice-core stations: Camp Century, Dye-3, GRIP, GISP2, Renland and NorthGRIP. *Journal of Quaternary Science*, 16(4):299–307.
- Jordan, T., Ferraccioli, F., Vaughan, D., Holt, J., Corr, H., Blankenship, D., and Diehl, T. (2009). Aerogravity evidence for major crustal thinning under the Pine Island Glacier region (West Antarctica). *Geological Society of America Bulletin*, 122:714–726.
- Joughin, I., Bamber, J. L., Scambos, T., Tulaczyk, S., Fahnestock, M., and MacAyeal, D. R. (2006). Integrating satellite observations with modelling: basal shear stress of the Filcher-Ronne ice streams, Antarctica. *Philosophical Transactions of The Royal Society A*, 364:1795–1814.
- Joughin, I., Gray, L., Bindschadler, R., Price, S., Morse, D., Hulbe, C., Mattar, K., and Werner, C. (1999). Tributaries of West Antarctic Ice Streams Revealed by RADARSAT Interferometry. *Science*, 286:283–286.
- Joughin, I., Rignot, E., Rosanova, C. E., Lucchitta, B. K., and Bohlander, J. (2003). Timing of Recent Accelerations of Pine Island Glacier, Antarctica. *Geophysical Research Letters*, 30(13).

- Joughin, I., Smith, B. E., and Holland, D. M. (2010). Sensitivity of 21st century sea level to ocean-induced thinning of Pine Island Glacier, Antarctica. *Geophysical Research Letters*, 37.
- Joughin, I. and Tulaczyk, S. (2002). Positive Mass Balance of the Ross Ice Streams, West Antarctica. *Science*, 295:476–480.
- Joughin, I., Tulaczyk, S., Bamber, J. L., Blankenship, D., Holt, J. W., Scambos, T., and Vaughan, D. G. (2009). Basal conditions for Pine Island and Thwaites Glaciers, West Antarctica, determined using satellite and airborne data. *Journal of Gl*, 55(109):245–257.
- Joughin, I., Tulaczyk, S., Bindschadler, R. A., and Price, S. F. (2002). Changes in west Antarctic ice stream velocities: Observation and analysis. *Journal of Geophysical Research*, 107.
- Karlsson, N. B., Rippin, D. M., Vaughan, D. G., and Corr, H. F. J. (2009). The internal layering of Pine Island Glacier, West Antarctica, from airborne radar-sounding data. *Annals of Glaciology*, 50(51):141–146.
- King, E. C. (2009). Flow dynamics of the Rutford Ice Stream ice-drainage basin, West Antarctica, from radar stratigraphy. *Annals of Glaciology*, 50:42–49.
- Kreyszig, E. (1999). *Advanced Engineering Mathematics*. John Wiley and sons, Inc.
- Larsen, J. and Dahl-Jensen, D. (2000). Interior Temperatures of the Northern Polar Cap on Mars. *Icarus*, 144:456–462.
- Le Brocq, A. M., Payne, A. J., and Vieli, A. (2010). An improved Antarctic dataset for high resolution numerical ice sheet models (ALBMAP v1). *Earth System Science Data*, 3:195–230.
- Leysinger Vieli, G. J.-M. C., Hindmarsh, R. C. A., and Siegert, M. J. (2007). Three-dimensional flow influences on radar layer stratigraphy. *Annals of Glaciology*, 46:22–28.
- Leysinger Vieli, G. J.-M. C., Siegert, M. J., and Payne, A. J. (2004). Reconstructing ice-sheet accumulation rates at ridge B, East Antarctica. *Annals of Glaciology*, 39:326–330.
- Lowe, A. L. and Anderson, J. B. (2002). Reconstruction of the West Antarctic ice sheet in Pine Island Bay during the Last Glacial Maximum and its subsequent retreat history. *Quaternary Science Reviews*, 21:1879–1897.

- Lowe, A. L. and Anderson, J. B. (2003). Evidence for abundant subglacial melt-water beneath the paleo-ice sheet in Pine Island Bay, Antarctica. *Journal of Glaciology*, 49:125–138.
- Lythe, M. B., Vaughan, D. G., and the BEDMAP Consortium (2001). BEDMAP: A new ice thickness and subglacial topographic model of Antarctica. *Journal of Geophysical Research*, 106(B6):11335–11351.
- MacAyeal, D. R. (1992). Irregular oscillations of the West Antarctic ice sheet. *Nature*, 359:29–32.
- MacGregor, J. A., Matsuoka, K., Koutnik, M. R., Waddington, E. D., Studinger, M., and Winebrenner, D. P. (2009). Millennially averaged accumulation rates for the Vostok Subglacial Lake region inferred from deep internal layers. *Annals of Glaciology*, 50:25–33.
- Magand, O., Genthon, C., Fily, M., Krinner, G., Picard, G., Frezzotti, M., and Ekaykin, A. A. (2007). An up-to-date quality-controlled surface mass balance data set for the 90°-180° E Antarctica sector and 1950-2005 period. *Journal of Geophysical Research*, 112.
- Martín, C., Gudmundsson, G. H., Pritchard, H. D., and Gagliardini, O. (2009). On the effects of anisotropic rheology on ice flow, internal structure, and the age-depth relationship at ice divides. *Journal of Geophysical Research*, 114.
- Masson, V., Vimeux, F., Jouzel, J., Morgan, V., Delmotte, M., Ciais, P., Hammer, C. U., Johnsen, S., Lipenkov, V., Mosley-Thompson, E., Petit, J. R., Steig, E. J., Stievenard, M., and Vaikmae, R. (2000). Holocene Climate Variability in Antarctica Based on 11 Ice-Core Isotopic Records. *Quaternary Research*, 54:348–358.
- Matsuoka, K., Furukawa, T., Fujita, S., Maeno, H., Uratsuka, S., Naruse, R., and Watanabe, O. (2003). Crystal orientation fabrics within the Antarctic ice sheet revealed by a multipolarization plane and dual-frequency radar survey. *Journal of Geophysical Research*, 108(B10).
- McKay, R., Browne, G., Carter, L., Cowan, E., Dunbar, G., Krissek, L., Naish, T., Powell, R., Reed, J., Talarico, F., and Wilch, T. (2009). The stratigraphic signature of the late Cenozoic Antarctic Ice Sheets in the Ross Embayment. *Geological Society of America Bulletin*, 121:1537–1561.
- Mercer, J. H. (1978). West Antarctic ice sheet and CO<sub>2</sub> greenhouse effect: a threat of disaster. *Nature*, 271:321–325.

- Millar, D. H. M. (1981). Radio-echo layering in polar ice sheets and past volcanic activity. *Nature*, 292:441–443.
- Miners, W. D. (1998). *Electromagnetic reflections inside ice sheets*. PhD thesis, Open University.
- Miners, W. D., Wolff, E. W., Moore, J. C., Jacobel, R., and Hempel, L. (2002). Modeling the radio echo reflections inside the ice sheet at Summit, Greenland. *Journal of Geophysical Research*, 107.
- Naish, T., Powell, R., Levy, R., Wilson, G., Scherer, R., Talarico, F., Krissek, L., Niessen, F., Pompilio, M., Wilson, T., Carter, L., DeConto, R., Huybers, P., McKay, R., Pollard, D., Ross, J., Winter, D., Barrett, P., Browne, G., Cody, R., Cowan, E., Crampton, J., Dunbar, G., Dunbar, N., Florindo, F., Gebhardt, C., Graham, I., Hannah, M., Hansaraj, D., Harwood, D., Helling, D., Henrys, S., Hinnov, L., Kuhn, G., Kyle, P., Läufer, A., Maffioli, P., Magens, D., Mandernack, K., McIntosh, W., Millan, C., Morin, R., Ohneiser, C., Paulsen, T., Persico, D., Raine, I., Reed, J., Riesselman, C., Sagnotti, L., Schmitt, D., Sjunneskog, C., Strong, P., Taviani, M., Vogel, S., Wilch, T., and Williams, T. (2009). Obliquity-paced Pliocene West Antarctic ice sheet oscillations. *Nature*, 458:322–329.
- National Snow and Ice Data Center (2010).
- Navarro, F. J., Otero, J., Macheret, Y. Y., Vasilenko, E. V., Lapazaran, J. J., Ahlstrøm, A. P., and Machio, F. (2009). Radioglaciological studies on Hurd Peninsula glaciers, Livingstone Island, Antarctica. *Annals of Glaciology*, 50:17–24.
- Naylor, S., Siegert, M., Dean, K., and Turchetti, S. (2008). Science, geopolitics and the governance of Antarctica. *Nature Geoscience*, 1:143–145.
- Nereson, N. A., Raymond, C. F., Jacobel, R. W., and Waddington, E. D. (2000). The accumulation pattern across siple dome, west antarctica, inferred from radar-detected internal layers. *Journal of Glaciology*, 46:75–87.
- Neumann, T. A., Conway, H., Price, S. F., Waddington, E. D., Catania, G. A., and Morse, D. L. (2008). Holocene accumulation and ice sheet dynamics in central West Antarctica. *Journal of Geophysical Research*, 113.
- Ng, F. and Conway, H. (2004). Fast-flow signature in the stagnated kamb ice stream, west antarctica. *Geology*, 32:481–484.

- Nick, F. M., Vieli, A., Howat, I. M., and Joughin, I. (2009). Large-scale changes in Greenland outlet glacier dynamics triggered at the terminus. *Nature Geoscience*, 2:110–114.
- North Greenland Ice Core Project members (2004). High-resolution record of Northern Hemisphere climate extending into the last interglacial period. *Nature*, 431:147–151.
- Nye, J. F. (1952). A Method of Calculating the Thicknesses of the Ice-Sheets. *Nature*, 169:529–530.
- Nye, J. F. (1959). The motion of ice sheets and glaciers. *Journal of Glaciology*, 3:493–507.
- Oerlemans, J., Anderson, B., Hubbard, A., Huybrechts, P., Johannesson, T., Knap, W., Schmeits, M., Stroeven, A., van de Wal, R., Wallinga, J., and Zuo, Z. (1998). Modelling the response of glaciers to climate warming. *Climate Dynamics*, 14:267–274.
- Paren, J. G. and Robin, G. (1975). Internal reflections in polar ice sheets. *Journal of Glaciology*, 14:251–259.
- Parrenin, F. and Hindmarsh, R. (2007). Influence of a non-uniform velocity field on isochrone geometry along a steady flowline of an ice sheet. *Journal of Glaciology*, 53(183):612–622.
- Parrenin, F., Hindmarsh, R., and Rémy, F. (2006). Analytical solutions for the effect of topography, accumulation rate and lateral flow divergence on isochrone layer geometry. *Journal of Glaciology*, 52(177):191–202.
- Parrenin, F., Remy, F., Ritz, C., Siegert, M., and Jouzel, J. (2004). New modeling of the Vostok ice flow line and implication for the glaciological chronology of the Vostok ice core. *Journal of Geophysical Research*, 109.
- Paterson, W. S. B. (1977). Secondary and tertiary creep of glacier ice as measured by borehole closure rates. *Reviews of Geophysics*, 15(1):47–55.
- Paterson, W. S. B. (2002). *The Physics of Glaciers*. Butterworth-Heinemann.
- Pattyn, F. (2003). A new three-dimensional higher-order thermomechanical ice sheet model: Basic sensitivity, ice stream development, and ice flow across subglacial lakes. *Journal of Geophysical Research*, 108(B8):2382.

- Pattyn, F. (2006). GRANTISM: An Excel™ model for Greenland and Antarctic ice-sheet response to climate changes. *Computers & Geosciences*, 32(3):316–325.
- Payne, A. (2005). Numerical modelling of ice sheets and ice shelves. Presentation at Karthaus Summer School.
- Payne, A. J., Hunt, J. C. R., and Wingham, D. J. (2006). Evolution of the Antarctic ice sheet: new understanding and challenges. *Philosophical Transactions of The Royal Society A*, 364:1867–1872.
- Payne, A. J., Huybrechts, P., Abe-Ouchi, A., Calov, R., Fastook, J. L., Greve, R., Marshall, S. J., Marsiat, I., Ritz, C., Tarasov, L., and Thomassen, M. (2000). Results from the EISMINT model intercomparison: the effects of thermomechanical coupling. *Journal of Glaciology*, 46(153):221–238.
- Payne, A. J., Vieli, A., Shepherd, A. P., Wingham, D. J., and Rignot, E. (2004). Recent dramatic thinning of largest West Antarctic ice stream triggered by oceans. *Geophysical Research Letters*, 31.
- Peters, L. E., Anandakrishnan, S., Alley, R. B., Winberry, J. P., Voigt, D. E., Smith, A. M., and Morse, D. L. (2006). Subglacial sediments as a control on the onset and location of two Siple Coast ice streams, West Antarctica. *Journal of Geophysical Research*, 111.
- Peters, M. E., Blankenship, D. D., and Morse, D. L. (2005). Analysis techniques for coherent airborne radar sounding: Application to West Antarctic ice streams. *Journal of Geophysical Research*, 110:1–17.
- Petit, J. R., Jouzel, J., Raynaud, D., Barkov, N. I., Barnola, J.-M., Basile, I., Bender, M., Chappellaz, J., Davis, M., Delaygue, G., Delmotte, M., Kotlyakov, V. M., Legrand, M., Lipenkov, V. Y., Lorius, C., PEPin, L., Ritz, C., Saltzman, E., and Stievenard, M. (1999). Climate and atmospheric history of the past 420,000 years from the Vostok ice core, Antarctica. *Nature*, 399:429–436.
- Philberth, K. and Federer, B. (1971). On the temperature profile and the age profile in the central part of cold ice sheets. *Journal of Glaciology*, 10:3–14.
- Plewes, L. A. and Hubbard, B. (2001). A review of the use of radio-echo sounding in glaciology. *Progress in Physical Geography*, 25(2):203–236.
- Plotnick, R. E., Gardner, R. H., Hargrove, W. W., Prestegard, K., and Perlmutter, M. (1996). Lacunarity analysis: A general technique for the analysis of spatial patterns. *Physical Review E: Statistics*, 53(5):5461–5468.

- Pollard, D. and DeConto, R. M. (2009). Modelling West Antarctic ice sheet growth and collapse through the past five million years. *Nature*, 458:329–333.
- Pritchard, H. D., Arthern, R. J., Vaughan, D. G., and Edwards, L. A. (2009). Extensive dynamic thinning on the margins of the Greenland and Antarctic ice sheets. *Nature*, 46:971–975.
- Raymond, C., Conway, H., and Catania, G. (2006). Compilation of antarctic radar data, siple coast, 2000-2002. Technical report, Boulder, Colorado, USA: National Snow and Ice Data Center.
- Raymond, C. F., Echelmeyer, K. A., M., W. I., and M., D. C. S. (2001). Ice stream shear margins. In Alley, R. B. and Bindschadler, R. A., editors, *The West Antarctic ice sheet: behavior and environment*, volume 77 of *Antarctic Research Series*, page 137–155.
- Rémy, F. and Tabacco, I. E. (2000). Bedrock features and ice flow near the EPICA ice core site (Dome C, Antarctica). *Geophysical Research Letters*, 27(3):405–408.
- Retzlaff, R., Lord, N., and Bentley, C. R. (1993). Airborne-radar studies: Ice Streams A, B and C, West Antarctica. *Journal of Glaciology*, 39(133):495–506.
- Rignot, E. (1998). Fast Recession of a West Antarctic Glacier. *Science*, 281:549–551.
- Rignot, E. (2002). Ice-shelf changes in Pine Island Bay, Antarctica. *Journal of Glaciology*, 48:247–256.
- Rignot, E. (2006). Changes in ice dynamics and mass balance of the Antarctic ice sheet. *Philosophical Transactions of The Royal Society A*, 364:1637–1655.
- Rignot, E. (2008). Changes in West Antarctic ice stream dynamics observed with ALOS PALSAR data. *Geophysical Research Letters*, 35.
- Rignot, E., Bamber, J. L., van den Broeke, M. R., D., C., Li, Y., van de Berg, W. J., and van Meijgaard, E. (2008). Recent Antarctic ice mass loss from radar interferometry and regional climate modelling. *Nature Geoscience*, 1:106 – 110.
- Rignot, E., Thomas, R., Kanagaratnam, P., Casassa, G., Frederick, E., Gogineni, S., Krabill, W., Rivera, A., Russell, R., Sonntag, J., Swift, R., and Yungel, J. (2004). Improved estimation of the mass balance of the glaciers draining into the Amundsen Sea sector of West Antarctica from the NASA/CECS 2002 campaign. *Annals of Glaciology*, 39:231–237.

- Rignot, E. and Thomas, R. H. (2002). Mass balance of polar ice sheets. *Science*, 297:1502–1506.
- Rignot, E., Vaughan, D. G., Schmeltz, M., Dupont, T., and MacAyeal, D. (2002). Acceleration of Pine Island and Thwaites Glaciers, West Antarctica. *Annals of Glaciology*, 34:189–194.
- Rippin, D. M., Bamber, J. L., Siegert, M. J., Vaughan, D. G., and Corr, H. F. J. (2003a). Basal topography and ice flow in the Bailey//Slessor region of East Antarctica. *Journal of Geophysical Research*, 108.
- Rippin, D. M., Siegert, M. J., and Bamber, J. L. (2003b). The englacial stratigraphy of Wilkes Land, East Antarctica, as revealed by internal radio-echo sounding layering, and its relationship with balance velocities. *Annals of Glaciology*, 30:189–196.
- Rippin, D. M., Siegert, M. J., Bamber, J. L., and Vaughan, D. G. (2006). Switch-off of a major enhanced ice flow unit in East Antarctica. *Geophysical Research Letters*, 30.
- Rippin, D. M., Vaughan, D. G., and Corr, H. F. J. (2010). The basal roughness of pine island glacier, west antarctica. *Journal of Glaciology*.
- Robin, G. (1975). Radio-echo sounding: glaciological interpretations and applications. *Journal of Glaciology*, 15:49–64.
- Robin, G., Evans, S., and Bailey, J. T. (1969). Interpretation of radio echo sounding in polar ice sheets. *Philosophical Transactions of The Royal Society, London, Series A*, 265:437–505.
- Robin, G. D. (1977). Ice cores and climatic change. *Philosophical Transactions of The Royal Society B*, 280:143–168.
- Robin, G. Q. and Millar, D. (1982). Flow of ice sheets in the vicinity of subglacial peaks. *Annals of Glaciology*, 3:290–294.
- Rutt, I. C. (2009). Ice sheet models. Talk. Talk at UK Polar Network Cryospheric Science Workshop.
- Scherer, R. P., Aldahan, A., Tulaczyk, S., van Pelt, G., Engelhardt, H., and Kamb, B. (1998). Pleistocene Collapse of the West Antarctic Ice Sheet. *Science*, 281:82–85.

- Schmeltz, M., Rignot, E., Dupont, T. K., and MacAyeal, D. R. (2002). Sensitivity of Pine Island Glacier, West Antarctica, to changes in ice-shelf and basal conditions: A model study. *Journal of Glaciology*, 48:552–558.
- Scott, J. B. T., Gudmundsson, G. H., Smith, A. M., Bingham, R. G., Pritchard, H. D., and Vaughan, D. G. (2009). Increased rate of acceleration on Pine Island Glacier strongly coupled to changes in gravitational driving stress. *The Cryosphere*, 3:125–131.
- Shapiro, N. M. and Ritzwoller, M. H. (2004). Inferring surface heat flux distributions guided by a global seismic model: particular application to antarctica. *Earth and Planetary Science Letters*, 223(1-2):213 – 224.
- Shepherd, A. and Wingham, D. (2007). Recent Sea-Level Contributions of the Antarctic and Greenland Ice Sheets. *Science*, 315:1529–1532.
- Shepherd, A., Wingham, D., and Rignot, E. (2004). Warm ocean is eroding West Antarctic Ice Sheet. *Geophysical Research Letters*, 31:L23402.
- Shepherd, A., Wingham, D. J., and Mansley, J. A. D. (2002). Inland thinning of the Amundsen Sea sector, West Antarctica. *Geophysical Research Letters*, 29.
- Shepherd, A., Wingham, D. J., Mansley, J. A. D., and Corr, H. F. J. (2001). Inland Thinning of Pine Island Glacier, West Antarctica. *Science*, 291:862–864.
- Siegert, M. J. (1999). On the origin, nature and uses of Antarctic ice-sheet radio-echo layering. *Progress in Physical Geography*, 23(2):159–179.
- Siegert, M. J. (2005). Lakes beneath the ice sheet: The occurrence, analysis and future exploration of lake wostok and other antarctic subglacial lakes. *Annual Review of Earth and Planetary Sciences*, 33:215–245.
- Siegert, M. J., Carter, S., Tabacco, I., Popov, S., and Blankenship, D. D. (2005a). A revised inventory of Antarctic subglacial lakes. *Antarctic Science*, 17(3):453–460.
- Siegert, M. J., Dowdeswell, J. A., Gorman, M. R., and McIntyre, N. F. (1996). An inventory of Antarctic sub-glacial lakes. *Antarctic Science*, 8:281–286.
- Siegert, M. J., Hindmarsh, R. C., and Hamilton, G. S. (2003a). Evidence for a large surface ablation zone in central East Antarctica during the last Ice Age. *Quaternary Research*, 59:114–121.

- Siegert, M. J., Hodgkins, R., and Dowdeswell, J. A. (1998). A chronology for the Dome C deep ice-core site through radio-echo layer correlation with the Vostok ice core, Antarctica. *Geophysical Research Letters*, 25(7):1019–1022.
- Siegert, M. J. and Payne, A. J. (2004). Past rates of accumulation in central West Antarctica. *Geophysical Research Letters*, 31.
- Siegert, M. J., Payne, A. J., and Joughin, I. (2003b). Spatical stability of Ice Stream D and its tributaries, West Antarctica, revealed by radio-echo sounding and interferometry. *Annals of Glaciology*, 37:377–382.
- Siegert, M. J., Pokar, M., Dowdeswell, J. A., and Benham, T. (2005b). Radio-echo layering in West Antarctica: a spreadsheet dataset. *Earth surface processes and landforms*, 30:1583–1591.
- Siegert, M. J., Taylor, J., and Payne, A. J. (2005c). Spectral roughness of subglacial topography and implications for former ice-sheet dynamics in East Antarctica. *Global and Planetary Change*, 45:249–263.
- Siegert, M. J., Taylor, J., Payne, A. J., and Hubbard, B. (2004a). Macro-scale bed roughness of the Siple Coast ice streams in West Antarctica. *Earth Surface Processes and Landforms*, 29:1591–1596.
- Siegert, M. J., Welch, B., Morse, D., Vieli, A., Blankenship, D. D., Joughin, I., King, E. C., Vieli, G. J.-M. C. L., Payne, A. J., and Jacobel, R. (2004b). Ice Flow Direction Change in Interior West Antarctica. *Science*, 305:1948–1951.
- Sime, L. C., Hindmarsh, R. C. A., and Corr, H. F. J. (2010). Automated Processing of Internal Ice Layer Dips in Radio-Echo Soundings. *Journal of Glaciology*.
- Smith, B. E., Fricker, H. A., Joughin, I. R., , and Tulaczyk, S. (2009). An inventory of active subglacial lakes in Antarctica detected by ICESat (2003–2008). *Journal of Glaciology*, 55(192):573–595.
- Smith, G. D. (1985). *Numerical solution of partial differential equations: finite difference methods*. Clarendon Press, Oxford, 3 edition.
- Snyder, J. P. (1987). *Map Projections - A Working Manual*. U. S. Geological Survey.
- Solomon, S., Qin, D., Manning, M., Chen, Z., Marquis, M., Averyt, K., Tignor, M., and Miller, H., editors (2007). *Contribution of Working Group I to the Fourth Assessment Report of the Intergovernmental Panel on Climate Change, 2007*. Cambridge University Press.

- Stenoién, M. D. and Bentley, C. R. (2000). Pine Island Glacier, Antarctica: A study of the catchment using interferometric synthetic aperture radar measurements and radar altimetry. *Journal of Geophysical Research*, 105:21761–21779.
- Stone, J. O., Balco, G. A., Sugden, D. E., Caffee, M. W., Sass, L. C., Cowdery, S. G., and Siddoway, C. (2003). Holocene Deglaciation of Marie Byrd Land, West Antarctica. *Science*, 299:99–102.
- Sugden, D. E., Bentley, M. J., and Ó Cofaigh, C. (2006). Geological and geomorphological insights into Antarctic ice sheet evolution. *Philosophical Transactions of The Royal Society A*, 364:1607–1625.
- Sugden, D. E. and John, B. S. (1976). *Glaciers and Landscape: A Geomorphological Approach*. Edward Arnold, London.
- Tabacco, I., Passerini, A., Corbelli, F., and Gorman, M. (1998). Determination of the surface and bed topography at Dome C, East Antarctica. *Journal of Glaciology*, 44:185–191.
- Taylor, J., Siegert, M. J., Payne, A. J., and Hubbard, B. (2004). Regional-scale bed roughness beneath ice masses: measurement and analysis. *Computers and Geosciences*, 30:899–908.
- Thomas, R., Rignot, E., Casassa, G., Kanagaratnam, P., Acuna, C., Akins, T., Brecher, H., Frederick, E., Gogineni, P., Krabill, W., Manizade, S., Ramamoorthy, H., Rivera, A., Russell, R., Sonntag, J., Swift, R., Yungel, J., and Zwally, J. (2004a). Accelerated Sea-Level Rise from West Antarctica. *Science*, 306:255–258.
- Thomas, R., Rignot, E., Kanagaratnam, P., Krabill, W., and Casassa, G. (2004b). Force-perturbation analysis of Pine Island Glacier, Antarctica, suggests cause for recent acceleration. *Annals of Glaciology*, 39(1):133–138.
- Thomas, R. H. (1979). The Dynamics of Marine Ice Sheets. *Journal of Glaciology*, 24(90):167–177.
- Thompson, D. W. J. and Wallace, J. M. (2000). Annular Modes in the Extratropical Circulation. Part I: Month-to-Month Variability. *Journal of Climate*, 13:1000–1016.
- Thorsteinsson, T., Raymond, C. F., Gudmundsson, G. H., Bindschadler, R. A., Vornberger, P., and Joughin, I. (2003). Bed topography and lubrication inferred

- from surface measurements on fast-flowing ice streams. *Journal of Glaciology*, 49:481–490.
- Turchetti, S., Dean, K., Naylor, S., and Siegert, M. (2008). Accidents and opportunities: a history of the radio echo-sounding of Antarctica, 1958-79. *The British Journal for the History of Science*, 41(3):417–444.
- van den Broeke, M. R., van de Berg, W. J., and van Meijgaard, E. (2006). Snowfall in coastal West Antarctica much greater than previously assumed. *Geophysical Research Letters*, 33.
- van den Broeke, M. R. and van Lipzig, N. P. M. (2004). Changes in Antarctic temperature, wind and precipitation in response to the Antarctic Oscillation. *Annals of Glaciology*, 39:119–126.
- van der Veen, C. J. (1999). *Fundamentals of Glacier Dynamics*. Balkema.
- van der Veen, C. J. (2001). Greenland ice sheet response to external forcing. *Journal of Geophysical Research*, 106:34047–34058.
- Vaughan, D. G. (2008). West Antarctic Ice Sheet collapse - the fall and rise of a paradigm. *Climatic Change*, 91:65–79.
- Vaughan, D. G. and Arthern, R. (2007). Why is it hard to predict the future of ice sheets? *Science*, 315:1503–1504.
- Vaughan, D. G., Corr, H. F., Smith, A. M., Pritchard, H. D., and Shepherd, A. (2008). Flow-switching and water piracy between Rutford Ice Stream and Carlson Inlet, West Antarctica. *Journal of Glaciology*, 54(184):41–48.
- Vaughan, D. G., Corr, H. F. J., Doake, C. S. M., and Waddington, E. D. (1999). Distortion of isochronous layers in ice revealed by ground-penetrating radar. *Nature*, 398:232–326.
- Vaughan, D. G., Corr, H. F. J., Ferracioli, F., Frearson, N., O'Hare, A., Mach, D., Holt, J. W., Blankenship, D. D., Morse, D. L., and Young, D. A. (2006). New boundary conditions for the West Antarctic ice sheet: Subglacial topography beneath Pine Island Glacier. *Geophysical Research Letters*, 30.
- Vaughan, D. G., Smith, A. M., Corr, H. F. J., Jenkins, A., Bentley, C. R., Stenoién, M. D., Jacobs, S. S., Kellogg, T. B., Rignot, E., and Luccitta, B. K. (2001). A review of Pine Island Glacier, West Antarctica: Hypotheses of instability vs. observations of change. In Alley, R. B. and Bindshadler, R. A.,

- editors, *The West Antarctic ice sheet: behavior and environment*, volume 77 of *Antarctic Research Series*, pages 237–256.
- Vaughan, D. G., Smith, A. M., Nath, P. C., and Meur, E. L. (2003). Acoustic impedance and basal shear stress beneath four Antarctic ice streams. *Annals of Glaciology*, 36:225–232.
- Vieli, A., Funk, M., and Blatter, H. (2000). Tidewater glaciers: frontal flow acceleration and basal sliding. *Annals of Glaciology*, 31:217–221.
- Vinther, B. M., Buchardt, S. L., Clausen, H. B., Dahl-Jensen, D., Johnsen, S. J., Fisher, D. A., Koerner, R. M., Raynaud, D., Lipenkov, V., Andersen, K. K., Blunier, T., Rasmussen, S. O., Steffensen, J. P., and Svensson, A. M. (2009). Holocene thinning of the Greenland ice sheet. *Nature*, 461:385–388.
- Waite, A. and Schmidt, S. J. (1962). Gross errors in height indication from pulsed radar altimeters operating over thick ice or snow. *Proceedings of the Institute of Radio Engineers*, 50:1515–1520.
- Weertman, J. (1974). Stability of the junction of an ice sheet and an ice shelf. *Journal of Glaciology*, 13(67):3–11.
- Weertman, J. (1976). Sliding-no sliding zone effect and age determination of ice cores. *Quaternary Research*, 6(2):203–207.
- Welch, B. C. and Jacobel, R. W. (2003). Analysis of deep-penetrating radar surveys of West Antarctica, US-ITASE 2001. *Geophysical Research Letters*, 30(8).
- Welch, B. C., Jacobel, R. W., and Arcone, S. A. (2009). First results from radar profiles collected along the US-ITASE traverse from Taylor Dome to South Pole (2006-2008). *Annals of Glaciology*, 50:35–42.
- Whillans, I. M., Bolzan, J., and Shabtaie, S. (1987). Velocity of Ice Stream B and C, Antarctica. *Journal of Geophysical Research*, 92:8895–8902.
- Wilch, T. I., McIntosh, W. C., and Dunbar, N. W. (1999). Late Quaternary volcanic activity in Marie Byrd Land: Potential  $^{40}\text{Ar}/^{39}\text{Ar}$ -dated time horizons in West Antarctic ice and marine cores. *Geological Society of America Bulletin* October 1999 v. 111 no. 10 p. 1563-1580, 111:1563–1580.
- Wingham, D., Francis, C., Baker, S., Bouzinac, C., Brockley, D., Cullen, R., de Chateau-Thierry, P., Laxon, S., Mallow, U., Mavrocordatos, C., Phalippou,

- L., Ratier, G., Rey, L., Rostan, F., Viau, P., and Wallis, D. (2006). CryoSat: A mission to determine the fluctuations in Earth's land and marine ice fields. *Advances in Space Research*, 37:841–871.
- Wingham, D. J., Wallis, D. W., and Shepherd, A. (2009). Spatial and temporal evolution of Pine Island Glacier thinning, 1995-2006. *Geophysical Research Letters*, 36.
- Wolff, E., Brook, E., Dahl-Jensen, D., Fujii, Y., Jouzel, J., Lipenkov, V., and Severinghaus, J. (2006). Ipics white paper: The oldest ice core: A 1.5 million year record of climate and greenhouse gases from Antarctica. Technical report, The International Partnerships in Ice Core Sciences.
- Zwally, H. J., Schutz, B., Abdalati, W., Abshire, J., Bentley, C., Brenner, A., Bufton, J., Dezio, J., Hancock, D., Harding, D., Herring, T., Minster, B., Quinn, K., Palm, S., Spinhirne, J., and Thomas, R. (2002). Icesat's laser measurements of polar ice, atmosphere, ocean, and land. *Journal of Geodynamics*, 34(3-4):405 – 445.



# Appendix A

## Construction of a Two-Dimensional Ice Flow Model

As described in Section 4.3.2 the two-dimensional flow model used in this thesis is based on a solution of the age equation (Equation 2.10 from Chapter 2). In this appendix a short iteration will be given of the main equations and then the construction of the two-dimensional model will be discussed in more detail.

The two-dimensional model calculates internal layering by solving the age equation in two dimensions:

$$\frac{\partial X}{\partial t} + u \frac{\partial X}{\partial x} + w \frac{\partial X}{\partial z} = 1 \quad (\text{A.1})$$

In order to achieve this aim the differential equation is approximated by finite differences (as discussed in Section 4.3.2). The time derivative is solved for by using Crank-Nicholson's method that states that:

$$\frac{X^{n+1} - X^n}{\Delta t} = \frac{1}{2} \left( \left. \frac{\partial X}{\partial t} \right|^{n+1} + \left. \frac{\partial X}{\partial t} \right|^n \right) \quad (\text{A.2})$$

The spatial components are solved using a second-order, upstream, finite difference for the  $z$ -component:

$$\frac{\partial X}{\partial z} = \frac{3X(x_i, z_i) - 4X(x_i, z_{i-1}) + X(x_i, z_{i-2})}{2\Delta z} \quad (\text{A.3})$$

and a first-order, upstream, finite difference for the  $x$ -component:

$$\frac{\partial X}{\partial x} = \frac{X(x_i, z_i) - X(x_{i-1}, z_i)}{\Delta x} \quad (\text{A.4})$$

Rearranging Equation A.1 and inserting it into Equation A.2 gives

$$\begin{aligned} \frac{X^{n+1} - X^n}{\Delta t} &= \frac{1}{2} \left( \left(1 - u \frac{\partial X}{\partial x} \Big|^{n+1} - w \frac{\partial X}{\partial z} \Big|^{n+1}\right) + \left(1 - u \frac{\partial X}{\partial x} \Big|^n - w \frac{\partial X}{\partial z} \Big|^n\right) \right) \rightarrow \\ X^{n+1} - \frac{\Delta t}{2} \left(1 - \left(u \frac{\partial X}{\partial x} \Big|^{n+1} + w \frac{\partial X}{\partial z} \Big|^{n+1}\right)\right) &= X^n + \frac{\Delta t}{2} \left(1 - \left(u \frac{\partial X}{\partial x} \Big|^n + w \frac{\partial X}{\partial z} \Big|^n\right)\right) \end{aligned} \quad (\text{A.5})$$

From Equations A.3 and A.4 the two spatial components are now written

$$\begin{aligned} u \frac{\partial X}{\partial x} + w \frac{\partial X}{\partial z} &= u_{ij} \frac{X_{ij} - X_{i-1,j}}{\Delta x} + w_{ij} \frac{3X_{i,j} - 4X_{i,j-1} + X_{i,j-1}}{2\Delta z} \\ &= \left(\frac{u_{ij}}{\Delta x} + 3/2 \frac{w_{ij}}{\Delta z}\right) X_{ij} - \frac{u_{ij}}{\Delta x} X_{i-1,j} - \frac{2w_{ij}}{\Delta z} X_{i,j-1} + \frac{w_{ij}}{2\Delta z} X_{i,j-2} \end{aligned} \quad (\text{A.6})$$

And Equation A.6 is now inserted into Equation A.5:

$$\begin{aligned} X_{ij}^{n+1} - \frac{\Delta t}{2} \left(1 - \left(\frac{u_{ij}}{\Delta x} + \frac{3w_{ij}}{2\Delta z}\right) X_{ij}^{n+1} - \frac{u_{ij}}{\Delta x} X_{i-1,j}^{n+1} - \frac{2w_{ij}}{\Delta z} X_{i,j-1}^{n+1} + \frac{w_{ij}}{2\Delta z} X_{i,j-2}^{n+1}\right) &= \\ X_{ij}^n + \frac{\Delta t}{2} \left(1 - \left(\frac{u_{ij}}{\Delta x} + \frac{3w_{ij}}{2\Delta z}\right) X_{ij}^n - \frac{u_{ij}}{\Delta x} X_{i-1,j}^n - \frac{2w_{ij}}{\Delta z} X_{i,j-1}^n + \frac{w_{ij}}{2\Delta z} X_{i,j-2}^n\right) \end{aligned} \quad (\text{A.7})$$

Rearranging the terms according the  $X$ -terms gives

$$\begin{aligned} \left(1 + \frac{\Delta t}{2} \left(\frac{u_{ij}}{\Delta x} + \frac{3w_{ij}}{2\Delta z}\right)\right) X_{ij}^{n+1} + \frac{\Delta t u_{ij}}{2\Delta x} X_{i-1,j}^{n+1} + \frac{\Delta t w_{ij}}{\Delta z} X_{i,j-1}^{n+1} - \frac{\Delta t w_{ij}}{4\Delta z} X_{i,j-2}^{n+1} &= \\ \left(1 - \frac{\Delta t}{2} \left(\frac{u_{ij}}{\Delta x} + \frac{3w_{ij}}{2\Delta z}\right)\right) X_{ij}^n - \frac{\Delta t u_{ij}}{2\Delta x} X_{i-1,j}^n - \frac{\Delta t w_{ij}}{\Delta z} X_{i,j-1}^n + \frac{\Delta t w_{ij}}{4\Delta z} X_{i,j-2}^n + \Delta t \end{aligned} \quad (\text{A.8})$$

In order to simplify the expression the following terms are now defined:

$$\begin{aligned} \alpha_{ij} &= 1 + \frac{\Delta t}{2} \left(\frac{u_{ij}}{\Delta x} + \frac{3w_{ij}}{2\Delta z}\right) \\ \beta_{ij} &= 1 - \frac{\Delta t}{2} \left(\frac{u_{ij}}{\Delta x} + \frac{3w_{ij}}{2\Delta z}\right) \\ \gamma_{ij} &= \frac{\Delta t u_{ij}}{2\Delta x} \\ \epsilon_{ij} &= \frac{\Delta t w_{ij}}{\Delta z} \\ \lambda_{ij} &= \frac{\Delta t w_{ij}}{4\Delta z} \end{aligned}$$

The subscripts  $ij$  have been added to emphasise that the parameters above are not constant in space. In the following the subscript will occasionally be omitted to avoid cluttering. Inserted into Equation A.8 this leads to the following expression:

$$\alpha X_{ij}^{n+1} + \gamma X_{i-1,j}^{n+1} + \epsilon X_{i,j-1}^{n+1} - \lambda X_{i,j-2}^{n+1} = \beta X_{ij}^n - \gamma X_{i-1,j}^n - \epsilon X_{i,j-1}^n + \lambda X_{i,j-2}^n + \Delta t \quad (\text{A.9})$$

Based on Equation A.9 two tri-diagonal matrices  $\bar{\bar{\mathbf{A}}}$  and  $\bar{\bar{\mathbf{B}}}$  can now be constructed such that

$$\bar{\bar{\mathbf{A}}}\mathbf{X}_v^{n+1} = \Delta t + \bar{\bar{\mathbf{B}}}\mathbf{X}_v^n \tag{A.10}$$

where  $\mathbf{X}_v$  is the agefield  $\bar{\bar{\mathbf{X}}}$  converted from matrix to vector:

$$\bar{\bar{\mathbf{X}}} = \begin{pmatrix} X_{11} & X_{21} & \cdots & \cdots & X_{k1} \\ X_{12} & X_{22} & \cdots & \cdots & \vdots \\ \vdots & \vdots & \ddots & & \vdots \\ X_{1,m-1} & X_{2,m-1} & & \ddots & X_{k,m-1} \\ X_{1m} & X_{2m} & \cdots & \cdots & X_{km} \end{pmatrix} \implies \mathbf{X}_v = \begin{pmatrix} X_{11} \\ X_{12} \\ \vdots \\ X_{i,j-1} \\ X_{ij} \\ X_{i,j+1} \\ \vdots \\ X_{km} \end{pmatrix}$$

This means that if the agefield is a matrix of the dimensions  $k \times m$ , the matrices  $\bar{\bar{\mathbf{A}}}$  and  $\bar{\bar{\mathbf{B}}}$  needs to be of the dimensions  $k * m \times k * m$ . Thus from Equation A.9

$$\bar{\bar{\mathbf{A}}} = \begin{pmatrix} \cdots & \cdots & \cdots & & & & & & 0 \\ \cdots & & \cdots & \cdots & \cdots & & & & \\ \cdots & \gamma_{ij} & \cdots & \epsilon_{ij} & -\lambda_{ij} & \alpha_{ij} & \cdots & \cdots & \\ & & \cdots & & \cdots & \cdots & \cdots & & \\ 0 & & & \gamma_{km} & \cdots & \epsilon_{km} & -\lambda_{km} & \alpha_{km} & \end{pmatrix}$$

$$\bar{\bar{\mathbf{B}}} = \begin{pmatrix} \cdots & \cdots & \cdots & & & & & & 0 \\ \cdots & & \cdots & \cdots & \cdots & & & & \\ \cdots & -\gamma_{ij} & \cdots & -\epsilon_{ij} & \lambda_{ij} & \beta_{ij} & \cdots & \cdots & \\ & & \cdots & & \cdots & \cdots & \cdots & & \\ 0 & & & -\gamma_{km} & \cdots & -\epsilon_{km} & \lambda_{km} & \beta_{km} & \end{pmatrix}$$

In order to arrive at a solution for  $\mathbf{X}_v^{n+1}$  the matrix  $\bar{\bar{\mathbf{A}}}$  in Equation A.10 is inverted and the equation thus reads

$$\mathbf{X}_v^{n+1} = \bar{\bar{\mathbf{A}}}^{-1}(\Delta t + \bar{\bar{\mathbf{B}}}\mathbf{X}_v^n) \tag{A.11}$$

as can be seen from the equation above this means that knowledge of  $\mathbf{X}_v^n$  is necessary in order to calculate  $\mathbf{X}_v^{n+1}$ . In other words an initial guess of the age field is needed. This initial guess is calculated from the original Equation A.1 using the same finite differences but as a time-independent equation guess such

that

$$u \frac{\partial X}{\partial x} + w \frac{\partial X}{\partial z} = 1 \quad (\text{A.12})$$

$$X_{ij} + \left( \frac{u_{ij}}{\Delta x} + \frac{3w_{ij}}{2\Delta z} \right) X_{ij} - \frac{u_{ij}}{\Delta x} X_{i-1,j} - \frac{2w_{ij}}{\Delta z} X_{i,j-1} + \frac{w_{ij}}{2\Delta z} X_{i,j-2} = 1 \quad (\text{A.13})$$

which leads to a solution of the kind

$$\bar{\bar{\mathbf{C}}}\mathbf{X}_v = \mathbf{1} \quad (\text{A.14})$$

where  $\bar{\bar{\mathbf{C}}}$  can be constructed in a way similar to that described above for the matrices  $\bar{\mathbf{A}}$  and  $\bar{\mathbf{B}}$ .

The difference between the solution for Equation A (time-independent) and for Equation A.10 (time-dependent) is in the end very small since the mass balance and the ice thickness is set to be constant in time. Thus the velocity field does not change. Running the model with the time-dependent solution corresponds essentially to iterate the solution until steady state is reached.